

Investigation of the mechanistic basis of substrate recognition and translocation by the MFS flippase LtaA

Inauguraldissertation

zur

Erlangung der Würde eines Doktors der Philosophie

vorgelegt der

Philosophisch-Naturwissenschaftlichen Fakultät

der Universität Basel

von

Elisabeth Lambert

Basel, 2022

Originaldokument gespeichert auf dem Dokumentenserver der Universität

Basel <https://edoc.unibas.ch>

Genehmigt von der Philosophisch-Naturwissenschaftlichen Fakultät
auf Antrag von

Prof. Dr. Camilo Perez
Prof. Dr. Timm Maier
Prof. Dr. Christine Ziegler

Basel, den 16.11.2021

Prof. Dr. Marcel Mayor
(Dekan)

Abstract

Lipoteichoic acids (LTA) are essential cell-wall components in Gram-positive bacteria, including the human pathogen *Staphylococcus aureus*. They contribute to cell growth, cell stability, virulence and cell division. Interrupting their biogenesis pathway leads to severe growth defect such as longer LTAs, larger cells, and misplaced septa. *S. aureus* LTA is composed out of a polyglycerol chain on a gentiobiosyl-diacylglycerol anchor. Their synthesis starts on the cytoplasmic leaflet of the membrane by the glycosyltransferase YpfP, followed by translocation of the lipid-linked disaccharide across the plasma membrane, followed by polymerization of the chain at the extracellular side of the membrane. Genetic evidence has suggested that LtaA is the flippase responsible for the translocation of the lipid-linked disaccharide.

In the first part of this thesis, we confirm that LtaA is indeed the flippase performing the translocation of gentiobiosyl-diacylglycerol anchor during LTA biosynthesis. We present the outward-open crystal structure of LtaA and identify that LtaA contains the Major Facilitator Superfamily (MFS) topology. Investigation of the structure showed that LtaA contains a amphiphilic cavity, which was never observed before. In this cavity the N-terminal cavity consist of polar residues whereas the C-terminal cavity is composed of hydrophilic residues. Using our established *in vitro* flipping activity assay, and *S. aureus* Δ LtaA strains, we demonstrate the importance of the hydrophobic cavity. We show that LtaA is a proton-coupled antiporter, which is essential for *S. aureus* to combat physiological acidic stress conditions. Elucidation of the LtaA structure identified the first MFS flippase, and the first proton-coupled flippase.

Flipping of lipids with large polar headgroups is an energetically costly reaction, that is frequently coupled to ABC transporters. However, ion-coupled lipid transporters of the MFS, such as LtaA, have been shown to play essential roles in cell wall synthesis, brain development and function, lipids recycling, and cell signaling. Structures of MFS transporters showed overlapping architectures pointing to a common mechanism. Whereas studies on ATP-driven transporters have shown to operate via a 'trap-and-flip' or 'credit-card' mechanism, the mechanism of ion-coupled MFS lipid transporters is largely unknown. The second part of this thesis investigates the flipping mechanism used by LtaA as a representative system of MFS flippases.

We show using cysteine-crosslinking that LtaA adopts alternating conformations, and that alternating access to the cavity is essential for transport. We reveal that LtaA adopts asymmetric openings with distinct functional relevance during transport of the glycolipid. We characterized the hydrophobic cavity using *in vivo* and *in vitro* assays, showing that the entire amphipathic cavity of LtaA contributes to lipid binding. Although, the N-terminal hydrophilic

pocket imposes the substrate specificity. Based on these results, we propose that LtaA catalyzes lipid translocation using a 'trap-and-flip' mechanism that might be shared within the MFS lipid transporters subfamily.

Taken together, a thorough investigation of LtaA is performed in this thesis. Our results unveil important structural and mechanistic details showing that LtaA recognizes the gentiobiosyl-diacylglycerol by its gentiobiosyl headgroup and adapts an asymmetric lateral opening to load the substrate into the cavity. In the cavity the sugar headgroup interacts with the N-terminal hydrophilic pocket, and the lipid tails are embedded in the hydrophobic C-terminal pocket. After conformational changes, the substrate is released via both lateral gates at the extracellular side. This is followed by protonation of LtaA, inducing conformational changes to an inward-facing conformation. These mechanistic results provide foundations for developments of new strategies to counteract live-threatening *S. aureus* infections, as well as a basis for drugs and lipid-linked-bioactive molecules targeting cells expressing pharmacologically important proteins from the MFS.

Acknowledgements

This thesis wouldn't have been possible without the help of many people! I would like to thank everyone who supported me during this time both scientifically and personally.

First and foremost, I would like to thank my supervisor Prof. Dr. Camilo Perez for the opportunity to conduct my PhD thesis in his lab. It has been a bumpy ride with unpurifiable proteins and being scooped, but as they say 'three is a charm', and project number 3 was indeed my lucky number. It was not the most straightforward way, but it gave me the opportunity to learn a lot of different techniques and perform many different experiments, something I am very happy about. Thank you for your guidance, I am very grateful to have learned from you, both in the beginning when you helped me a lot in the lab, as later during our many scientific discussions.

Thank you to my thesis committee members Prof. Dr. Timm Maier and Prof. Dr. Christine Ziegler for your guidance and advice during this thesis, especially for your insightful comments on my project.

I would like to thank Prof. Dr. Jan-Willem Veening, and Dr. Xue Liu for the nice collaboration which led to a really great story! I am also very grateful for the warm welcome when I came to the lab in Lausanne, especially to Xue for teaching me to work with *Staphylococcus*, and for all the advice you gave me when I performed following-up experiments. I wish you all the best in your own lab!

Furthermore, I would like to thank Dr. Ahmad Reza Medhipour and Prof. Dr. Gerhard Hummer for the nice all the models and MD data. In particular, thank you to Reza for all the interesting discussions. I hope that you will feel at home in Gent as much as I do.

I would like to thank all members of the Perez lab for all the interesting and nice moments during the past four years! Bing, thank you for letting me in on this interesting project! In ten years, when you come back with your kids, I will cook some typical Belgian food, I promise! Thank you to Natalie for showing me around in the Biozentrum, and introducing me to all the amazing things Basel has to offer. Gonzalo, thank you for always being there to help me around in the lab! Also thank you for listening when I had to complain (over and over again). If your scientific career doesn't work out, I am sure you will be a good lab DJ! Thank you to Arantza for all your compassion during lunches and coffee breaks. Xiaochun, thank you, for all your help with the expressions of the many mutants that I had! Firas, from who will you now steal the Biobeads? ;)

I would also like to thank all the people at the Biozentrum that make it an amazing place to do science. In particular, I would like to thank Alex and Ulrike from the mass spec facility for all their help with my different projects, Tim Sharpe from the Biophysics facility to always take the time to discuss my scientific problems, and to help finding the best solutions. I would also like to thank Susanna for all her help with the paper work, and to Simone and Angie of the PhD student office for all the support.

I am very grateful to Gonzalo, Johanna, Anne and Firas for their input and corrections of this thesis and to Sarah to help me with lay-outing this thesis.

I would like to thank the Biozentrum fellowship for my financial support during my thesis, for all the nice travels and the freedom to choose my own project within the institute.

Thomas, thank you for providing me with coffee during this writing process! It was highly appreciated!

A special thanks goes as well to all the people that made Basel my second home! Lieve Elieke, waarschijnlijk hadden we elkaar nooit ontmoet als je niet mijn kamergenoot was tijdens de 'fellowship week', en hadden we al die jaren later niet zo'n echte vriendschap gehad. Dus ik ben heel blij dat ik toen een kamer met jou moest delen! Milena, our many 'wine at the Rhine' evenings kept me sane during those crazy times! They are memories that I will always cherish. Sheida, after our coffee breaks, I always felt better, thank you for providing me with cookies and an ear when I needed it! Anne, thank you for always being there whatever I need, it's comforting to know that there's always a hug available. Chris, we had so many discussions about science and life, talking to you always changed my perspective on things. I know that you'll do great during your own PhD! Polina, it was always great to have drinks on Friday evening, and get everything out of our system ;) Clément, it's funny how a bet about my favorite word and Belgian beer turned out in such a special friendship. Thank you for always having your rational answers to my over-emotional thoughts. Dear Johanna, thank you for being there after tough days and always providing food and hugs whenever I needed it! It was a real pleasure to have you as my flatmate during this time!

I also wanted to thank all my friends from back home! I am surprised that I stayed in contact with so many of you. When I went back to Belgium, it was always a whole puzzle with personal engagements, but it was always a pleasure to meet up! Thank you for all the phone and skype calls, especially during the pandemic. I was always very happy to play guide whenever you came to visit me :)

Hélène, ik kon altijd mijn hart luchten bij jou, wat er ook was. Dank je wel voor je vele (bijna dagelijkse) berichtjes om te vragen hoe het met me ging! Margot en Charlotte, we hoorden elkaar soms lang niet, dan met periodes weer vaker, maar ik weet dat jullie er altijd zijn voor

mij. We hebben elkaar niet zo vaak gezien de voorbije vier jaar, maar wanneer we elkaar zagen, had ik altijd het gevoel dat het sinds vorige week geleden was, en dat is een fantastisch gevoel!

Oma, dank je wel voor alle post die naar de Letziturm gestuurd is, het bracht me altijd een beetje dichterbij het vaderland. Broer en Zus, sorry dat het rondom mij draaide als ik dan eens thuis was. Jullie zijn twee zo'n fantastische mensen en ik ben heel blij dat ik jullie heb om alles mee te delen. Danny, dank je wel om altijd mee te draaien voor al mijn plannen, voor alle taxi's van en naar de luchthaven en zelfs tot in Basel. Hoe toevallig hè dat je net hier aan het wandelen bent ;) Ik vond het altijd heel leuk als ik mee op pad ging! Papa, dank je wel om me altijd raad en af en toe een push te geven, zelfs als ik het niet altijd wou. Ik ben nog altijd beetje chagrijnig dat ik jou niet mocht helpen, vandaar dat ik nu mijn eigen doctoraat wou schrijven ;) Mama, dank je wel om altijd maar een telefoontje weg te zijn, wat er ook was! Het feit dat ik je altijd kon bellen, gaf me vaak veel moed om door te zetten. Maar ik wil je vooral bedanken om zo'n fantastisch voorbeeld van een sterke vrouw te zijn!

Ik zou dit niet gekund hebben zonder jullie steun!

List of Abbreviations

AATGal	2-acetamido-4-amino-2,4,6-trideoxy-D-galactose
ABC	ATP-binding cassette
ACMA	9-amino-6-chloro-2-methoxyacridine
AMP	adenosine-monophosphate
anchor-LLD	anchor lipid-linked-disaccharide gentiobiosyl-diacylglycerol
APC	amino acid-polyamine-organocation
ATP	adenosine-triphosphate
<i>aux</i>	auxiliary factors
CID	collision-induced dissociation
DAG	diacylglycerol
DDM	N-dodecyl- β -D-maltopyranoside
DHA	docosahexaenoic acid
dit.	dithionite
<i>E. coli</i>	<i>Escherichia coli</i>
EM	electron microscopy
<i>fem</i>	factors essential for methicillin resistance
G6P	glucose-6-phosphate
Gal	galactose
Gal ₂ -DAG	digalactosyl-diacylglycerol
Glc	glucose
Glc ₂ -DAG	gentiobiosyl-diacylglycerol
GlcN	glycylamine
GlcNAc	N-acetylglucosamine
GPCR	G-protein coupled receptor
GroP	glycerolphosphate
HCD	high-collision-dissociation
HL	helical loop
INW_M	inward-facing models
IPTG	isopropyl β -D-1-thiogalactopyranoside
LB	luria-bertani
LC-MS	liquid-chromatography- mass spectrometry
LLO	lipid-linked-oligosaccharide
LMNG	Lauryl Maltose Neopentyl Glycol
LPA	lysophosphatidic acids
LPC	lysophosphatidylcholine
LPE	lysophosphatidylethanolamine
LPG	lysophosphatidylglycerol
LPS	lipopolysaccharides
LTA	lipoteichoic acid
ManNAc	N-acetyl-D-mannosamine
MATE	multidrug and toxic compound extrusion
MD	molecular dynamics
MDR-MFS	multidrug resistance-major facilitator superfamily

MFS	major facilitator superfamily
MIC	minimal inhibitory concentration
MOP	multidrug/oligosaccharidyl-lipid/polysaccharide
mPEG5k	5-kDa PEG-maleimide
MR	molecular replacement
MRSA	methicillin-resistant <i>S. aureus</i>
MurNAc	N-acetylmuramic acid
NBD	nitrobenzoxadiazole
NSS	neurotransmitter sodium symporter
o-PDM	N,N'-(o-phenylene)-dimaleimide
OD	optical density
OWF	outward-facing structure
P-Cho	phosphocholine
PBP	penicillin-binding protein
PCR	polymerase chain reaction
PDB	protein database
PG	peptidoglycan
pmf	proton-motive-force
POPE	1-Palmitoyl-2-Oleoyl-sn-Glycero-3-Phosphoethanolamine
POPG	1-Palmitoyl-2-Oleoyl-sn-Glycero-3-Phosphoglycerol
PRM	parallel reaction-monitoring
r.m.s.d.	root mean square deviation
RboP	ribitolphosphate
RND	resistance-nodulation-cell division
<i>S. aureus</i>	<i>Staphylococcus aureus</i>
s.d.	standard deviation
S1P	sphingosine 1-phosphate
SAD	single-wavelength anomalous diffraction
SCC <i>mec</i>	staphylococcal cassette chromosome <i>mec</i>
SEC	size Exclusion chromatography
SeMet	selenomethionine
smf	sodium-motive-force
SMR	small multidrug resistance
TA	teichoic acid
TB	terrific Broth
TCEP	tris(2-carboxyethyl) phosphine
TEAB	triethylammonium bicarbonate
TEM	Transmission electron microscopy
TEV	tobacco etch virus
TLC	thin-layer chromatography
TLR	toll-like receptor
TM	transmembrane
UDP	uridine-diphosphate
Und-PP	undecaprenol pyrophosphate
VRSA	vancomycin-resistant <i>S. aureus</i>
wt	wild type

List of Abbreviations

WTA	wall teichoic acid
XIC	extracted ion chromatogram

Amino Acid	3 letter code	1 letter code
Alanine	Ala	A
Arginine	Arg	R
Asparagine	Asn	N
Aspartic acid	Asp	D
Cysteine	Cys	C
Glutamic acid	Glu	G
Glutamine	Gln	Q
Glycine	Gly	G
Histidine	His	H
Isoleucine	Ile	I
Leucine	Leu	L
Lysine	Lys	K
Methionine	Met	M
Phenylalanine	Phe	F
Proline	Pro	P
Serine	Ser	S
Threonine	Thr	T
Tryptophan	Trp	W
Tyrosine	Tyr	Y
Valine	Val	V

Table of contents

Abstract	i
Acknowledgements	iii
List of Abbreviations	vi
Table of contents	ix
1. Introduction	1
1.1 <i>Staphylococcus aureus</i>	1
1.2 <i>Defense mechanisms of S. aureus</i>	2
1.2.1 <i>Defense mechanisms of S. aureus against immune responses</i>	2
1.2.2 <i>Mechanisms of acquiring antibiotic resistance</i>	2
1.2.3 <i>Methicillin-resistant S. aureus (MRSA) and Vancomycin-resistant S. aureus (VRSA)</i>	4
1.3 <i>Cell wall biogenesis of S. aureus</i>	5
1.3.1 <i>General features of the cell wall</i>	6
1.3.2 <i>Lipoteichoic acids</i>	8
1.4 <i>LtaA as drug target</i>	11
1.5 <i>Protein transporters</i>	12
1.5.1 <i>Secondary transporters</i>	13
1.5.2 <i>Alternating access mechanism</i>	14
1.5.3 <i>Transporter catalyzed lipid translocation</i>	16
1.5.4 <i>General mechanisms of lipid translocation</i>	18
1.6 <i>Major Facilitator Superfamily</i>	20
1.6.1 <i>General features of the MFS</i>	21
1.6.2 <i>Structural details of the MFS transport cycle</i>	22
1.6.3 <i>Energy sources</i>	25
1.6.4 <i>Substrate binding pockets of MFS transporters</i>	25
1.6.5 <i>Flippases within the MFS</i>	26
1.7 <i>Aim of this work</i>	26
2. Structure of a proton-dependent lipid transporter involved in lipoteichoic acids biosynthesis	28
Article.....	29
Supplementary materials	41
3. Evidence for a ‘trap-and-flip’ mechanism in a proton-dependent lipid transporter	51
Manuscript.....	52
Supplementary materials	86

Table of contents

4.	Further characterization of the amphiphilic cavity.....	99
4.1	<i>The hydrophilic N-terminal pocket is specific for a disaccharide anchor headgroup.....</i>	99
4.2	<i>LtaA has a preference for Glc₂-DAG with longer lipid lengths</i>	100
5.	Discussion	101
6.	Conclusions and perspectives.....	108
7.	Bibliography.....	111
8.	Curriculum Vitae	124

1. Introduction

1.1 *Staphylococcus aureus*

Staphylococcus aureus is a commensal gram-positive bacterium of the *Firmicutes* phylum. Approximately 30% of the human population is a continuous carrier of *S. aureus*, while other persons are only sporadically host¹. *S. aureus* cells are found in the nasal cavity, as well as on the skin and in the gastrointestinal tract^{2–4}. The cultures form clusters of cocci, and have a round bacterial cell wall, looking like grapes. Hence, its name originating from the Greek word “staphylos” (grape) (fig. 1.1).

S. aureus is linked to a variety of diseases, including skin and soft tissue infections such as acne, boils, pimples and impetigo. However, *S. aureus* infections can also evolve into pneumonia, osteomyelitis, infectious arthritis, bloodstream infections, endocarditis or sepsis^{5–7}. Furthermore, *S. aureus* colonizes sites of disrupted mucosal barriers, for example in abscesses or surgical wounds. Certain strains of *S. aureus* have been found to be responsible for toxic shock syndrome⁸.

Transmission of *S. aureus* happens in several ways, both in community and healthcare settings⁹. Transmission can occur during close contact with *S. aureus* carriers, such as hand contacts and mother-infant contact, but also during invasive procedures involving intravascular catheters, endotracheal tubes and urinary catheters¹⁰. As for most pathogens, antibiotic resistant *S. aureus* strains, such as methicillin-resistant *S. aureus* (MRSA) and vancomycin-resistant *S. aureus* (VRSA) are emerging problems due to persistence after treatment¹¹. Therefore, the World Health Organization categorized *S. aureus* as a high priority (class 2) for research and development¹².

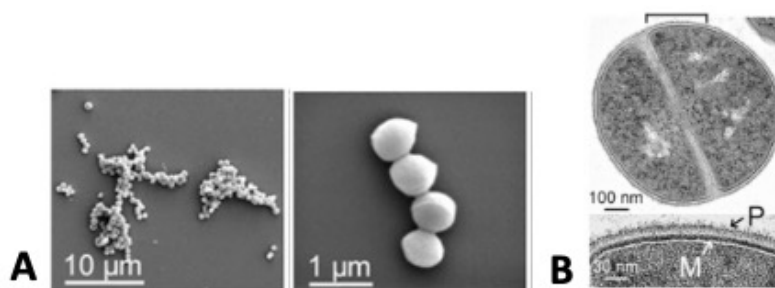


Figure 1.1: Scanning (A) and thin-section transmission (B) electron microscopy of *Staphylococcus aureus* cells. Scale bars are shown on each micrograph. B. Bracket in the upper micrograph indicates the position of the enlarged image sections shown below. M: plasma membrane; P: peptidoglycan layer. Pictures adapted from Richter *et al.*¹³

1.2 Defense mechanisms of *S. aureus*

1.2.1 Defense mechanisms of *S. aureus* against immune responses

The success of *S. aureus* as a pathogen relies to a large part on its ability to evade the host immune system. Entry of *S. aureus* and its replication in the host tissue releases staphylococcal products, such as lipoproteins or peptidoglycans and produces inflammatory signals¹ which are detected by the host immune system via Toll-like receptors (TLRs) and G protein-coupled receptors (GPCR). These receptors then transmit inflammatory signals to finally activate the cognate immune responses¹⁴. However, *S. aureus* evolved a variety of strategies to interfere with the host's innate and adaptive immune response in order to prevent phagocytosis and killing by neutrophils¹.

The thick peptidoglycan (PG) -layer together with the teichoic acids (TAs) represent the first protective barrier during host infection. These adaptations prevent access of immune cells to the *S. aureus* cell membrane leading to reduced efficacy of the membrane attack complex, a protein complex activated by the alternative complement pathway¹⁵. Moreover, the thick PG-layer also helps *S. aureus* to escape Neutrophil-mediated killing^{16–18}. Another way of immune evasion used by *S. aureus* is so-called agglutination, the conversion of fibrinogen to a crosslinked fibrin meshwork. It is an innate defense mechanism used by all vertebrates to immobilize microbial invaders and attract immune cells for phagocytic clearance of bacteria. However, by secretion of two coagulases (Coa and vNbp) *S. aureus* bypasses activation of coagulation and the secretion of inflammatory factors¹⁹. Furthermore, *S. aureus* secretes *Staphylococcus* protein A (SpA), a sortase-anchored surface protein that is stored in the cell envelope and subsequently released by cell wall hydrolases²⁰. SpA has a very high affinity for immunoglobulin, including the most common human IgA, IgD, IgG, IgM and IgE²¹. It binds to the Fc regions of the immunoglobulin, thereby interfering with opsonization and phagocytosis of *Staphylococcus* cells²². Besides these examples, it has also been shown that *S. aureus* can interfere with inhibition of neutrophil extravasation, chemotaxis, complement activation, evasion of T cell responses and phagocytosis¹.

1.2.2 Mechanisms of acquiring antibiotic resistance

Antimicrobial resistance is a global threat to human, animal and environmental health. After the finding of penicillin by Alexander Fleming the golden era of antibiotics started with the discovery of many new antimicrobial agents. However, due to overuse and a decreased rate of newly discovered antibiotics, drug-resistant pathogens have become a world-wide major concern. The main mechanisms of antimicrobial agent activity are inhibition of the cell wall synthesis, depolarization of the membrane, inhibition of protein synthesis, nucleic acid synthesis and metabolic pathways²³.

Antimicrobial resistance can be intrinsic, adaptive or acquired²⁴. Intrinsic resistance is the resistance due to the natural properties of the bacterium itself, e.g. the outer membrane of gram-negative bacteria renders the cell wall impermeable for some antibiotic reagents²⁵.

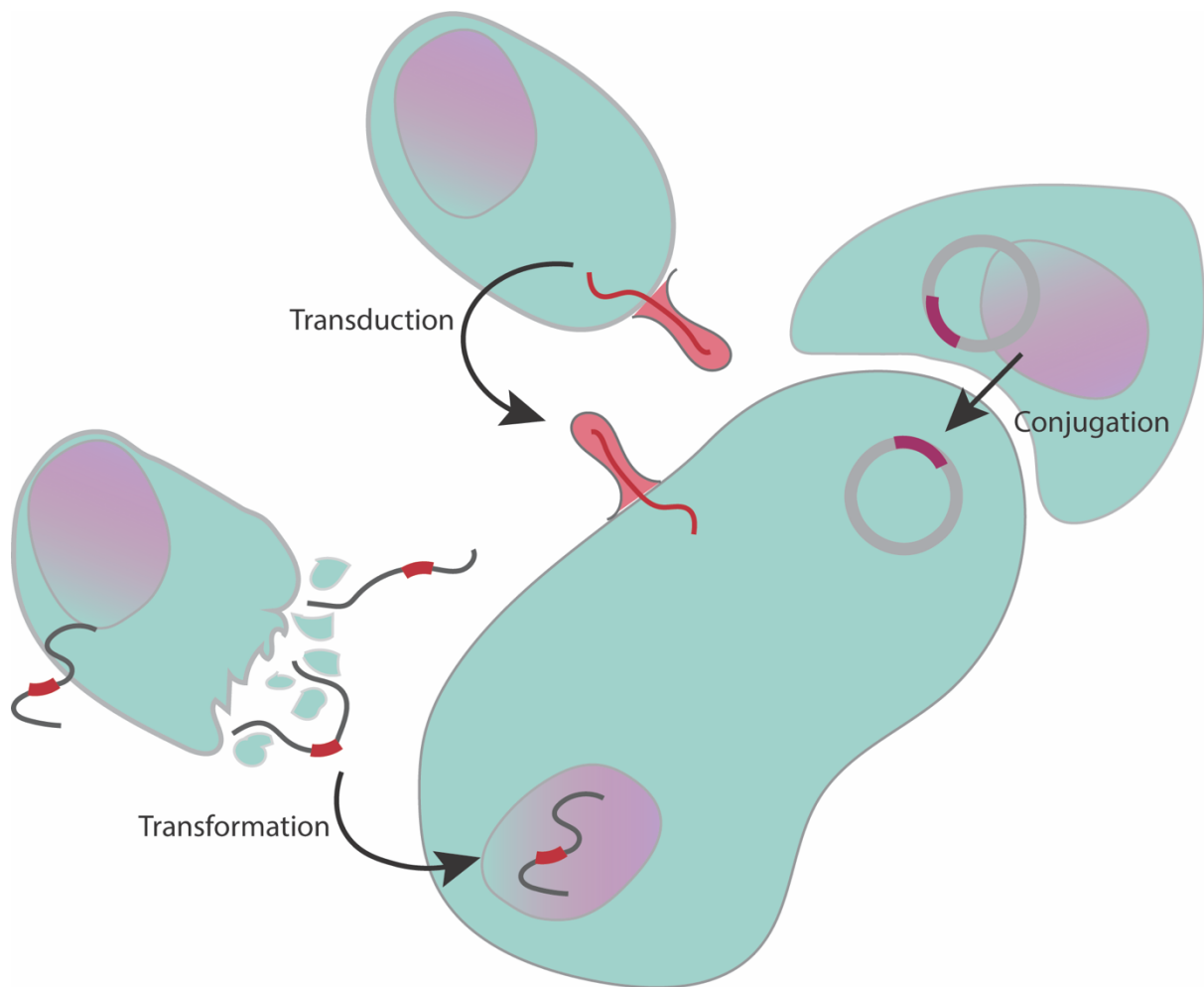


Figure 1.2: Transmission of genetic material between microorganisms. Transformation: Some bacteria are able to take up free DNA from the environment and incorporate it into their chromosome. Transduction: Bacteriophages mediate transfer between different bacteria. The DNA from a donor bacterium is packed into a virus particle and transferred into a recipient bacterium during infection. Conjugation: A plasmid is transferred from one bacterium to another through a sex pilus. Figure adapted from Holmes *et al.*²⁷

Adaptive resistance is transient, and often induced by specific conditions (stress, nutrient conditions, pH, *etc*). This allows bacteria to quickly adapt to stress conditions, such as the presence of the antibiotic, usually, by gene expression. Once the inducing signal disappears the bacterium returns to its original state²⁶.

Acquired resistance, on the other hand requires the acquisition of genetic material through horizontal gene transfer, this includes three main mechanisms: transformation, transduction or conjugation (fig 1.2)^{27,28}. Transformation is the process in which free DNA from the environment is taken up by the bacterium and is incorporated into their chromosome. Transduction is mediated by bacteriophages transferring genetic material during infection. The most used mechanism is conjugation, requiring a direct physical contact between two

bacteria. The sex pilus formed between the two bacterial cell walls is then used to transfer genetic material from one to another.

All above mentioned resistance types are found to exploit a wide variety of mechanisms for the protection against harmful substances: inactivation of the antibiotic, modification of the antibiotic target, reduction of antibiotic accumulation within the cell by limiting the uptake and increasing the active drug efflux (fig. 1.3). However, due to the lack of an outer membrane containing lipopolysaccharides (LPS), gram-positive bacteria cannot limit the uptake of drugs via their cell membrane²⁹. Drug inactivation happens via two different mechanisms, either by alteration of the drug or by degradation of the drug. In case of drug alteration, a chemical moiety is transferred to the antibiotic, usually an acetyl, phosphoryl and adenylyl moiety, e.g. chloramphenicol resistance accomplished through acetylation³⁰. Degradation, on the other hand, is achieved through hydrolyzation of the molecule. The most known example is β -lactamase that opens the amide bond of the β -lactam ring, hereby rendering the antibiotic ineffective³¹.

Methods of drug target modification include target alterations, bypassing of the target, and protection of the target cells^{23,26}. One of the most known examples is the alteration of structure and number of penicillin-binding proteins (PBPs), leading to a change in the ability and the amount of the drug necessary to bind³². PBPs are membrane-anchored peptidase enzymes responsible for catalyzation of the crosslinking of the peptide bridges between the different glycan strands of the PG. They are the main targets of β -lactam antibiotics³³.

Biofilm formation, a further resistance mechanism, protects bacteria from both an attack of the host immune system, as well as from antimicrobial agents. This would lead to a higher dose of drugs necessary to obtain a suitable effect of killing the bacteria. Furthermore, since horizontal transfer of genes is facilitated by the proximity of other bacterial cells, biofilms are an excellent environment for sharing resistance genes^{34,35}. In addition, bacteria contain genes encoded in their DNA for efflux pumps. They can be expressed constitutively, or induced and overexpressed under certain environmental stimuli^{36,37}. The main function of these pumps is to get rid of toxic substance for the bacterial cell, and in most of the cases they will transport a large variety of compounds. There exist different families of efflux pumps, that have been classified based on their structure and energy source: the ATP-binding cassette (ABC) family, the multidrug and toxic compound extrusion (MATE) family, the small multidrug resistance (SMR) family, the major facilitator superfamily (MFS), and the resistance-nodulation-cell division (RND) family²³.

1.2.3 Methicillin-resistant *S. aureus* (MRSA) and Vancomycin-resistant *S. aureus* (VRSA)

Methicillin-resistant *S. aureus* (MRSA) is one of the most successful bacterial pathogens. Aside from the large amount of protection mechanisms, *S. aureus* also emerged a range of antibiotic

resistance mechanisms. MRSA causes hospital-acquired infections worldwide, associating it with high morbidity and mortality⁸. Methicillin, a semi-synthetic anti-staphylococcal antibiotic, was thought to bring relief after the resistance against penicillin. Nonetheless, resistance strains emerged quickly after its discovery¹⁰. MRSA strains are resistant to all known β -lactam antibiotics, as well as, other non- β -lactam antibiotics, limiting the impact of available antimicrobial therapy.

Resistance of MRSA strains against β -lactam antibiotics works in two primary ways, through the expression of β -lactamase, and expression of PBP2a (fig 1.3)^{11,38}. Acquisition of the *blaZ* gene, encoding for enzyme β -lactamase, enables the hydrolysis of the amide bond of the four-membered β -lactam ring characterizing β -lactam antibiotics, rendering the drug before it reaches its target, the PBPs in the PG³⁸. The mobile genetic element 'staphylococcal cassette chromosome *mec*' (SCC*mec*)³⁹, containing *mecA*, enables the expression of penicillin-binding protein 2a (PBP2a). As mentioned above, PBPs are responsible for catalyzing crosslinking the peptide bridges between the different glycan strands within the PG. As they are the main targets for β -lactam antibiotics³³, the expressed PBP2a is highly resistant to inhibition by β -lactam antibiotics and can maintain peptidoglycan crosslinking in the presence of β -lactam antibiotics, allowing survival⁴⁰⁻⁴². Furthermore, the *aux* (auxiliary factors) and *fem* (factors essential for methicillin resistance) contribute to PBP2a-mediated β -lactam resistance^{43,44}.

MRSA is still susceptible to so-called last-line drug vancomycin and new antibiotics such as daptomycin and linezolid¹¹. Although resistance against these last-line drugs is at moment still uncommon, more and more vancomycin-resistance *S. aureus* (VRSA) strains are emerging. Vancomycin, a glycopeptide, inhibits cell wall synthesis by binding to the D-Ala-D-Ala endings of the stem peptides, hereby preventing correct incorporation into PG and altering the bacterial cell membrane integrity⁴⁵. Although it has been shown that resistance emerges through plasmid transfer of the *vanA* operon from vancomycin-resistant *Enterococcus faecalis*^{46,47}, vancomycin resistance is not yet completely understood. Resistance is further linked with mutations that alter genes encoding core components of the cell membrane (*mprF*), cell wall synthesis and autolysis (*yycH*), and teichoic acid synthesis (*dltA*)⁴⁸.

1.3 Cell wall biogenesis of *S. aureus*

In contrast to gram-negative bacteria, gram-positives do not present an outer cell wall for protection against their harmful environment⁵⁰. However, gram-positive bacteria possess several distinct features for maintenance of the cell shape and size, regulation of the cell pressure and protection against a harmful environment.

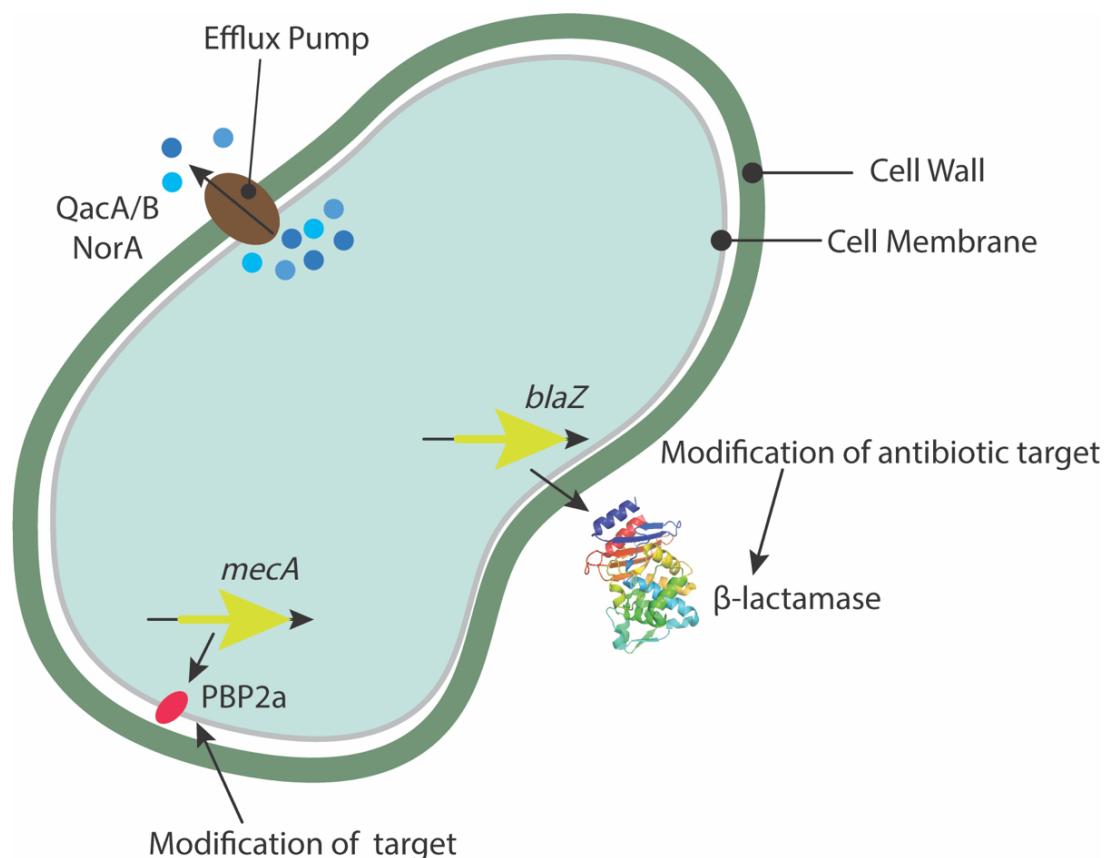


Figure 1.3: Molecular mechanism of antibiotic resistance in *Staphylococcus aureus*. General mechanisms of antibiotic resistance mechanisms with two primary ways of *S. aureus* resistance. β -lactamase: PDB-ID 4s2i⁴⁹. Adapted from Lade *et al*⁴¹.

1.3.1 General features of the cell wall

The gram-positive bacterial cell wall is composed of a thick, heavily crosslinked PG, wall associated proteins and teichoic acids (TA)^{51,52} (fig. 1.4). The PG matrix is composed out of glycan strands containing N-acetylglucosamine (GlcNAc) and N-acetylmuramic acid (MurNAc) connected through β -(1,4)-glycosidic bonds⁵³. Compared with gram-negative bacteria, the PG of gram-positives is much thicker, the *S. aureus* PG has a thickness of around 25 nm⁵⁴. The glycan strands are crosslinked through so-called 'stem-peptides' and flexible peptide bridges, resulting in a mesh-like structure that surrounds the cell. The *S. aureus* stem-peptides are pentapeptides composed out of L-alanine, iso-D-glutamine, L-lysine, D-alanine and D-alanine with a peptide bridge composed of pentaglycine attached to each MurNAc residue⁵⁵.

In gram-positive bacteria, two different types of TAs can be found, wall teichoic acids (WTA) attached to PG and lipoteichoic acids (LTA) anchored via lipid domains within the cell membrane^{52,56}. TAs are important for a variety of functions, such as control of bacterial cell division, protection from environmental stress, host cell adhesion, antibiotic resistance, biofilm formation, as well as virulence and immune evasion^{31,32,34-44}. Of the known TAs, WTAs and LTAs contain slightly different functions. While WTAs are important for efficient blockage

of antibody recognition and phage intrusion, lysozyme access, colonization and facilitation of horizontal gene transfer, LTAs contribute to cell growth, cell stability, virulence and cell division³⁸.

TAs are zwitterionic, as they contain negatively charged phosphate groups and positively charged D-alanine residues on the repeating units⁶⁸⁻⁷⁰. *S. aureus* WTAs consist of 1,5-linked ribitol phosphate subunits attached via a disaccharide linkage unit (GlcNAc and ManNAc) to PG, whereas LTAs are 1,3-linked glycerol phosphate repeat units tethered to membrane-anchored gentiobiosyl-diacylglycerol (Glc₂-DAG) embedded in the cell membrane (fig 1.4)⁵¹.

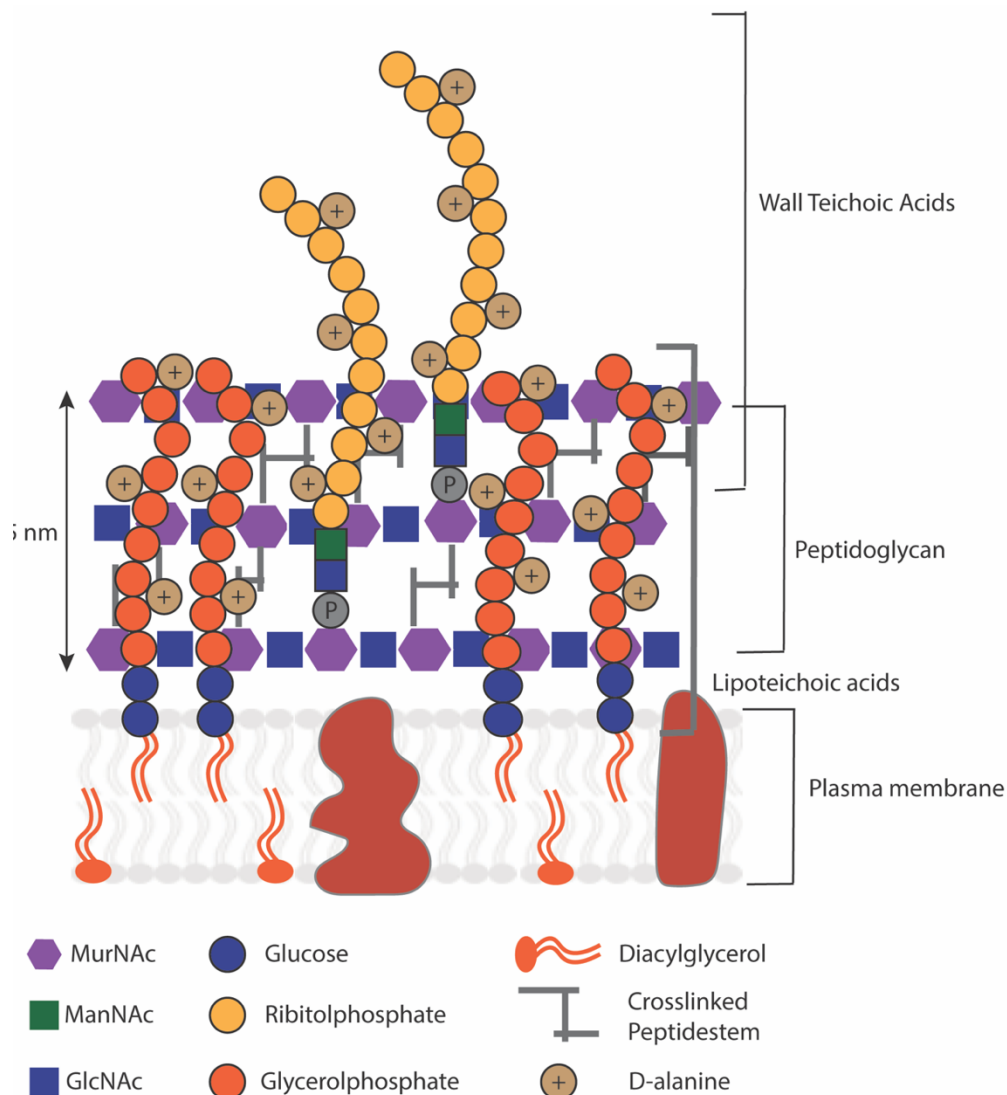


Figure 1.4: Cell wall structure of Gram-positive bacteria. The gram-positive cell wall contains a thick peptidoglycan (PG) layer, together with two types of teichoic acids; lipoteichoic acids anchored in the plasma membrane and wall teichoic acids attached to the PG, both decorated with D-alanine residues. MurNAc: N-acetylmurine; ManNAc: N-acetylmannosamine; GlcNAc: N-acetylglucosamine

1.3.2 Lipoteichoic acids

The individual structures of LTAs differ in gram-positive bacteria and are categorized into five types (fig 1.5), of which type I, the polyglycerolphosphate is best characterized to date⁵². It is found among a large variety of different gram-positive bacteria that belong to the genus *Firmicutes*, including *Bacillus subtilis*, *Listeria monocytogenes* and *S. aureus*. Type I LTAs are recognized by TLR2 and are associated with various inflammatory diseases ranging from minor skin diseases to severe sepsis⁷¹⁻⁷³.

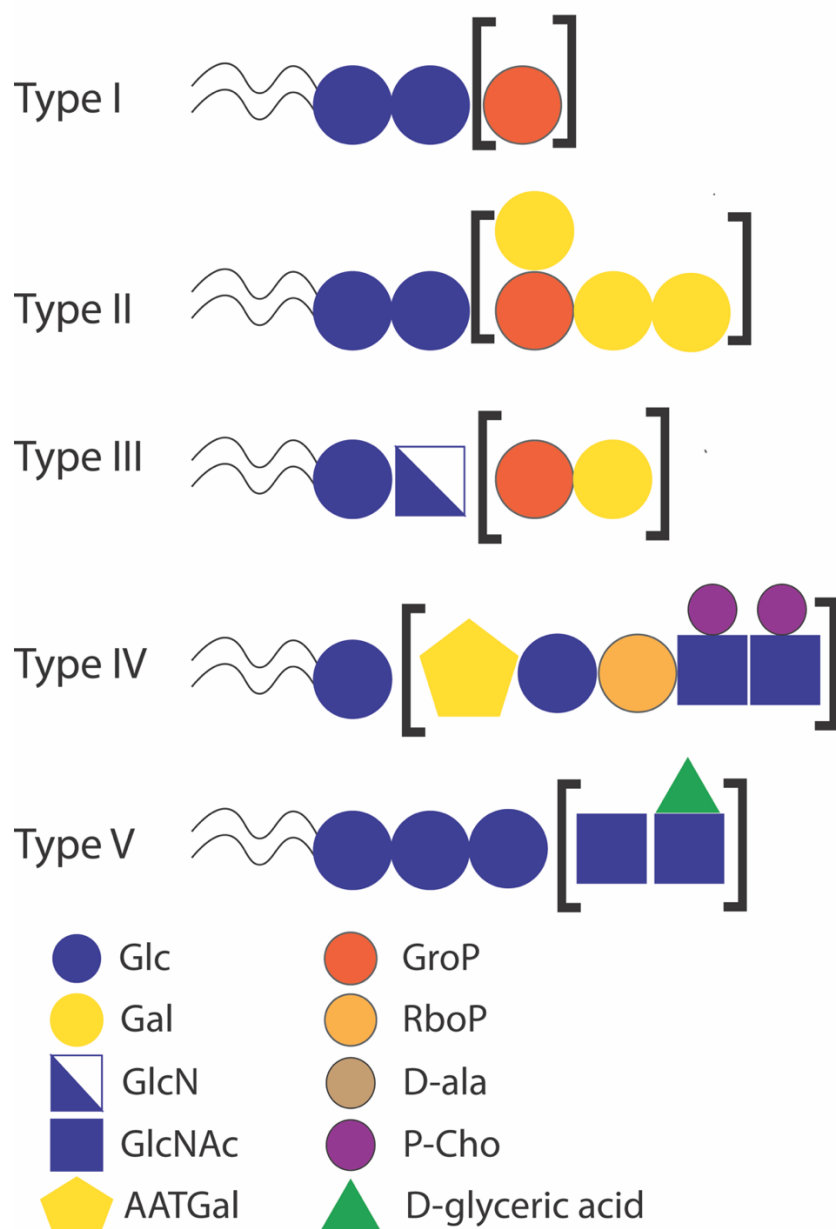


Figure 1.5: Types of known LTA in gram-positive bacteria. Glc: glucose; Gal: galactose; GlcN: glucylamine; GlcNAc: N-acetylglucosamine; AATGal; 2-acetamido-4-amino-2,4,6-trideoxy-D-galactose; GroP: glycerolphosphate; RboP: ribitolphosphate; D-ala: D-alanine; P-Cho: phosphocholine.

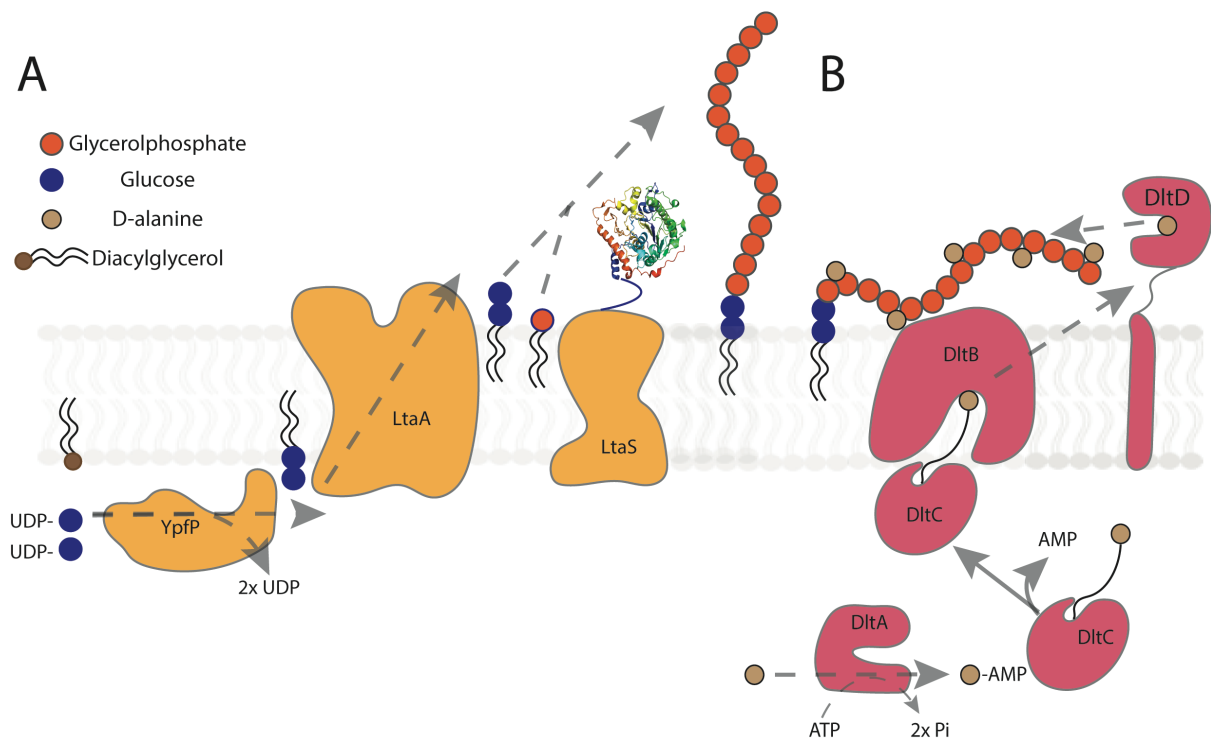


Figure 1.6: Schematic representation of *S. aureus* LTA synthesis. A. *S. aureus* LTA biosynthesis pathway. YpfP synthesizes the glycolipid anchor Glc₂-DAG, followed by flipping to the outer leaflet of the membrane by LtaA. The GroP polymer is synthesized by LtaS on the outside of the cell. Structure of the extracellular domain of LtaS is shown (PDB-ID: 4u00). B. Current model for D-alanine modification of LTA. An activated alanine is attached by DltA to the phosphopantetheine prosthetic group of the carrier protein DltC. DltC binds to DltB, leading to transfer of D-alanine onto DltD, which transfers it onto the LTA polymer. Figure adapted from Rismondo *et al.*⁷⁴

WTAs and LTAs are synthesized in different pathways, and the structures of both WTA and LTA vary among gram-positive bacteria. In *S. aureus*, the LTA synthesis starts on a diacylglycerol (DAG) lipid embedded in the cytosolic leaflet of the cell membrane. As a first step the glycosyltransferase YpfP uses a nucleotide-activated glucose (UDP-glucose) as substrate and will attach two glucose residues via a $\beta(1\rightarrow6)$ -bond to a DAG lipid forming a Glc₂-DAG^{63,75,76}. Next, the flippase LtaA will translocate this Glc₂-DAG to the extracellular leaflet of the membrane⁷⁷, followed by an extension of the LTA 1,3-glycerol-phosphate polymer by the LTA synthase (LtaS), adding glycerol-phosphate in a 1,3 bond^{78–80} (figure 1.6a). On average, the length of a LTA polymer is about 25 glycerolphosphate (GroP) residues⁸¹. The LTA structure intercalates into the peptidoglycan-layer however, without reaching the cell surface^{82,83}.

In a next step, the LTAs are modified with the attachment of D-Ala to the repeating units by enzymes encoded by the *dltABCD* operon. DltA activates D-ala using ATP by forming a D-alanyl-AMP intermediate for a following transfer step to the phosphopantetheinyl prosthetic group of the protein DltC^{84–86}. Subsequently, DltC will bind to DltB on the cytoplasmic side of the membrane and DltB is then thought to either transfer D-alanine onto a lipid carrier as an

intermediate step or directly onto DltD, which as a final step will transfer D-alanine to the LTA^{74,87,88} (fig 1.6b). Salt stress-induced LTA glycosylation was reported for *S. aureus*⁸⁹. Modification of LTAs with D-alanyl is shown to play an important role in autolysis, cation homeostasis, host cell adhesion and invasion, biofilm formation and to be essential for the virulence of *S. aureus*^{52,60,90}.

The flippase LtaA was first described by Gründling and Schneewind⁷⁷. The *ltaA* locus tag SAV1016 lays within the same operon as *yypP*, and the predicted starting site overlaps the 3' end of the *yypP* coding sequence. Genes located in the same operon usually encode proteins that are involved in the same biological pathway. Therefore, the authors speculated that this new discovered gene must be involved in LTA or Glc₂-DAG biosynthesis. Preparation of *S. aureus* Δ *ltaA* gave cells with longer LTAs, but did not interfere with the Glc₂-DAG synthesis indicating that the proposed function lays downstream of YpfP. This led to the hypothesis that LtaA is to be responsible for the transport of Glc₂-DAG from the inner to the outer leaflet of the membrane.

Although *S. aureus* Δ *ltaA* still contains LTAs, they are longer compared to those found in *S. aureus* WT and do not contain a gentiobiose headgroup. Here, LtaS can use phosphatidylglycerol as starting block and attaches GroP units directly to the diacylglycerol resulting in LTAs lacking the sugar headgroup and with a length of 20 GroP repeat units longer than WT LTA⁹¹. *S. aureus* Δ *ltaA* shows not only longer LTAs, but also a larger cell size and several cell division defects, such as multiple and misplaced septa (fig 1.7)⁵⁸. The misconstructed LTAs were shown to lead to virulence defects in murine models, since *S. aureus* Δ *ltaA* failed to efficiently infect kidneys and liver tissues⁷⁷. *S. aureus* Δ *ltaA* seems to be susceptible for daptomycin, a calcium-dependent lipopeptide antibiotic frequently used to treat *S. aureus* infections⁹². In addition, the knock-out of *ltaA* in a MRSA background increased the susceptibility to methicillin antibiotics⁵⁸. Interestingly, it was found that *S. aureus* Δ *ltaA* strains containing abnormal long LTAs are susceptible to cell lysis in the presence of an DltB inhibitor suggesting that D-alanylation controls the activity of cell wall hydrolases⁵⁸. In conclusion, LTAs lacking the Glc₂-DAG anchor result in longer LTAs, division defects, decreased virulence and a higher sensitivity to β -lactam antibiotics and other stressors, such as cell wall hydrolases.

Similar for *S. aureus* Δ *ltaA* strains, *S. aureus* Δ *yypP* strains (or also called Δ *ugtP* strains) contain LTAs without the gentiobiose headgroup, but also in this case the enzyme LtaS uses a phosphatidylglycerol lipid as the starting molecule for LTA assembly. As a consequence of the knock-out a Glc₂-DAG cannot be formed, as the UDP-Glc residues are not attached to the DAG⁹³. This results in growth defects such as longer LTAs, larger cells, and misplaced septa (fig. 1.7). The LTAs of *S. aureus* Δ *yypP* strains have been found to be even larger than in Δ *ltaA* strains, leading to the hypothesis that in Δ *ltaA* strains, still a part of the Glc₂-DAG can be translocated across the cell membrane by an unknown mechanism⁷⁷.

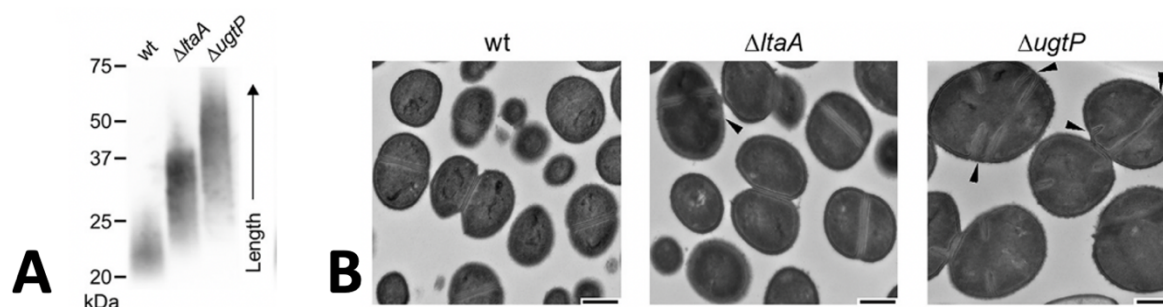


Figure 1.7: *S. aureus* mutants unable to synthesize LTA on Glc₂-DAG show abnormal long LTAs, and have cell size and division defects. A. Anti-LTA Western blot of exponential-phase *S. aureus* RN4220 lysates. B. Transmission electron microscopy (EM) of *S. aureus* RN4220. Arrowheads indicate septal defects. Scale bars shown in right bottom corner are 500 nm. Adapted from Hesser, *et al.*⁵⁸.

S. aureus Δ *ltaS* strains are characterized by a significantly reduced cell viability caused by defects in the cell envelope assembly that in turn can be explained by the small amount of GroP containing LTAs⁷⁸. Therefore, the LTA biosynthesis enzymes represent a promising target for the development of novel antimicrobial agents. Information about their structure and function becomes essential to combat the current threat by emerging antibiotic resistant bacterial strains. Except for the structure of LtaA, determined in this project (Chapter 2), only the structure of extracellular domain of LtaS has been elucidated so far⁷⁹.

1.4 LtaA as drug target

Antibiotics are used to eradicate the infecting bacterial pathogen from its host. Consequently, targets of antibiotics should be absent in eukaryotic cells not to damage them, making the cell wall a primary target for antibiotics. As TAs play critical roles in bacterial viability, during cell division, immune evasion, resistance and pathogenesis, they are promising antibiotics targets. Especially enzymes involved in the biogenesis pathway of LTAs are excellent targets, as a result of the essential role of LTAs in cell survival. Inhibition of the LTA biosynthesis, increases cell lysis and sensitivity against β -lactam antibiotics in MRSA strains. Of the biosynthesis pathway, LtaA and LtaS are the most promising targets, considering their exposure to the extracellular milieu and absence of human homologues⁹⁴. Since LTA are important for recognition by TLR2 to initiate immune responses⁷¹⁻⁷³, the LTA structure may be also a promising target for vaccine development^{95,96}.

Compounds inhibiting LTA biosynthesis have been developed in the past (fig 1.8). The first LTA inhibitor discovered, compound 1771, was shown to inhibit the growth of MRSA with a minimal inhibitory concentration (MIC) of 5.3 mg/ml^{13,94}. At first, compound 1771 was proposed to be an LtaS inhibitor, although, later this was countered and argued that the effect possible reflects the inhibition of polymer production, such as the phosphatidylglycerol pathway⁸⁰. Later, the azo dye Congo red was validated as an LtaS inhibitor, and proposed as a starting point for development of more potent LtaS inhibitors⁸⁰.

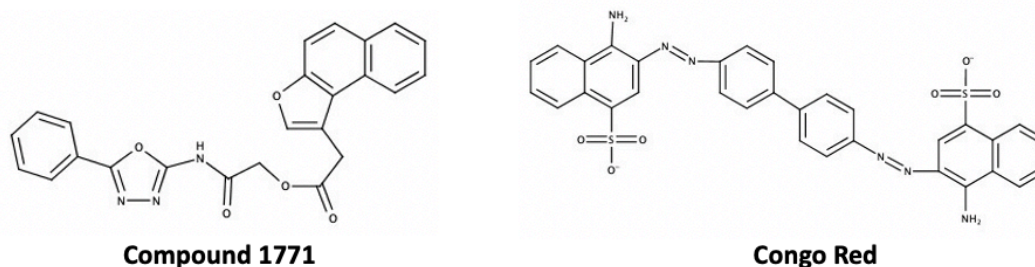


Figure 1.8: Inhibitors of *S. aureus* LTA synthesis. Structures drawn with MarvinSketch.

The essential role in providing Glc₂-DAG anchors at the extracellular side of the membrane, together with the susceptibility of Δ *ltaA* strains for other drugs (β -lactam antibiotics and *dltB* inhibitors) and the impaired virulence make LtaA a central player for lipoteichoic acids assembly. Therefore, LtaA is a potential target for drugs aiming to counteract antimicrobial resistant *S. aureus* strains e.g., methicillin-resistance *S. aureus* (MRSA) and vancomycin-resistant *S. aureus* (VRSA).

1.5 Protein transporters

Membranes are physical barriers found in all kingdoms of life. They separate cells from the external environment, or create a separate compartment. Membranes are composed out of amphiphilic molecules, lipids, containing a hydrophilic headgroup, and hydrophobic tails. Transport of polar molecules across these biological membranes is an essential process for cellular life, mediated by membrane proteins. Between three to 16% of prokaryotic, and 20 to 30% of eukaryotic open reading frames are predicted to encode integral membrane proteins^{97,98}.

In bacteria, three different types of membrane transporters are found to transport molecules across the lipid bilayer⁹⁹. Primary transporters are consuming the energy released by ATP hydrolysis to transport substrates against concentration gradient, such as ATP-binding cassette (ABC) transporters and P-type ATPases. Secondary active transporters are using the energy stored in gradients, protons or sodium molecules, to transport their substrate uphill against the concentration gradient, while coupling it with downhill transport of ions, H⁺ and Na⁺. This is also called the proton-motive-force (pmf) or sodium-motive-force (smf). Energy-independent proteins transport their substrate down its concentration gradient, there are two different types: facilitators and channels. A channel is permeable to both sides of the membrane simultaneously, whereas a facilitator keeps at least one gate close¹⁰⁰ (fig. 1.9a).

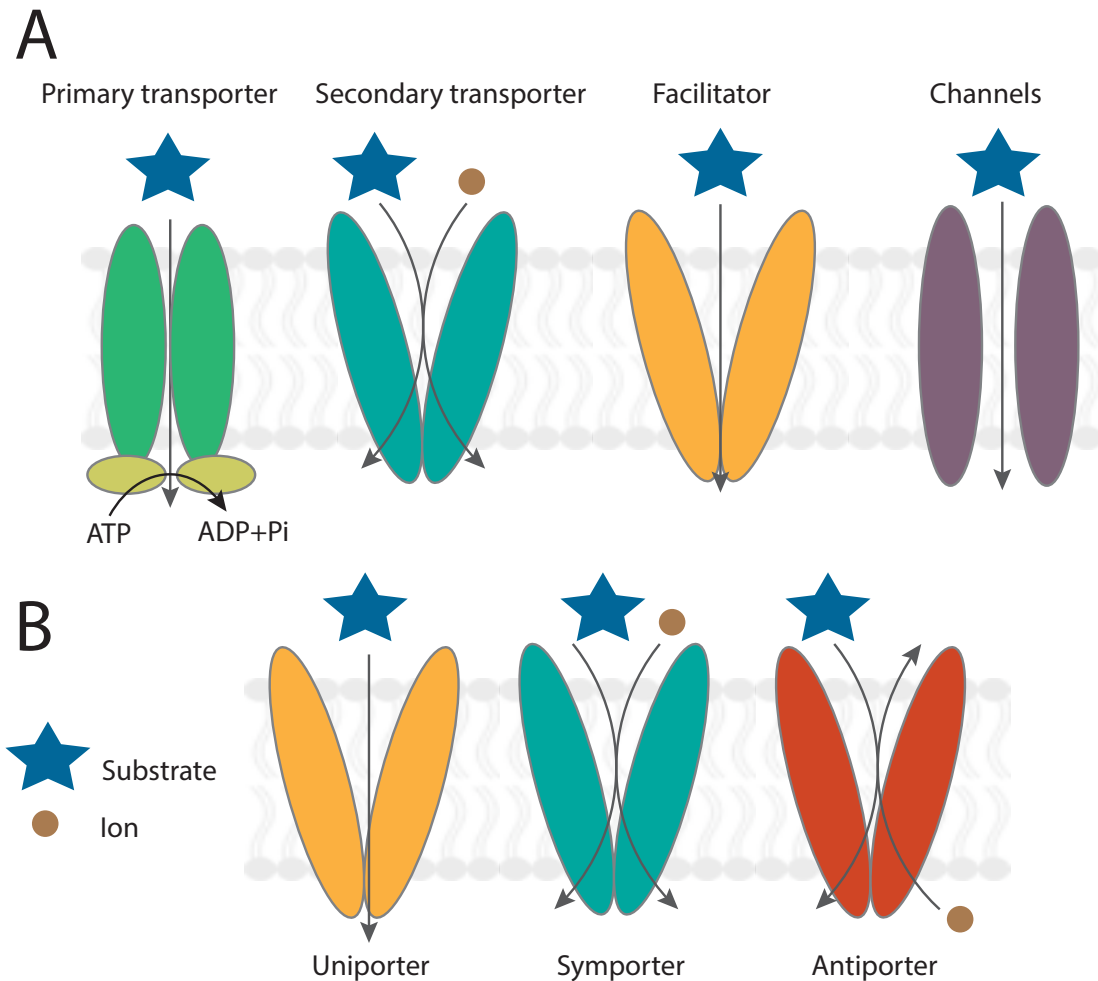


Figure 1.9: Mechanism of transport across membranes. A. Classification of membrane transport proteins, based on their energy sources. Primary transporters use the energy released from ATP hydrolysis, secondary transporters use the energy stored in proton or sodium gradients and facilitators and channels transport substrates along the concentration gradient. B. Different mechanisms used by transporters. Uniporters move the substrate across the concentration gradient, symporters transport the substrate in the same direction as the energy source, and antiporters transport the substrate in the opposite directions.

1.5.1 Secondary transporters

Secondary active transporter, or short secondary transporters, are membrane transporters using energy stored in an electrochemical gradient, protons or sodium ions, to transport their substrate across the cell membrane. These secondary transporters catalyze translocation of their substrate across the membrane via uniport, symport or antiport¹⁰¹ (fig. 1.9b). Uniporters, also called facilitators, transport their substrate along the concentration gradient. This could be in either direction, as import or export. Symporters and antiporters translocate their substrate using the energy stored in the pmf or sdf. Symporters translocate the substrate and the energy source in the same direction, whereas antiporters translocate them in opposite directions. Within the same family of transporters, uniport, symport and antiport can be observed¹⁰¹, indicating that the structural fold does not provide information about the direction of the transport. The energy use of electrochemical ion gradients coupled to

transport of molecules across the cell membrane was described in the past, using single molecule fluorescence resonance energy transfer¹⁰².

Transporters are further classified by sequence, mechanism and substrate into transporter classes, subclasses, family or superfamily, subfamily, and substrate¹⁰³. Secondary transporters are classified in different families, which exhibit a broad substrate variability¹⁰⁴. Remarkably, members of different families, can contain the same structural fold, albeit they do not share any significant sequence similarity. A structural fold is defined by sharing the same fold by at least two distinct transporters that do not have apparent sequence similarity¹⁰⁵. Further analysis based on folds could lead to the reclassification of transporters. For example nine transporter families containing the LeuT fold were grouped together into the amino acid-polyamine-organocation (APC) superfamily¹⁰⁵. Of all the secondary transporter families, the MFS family is the largest evolutionary related superfamily of transporters, containing its own MFS fold¹⁰⁶.

1.5.2 Alternating access mechanism

To accomplish transport of molecules across the membrane, transporters have to switch between different conformations. During the transport cycle, the transporter switches between outward-open and inward-open conformations, via an occluded state. Every transporter should form at least two different conformations to provide access to the central cavity from both sides of the membrane. In between the open states, the transporter forms an occluded state, in which the central binding pocket is not accessible from either side of the membrane. Jardetzky proposed this alternating access mechanism already in 1966¹⁰⁷ (fig 1.10).

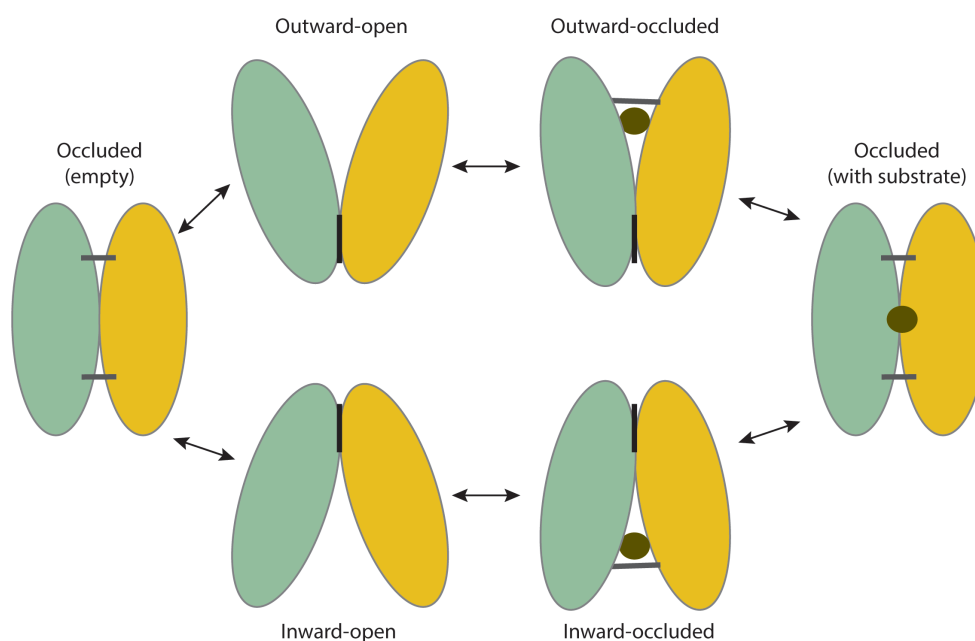


Figure 1.10: The alternating access mechanism-model. During the transport cycle, the transporter alternates between the outward-open, occluded and inward-open state with the substrate bound, and back to an outward-open state without substrate to prepare for the next cycle.

As transporters do not open to both sides of the membrane simultaneously, they need to undergo transitions during the transport cycle, allowing access in an alternating way to the substrate binding site. Therefore, they undergo structural changes within the transmembrane helices. To elucidate the mechanism of transporters, protein structures of the same transporter in different conformations are necessary. Structures do not reveal only the inward-open, outward-open and occluded state, but also intermediate states. Within the alternating access model, three different mechanisms have been identified: the rocker switch, the rocker-bundle, and the elevator mechanism (figure 1.11)¹⁰⁸.

The rocker-switch mechanism is used by transporters containing two structurally similar half-transporters, where the two helical bundles are related by a pseudo-2-fold-symmetry perpendicular to the plane of the membrane such as the MFS fold^{109,110}. For this kind of mechanism, the substrate-binding site is located at the interface between the two half-domains of the transporter, approximately half-way across the membrane¹⁰⁸. Alternating-access to the substrate binding site is obtained by movements of both domains around the substrate in the central substrate binding pocket^{111,112} (fig. 1.11a).

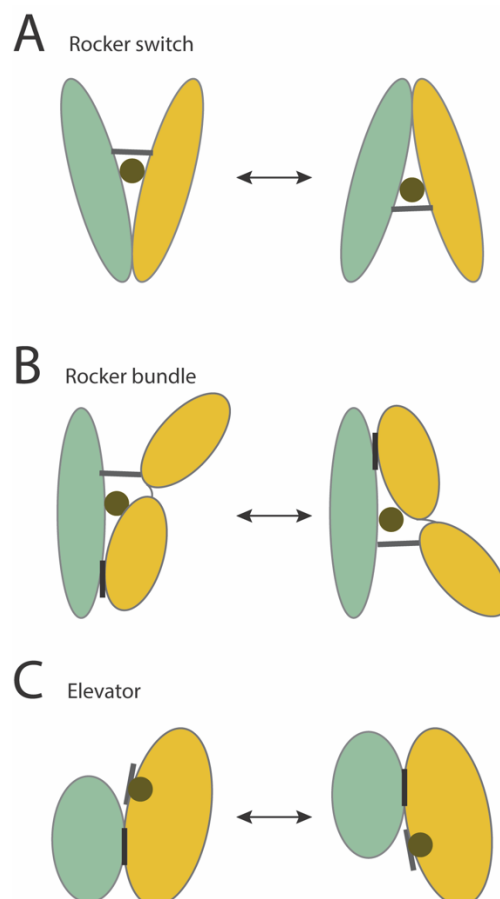


Figure 1.11: Alternating-access mechanisms. Major conformations of the moving-barrier observed in rocker switch (A) and rocker bundle (B) proteins. The substrate (brown sphere) binds both domains, leading to rearrangement of the protein around the central substrate-binding site. A fixed-barrier alternating access mechanism is observed for elevator (C) proteins. The substrate (brown sphere) binds to one of the domains which moves around the fixed barrier.

The rocker-bundle mechanism involves the asymmetrical movement of the two domains. Similar to the rocker-switch mechanism, the substrate binding site is also centrally located. However, the transporter will only undergo major conformational changes in one half-transporter, because both bundles are structurally different¹¹³. The transporter contains also a pseudo-2-fold- symmetry, but the axis runs through the center of the transporter (fig. 1.11b). This mechanism of transport is used among others by LeuT, a bacterial homolog of the neurotransmitter sodium symporter (NSS) family, and by extension other transporters containing the LeuT fold^{105,114,115}.

The elevator mechanism translocates the substrate across the cell membrane, rather than the two domains of the transporter moving around the substrate. Typically, elevator transporters are made up by two distinct domains, like the rocker-bundle transporters. However, the substrate binding pocket is only located on a single domain (fig. 1.11c). The mechanism was first seen in glutamate transporters¹¹⁶ and sodium-proton exchangers¹¹⁷, and later proposed to be used by other transporters as well^{118–123}.

It has to be noted that the above-described mechanisms are models unable to take all molecular details into account. Therefore, they will be finetuned for each individual transporter or transporter family. Both the rocker-switch and the rocker-bundle models break down when intermediate and occluded conformations are included¹⁰⁸. Therefore, different models have been proposed such as the ‘clamp-and-switch’ model for MFS transporters¹²⁴.

1.5.3 Transporter catalyzed lipid translocation

Similar to small soluble molecules, the barrier for spontaneous transport of lipids with a polar headgroup across the lipid bilayer is energetically unfavorable^{125–127}. As mentioned above, transporters are classified on their energy sources. Transport of lipids has been reported for all types of membrane transporters (fig 1.12):

- (i) Primary active transporters using ATP; ABC transporters translocating lipids from the inner leaflet to the outer one^{128–131}, and P4-ATPases carrying out the translocation from the outer leaflet to the inner leaflet^{132,133}.
- (ii) Secondary transporters requiring proton or sodium gradients; lipid transporters have been identified in different families of secondary transporters^{134,135}.
- (iii) Scramblases acting energy-independent, and perform bidirectional and unspecific lipid transport along the concentration gradient^{136,137}.

Lipid transporters that use energy, both primary and secondary transporters, are called flippases¹³⁸.

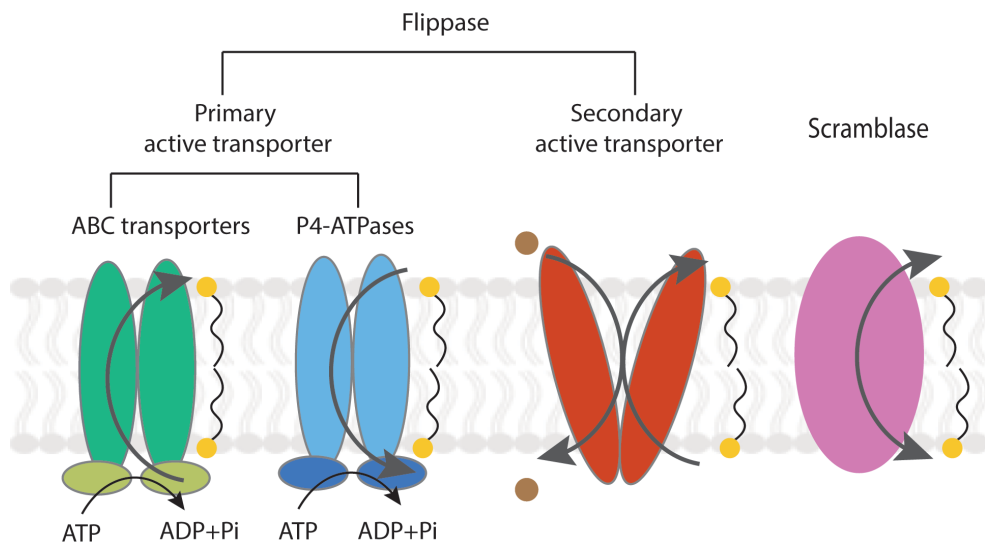


Figure 1.12: Transporters catalyzing lipid translocation. ABC transporters translocate the lipid substrate from the inner to the outer leaflet, while P4-ATPases transport from outer to inner leaflet. Both use ATP as their energy source. Secondary active transporters use the gradient of an ion as energy source to translocate their lipid substrate. Scramblases perform bidirectional transport. ABC transporter, P4-ATPases and secondary active transporters are also called flippases.

The most common substrates of flippases are phospholipids. However, also more complex molecules like glycolipids are transported. Complex polysaccharides are essential for a range of biological processes, such as biosynthesis of the bacterial cell wall¹³⁹, N-glycosylation¹⁴⁰ as well as exo- and endocytosis¹⁴¹. Their biosynthesis requires complex pathways. In some cases, a lipid anchor is part of the final glycoconjugate structure (e.g. lipopolysaccharide (LPS) in gram-negative bacteria, LTA in gram-positives, mycolic acid in *Mycobacterium*). In other cases a lipid carrier, in the form of an undecaprenol pyrophosphate (Und-PP) lipid, is used as a tool for export of the polysaccharide precursor. Biosynthesis of complex polysaccharides starts on the cytoplasmic leaflet, followed by translocation across the membrane by a flippase and further polymerization on the extracellular leaflet for these glycol complexes¹⁴².

At the moment five structures of flippases mediating glycolipid transport are elucidated; four ABC transporters and one secondary transporter.

1. The ABC lipid-linked-oligosaccharide (LLO) transporter PglK of *Campylobacter jejuni* translocating an LLO used as a donor for proteins requiring N-glycosylation¹²⁸.
2. The ABC transporter MsbA flipping lipid A and the core oligosaccharide of LPS across the inner membrane of gram-negative bacteria¹²⁹.
3. The O-antigen exporter of gram-negative bacteria Wzm-Wzt, translocating the variable O-antigens of the LPS molecules across the inner membrane^{130,143}.
4. The *Alicyclobacillus herbarius* homologue of *S. aureus* ABC transporter TarGH, exporting WTA precursors to the cell surface for attachment to peptidoglycan¹³¹.

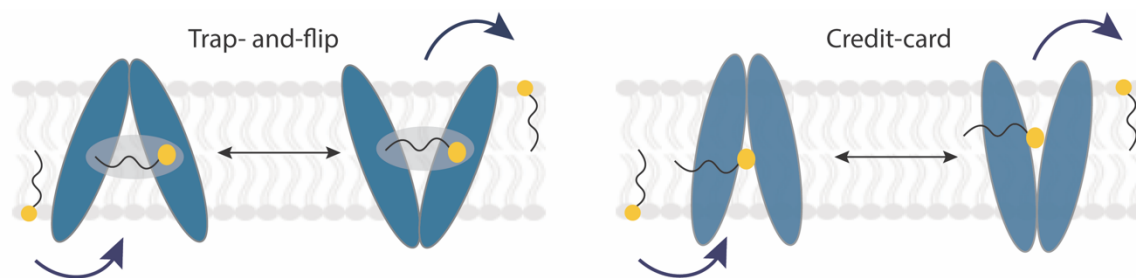


Figure 1.13: General mechanisms for lipid translocation across the lipid bilayer. ‘Trap-and-flip’ model (left): The lipid is captured from the membrane, completely enclosed into the central substrate cavity, and then delivered to the other leaflet of cell membrane. ‘Credit-card’ model (right): The polar headgroup is translocated across the membrane through a hydrophilic cleft or cavity in the transport protein, while the aliphatic tails remain embedded in the membrane.

5. The secondary multidrug/oligosaccharidyl-lipid/polysaccharide (MOP) transporter MurJ, translocating lipid II, a building block of the PG, GlcNAc-MurNAc-pentapeptide^{134,144}.

1.5.4 General mechanisms of lipid translocation

Different models of lipid translocation have been proposed. On one hand the ‘trap-and-flip’ model, in which the lipid is captured from the membrane, completely enclosed into the central substrate cavity, and then delivered to the other leaflet of cell membrane. On the other hand the ‘credit-card’ model, in which the polar headgroup is translocated across the membrane through a hydrophilic cleft or cavity in the transport protein, while the aliphatic tails remain embedded in the membrane (fig. 1.13).

The ‘trap-and-flip’ mechanism was the first time described for MsbA, the LPS flippase. A cryo-electron microscopy (EM) structure revealed an LPS molecule embedded in the central cavity of the flippase¹²⁹. Other transporters, such as the human phosphatidylcholine transporter ABCB4¹⁴⁵ and the human multidrug exporter P-glycoprotein¹⁴⁶, have been identified to use the ‘trap-and-flip’ mechanism as well.

The ‘credit-card’ mechanism was first described by Pomorski-Menon for phospholipids¹⁴⁷. This model departs from the classical alternating-access mechanism for small-molecules, actively transporting the polar head-group through a polar groove of the transporter, whereas the lipid tails remain embedded in the membrane. Cryo-EM structures of the human P4-ATPase ATP8A1-CDC50a showed different intermediate states, revealing the transport cycle of this lipid flippase¹⁴⁸. Together with structural determination of its yeast homologue Drs2p-Cdc50p the translocation mechanism of P4-ATPases is well determined^{132,133}. Besides the P4-ATPases, the credit-card mechanism was also proposed for the LLO transporter PglK¹²⁸, the calcium-activated TMEM16 scramblase¹³⁶ and the photoreceptor rhodopsin¹³⁷.

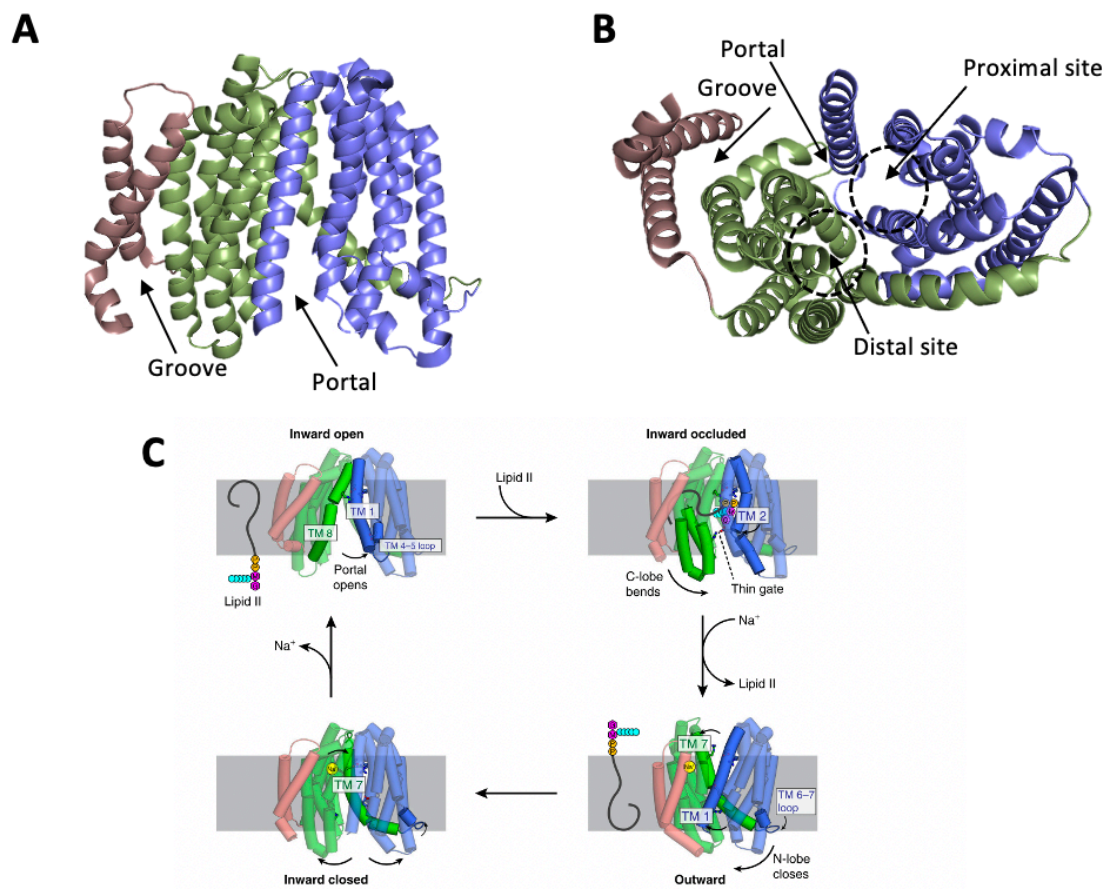


Figure 1. 14: The secondary flippase MurJ. Side view(A) and cytoplasmic view (B) of MurJ (PDB 5T77). C. Proposed flipping mechanism of MurJ. N-terminal (TM1-6), C-terminal(TM7-12) lobe and hydrophobic extension (TM13-14) are colored in blue, green and red. A.+B.: adapted from Kuk *et al.*(2017)¹³⁴, C. Adapted from Kuk *et al.* (2019)¹⁴⁴.

As with all models, the ‘credit-card’ model is a starting point to describe pathways for lipid translocations, and modifications have been observed during the revelation of more structures and mechanisms. One of the most prominent modifications is the ‘outward-only’ mechanism of the LLO flippase PgIk^{128,149}. The authors proposed in this model that only outward-open conformations are necessary for translocation of the LLO. It remains to be investigated if this mechanism is shared by other transporters such as the human lipid exporter ABCA1¹⁵⁰.

However, all the previous mentioned flippases, are primary active transporters using ATP. The Lipid II flippase MurJ is one of the only described secondary flippase^{134,144}. MurJ belongs to the MOP family of transporters (fig. 1.14a,b), and plays a role in assembly of the PG. The MurJ structure revealed 14 transmembrane helices (TM), organized in a N-terminal (TM1-6), and C-terminal (TM7-14) lobe, with TM13 and TM14 extending out from the core to form a hydrophobic groove (fig 1.14a,b). The structure of the transporter revealed a large central

cavity linked with a hydrophobic groove formed by TM 13 and 14. The portal to the large cavity is formed between TM1 and 8, and is linked with the hydrophobic groove. The large cavity can be subdivided into proximal and distal sites with respect to the groove. Based on structural analysis, it was proposed that the sugar moieties and diphosphate of Lipid II headgroup bind into proximal site, whereas the pentapeptide moiety is located in the distal site of this cavity and the undecaprenyl tail associates with the hydrophobic groove (fig. 1.14a,b). During translocation, the polar sugar headgroup is actively transported, while the undecaprenyl tail slides into the hydrophobic groove made up by TM 13 and 14 (fig 1.14c). MurJ was shown to use the alternating access mechanism¹⁵¹.

The flippase LtaA was predicted to be a secondary transporter and to contain the MFS-fold⁶⁷. At the start of this project there were no structures and mechanistic details available for predicted MFS flippases. So further investigation was performed to enlighten the structure and mechanism of LtaA, and in the broader view for other flippases of the MFS family. In the meantime, the structure of the mammalian docosahexaenoic acid (DHA) transporter MFSD2A was described, underling the importance to understand the mechanism of MFS flippases^{152,153}.

1.6 Major Facilitator Superfamily

The MFS of protein transporters plays a role in nutrient uptake, metabolite extrusion, and multidrug resistance. Members of this superfamily are found in all kingdoms of life¹⁵⁴. Currently more than 89 families are classified within the MFS, based on their type of substrate, as listed on the Transporter Classification Database (www.tcdb.org)^{155–157}. Bacteria use MFS transporters for the uptake of nutrients and extrusion of deleterious compounds, whereas human MFS transporters are important for transport of nutrients and signaling. Malfunction of MFS members occurs in multiple diseases, e.g. cancer and metabolic diseases^{124,158,159}. Members of the MFS are secondary transporters. Uniporters, symporters and antiporters have been identified within the family^{109,160,161}.

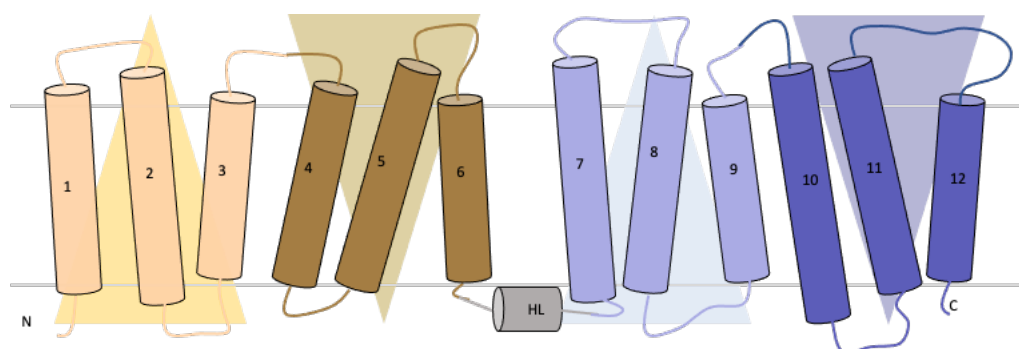


Figure 1.15: Canonical Major Facilitator Superfamily-fold. The N-terminal (brown) and C-terminal domains (blue) are connected by a helical loop (HL) (grey). The inverted repeat of three helices within each domain are shown in lighter and darker colors, resulting to the internal symmetry of 3x4.

1.6.1 General features of the MFS

Members of the MFS superfamily contain the same structural fold (fig. 1.15), composed out of 12 transmembrane helices (TM1-12). Some members contain 11 or 14 helices¹⁵⁵, as recently proven by the crystal structure of ENT1¹⁶². The transmembrane helices are divided into two structural similar domains, the N-terminal (TM1-6) and C-terminal (TM7-12) domains, each containing six TM helices, related with a pseudo-rotational two-fold symmetry axis, perpendicular to the membrane¹⁶³⁻¹⁶⁵. The two domains are connected by a unstructured loop or α -helical loop^{109,166-170}. The substrate-binding cavity is formed by residues from both domains¹⁷¹. The N- and C-terminal domains can both be further divided into two inverted repeat of three helices, leading to an internal symmetry of 3x4^{155,165} (fig. 1.15). Although members of the MFS have the same structural fold, their sequence conservation is low, between 12-18%, with a higher conservation between members of the same subfamily¹⁷².

Despite the general low sequence identity between members of the MFS family, conserved sequence motives are observed¹⁷³. Motive A is a highly positive charged motif with the sequence 'GX₃D(R/K)XGR(R/K)' and is located in the loop between TM2 and TM3¹⁷⁴. Motif A seems to be important for gating interactions¹⁷⁵, in particular for lactose and tetracycline transport across the membrane^{176,177} and for the stabilization of the outward conformation in the multidrug/H⁺ antiporter YajR¹⁷⁸. Due to the internal symmetry of MFS transporters, the loops between TM5-TM6, TM8-TM9 and TM11-TM12 have similar motif A-like regions. Motif B 'RX₂QG' in TM4 is proposed to be involved in proton-coupling, and substrate-binding conformational change. Motif C "GX₈GX₃GPX₂GG", the so called antiporter motif, lays within TM5, and is thought to be responsible for the substrate binding and facilitation of transport^{173,174,179,180}. Its duplication, motif G, found within TM11, plays an important role for conformational changes during the transport cycle^{181,182}.

New functions for MFS transporters besides uptake of nutrients and extrusion of deleterious compounds have been reported. These functions included the transport of lipids across the cell membrane, like LtaA^{67,77} and others (see chapter 1.6.5)¹⁸³⁻¹⁸⁸, as well as enzymatic, regulatory and signaling functions. MFS transporters fulfilling receptor function are called transceptors^{189,190}. They can be substrate sensors that transport their own substrate, like the H⁺-coupled nitrate symporter NRT1.1^{191,192} and the *E.coli* glucose-6-phosphate (G6P) sensor protein UhpC. UhpC induces expression of the G6P transport protein UhpT, and transports G6P itself^{193,194}. Transceptors can also perform a sensor function by binding the substrate without transport, such as yeast Rgt3 and Snf3 binding D-glucose although incapable of transport¹⁹⁵⁻¹⁹⁷ and mammalian transporter UNC93B1 acting as a trafficking chaperone for TLRs¹⁹⁸.

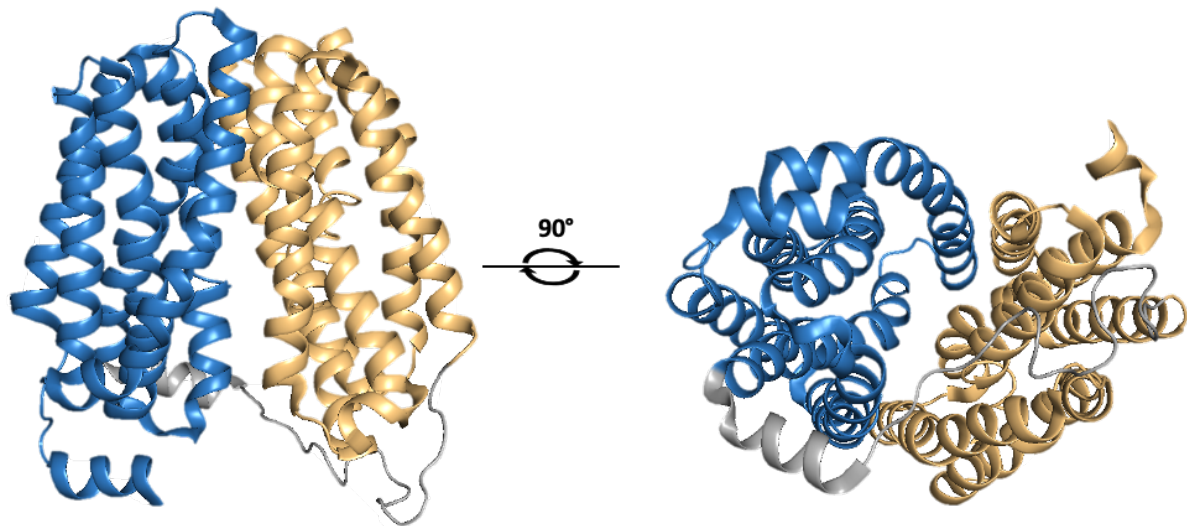


Figure 1. 16: Structure of *Escherichia coli* lactose permease LacY. Front view (left) and bottom view (right). The N- and C-terminal domains are connected by a helical loop and colored in yellow, blue and grey, respectively. PBD-ID: 1PV6.

The first structural characterized MFS transporters were the *Escherichia coli* lactose permease LacY¹⁰⁹ in an inward-open conformation (fig. 1. 16) and *E. coli* glycerol-3-phosphate transporter GlpT¹⁹⁹. At the moment, there are more than 24 unique bacterial and 12 unique eukaryotic structures known²⁰⁰. The number of unique structures has exponentially grown in the last years, thanks to the developments in cryo-electron microscopy (EM). Most of these structures solved by cryo-EM are in complex with Fab fragments, although recently, there was also a structure in complex with a nanobody²⁰¹.

The sugar porters MFS and the multidrug resistance MFS (MDR-MFS) are the best characterized families within the MFS. Particularly, the lactose permease LacY is heavily studied and therefore used as a model system. LacY is a proton-coupled symporter using active transport of lactose coupled to the release of free energy from energetically favorable movement down to the proton gradient²⁰². The MDR-MFS, are antiporters, recognizing and extruding a large range of structurally unrelated drugs from the cell using the free energy released from the downhill flux of ions along their electrochemical gradient²⁰³. Structures of multiple MDR-MFS transporters have been solved, including *E. coli* MdfA in different conformations^{169,204–206}.

1.6.2 Structural details of the MFS transport cycle

Structural characterization of MFS transporters in different conformations revealed their transporter mechanism. The best characterized transporters are the ones participating in nutrient uptake, and extrusion of drugs. Transport of substrates across the membrane, requires alternating access mechanism, in which the transporter switches between outward-open and inward-open conformations, via an occluded state (fig. 1.10)¹⁰⁷. This involves local structural rearrangements within the TM helices. In the outward-open and inward-open

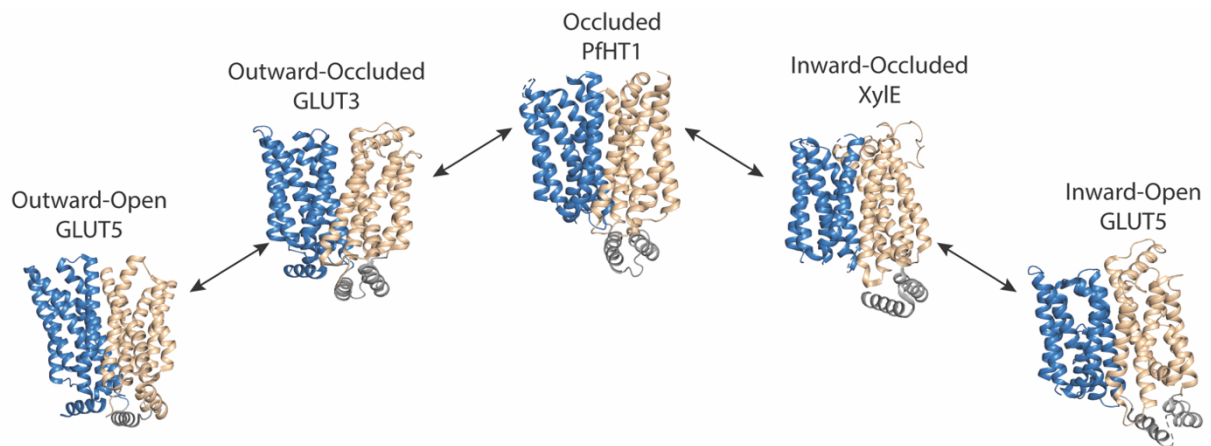


Figure 1.17: First completed Major Facilitator Superfamily (MFS) cycle, the mechanism describes the rocker-switch mechanism for sugar transport. The observed structural states are shown: Outward-open rat GLUT5 (PDB 4YBQ), outward- occluded human GLUT3 (PDB 4ZWB), fully occluded PfHT1 (PDB 6RW3), inward-occluded Xyle (PDB 4JA3) and inward-open bovine GLUT5 (PDB 4YB9). The N- and C-terminal domains and connecting helical loop are colored in yellow, blue and grey, respectively. Adapted from Qureshi *et al.*²⁰⁹

conformation, a crevice is formed between the two half domains on the extracellular, or cytoplasmic side, respectively¹²⁴. Multiple MFS transporters have been observed in inward-facing, outward-facing and intermediate states, but the fully occluded states are rare and have only been identified three times: the multidrug transporter EmrD²⁰⁷, the nitrate/nitrite antiporter NarK²⁰⁸, and the hexose transporter PfHT1²⁰⁹. MFS transporters are thought to operate by rocker-switch mechanism (fig 1. 11a)¹⁰⁸, however this model was updated by Quistgaard *et al* to ‘Clamp-and-switch-model’ to explain how the occluded states are formed¹²⁴. The occluded PfHT1 structure, together with other sugar transporters in different conformational states, shows the most complete MFS transport cycle (fig. 1.17)²⁰⁹.

Movement of the transmembrane helices during the transport cycle results in the formation and disruption of interactions between residues and enables the formation of the different states. In the inward-open, and outward-open conformation TM2 interacts with TM11, and TM5 with TM8 at the periplasmic and cytosolic side respectively¹²⁴. However, bending of helices TM2, TM5, TM8 and TM11 describes only the open states, and not the occluded states. Occlusion of the substrate involves the bending of TM1, TM4, TM7 or TM10. From the cytoplasmic side bending of TM4 and TM10 is observed, while bending of TM1 and TM7 is noted at the extracellular side. A specific set of these residues that undergo formation and disruption of bonds during the transport cycle by moving close towards or far away from each other are called ‘gating residues’¹²⁴. They can perform local fine-tuning to the substrate transported²⁰⁰, leading to asymmetrical rearrangements of the N- and C-terminal bundles^{124,209–213}. These local changes in the TM helices are observed during partially occluded states (outward-occluded and inward-occluded), preventing the substrate from exiting.

The elucidation of the occluded PfHT1 structure resulted in the first whole cycle of the alternating access mechanism within the MFS fold²⁰⁹ (fig 1.17). During sugar transport, global rearrangements are coupled to local rearrangements in the gating helices TM7b and TM10a, which are involved in gating of the sugar binding site²⁰⁹. During transition of outward-occluded to occluded state, TM7 will “break” and TM7b will extend closer to TM1, as seen in inward-facing structures. Further transitions to the inward-occluded state make the substrate interact more strongly with TM10b then TM7b, to finally transition to inward-open state showing the largest movement for TM10b, followed by substrate release^{200,209} (fig. 1.18).

However, investigation and comparison of both the transport cycles of MDR-MFS transporters and MFS sugar transporters by Drew *et al* reveals that the multidrug transporters seems to follow the classical rocker-switch mechanism, whereas the monosaccharide transporters operates between the rocker-switch and the rocking-bundle mechanism, as the conformational asymmetry is visible from the structures²⁰⁰. It seems that different families within the MFS show a high adaptability within their substrate translocation mechanism. Therefore, it might be possible that MFS flippases use a completely different mechanism, requiring further investigation.

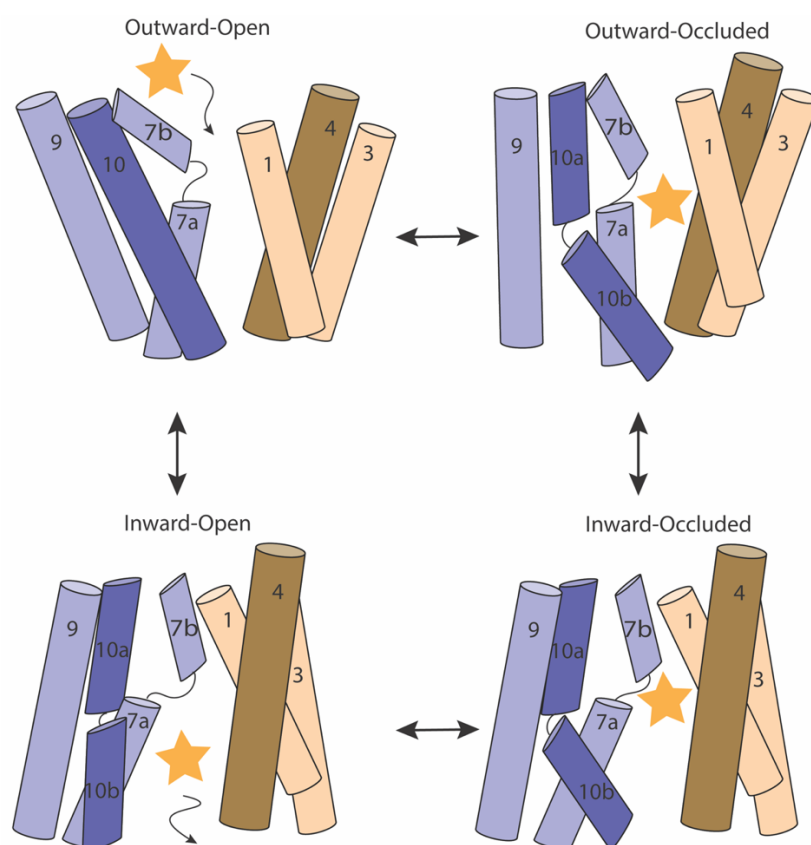


Figure 1. 18: Schematic drawing highlighting the local substrate gating rearrangements by TM7b and TM10b. TM7b is responsible for gating the outward-open to the outward-occluded state, and TM10b for gating between the inward-occluded state to the inward-open state. Helices are colored according to the canonical fold of the MFS.

1.6.3 Energy sources

Transporters of the MFS are secondary transporters, using energy stored in chemiosmotic ion gradients in the form of protons (H^+) or sodium-ions (Na^+) for transport of their substrates¹⁰¹. However, some MFS transporters have been identified as facilitators, hence using the concentration gradient as their only energy source, e.g. the well-characterized human GLUT transporters²¹³.

Proton-coupled symporters are usually nutrient importers that accumulate substrates in the cell, while proton-coupled antiporters, are often multidrug exporters that deplete substrates from the cell¹²⁴. In the case of proton transport, protonation and deprotonation is required which most frequently happens on a Glu/Asp/His and to lesser extent on a Lys/Arg/Tyr¹⁶⁵. In order for these residues to be able to protonate/deprotonate at physiological conditions, and to undergo pKa shifts during the transport cycle, residues important for proton-driven translocation are in close contact with the substrate-binding site^{169,202,214,215}. As the environment is important for the pKa-value of an amino acid side chain, the pKa of an amino acid side chain in a folded protein is influenced by interactions with other residues in its proximity^{216,217}.

The MFS transporters, both symporters and antiporters, have their key residues for H^+ translocation located on helices TM1, TM4, TM7 and TM10¹⁶⁵. Although the majority of transporters investigated have their H^+ site located on TM1, in proximity of the substrate binding site^{166,169,218,219}, LacY is an exception. LacY residue E325 on TM10 was recognized to be directly involved in H^+ translocation²²⁰. However, superimposition of LacY and XylE suggest functional homology between LacY E325 and XylE D27²¹⁸. As mentioned above, both TM1 and TM10 are involved in gating during the alternating access transport cycle. This means that the residues involved in proton-coupling are gating residues, driving conformational changes and leading to the transition between outward-and inward-open states. Although most of the MFS transporters use the pmf as their main energy source, there are also reports of sodium-coupled transporters, such as the Na^+ /melibiose symporter MelB²²¹. The kinetic model was proposed to be the same regardless of the coupling cation.

1.6.4 Substrate binding pockets of MFS transporters

The substrate-binding pocket of the MFS transporters is located in the center of the transporter and formed by residues on both the N-terminal and C-terminal domain¹⁵⁴. The nature of the substrate-binding cavity of the MFS transporters is chemically diverse, adapted specifically to the substrate. The first structure of a substrate bound MFS transporter was the xylose/ H^+ in complex with D-xylose, revealing for the first time the substrate coordination¹⁶⁸.

Pockets of sugar transporters contain polar and aromatic residues, without charged residues, leading to a hydrophobic pocket, as required for sugar transport^{109,168}. In contrast, the pockets of MDR-MFS have a large pocket, containing hydrophobic, polar and charged residues¹⁶⁰ and

bind their substrates through nonspecific electrostatics and hydrophobic interactions, like the multidrug exporter MfdA^{160,222}. A chemically different N-and C- terminal pocket was observed for the fucose transporter FucP¹⁶⁶ and peptide transporter YbgH²¹⁹. FucP has an N-terminal domain with residues making a negative electrostatic potential, whereas the C-terminal part contains hydrophobic residues in the center of the protein, and positive charged residues on the edges of the binding-pocket¹⁶⁶. The peptide transporter YbgH contains an N-domain that is positively charged, while it's C-domain is negatively charged²¹⁹. It was argued that difference in chemical nature between the N-and C-terminal domain enables the correct substrate orientation within the binding-pocket.

1.6.5 Flippases within the MFS

Despite the broad understanding of MFS transporters with water soluble substrates, at the start of this project no structural and mechanistic details were known about MFS transporters involved in the translocation of lipids. However, multiple transporters have been proposed to be MFS flippases: the bacterial lysophospholipid transporter LpIT, involved in lipids recycling in gram-negative bacteria^{183,223}; the human transporter MFSD2A, expressed at the blood-brain- and blood-retinal-barrier, contributing to major uptake of docosahexaenoic acid (DHA)^{184,185,224,225}; the human transporters Spns2^{187,188}, and MFSD2B¹⁸⁶, which both contribute to transport of sphingosine 1-phosphate (S1P) in endothelial cells and erythrocytes; and the gentiobiosyl-diacylglycerol transporter LtaA, involved in cell wall synthesis in *S. aureus*⁷⁷.

1.7 Aim of this work

At the beginning of this project, the outward-open crystal structure of the Glc₂-DAG flippase LtaA (PDB-ID: 6S7V) was determined in our group by Bing Zhang²²⁶. Elucidation of the structure confirmed that LtaA contained the predicted MFS-fold. In addition, it revealed a never observed amphiphilic cavity. The N-terminal part of the cavity is composed out of hydrophilic residues, whereas the C-terminal cavity is formed by hydrophobic residues.

Despite structural characterization of LtaA in one conformation, questions about the activity and flipping mechanism of LtaA remained. At that time, there was no other characterized MFS flippase, no details of the mechanism in MFS flippases known, and barely any details of flipping in secondary transporters available. In this project, the following points were addressed to investigate the flipping mechanism of LtaA, which could serve as a model for MFS flipping:

- Production and characterization of the LtaA substrate Glc₂-DAG, in order to establish *in vitro* flipping assays
- Investigation of LtaA mechanism using *S. aureus* Δ LtaA cells
- Investigation of the importance of the hydrophilic N-terminal and hydrophobic C-terminal pocket of LtaA by *in vitro* flipping assays

- Investigation of the hydrophilic N-terminal and hydrophobic C-terminal pocket of LtaA by *in vivo* assays using *S. aureus* Δ *ltaA*
- Investigation of the alternating-access mechanism through cysteine-mediate crosslinking
- Investigation of the dynamics of the lateral openings of LtaA using cysteine-mediate crosslinking and flipping assays.

Taken together these points will provide mechanistic details of the translocation mechanism used by the MFS flippase LtaA, which might be shared with other MFS flippases. Unraveling these details is not only important for the understanding of the mechanistic details, but will also provide foundations for the basic understanding used for drug design, such as LtaA inhibitors for *S. aureus* MRSA and VRSA strains or for lipid/linked-drug design of bioactive molecules targeting cells or organs expressing MFS transporters.

2. Structure of a proton-dependent lipid transporter involved in lipoteichoic acids biosynthesis

Bing Zhang^{1*}, Xue Liu^{2*}, **Elisabeth Lambert^{1*}**, Guillaume Mas¹, Sebastian Hiller¹, Jan-Willem Veening², Camilo Perez^{1‡}

¹Biozentrum, University of Basel, 4056 Basel, Switzerland

²Department of Fundamental Microbiology, Faculty of Biology and Medicine, University of Lausanne, 1015 Lausanne, Switzerland

Abbreviated title: pH sensing flippase

* These authors contributed equally to this work

‡Corresponding author: Camilo Perez

Reference:

Zhang, B., Liu, X., Lambert, E. et al. Structure of a proton-dependent lipid transporter involved in lipoteichoic acids biosynthesis. *Nat Struct Mol Biol* 27, 561–569 (2020). <https://doi.org/10.1038/s41594-020-0425-5>

Author contributions:

- I performed preparation and characterization of the Glc₂-DAG reaction product
- I performed *in vitro* flipping assays and data analysis
- I performed *in vivo* *S. aureus* experiments and analyzed the data together with Xue Liu
- I participated in preparation of the manuscript



Structure of a proton-dependent lipid transporter involved in lipoteichoic acids biosynthesis

Bing Zhang^{1,3}, Xue Liu^{2,3}, Elisabeth Lambert^{1,3}, Guillaume Mas¹, Sebastian Hiller¹,
Jan-Willem Veening² and Camilo Perez¹✉

Lipoteichoic acids (LTAs) are essential cell-wall components in Gram-positive bacteria, including the human pathogen *Staphylococcus aureus*, contributing to cell adhesion, cell division and antibiotic resistance. Genetic evidence has suggested that LtaA is the flippase that mediates the translocation of the lipid-linked disaccharide that anchors LTA to the cell membrane, a rate-limiting step in *S. aureus* LTA biogenesis. Here, we present the structure of LtaA, describe its flipping mechanism and show its functional relevance for *S. aureus* fitness. We demonstrate that LtaA is a proton-coupled antiporter flippase that contributes to *S. aureus* survival under physiological acidic conditions. Our results provide foundations for the development of new strategies to counteract *S. aureus* infections.

The Gram-positive pathogen *S. aureus* is one of the leading causes of nosocomial infections around the globe^{1,2}. Multiple strains have acquired resistance to clinically used antibiotics^{1,2}, and methicillin-resistant *S. aureus* (MRSA) is one of the most successful modern pathogens^{1–4}. The cell wall of Gram-positive bacteria is primarily composed of peptidoglycan, wall-associated proteins, capsular polysaccharide and teichoic acids (TA)^{5,6}. TA are divided in LTA and wall-teichoic acids (WTAs)^{5–7}, both of which are necessary for proper localization of the cell-wall elongation and division machinery, contribute to immune evasion by concealing cell-wall epitopes, prevent recognition and opsonization by antibodies and have been shown to be important for adhesion, colonization and biofilm formation^{8–12}. By altering TA composition, Gram-positive bacteria are able to resist the action of hydrophobic antibacterial agents, cationic antimicrobial peptides, β -lactam and glycopeptide antibiotics^{7,13,14}.

From the five types of LTA known to date^{5,15}, the best characterized is type I LTA from *S. aureus*, which is recognized by Toll-like receptor 2 and has been associated with various inflammatory diseases ranging from minor skin diseases to severe sepsis^{16,17}. *S. aureus* LTA are composed of a polymer of 1,3-glycerol-phosphate repeat units attached to C-6 of the non-reducing glucosyl of the anchor lipid-linked-disaccharide gentiobiosyl-diacylglycerol (anchor-LLD) embedded in the extracellular side of the plasma membrane^{5–7,18}. Synthesis of the anchor-LLD occurs at the cytoplasmic leaflet of the membrane^{19–22}. Thus, translocation of anchor-LLD across the plasma membrane is a requisite for extracellular assembly of LTA^{7,19,23} (Fig. 1a), thus constituting a rate-limiting step in LTA synthesis since it regulates the pool of precursor anchor-LLD available. This translocation reaction is presumed to be catalyzed by the flippase LtaA, although its flippase activity has not been demonstrated. LtaA is found in all known *S. aureus* strains and also in closely related *Staphylococcus* species¹⁹. Deletion of the *ltaA* gene in *S. aureus* leads to attenuated virulence during animal infection and alterations in LTA composition, such as anchoring to phosphatidylglycerol and longer polymer length^{7,19}. Despite the clear relevance of LtaA in LTA biogenesis, remarkably little is known about its mechanism and function, in part owing to the lack of structural

information and the absence of comprehensive functional characterization in vitro and in vivo.

LtaA is a member of the major facilitator superfamily (MFS) of transporters¹⁹. The MFS superfamily, ubiquitously distributed across all kingdoms of life, consists of 74 families classified on the basis of their type of substrate²⁴. In bacteria, MFS transporters are mainly used for the uptake of nutrients and extrusion of deleterious compounds. Whereas in humans, they are implicated in the transport of a wide range of toxins and drugs, and their malfunction leads to multiple diseases^{25–27}. Currently, only six different MFS families have been structurally characterized^{28–34}. However, there are no reports that describe the structure of flippases in any of the 74 MFS families.

To elucidate the mechanism of LtaA-catalyzed anchor-LLD flipping, we determined the structure of *S. aureus* LtaA, characterized its transport properties by in vitro flipping assays, and investigated its function and relevance in live *S. aureus* cells. The structure of LtaA revealed a 12 transmembrane helices (TM) MFS fold and displays an outward-facing conformation. The central cavity of LtaA shows a unique amphiphilic architecture never seen before in any of the structurally characterized MFS transporters. We show that LtaA is an antiporter flippase that couples anchor-LLD translocation to proton antiport, which confers LtaA pH-sensing properties used by *S. aureus* to cope with the acidic stress found under normal physiological conditions.

Results

LtaA displays in vitro flipping activity. To characterize the flipping mechanism of LtaA in vitro, it is essential to establish reliable measurements of lipid translocation activity of wild-type (WT) LtaA and variants. Lipid translocation has been investigated for other lipid transporters using fluorescently labelled substrates that, when exposed on the outer leaflet of proteoliposomes, are quenched by sodium dithionite, a membrane-impermeable reducing agent^{35–37}. Because a suitable fluorescently labeled lipid substrate was so far not available for LtaA at the time of our study, we performed the chemoenzymatic synthesis of a nitrobenzoxadiazole (NBD)-labeled anchor-LLD (NBD-anchor-LLD) using recombinantly expressed

¹Biozentrum, University of Basel, Basel, Switzerland. ²Department of Fundamental Microbiology, Faculty of Biology and Medicine, University of Lausanne, Lausanne, Switzerland. ³These authors contributed equally: Bing Zhang, Xue Liu, Elisabeth Lambert. ✉e-mail: camilo.perez@unibas.ch

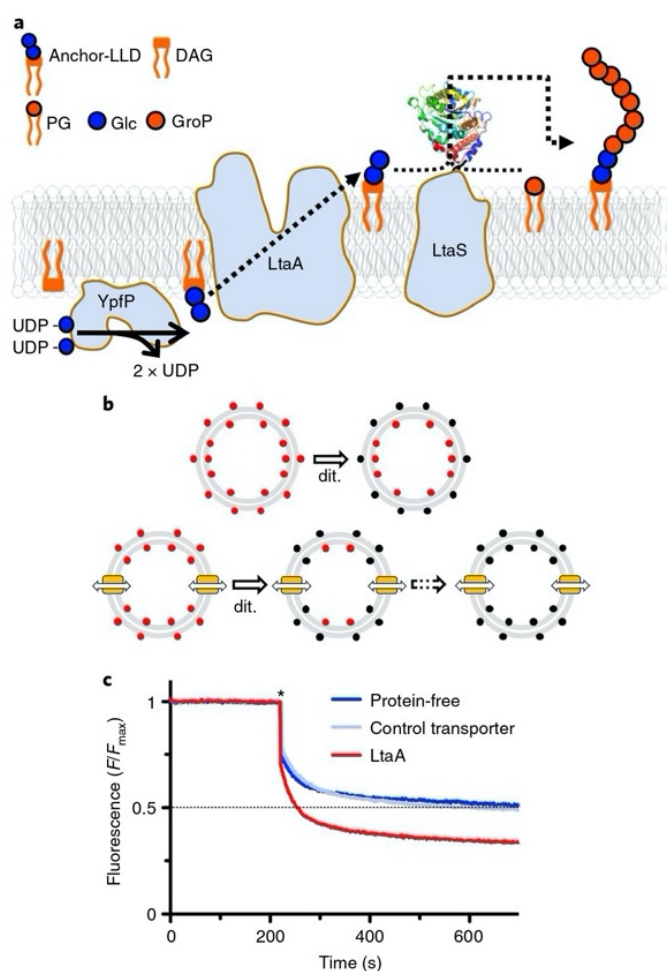


Fig. 1 | LtaA-catalyzed anchor-LLD flipping. **a**, LTA-synthesis pathway in *S. aureus*⁵. YpfP synthesizes the LTA anchor-LLD on the cytoplasmic leaflet of the membrane, and LtaA performs anchor-LLD flipping towards the extracellular side of the membrane, where the LtaS polymerase assembles the 1,3-glycerol-phosphate polymer on anchor-LLD. The structure of the periplasmic domain of LtaS (PDB: 4U00)²² is shown. PG, phosphatidylglycerol; DAG, diacylglycerol; Glc, glucose; GroP, glycerol-phosphate; anchor-LLD, gentiobiosyl-diacylglycerol. Figure adapted from Percy and Gründling⁵. **b**, Scheme of flipping assay. NBD-anchor-LLD lipids (red spheres) are irreversibly reduced (black spheres) by dithionite (dit.). In protein-free liposomes, only outer-leaflet fluorophores are reduced. In proteoliposomes containing LtaA (yellow boxes), a larger proportion of the fluorophores are reduced owing to exchange. Full fluorescence quenching will be achieved after prolonged incubation (dashed arrow). **c**, Flipping of NBD-anchor-LLD by LtaA. Representative traces shown are from protein-free liposomes and proteoliposomes containing either LtaA or a functionally unrelated transporter (bacterial choline transporter) ($n \geq 3$). Asterisk marks addition of dithionite. F corresponds to the fluorescence intensity measured for each time point. F_{max} is the average fluorescence measured during the first 200 seconds.

and purified YpfP^{20,21}. In *S. aureus*, YpfP synthesizes the native LtaA substrate during LTA assembly (Fig. 1a). In an in vitro reaction, purified YpfP catalyzed the reaction between UDP-Glc and NBD-labeled diacylglycerol (NBD-DAG) to produce NBD-anchor-LLD. Tandem mass spectrometry (MS/MS), parallel-reaction monitoring (PRM), high-resolution liquid chromatography–mass spectrometry (HPLC–MS) and one-dimensional

proton nuclear magnetic resonance (1D ¹H NMR) spectroscopy confirmed the presence of NBD-anchor-LLD in enriched extracts (Supplementary Figs. 1–8 and Supplementary Tables 1–6).

For the functional flipping assay, we incorporated NBD-anchor-LLD into protein-free liposomes or into LtaA proteoliposomes. Upon the addition of dithionite, the fluorescence of protein-free liposomes plateaus at about 50% of the total fluorescence (Fig. 1b,c), consistent with the expectation that NBD-anchor-LLD distributes symmetrically between the two leaflets and that it does not show spontaneous transbilayer diffusion, owing to its prominent hydrophilic disaccharide headgroup. In contrast, in LtaA-proteoliposomes, the NBD-anchor-LLD fluorescence plateaus at about 35% of the initial intensity, clearly demonstrating that LtaA possesses NBD-anchor-LLD flipping activity (Fig. 1b,c).

To verify that the flipping activity detected was LtaA-specific, we performed the same type of experiment but with a functionally unrelated protein (choline transporter) reconstituted in proteoliposomes (Fig. 1c). In this experiment, quenching by dithionite led to a fluorescence plateau of 50%, validating that the flipping activity observed in LtaA proteoliposomes is catalyzed by LtaA. Furthermore, control experiments with protein-free liposomes containing the precursor molecule NBD-DAG plateau at about 30% (Extended Data Fig. 1), consistent with spontaneous transbilayer diffusion of NBD-DAG due to its prominent hydrophobicity. Together, these experiments demonstrate that LtaA displays anchor-LLD flippase activity.

Structure of *S. aureus* LtaA. We determined the structure of LtaA from *S. aureus* at 3.3 Å resolution (Fig. 2a,b, Extended Data Figs. 2–4 and Table 1). Experimental phases were determined by single-wavelength anomalous diffraction (SAD) from selenomethionine (SeMet)-derivative crystals. The register of the resulting model was confirmed by the anomalous densities of 16 SeMet residues along the polypeptide chain (Extended Data Fig. 4). LtaA crystals commonly diffracted X-rays up to 7 Å resolution; however, by optimizing in situ annealing conditions³⁸, we were able to increase the diffraction resolution up to 3.3 Å, accompanied by an up to 18% reduction of the unit cell volume (Extended Data Fig. 2c).

LtaA displays the fold of MFS transporters, which consists of 12 TM divided into two 6TM domains (amino- and carboxy-terminal domains) related by a pseudo-rotational two-fold symmetry axis perpendicular to the plane of the membrane (Fig. 2a and Extended Data Fig. 5a). The fold of both domains is similar, showing an r.m.s. deviation (r.m.s.d.) of 3.2 Å upon secondary-structure superposition. Both domains are connected through a cytoplasmic helical loop, a structural feature observed in many other MFS fold transporters^{39,40}. The LtaA structure displays an outward-facing state with two prominent lateral hydrophobic entrances (Fig. 2a and Extended Data Fig. 5b). One of the entrances is flanked by TMs 2 and 11, whereas TMs 5 and 8 flank the entrance on the opposite side. TM11 delimiting one of the hydrophobic entrances displays the antiporter motif⁴¹ G (G³⁴⁵(X)₈G(X)₃GP(X)₂GG³⁶³), whereas on the opposite entrance, TM5 displays a similar motif-G-like sequence at the same position (Extended Data Fig. 5c). Access to the central cavity from the cytoplasmic face is sealed off by multiple interactions between TMs 2, 4 and 5 from the N-terminal domain, and TMs 8, 10 and 11 from the C-terminal domain, and cytoplasmic loops connecting TMs 4–5 and TMs 10–11 (Extended Data Fig. 5d).

One striking structural feature of LtaA architecture is the presence of a large amphiphilic central cavity whose hydrophilic part is harbored by the N-terminal domain of the flippase with the participation of residues E32, R35, D68, W127 and W150, located in TMs 1, 2, 4 and 5 (Fig. 2a,c). On the other hand, the hydrophobic part of the cavity is harbored by the C-terminal domain of the flippase with the participation of 8 hydrophobic residues located in TMs 7, 8, 9 and 10 (Fig. 2a,c). Such an amphiphilic cavity has

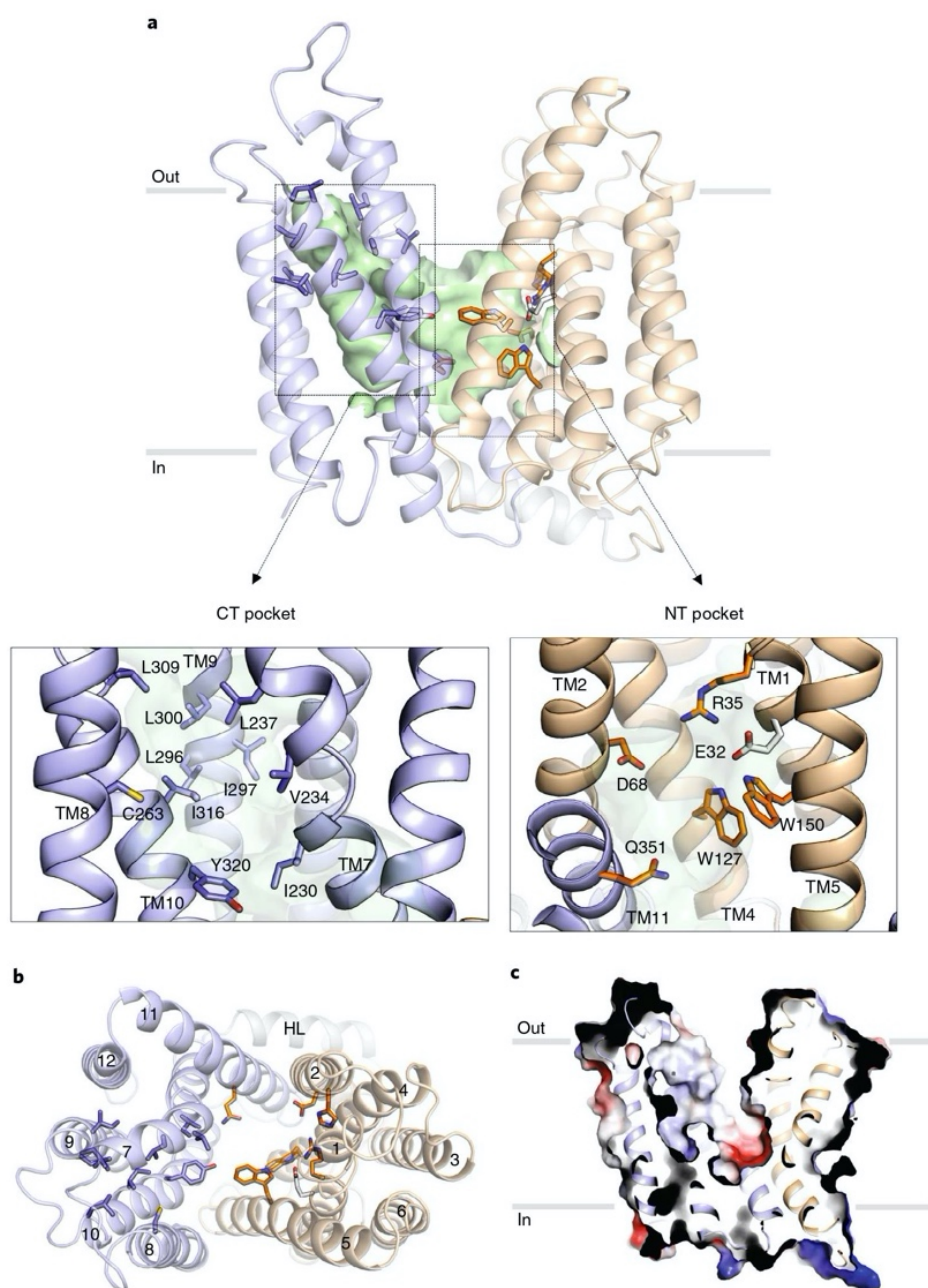


Fig. 2 | *S. aureus* LtaA structure. **a**, Structure of LtaA showing its central cavity (green surface). CT, C-terminal, NT, N-terminal. The N-terminal domain is shown in light orange, and the C-terminal domain is shown in light blue. Residues forming the hydrophobic C-terminal pocket and the hydrophilic N-terminal pocket are shown. **b**, Top view of LtaA. Residues in sticks participate in the formation of the amphiphilic cavity. TM segments are numbered. HL, helical loop. **c**, Vacuum electrostatic surface representation of LtaA, showing the internal cavity.

not been observed in any other MFS fold transporter described to date. Sequence-conservation analysis revealed that residues forming the N-terminal hydrophilic pocket are highly conserved among LtaA homologues found in other *Staphylococcus* species or further Gram-positive bacteria, whereas residues forming the C-terminal hydrophobic pocket are less conserved, although their positions are prominently occupied by amino acids with aliphatic side chains (Extended Data Fig. 6 and Supplementary Fig. 9).

LtaA displays high selectivity towards the headgroup of its substrate. We used computational docking to test whether the binding of anchor-LLD to outward-facing LtaA was feasible. The

ligand-docking analysis suggests that the gentiobiosyl headgroup of the anchor-LLD is preferentially accommodated in the N-terminal hydrophilic pocket, whereas the diacylglycerol aliphatic tails are docked with one or both chains in the C-terminal hydrophobic pocket in multiple conformations (Fig. 3a and Extended Data Fig. 7a). This, together with the high sequence conservation of the residues forming the hydrophilic pocket, led us to hypothesize that LtaA might display high selectivity towards the anchor-LLD headgroup. To test this hypothesis, we assessed flipping activity in the presence of different disaccharide compounds (Fig. 3b–c and Extended Data Fig. 7b). If LtaA displays high selectivity towards the disaccharide headgroup of its substrate, one would expect to see

Table 1 | Data collection and refinement statistics

	LtaA (SeMet) ^a (PDB 6S7V)
Data collection	
Space group	C222 ₁
Cell dimensions	
<i>a</i> , <i>b</i> , <i>c</i> (Å)	51.39, 162.47, 191.05
α , β , γ (°)	90, 90, 90
Resolution (Å)	20–3.3 (3.4–3.3) ^b
<i>R</i> _{meas} (%)	13.5 (153.7) [22.1 (414.8)] ^c
<i>I</i> / σ (<i>I</i>)	12.76 (1.64) [6.93 (1.36)]
CC _{1/2} (%)	99.9 (94.4) [100 (86.8)]
Completeness (%)	83.37 (32.3) [98.37 (97.55)]
Redundancy	40 (39)
Refinement	
Resolution (Å)	20–3.3 (3.4–3.3)
No. reflections	12,387 [19,539]
<i>R</i> _{work} / <i>R</i> _{free} (%)	27.05/28.94
No. atoms	
Protein	3,001
B factors	
Protein	84
R.m.s. deviations	
Bond lengths (Å)	0.006
Bond angles (°)	0.987

^aData are from one crystal. ^bValues in parentheses are for highest-resolution shell. ^cValues in square brackets are before anisotropic truncation.

reduced flipping activity in the presence of an excess of gentiobiose (β -D-Glc-(1,6)-D-Glc), a disaccharide with the same chemical composition and conformation as the anchor-LLD headgroup. Indeed, we found that increasing concentrations of gentiobiose inhibit LtaA-catalyzed flipping activity, whereas other disaccharides, that is lactose (β -D-Gal-(1,4)-D-Glc), sucrose (α -D-Glc-(1,2)- β -D-Fru) and trehalose (α -D-Glc-(1,1)- α -D-Glc) showed no inhibitory effect at a similar concentration (Fig. 3c). These results indirectly but strongly suggest that LtaA displays high selectivity towards the headgroup of its substrate.

LtaA N-terminal hydrophilic pocket is crucial for flipping activity. Next, we assessed the functional role of residues in the highly conserved N-terminal hydrophilic pocket. According to our docking model, this pocket might accommodate the anchor-LLD headgroup. First, we constructed a *S. aureus* NCTC8325 Δ *ltaA* mutant, which we then complemented with an ectopic copy of the *ltaA* gene carrying single point mutations, and evaluated growth on agar plates at 37°C and in the presence of 5% CO₂ (Fig. 3d). Strikingly, although *ltaA* was shown not to be essential under laboratory conditions¹⁹, we found that non-complemented Δ *ltaA* mutants are non-viable in the presence of 5% CO₂, demonstrating that LtaA is crucial for *S. aureus* fitness. Mutants Y320A and Q351A rescued the growth defect of the Δ *ltaA* strain, whereas mutants E32A, R35A, D68A, W127A and W150A did not. Notably, under overexpression conditions, the mutants R35A, D68A, W127A and W150A, but not E32A, rescued the growth defect (Extended Data Figs. 8 and 9), indicating that E32 has a key role in LtaA activity.

Next, for several of the mutants tested for their ability to rescue Δ *ltaA*, we examined for the capacity to perform flipping of NBD-anchor-LLD. In vitro flipping assays with LtaA double

mutants, which combine the five mutations that showed the stronger impact on *S. aureus* growth, revealed that the mutant R35A/D68A is not active and that the relative activity of mutants E32A/D68A and D68A/W150A is about half that of LtaA-WT (Fig. 3e,f). This agrees with our in vivo assays that revealed that the mutants E32A, R35A, D68A, W127A and W150A display a strong growth defect of the Δ *ltaA* strain (Fig. 3d). Taken together, these results indicate that slight modifications of the activity of LtaA are sufficient to perturb the assembly line of LTA, and in consequence, the fitness of *S. aureus*.

LtaA is a proton-coupled antiporter flippase. Charged residues located in substrate-binding sites of secondary transporters have been frequently associated with proton coupling because they may undergo pK_a shifts as a consequence of structural changes during the transport cycle^{39,42}. LtaA possesses three candidates for such pH-coupling residues, E32, R35 and D68, which are all located in the N-terminal hydrophilic part of the central amphiphilic cavity (Fig. 2a). We therefore explored whether anchor-LLD flipping could be energized by a proton-gradient by measuring LtaA catalyzed NBD-anchor-LLD flipping in proteoliposomes (Fig. 4a and Extended Data Fig. 10). In the absence of a proton gradient, quenching of the NBD-anchor-LLD reached a plateau at about 35% of the total fluorescence. Strikingly, if we imposed an inward proton gradient (low pH_{out}/high pH_{in}), larger quenching of NBD-anchor-LLD was observed. On the contrary, if we imposed an outward proton gradient (high pH_{out}/low pH_{in}), less quenching of NBD-anchor-LLD was observed, relative to no gradient conditions (Fig. 4a). As controls, we carried out the same type of experiment but with protein-free liposomes (Fig. 4b) and with a functionally unrelated protein reconstituted in proteoliposomes (Extended Data Fig. 10a); the result was that NBD-anchor-LLD quenching plateaued at about the same fluorescence level, independent of the pH gradient. In summary, these results reveal that LtaA performs vectorial flipping of anchor-LLD opposite to the direction of the proton gradient.

Protons transport mediated by LtaA was demonstrated using a fluorescence assay⁴³ in which proteoliposomes loaded with 100 mM KCl (pH 7.3) were diluted 20-fold into an assay buffer containing 10 mM KCl (pH 7.3). Under these conditions, if LtaA performs H⁺ transport, the addition of the K⁺-selective ionophore valinomycin will drive H⁺ influx and cause quenching of the fluorophore 9-amino-6-chloro-2-methoxyacridine (ACMA). The robust fluorescence decrease observed upon the addition of valinomycin reflects H⁺ influx into the proteoliposomes driven by the membrane potential (Fig. 4c). A control experiment with protein-free liposomes showed little fluorescence change (Fig. 4c).

We performed flipping assays and proton-transport assays with the single-point-mutant LtaA-E32A reconstituted in proteoliposomes (Fig. 4b,c). This residue was selected as the best candidate to undergo protonation and deprotonation because of its theoretical pK_a-value of 7.8 in the current outward-facing structure, compared to residues R35 and D68 with pK_a values of 14 and 3.4, respectively. Our results show that the E32A mutation is insensitive to transmembrane proton gradients, maintaining basal activity (Fig. 4b). Consistent with this is the observed decrease of H⁺ influx driven by the membrane potential (Fig. 4c). In summary, these data establish that LtaA works as a proton-coupled antiporter flippase, and that residue E32 plays a crucial role in proton coupling, presumably by being involved in proton transport. The importance of proton coupling for LtaA function in vivo becomes evident as pointed out by the strong growth defect of the *S. aureus* Δ *ltaA* strain expressing LtaA-E32A (Fig. 3d and Extended Data Fig. 9a).

LtaA is essential to combat acid stress. In *S. aureus* cells, synthesis of anchor-LLD by the glycosyltransferase YpfP occurs at the cytoplasmic leaflet without interruption as long as the levels of DAG

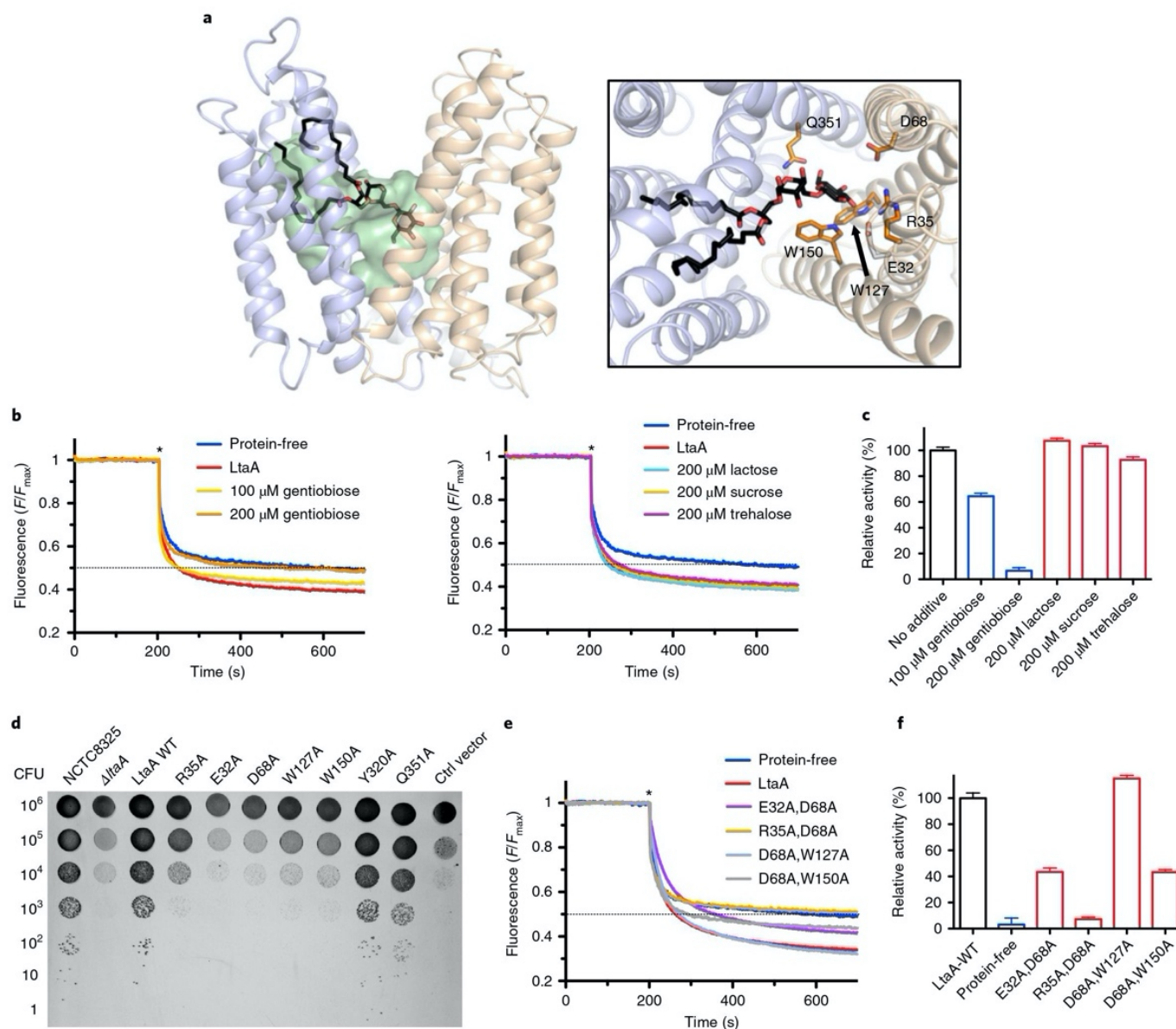


Fig. 3 | Amphiphilic cavity characterization. **a**, A model of lipid-linked-disaccharide docked into the amphiphilic cavity of LtaA (see also Extended Data Fig. 7a). The lipid tail length corresponds to C_{16} chains¹⁹. Right inset, top view of anchor-LLD binding pocket and residues coordinating its gentiobiosyl headgroup. **b**, Representative traces of LtaA-catalyzed flipping in the presence of different disaccharides at given concentrations ($n \geq 3$). **c**, Relative flipping activity of assays shown in **b**. Error bars indicate the s.d. of technical replicates, $n \geq 3$. **d**, Cell growth on IPTG-free C + Y agar plates at 37 °C and in the presence of 5% CO_2 . $\Delta ltaA$ represents the *S. aureus* NCTC8325 $\Delta ltaA$ mutant; LtaA WT represents the $\Delta ltaA$ mutant complemented with WT LtaA on a multicopy vector (pLOW); Ctrl vector indicates the $\Delta ltaA$ mutant complemented with pLOW carrying a nonrelated gene (*dcas9*); the other labels represent the $\Delta ltaA$ mutant complemented with LtaA with corresponding point mutations. **e**, Representative traces of flipping activity of LtaA-WT and variants. **f**, Relative flipping activity of assays shown in **e**. Asterisk marks addition of dithionite. Error bars indicate the s.d. of technical replicates, $n \geq 3$. F corresponds to the fluorescence intensity measured for each time point. F_{max} is the average fluorescence measured during the first 200 seconds.

and UDP-Glc in the cell are preserved^{20,21}. Under these conditions, healthy *S. aureus* displays an outward anchor-LLD gradient that would suffice to drive LtaA-facilitated flipping. Thus, we wondered whether the proton-coupling activity of LtaA could play an important role in the survival of *S. aureus* under physiological conditions encountered at the human nasopharynx and mucous membranes and on the skin, which present mild acidic environments ($5.0 < pH < 6.5$)^{44–46}.

To evaluate this hypothesis, we investigated the growth characteristics of *S. aureus* NCTC8325 $\Delta ltaA$ on plates at 37 °C under different pH conditions in the absence of CO_2 (ambient conditions)

(Fig. 4d). We found that at high pH, the $\Delta ltaA$ mutant does not show a growth defect compared with WT or LtaA-complemented *S. aureus*, in line with previous findings¹⁹. However, very strong growth retardation was observed in the $\Delta ltaA$ mutant at low pH, while complementation with LtaA-WT restored normal growth. Alternatively, the presence of 5% CO_2 , which acidifies the medium to about pH 6.0 owing to CO_2/HCO_3 equilibria, equivalently suffices to promote a strong growth defect of the $\Delta ltaA$ mutant (Fig. 4d). In the same way, point mutations of the proton-coupling E32 residue and others forming the N-terminal hydrophilic pocket showed a strong growth defect at low pH (Fig. 4e), consistent with their important role in

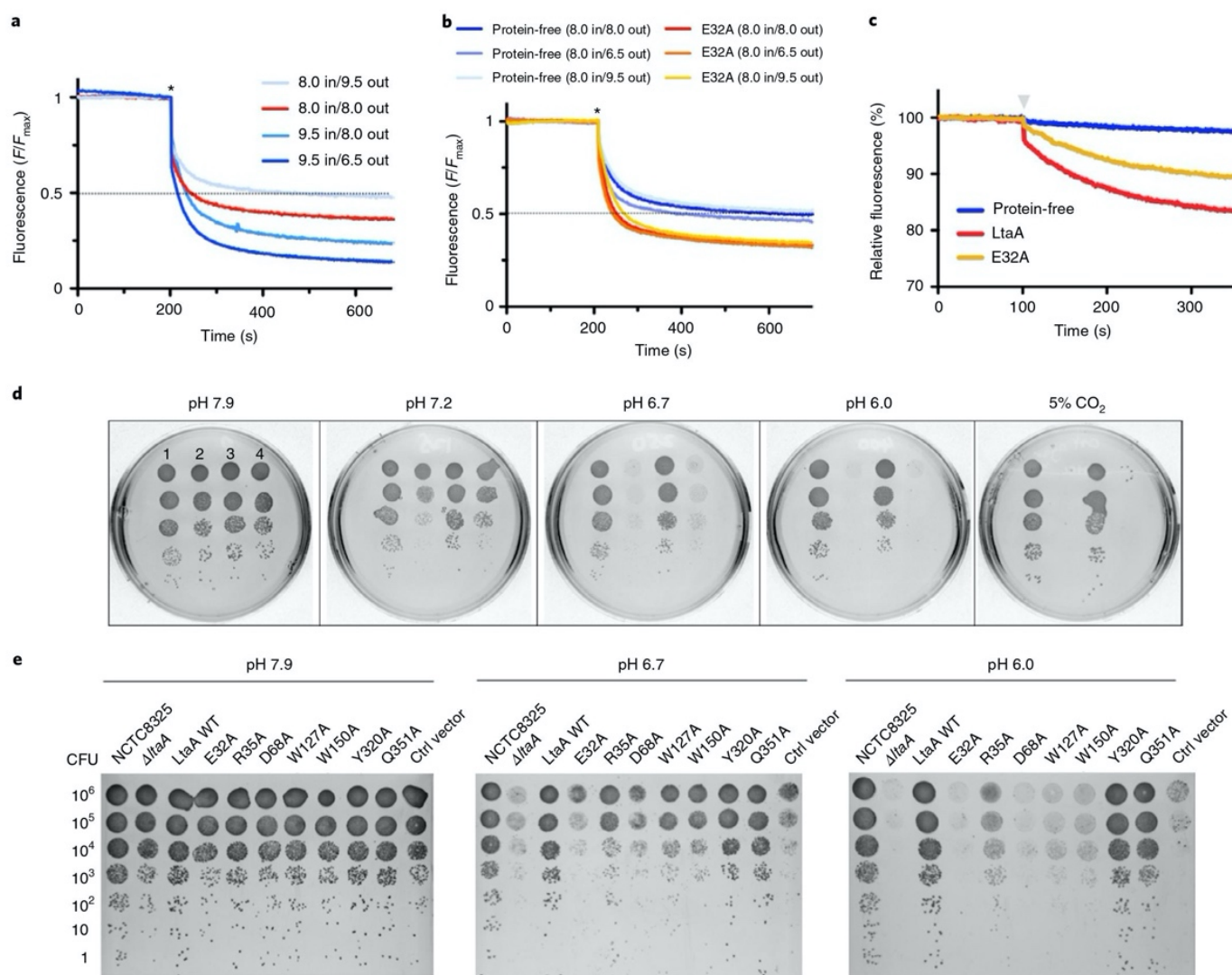


Fig. 4 | LtaA proton coupling and *S. aureus* Δ ltaA growth under acidic conditions. **a, b**, Representative traces of flipping assays with protein-free liposomes, LtaA-WT and LtaA-E32A, in the presence of different proton gradients; in and out denote the pH of the buffer inside and outside of liposomes, respectively ($n \geq 3$). Asterisk marks addition of dithionite. Traces in **(a)** are for LtaA-WT proteoliposomes. F correspond to the fluorescence intensity measured for each time point. F_{max} is the average fluorescence measured during the first 200 seconds. **c**, Proton-transport assay. Representative time courses are shown ($n \geq 3$). Proteoliposomes and protein-free liposomes containing 100 mM KCl were diluted in buffer containing 10 mM KCl and 9-amino-6-chloro-2-methoxyacridine (ACMA). H^+ influx was initiated by establishing a membrane potential by addition of the potassium ionophore valinomycin (gray triangle). **d**, Cell growth in IPTG-free C + Y agar plates under different pH conditions at 37 °C in the absence of CO₂ (ambient condition) or in the presence of 5% CO₂ (initial pH 7.9). 1 indicates *S. aureus* NCTC8325 WT, 2 indicates the Δ ltaA mutant, 3 indicates the Δ ltaA mutant complemented with WT *ltaA* on a multicopy vector (pLOW) and 4 indicates the Δ ltaA mutant complemented with pLOW carrying a functionally unrelated gene (*dcas9*). **e**, *S. aureus* NCTC8325 Δ ltaA mutant complemented with *ltaA* carrying corresponding point mutations. Shown is cell growth on IPTG-free C + Y agar plates under different pH conditions at 37 °C. LtaA WT represents Δ ltaA mutant complemented with wild type *ltaA*; Ctrl vector indicates Δ ltaA mutant complemented with a functionally unrelated gene (*dcas9*).

the coordination of the anchor-LLD headgroup and E32 essential role in proton transport, as shown above. The E32A mutant does not recover the growth defect at low pH even under overexpression conditions (Extended Data Fig. 9b). Fluorescence microscopy and transmission electron microscopy (TEM) of *S. aureus* NCTC8325 WT and Δ ltaA grown at 37 °C in LB medium at pH 6.5 or grown in the presence of 5% CO₂ (medium pH 6.5) showed that the *ltaA* deletion mutant displays aberrant cell morphologies, including enlarged cells, defects in the formation and localization of the division septum and abnormal cell-wall shape (Fig. 5a,b and Extended Data Fig. 9c).

Our results attribute an essential role to LtaA in the survival of *S. aureus* under acidic conditions. This is highly relevant because

such conditions are encountered in the most common niches of this bacteria in the human body^{44–47}. Thus, the development of drugs targeting LtaA might lead to new therapies for the treatment of *S. aureus* infections.

Discussion

Taken together, our biochemical and structural studies suggest a functional cycle in which LtaA performs anchor-LLD translocation energized by proton antiport (Fig. 6). The mechanism probably follows in its structural conformations the classic antiporter alternating-access cycle^{48,49}. However, owing to the amphiphilic nature of the substrate, the conformational and energy landscape of lipid flipping by LtaA might look very different than that of canonical

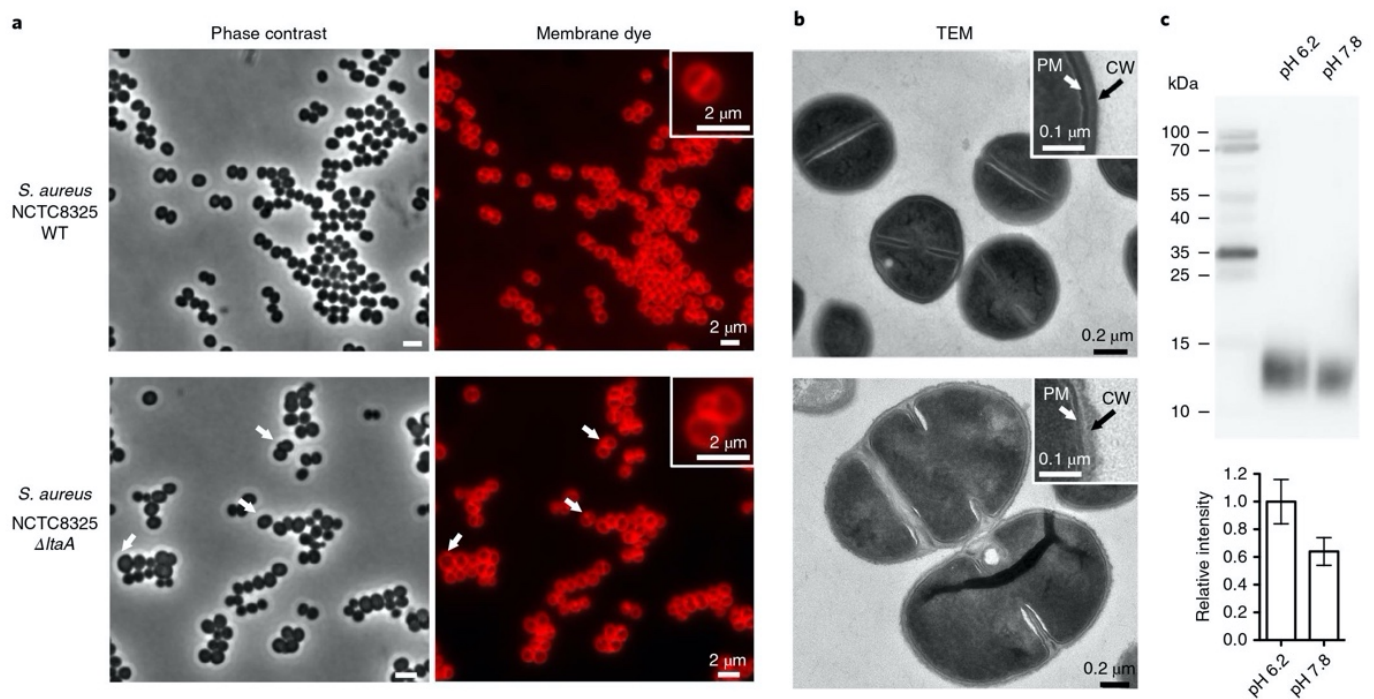


Fig. 5 | Morphology of *S. aureus* NCTC8325 WT and Δ *ltaA* mutant, and LTA abundance. **a**, Phase contrast and fluorescence images. Bacteria were grown to mid-exponential phase in LB medium at 37 °C with 5% CO₂, causing acidification of the medium. The membrane dye used was Nile red. White arrows point to cells with aberrant morphology. **b**, Transmission electron microscopy (TEM) images. PM indicates plasma membrane. CW indicates cell wall. Low-magnification images are shown in Extended Data Fig. 9c. **c**, Detection of LTA by immunoblotting. *S. aureus* NCTC8325 was cultured in LB medium buffered with PBS to different pH (6.2 and 7.8) levels. Cell lysates were normalized on the basis of optical density. Samples were separated by 12% SDS-polyacrylamide gel electrophoresis and LTA was detected by an LTA (polyglycerolphosphate)-specific primary antibody. Histogram shows the relative amounts of LTA determined from band intensities ($n = 4$). Error bars indicate s.d. of technical replicates.

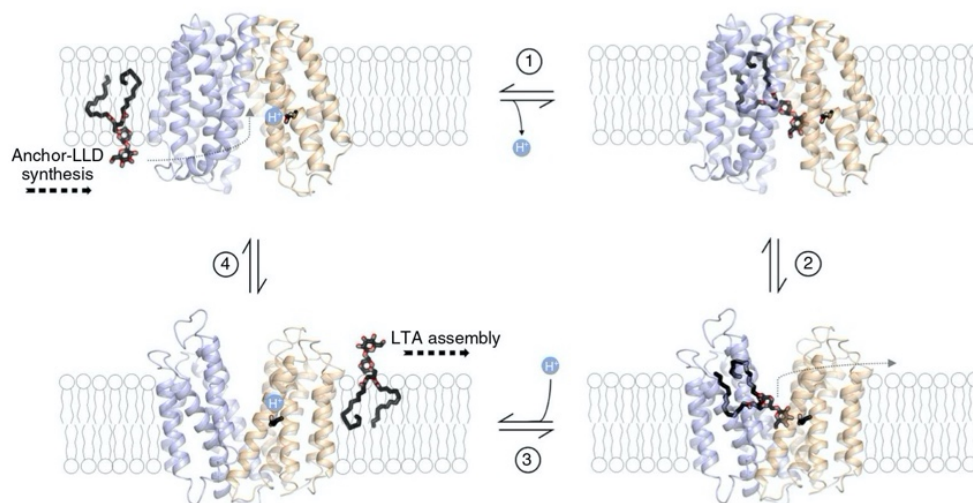


Fig. 6 | LtaA anchor-LLD flipping mechanism. 1, Binding of lipid-linked-disaccharide (black and red sticks) in the central cavity of LtaA in the inward-facing conformation (modeled conformation) and deprotonation of E32. 2, Transition to outward-facing state (structure determined in this study). 3, Substrate release into the membrane and protonation of E32. 4, Transition to inward-facing state (modeled conformation). The N-terminal domain is shown in light orange, and the C-terminal domain is shown in light blue. The inward-facing model of LtaA was constructed by rigid body alignment of the N-terminal domain (TM1–6) and the C-terminal domain (TM7–12) to those of inward-facing LacY (PDB: 2CFQ)⁶⁰.

transporters of water-soluble substrates. Specifically, substrate recognition, loading into the central cavity and release are expected to entail different mechanisms. In a first step, deprotonated LtaA in an inward-facing conformation recognizes and binds the anchor-LLD in its central cavity, positioning the lipid tails at the C-terminal hydrophobic pocket and the disaccharide headgroup at the N-terminal

hydrophilic pocket. Recognition and extraction of the anchor-LLD from the pool of surrounding lipids are facilitated by specific binding of the gentiobiosyl headgroup, which allows extraction of the lipid out of the membrane. Subsequently, LtaA will change its conformation to an outward-facing state promoting substrate release into the membrane. We suggest that the prominent lateral entrances observed in

the crystal structure might facilitate the toppling of the anchor-LLD back into the bilayer. After substrate release in the outward-facing state, residue E32 will become protonated, facilitating the transition to an inward-facing state, where it will then undergo deprotonation. This mechanism explains the stimulation of transport by a proton gradient, and while in the absence of it, LtaA performs antiport driven by the outward directed anchor-LLD gradient maintained by the activity of YpfP in *S. aureus* cells. In the absence of a proton gradient, anchor-LLD translocation will happen at a slower rate in the cell, in full agreement with our in vitro flipping assays.

The LtaA flipping mechanism proposed here has certain similarities to the flipping mechanism proposed for the lipid-II flippase MurJ^{50,51}. MurJ belongs to the multidrug/oligosaccharyl-lipid/poly-saccharide (MOP) family of transporters, and plays an important role in peptidoglycan assembly⁵². Similar to the C-terminal hydrophobic pocket observed in LtaA, in MurJ, a hydrophobic groove formed by C-terminal TM helices 13 and 14 contributes to binding of the undecaprenyl lipid tail of lipid-II. These similarities suggest that secondary transporter flippases might share a mechanism wherein part of the internal cavity specializes in binding specific lipid moieties, facilitating in this way loading and translocation of amphiphilic molecules. Thus, the amphiphilic cavities observed in LtaA and MurJ might constitute a general structural signature that may contribute to the identification of other flippases in silico. The architecture of the outward-open LtaA structure provides the basis to understand anchor-LLD recognition, binding and release into the membrane. These results, together with the apparent high selectivity of LtaA for the anchor-LLD headgroup and inhibition of the flipping activity by gentiobiose, provide the structural basis to design inhibitors targeting LTA assembly.

The mechanism by which LtaA contributes to *S. aureus* survival under acidic conditions is intimately related to its capacity to couple anchor-LLD flipping to proton transport. This mechanism makes LtaA a 'pH sensing' flippase that, by increasing anchor-LLD transport under low pH conditions, enlarges the population of LTA at the outer leaflet of the plasma membrane (Fig. 5c). Besides the already-known important functions of LTA for cell division and protection against environmental threats^{57–9}, we hypothesize that increased amounts of LTA in the cell wall will probably provide an efficient way to buffer against acidification thanks to the high negative charge of the LTA backbone polymer. Notably, the description of a pH-sensing mechanism in a lipid transporter represents a fundamental conceptual advance in the field of lipid transport.

Membrane transport proteins performing unidirectional active translocation of lipids (flipping) generate membrane asymmetry^{50,51,53–57}. On the other hand, membrane proteins that perform passive bidirectional translocation of lipids (scrambling) disrupt the membrane asymmetry^{36,37,58}. Lipid flipping energized by ATP hydrolysis has been well characterized for multiple protein families^{53,55–57}. Our results identify LtaA as a new class of flippase that energizes lipid translocation by coupling to a transmembrane proton gradient. These findings will potentiate the search of other ion-coupled flippases, not only in Gram-positive bacteria but in all prokaryotes. For example, it has been shown that the lipid-II flippase MurJ requires a membrane potential for its function⁵⁹. In this case, in addition to driving export of lipid-II due to its intrinsic net negative charge, a membrane potential might drive lipid-II flipping by transport of a coupling ion, but this remains to be shown.

Online content

Any methods, additional references, Nature Research reporting summaries, source data, extended data, supplementary information, acknowledgements, peer review information; details of author contributions and competing interests; and statements of data and code availability are available at <https://doi.org/10.1038/s41594-020-0425-5>.

Received: 11 September 2019; Accepted: 30 March 2020;
Published online: 4 May 2020

References

- Rivera, A. M. & Boucher, H. W. Current concepts in antimicrobial therapy against select Gram-positive organisms: methicillin-resistant *Staphylococcus aureus*, penicillin-resistant pneumococci, and vancomycin-resistant enterococci. *Mayo Clin. Proc.* **86**, 1230–1243 (2011).
- Cosgrove, S. E. et al. The impact of methicillin resistance in *Staphylococcus aureus* bacteremia on patient outcomes: mortality, length of stay, and hospital charges. *Infect. Control Hosp. Epidemiol.* **26**, 166–174 (2005).
- Turner, N. A. et al. Methicillin-resistant *Staphylococcus aureus*: an overview of basic and clinical research. *Nat. Rev. Microbiol.* **17**, 203–218 (2019).
- Brown, S. et al. Methicillin resistance in *Staphylococcus aureus* requires glycosylated wall teichoic acids. *Proc. Natl Acad. Sci. USA* **109**, 18909–18914 (2012).
- Percy, M. G. & Grundling, A. Lipoteichoic acid synthesis and function in Gram-positive bacteria. *Annu. Rev. Microbiol.* **68**, 81–100 (2014).
- Brown, S., Santa Maria, J. P. Jr. & Walker, S. Wall teichoic acids of Gram-positive bacteria. *Annu. Rev. Microbiol.* **67**, 313–336 (2013).
- Xia, G., Kohler, T. & Peschel, A. The wall teichoic acid and lipoteichoic acid polymers of *Staphylococcus aureus*. *Int. J. Med. Microbiol.* **300**, 148–154 (2010).
- Reichmann, N. T. et al. Differential localization of LTA synthesis proteins and their interaction with the cell division machinery in *Staphylococcus aureus*. *Mol. Microbiol.* **92**, 273–286 (2014).
- Sewell, E. W. & Brown, E. D. Taking aim at wall teichoic acid synthesis: new biology and new leads for antibiotics. *J. Antibiot. (Tokyo)* **67**, 43–51 (2014).
- Lee, J. H. et al. Surface glycopolymers are crucial for in vitro anti-wall teichoic acid IgG-mediated complement activation and opsonophagocytosis of *Staphylococcus aureus*. *Infect. Immun.* **83**, 4247–4255 (2015).
- Gautam, S., Kim, T., Lester, E., Deep, D. & Spiegel, D. A. Wall teichoic acids prevent antibody binding to epitopes within the cell wall of *Staphylococcus aureus*. *ACS Chem. Biol.* **11**, 25–30 (2016).
- Bucher, T., Oppenheimer-Shaanan, Y., Savidor, A., Bloom-Ackermann, Z. & Kolodkin-Gal, I. Disturbance of the bacterial cell wall specifically interferes with biofilm formation. *Environ. Microbiol. Rep.* **7**, 990–1004 (2015).
- Campbell, J. et al. Synthetic lethal compound combinations reveal a fundamental connection between wall teichoic acid and peptidoglycan biosyntheses in *Staphylococcus aureus*. *ACS Chem. Biol.* **6**, 106–116 (2011).
- Peschel, A. et al. Inactivation of the *dlt* operon in *Staphylococcus aureus* confers sensitivity to defensins, protegrins, and other antimicrobial peptides. *J. Biol. Chem.* **274**, 8405–8410 (1999).
- Reichmann, N. T. & Grundling, A. Location, synthesis and function of glycolipids and polyglycerolphosphate lipoteichoic acid in Gram-positive bacteria of the phylum Firmicutes. *FEMS Microbiol. Lett.* **319**, 97–105 (2011).
- Hong, S. W. et al. Lipoteichoic acid of *Streptococcus* mutants interacts with Toll-like receptor 2 through the lipid moiety for induction of inflammatory mediators in murine macrophages. *Mol. Immunol.* **57**, 284–291 (2014).
- Kang, S.-S., Sim, J.-R., Yun, C.-H. & Han, S. H. Lipoteichoic acids as a major virulence factor causing inflammatory responses via Toll-like receptor 2. *Arch. Pharm. Res.* **39**, 1519–1529 (2016).
- Fischer, W., Koch, H. U., Rosel, P., Fiedler, F. & Schmuck, L. Structural requirements of lipoteichoic acid carrier for recognition by the poly(ribitol phosphate) polymerase from *Staphylococcus aureus* H. A study of various lipoteichoic acids, derivatives, and related compounds. *J. Biol. Chem.* **255**, 4550–4556 (1980).
- Grundling, A. & Schneewind, O. Genes required for glycolipid synthesis and lipoteichoic acid anchoring in *Staphylococcus aureus*. *J. Bacteriol.* **189**, 2521–2530 (2007).
- Jorasch, P., Wolter, F. P., Zahringer, U. & Heinz, E. A UDP glucosyltransferase from *Bacillus subtilis* successively transfers up to four glucose residues to 1,2-diacylglycerol: expression of *yfpP* in *Escherichia coli* and structural analysis of its reaction products. *Mol. Microbiol.* **29**, 419–430 (1998).
- Kiriukhin, M. Y., Debabov, D. V., Shinabarger, D. L. & Neuhaus, F. C. Biosynthesis of the glycolipid anchor in lipoteichoic acid of *Staphylococcus aureus* RN4220: role of YpfP, the diglycosyldiacylglycerol synthase. *J. Bacteriol.* **183**, 3506–3514 (2001).
- Grundling, A. & Schneewind, O. Synthesis of glycerol phosphate lipoteichoic acid in *Staphylococcus aureus*. *Proc. Natl Acad. Sci. USA* **104**, 8478–8483 (2007).
- Lu, D. et al. Structure-based mechanism of lipoteichoic acid synthesis by *Staphylococcus aureus* LtaS. *Proc. Natl Acad. Sci. USA* **106**, 1584–1589 (2009).
- Reddy, V. S., Shlykov, M. A., Castillo, R., Sun, E. I. & Saier, M. H. Jr. The major facilitator superfamily (MFS) revisited. *FEBS J.* **279**, 2022–2035 (2012).
- Cura, A. J. & Carruthers, A. Role of monosaccharide transport proteins in carbohydrate assimilation, distribution, metabolism, and homeostasis. *Compr. Physiol.* **2**, 863–914 (2012).
- Smith, D. E., Clemenson, B. & Hediger, M. A. Proton-coupled oligopeptide transporter family SLC15: physiological, pharmacological and pathological implications. *Mol. Aspects Med.* **34**, 323–336 (2013).

27. Quistgaard, E. M., Low, C., Guettou, F. & Nordlund, P. Understanding transport by the major facilitator superfamily (MFS): structures pave the way. *Nat. Rev. Mol. Cell Biol.* **17**, 123–132 (2016).
28. Iancu, C. V., Zmoon, J., Woo, S. B., Aleshin, A. & Choe, J.-Y. Crystal structure of a glucose/H⁺ symporter and its mechanism of action. *Proc. Natl Acad. Sci. USA* **110**, 17862–17867 (2013).
29. Deng, D. et al. Molecular basis of ligand recognition and transport by glucose transporters. *Nature* **526**, 391–396 (2015).
30. Sun, L. et al. Crystal structure of a bacterial homologue of glucose transporters GLUT1–4. *Nature* **490**, 361–366 (2012).
31. Pedersen, B. P. et al. Crystal structure of a eukaryotic phosphate transporter. *Nature* **496**, 533–536 (2013).
32. Zheng, H., Wisedchaisri, G. & Gonen, T. Crystal structure of a nitrate/nitrite exchanger. *Nature* **497**, 647–651 (2013).
33. Yan, H. et al. Structure and mechanism of a nitrate transporter. *Cell Rep.* **3**, 716–723 (2013).
34. Newstead, S. et al. Crystal structure of a prokaryotic homologue of the mammalian oligopeptide-proton symporters, PepT1 and PepT2. *EMBO J.* **30**, 417–426 (2011).
35. Menon, I. et al. Opsi is a phospholipid flippase. *Curr. Biol.* **21**, 149–153 (2011).
36. Brunner, J. D., Lim, N. K., Schenck, S., Duerst, A. & Dutzler, R. X-ray structure of a calcium-activated TMEM16 lipid scramblase. *Nature* **516**, 207–212 (2014).
37. Malvezzi, M. et al. Ca²⁺-dependent phospholipid scrambling by a reconstituted TMEM16 ion channel. *Nat. Commun.* **4**, 2367 (2013).
38. Hanson, B. L. & Bunick, G. J. Annealing macromolecular crystals. *Methods Mol. Biol.* **364**, 31–42 (2007).
39. Nagarathinam, K. et al. Outward open conformation of a major facilitator superfamily multidrug/H⁺ antiporter provides insights into switching mechanism. *Nat. Commun.* **9**, 4005 (2018).
40. Bibi, E. & Kaback, H. R. In vivo expression of the *lacY* gene in two segments leads to functional lac permease. *Proc. Natl Acad. Sci. USA* **87**, 4325–4329 (1990).
41. Varela, M. F., Sansom, C. E. & Griffith, J. K. Mutational analysis and molecular modelling of an amino acid sequence motif conserved in antiporters but not symporters in a transporter superfamily. *Mol. Membr. Biol.* **12**, 313–319 (1995).
42. Smirnova, I. N., Kasho, V. & Kaback, H. R. Protonation and sugar binding to LacY. *Proc. Natl Acad. Sci. USA* **105**, 8896–8901 (2008).
43. Feng, L., Campbell, E. B. & MacKinnon, R. Molecular mechanism of proton transport in CLC Cl⁻/H⁺ exchange transporters. *Proc. Natl Acad. Sci. USA* **109**, 11699–11704 (2012).
44. du Plessis, J. L., Stefaniak, A. B. & Wilhelm, K. P. Measurement of skin surface pH. *Curr. Probl. Dermatol.* **54**, 19–25 (2018).
45. Frank, D. N. et al. The human nasal microbiota and *Staphylococcus aureus* carriage. *PLoS ONE* **5**, e10598 (2010).
46. Harell, M., Mover-Lev, H., Levy, D. & Sade, J. Gas composition of the human nose and nasopharyngeal space. *Acta Otolaryngol.* **116**, 82–84 (1996).
47. Williams, M. R., Nakatsuji, T. & Gallo, R. L. *Staphylococcus aureus*: master manipulator of the skin. *Cell Host Microbe* **22**, 579–581 (2017).
48. Law, C. J., Maloney, P. C. & Wang, D. N. Ins and outs of major facilitator superfamily antiporters. *Annu. Rev. Microbiol.* **62**, 289–305 (2008).
49. Jardetzky, O. Simple allosteric model for membrane pumps. *Nature* **211**, 969–970 (1966).
50. Kuk, A. C., Mashalidis, E. H. & Lee, S.-Y. Crystal structure of the MOP flippase MurJ in an inward-facing conformation. *Nat. Struct. Mol. Biol.* **24**, 171–176 (2017).
51. Zheng, S. et al. Structure and mutagenic analysis of the lipid II flippase MurJ from *Escherichia coli*. *Proc. Natl Acad. Sci. USA* **115**, 6709–6714 (2018).
52. Sham, L. T. et al. Bacterial cell wall. MurJ is the flippase of lipid-linked precursors for peptidoglycan biogenesis. *Science* **345**, 220–222 (2014).
53. Timcenko, M. et al. Structure and autoregulation of a P4-ATPase lipid flippase. *Nature* **571**, 366–370 (2019).
54. Hiraizumi, M., Yamashita, K., Nishizawa, T. & Nureki, O. Cryo-EM structures capture the transport cycle of the P4-ATPase flippase. *Science* **365**, 1149–1155 (2019).
55. Perez, C. et al. Structure and mechanism of an active lipid-linked oligosaccharide flippase. *Nature* **524**, 433–438 (2015).
56. Mi, W. et al. Structural basis of MsbA-mediated lipopolysaccharide transport. *Nature* **549**, 233–237 (2017).
57. Bi, Y., Mann, E., Whitfield, C. & Zimmer, J. Architecture of a channel-forming O-antigen polysaccharide ABC transporter. *Nature* **553**, 361–365 (2018).
58. Kalienkova, V. et al. Stepwise activation mechanism of the scramblase nhTMEM16 revealed by cryo-EM. *Elife* **8**, e44364 (2019).
59. Rubino, F. A., Kumar, S., Ruiz, N., Walker, S. & Kahne, D. E. Membrane potential is required for MurJ function. *J. Am. Chem. Soc.* **140**, 4481–4484 (2018).
60. Mirza, O., Guan, L., Verner, G., Iwata, S. & Kaback, H. R. Structural evidence for induced fit and a mechanism for sugar/H⁺ symport in LacY. *EMBO J.* **25**, 1177–1183 (2006).

Publisher's note Springer Nature remains neutral with regard to jurisdictional claims in published maps and institutional affiliations.

© The Author(s), under exclusive licence to Springer Nature America, Inc. 2020

Methods

LtaA expression and purification. LtaA was overexpressed in *E. coli* BL21-Gold (DE3) (Stratagene) cells. Cells were transformed with a modified pET-19b vector (Novagen) carrying the gene encoding *S. aureus* LtaA with an N-terminal histidine 10 (His10) affinity tag. Cells were grown at 37 °C in Terrific Broth medium supplemented with 1% glucose (wt/vol) and induced with 0.2 mM IPTG. Cells were collected and resuspended in 50 mM Tris-HCl, pH 8.0; 500 mM NaCl; 5 mM β -mercaptoethanol; and 0.5 mM PMSF, disrupted and membranes were collected by ultracentrifugation. Membranes containing LtaA were solubilized in 50 mM Tris-HCl, pH 8.0; 200 mM NaCl; 20 mM Imidazole; 15% glycerol (vol/vol); 5 mM β -mercaptoethanol; 1% lauryl maltose neopentyl glycol (wt/vol) (LMNG, Anatrace); 1% N-dodecyl- β -D-maltopyranoside (wt/vol) (DDM, Anatrace) for 2 h at 4 °C. After centrifugation, the supernatant was loaded onto a Ni-NTA superflow affinity column (Qiagen), washed with 50 mM Tris-HCl, pH 8.0; 200 mM NaCl; 50 mM imidazole; 10% glycerol (vol/vol); 5 mM β -mercaptoethanol; 0.02% LMNG and 0.02% DDM and then washed a second time with the in the same buffer containing 200 mM Imidazole. Imidazole was removed by desalting using a PD-10 column (GE Healthcare). The His10 affinity tag was removed by overnight treatment with tobacco etch virus (TEV) protease. TEV protease was later removed by passing through Ni-NTA affinity column. LtaA was further purified by size exclusion chromatography (SEC) in buffer 10 mM Tris-HCl pH 8.0, 150 mM NaCl, 0.02% LMNG (Superdex 200 Increase 10/300 GL, GE Healthcare). The main peak was collected and the buffer exchanged to 10 mM Tris-HCl pH 8.0, 150 mM NaCl, 0.1% Cymal-7 (Anatrace) using a PD-10 desalting column⁶¹.

SeMet derivative production. *E. coli* BL21-Gold (DE3) (Stratagene) cells carrying the LtaA expression vector were grown in TB-glucose medium at 37 °C until an optical density at 600 nm (OD_{600}) of 0.5–1.0 was reached. These were then used to inoculate a preculture of M9 medium supplemented with vitamin B1 hydrochloride. Cells were then grown until OD_{600} was 0.5 and were used to inoculate 2 L of M9 medium supplemented with vitamin B1 hydrochloride. Cells were grown overnight at 37 °C until OD_{600} was ~0.9, followed by the addition of an amino acids/SeMet cocktail and incubation for 30 min. SeMet-LtaA expression was induced with 0.2 mM IPTG and 90 min incubation.

LtaA crystallization. LtaA was concentrated up to 6.0 mg per mL using a 30-kDa MWCO Vivaspine 20 concentrator (GE healthcare). After extensive optimization of crystallization conditions, LtaA crystals were obtained at 16 °C using sitting-drop vapor diffusion. Plate-shaped crystals were obtained in reservoir conditions containing 30–70 mM magnesium acetate, 80–120 mM glycine pH 9.5 and 30–34% PEG 300. Crystals appeared after 3–4 d and matured to full size within 1 week. Crystals were dehydrated and cryoprotected by gently increasing PEG 300 concentration in the drop followed by flash freezing by immersion in liquid nitrogen⁶¹.

In situ annealing and data collection. LtaA crystals diffracted X-rays up to about 6–7 Å resolution in general. Performing in situ annealing led to X-rays diffraction to higher resolution (3.8 Å to 3.3 Å, depending on the crystal)⁶¹. In situ annealing was performed by blocking the cold nitrogen stream with a thin film while the crystal was mounted on the goniometer. Annealing time, thickness of the film and distance of the cryo-stream to the crystal were critical parameters to optimize. The X-ray diffraction patterns displayed in Extended Data Fig. 2c show an example of diffraction before and after annealing. Enhancement in X-rays diffraction resolution was accompanied by a 10% to 18% reduction of the unit cell volume. The best datasets were collected from crystals exposed to X-rays only after annealing. An annealing time of about 10 s produced the best results. Three datasets collected from one LtaA crystal were merged and used to determine the structure. This LtaA crystal showed anisotropic diffraction up to 3.3 Å and belonged to the space group $C22_1$, with unit cell constants $a = 51.39$ Å, $b = 162.47$ Å and $c = 191.05$ Å, and $\alpha = 90^\circ$, $\beta = 90^\circ$ and $\gamma = 90^\circ$ (Table 1). Data were processed and merged with XDS⁶² and anisotropic scaling/ellipsoid truncation was performed. Resolution limits after ellipsoid truncation were $a^* = 3.0$ Å, $b^* = 4.0$ Å and $c^* = 3.5$ Å. We used a Karplus CC' (Pearson correlation coefficient)-based data-cutoff approach to determine the usable resolution of the datasets⁶³. The resolution limit was set taking into account a $CC_{1/2} > \sim 40\%$ based on data-merging statistics and a CC' analysis against unmerged intensities in Phenix package⁶⁴ satisfying Karplus CC' against CC_{work} and CC_{free} criteria, as well as R_{free} of the highest-resolution shell against the refined structure being less than or equal to ~50% (Table 1). A second criterion for limiting the resolution was the overall completeness percentage observed after anisotropic ellipsoid truncation, which was kept above 80%. Diffraction data were collected at the beamline X06SA at the Swiss Light Source (SLS, Villigen).

Structure determination. The structure of LtaA was solved by single-wavelength anomalous diffraction (SAD). SeMet positions were found using SHELX⁶⁵ and refined using CCP4i2 programs⁶⁶, CRANK2 (ref. ⁶⁷) and PHASER⁶⁸. Solvent flattening and density modification were performed using PARROT⁶⁹. The resulting phases and electron-density maps were used to build an initial model. The anomalous densities of 16 SeMet residues along the polypeptide chain aided

in tracing the correct amino acids register in the resulting model (Extended Data Fig. 4). Tracing of TM helices was facilitated by placing fractions of a LtaA homology model generated by Swissmodel⁷⁰ using as reference model the structure of the MFS transporter YajR⁷¹ (PDB: 3WDO). Model building was performed in Coot⁷². Subsequently, multiple rounds of molecular replacement combined with single-wavelength anomalous diffraction (MR-SAD) in CRANK2 (ref. ⁶⁷) contributed to further improvement of the initial phases and electron-density maps, facilitating the improvement of the model. Multiple rounds of refinement and model building were then performed using Phenix⁶⁴ and Coot⁷². Map sharpening was used to facilitate model building. X-ray data and refinement statistics are given in Table 1. The final refined structure has $R_{work} = 27.05\%$ and $R_{free} = 28.94\%$, with 93.35% of residues in the Ramachandran-favored region; 6.38% in Ramachandran allowed; and 0.27% as Ramachandran outliers. Molecular graphics were created in PyMOL⁷³. Surface electrostatics were calculated with the APBS PyMOL plugin.

YpFP expression and purification. YpFP with an N-terminal His10 affinity tag was overexpressed in *E. coli* BL21-Gold (DE3) (Stratagene) cells by IPTG induction. Cells were disrupted by sonication, and YpFP was purified using affinity chromatography. YpFP was desalted in buffer 50 mM Tris-HCl pH 8.0, 200 mM NaCl, 10% glycerol, concentrated to 2.4 mg per ml, flash frozen in liquid nitrogen and stored at –80 °C.

Synthesis of NBD-anchor-LLD. Synthesis of fluorescently labeled NBD-anchor-LLD was performed following a modification of the protocol described by Jorasch et al.²⁰ and Kiriukhin et al.²¹ and . Purified YpFP was incubated with 2 mM UDP-glucose (Sigma) and 2 mM 1-NBD-decanoyl-2-decanoyl-sn-glycerol (Cayman) at 30 °C for about 16 h. The reaction product was separated using thin-layer chromatography (TLC) in a solvent mixture consisting of chloroform:methanol:water (65:25:4, vol/vol/vol)¹⁹ (Supplementary Fig. 1). NBD-lipids were visualized in a fluorescence scanner (Amersham Typhoon Imaging System). The main product was extracted from the silica using a 50:50 mixture of chloroform:methanol, followed by evaporation of solvents. The extracted product was resuspended in buffer 50 mM Tris-HCl pH 8.0, 200 mM NaCl, 3% glycerol.

HPLC-MS product analysis. Samples of NBD-DAG (Cayman), completed reaction, and extracted product from preparative TLC (NBD-DAG-Glc₂) were subjected to HPLC-MS analysis using a ReproSil-Pur ODS-3 column (Dr. Maisch) and a flow rate of 1 mL per min with a solvent gradient elution of 0.1% acetic acid (Eluent A) against acetonitrile with 0.1% formic acid (Eluent B). The gradient consisted of 95% of eluent A to 95% of eluent B over a range of 22 min. The eluted species were analysed on a Bruker microTOF electrospray ionization mass spectrometer (Bruker Daltonics) in positive-ion mode with the following settings: capillary voltage, 4,500 V; nebulizer pressure, 2 bar; drying gas, 9 L per min at 220 °C; mass range, 50–2000 m/z .

MS/MS and PRM LC-MS analysis. Pure NBD-DAG (Cayman) and extracted NBD-DAG-Glc₂ (10 pmol per μ L in 30% acetonitrile/69.9% water/0.1% formic acid) were prepared and analyzed by high-resolution mass spectrometry on a Q-Exactive mass spectrometer equipped with a heated electrospray ionization (HESI-II) probe (both Thermo Fisher Scientific) with direct infusion. For both molecules, full and tandem mass spectra were acquired at a resolution of 140,000 FWHM (at 200 m/z). The three most intense fragment ions were manually selected for quantitative parallel-reaction monitoring (PRM) MS analysis⁷⁴. The setup of the μ RPLC-MS system was as described previously⁷⁵. The extracted ion chromatograms (XICs) were obtained using the most intense fragments selected before and employed for quantification (Supplementary Notes).

NMR product analysis. NBD-DAG and DGDG were dissolved in $CDCl_3$ at a concentration of 100 μ M and 75 μ M, respectively. NBD-anchor-LLD was extracted from TLC plates and dissolved in $CDCl_3$ for NMR analysis. The experiments were recorded at 298 K on a Bruker Ascend 600 MHz spectrometer running Topspin 3.2 equipped with a cryogenically cooled triple-resonance probe, using a 16 ppm spectral width, 30° flip angle, 1.5-s relaxation delay and 2.7-s acquisition time. All data were processed with Bruker TOPSPIN-NMR software (version 3.2, Bruker).

Formation of LtaA proteoliposomes. We reconstituted LtaA in unilamellar liposomes prepared by extrusion through polycarbonate filters (400-nm pore size) from a 3:1 (wt:wt) mixture of *E. coli* polar lipids and L- α -phosphatidylcholine (Avanti). Liposomes were diluted in buffer containing 20 mM Tris-HCl pH 8.0, 150 mM NaCl and 2 mM β -mercaptoethanol. After saturation with DDM (Anatrace), liposomes were mixed with purified protein at a 50:1 (wt/wt) lipid/protein ratio. Removal of detergent was performed by incubation with BioBeads (Biorad). Proteoliposomes containing a final concentration of 20 mg per mL lipids; 7.8 μ M LtaA were centrifuged, washed and resuspended before being used for NBD-anchor-LLD reconstitution or stored at –80 °C after being frozen in liquid nitrogen. Before flipping assays, proteoliposomes were thawed and β -mercaptoethanol was removed by freeze/thaw cycles and washing upon

ultracentrifugation. NBD-anchor-LLD was then incorporated into proteoliposomes performing freeze/thaw cycles and extrusion through a polycarbonate filter (400-nm pore size). LtaA/NBD-anchor-LLD proteoliposomes were then immediately used for flipping assays. Protein-free proteoliposomes were prepared in the same way, but without the addition of protein.

In vitro flipping assay. LtaA/NBD-anchor-LLD proteoliposomes, protein-free NBD-anchor-LLD liposomes and control transporter NBD-anchor-LLD proteoliposomes were diluted in buffer 20 mM Tris-HCl pH8.0, 150 mM NaCl before extrusion through polycarbonate filters (400-nm pore size). For sodium- and pH-gradient experiments, proteoliposomes were subjected to freeze/thaw cycles and resuspended in two steps: (1) in 200 μ L of the same 'internal buffer' before extrusion; and (2) dilution in 800 μ L of 'external buffer' before starting fluorescence recording. This was performed in order to minimize the effect of pH equilibration inside and outside proteoliposomes. Internal and external buffer compositions were 20 mM of either Tris pH 8.0, MES pH 6.5 or glycine pH 9.5, together with 150 mM NaCl or 150 mM KCl. Flipping of the NBD-anchor-LLD was measured by determining the percentage of NBD-fluorescence that is quenched by 5 mM sodium dithionite (Sigma) added after 200 s of starting fluorescence recording. At 100 s before data recording was finished, 0.5% Triton X100 was applied to permeabilize the liposomes, making all NBD-anchor-LLD molecules accessible to dithionite reduction. Fluorescence was recorded at 20 °C using a Jasco Fluorimeter. Excitation and emission wavelengths were 470 and 535 nm, respectively. For analysis, the fluorescence intensity was normalized to F/F_{\max} . Relative flipping activities were calculated as follows: relative activity = $100 \times ((F/F_{\max})_i - (F/F_{\max})_{\text{liposomes}}) / ((F/F_{\max})_{\text{wt}} - (F/F_{\max})_{\text{liposomes}})$, where i corresponds to each respective treatment/mutants, liposomes corresponds to liposomes without protein, wt corresponds to WT LtaA proteoliposomes and F/F_{\max} values correspond to the observed plateau for each recording. Curves were plotted using GraphPad Prism 5. Time courses of the dithionite-induced fluorescence decay in liposomes were repeated at least three times for each individual experiment.

Proton-transport assay. Purified LtaA WT or the variant LtaA-E32A were reconstituted into POPE:POPG (3:1) liposomes at a protein to lipid ratio of 1:50 (wt/wt). Synthetic anchor-LLD, produced from 1,2-dimyristoyl-sn-glycerol (Avanti) and 2 mM UDP-glucose, as described above, was incorporated into proteoliposomes after freeze/thaw cycles were performed. Proteoliposomes and protein-free liposomes were resuspended in 5 mM Tris-HCl/HEPES pH 7.3, 100 mM KCl and extruded through a polycarbonate filter (400-nm pore size). After a brief sonication, proteoliposomes were 20-fold diluted in buffer containing 5 mM Tris-HCl/HEPES pH 7.3, 10 mM KCl, 90 mM NaCl and 0.5 μ M 9-amino-6-chloro-2-methoxyacridine (ACMA). Fluorescence was measured at 20 °C using a Jasco Fluorimeter. Excitation and emission wavelengths were 410 nm and 480 nm, respectively. After the fluorescence signal was stable, H⁺ influx was initiated by establishing a membrane potential by the addition of the potassium ionophore valinomycin (5 nM). Time courses of the proton-transport assays were repeated at least three times for each individual experiment.

Mutagenesis. LtaA mutants were generated using Q5 Site-Directed Mutagenesis Kit (NEB). The sequence of the resulting constructs was confirmed by DNA sequencing (Microsynth).

Sequence-conservation analysis. The sequence conservation analysis shown in Extended Data Fig. 6 and Supplementary Fig. 9 were computed using the ConSurf server⁷⁶. Briefly, 76 LtaA homologues found in related *Staphylococcus* species or other Gram-positive bacteria were selected from a protein sequence BLAST search on the NCBI public database using *S. aureus* LtaA protein sequence as a query. We then generated a multiple-sequence alignment using the HHMER algorithm provided by ConSurf, with conservation scores plotted in PyMOL⁷³.

Docking of anchor-LLD. Docking of anchor-LLD (1,2-dihexadecanoic-3-O-(β -D-glucopyranosyl-1 \rightarrow 6-O- β -D-glucopyranosyl-sn-glycerol)) to the LtaA structure was done with Autodock Vina⁷⁷. Initial anchor-LLD coordinates were generated from two-dimensional geometry in Phenix (eLBOW)⁶⁴, and stereochemistry was corrected in Phenix (REEL)⁶⁵, with reference to the X-ray crystal structures of ligands PDB: 6GB and PDB: DDR. Docking was carried out over a search space of 60 \times 54 \times 36 Å covering the entire amphiphilic central cavity.

Construction of mutants in *Staphylococcus aureus* NCTC8325. Strains, plasmids and oligonucleotides used in this study are listed in Supplementary Table 7. A vector for efficient allelic replacement, pMAD⁷⁸, was used for knockout of ltaA in *Staphylococcus aureus* NCTC8325. Specifically, the upstream and downstream regions of the ltaA-coding region were amplified from genomic DNA by primer pairs OVL2253-OVL 2254 and OVL2255-OVL2256, respectively. A spectinomycin-resistance cassette was amplified with oligonucleotides OVL2257 and OVL2258 from plasmid pMAD-int2-luc-spc-gfp⁷⁹. Then the three fragments were assembled by gibson assembly to produce the fragment upstream-spectinomycin-downstream. The gibson assembly product was then used as template for amplification of the ltaA replacement fragment with

oligonucleotides OVL2259 and OVL2260 containing NcoI and BamHI sites. The ltaA replacement fragment and vector pMAD-int2-luc-spc-gfp were both ligated to produce the ltaA knockout plasmid pMAD- Δ ltaA construct, followed by transformation into *E. coli* strain IM08B⁸⁰. The previously described gene-deletion method for the temperature-sensitive vector pMAD⁷⁸ was used for the construction of the ltaA deletion strain in NCTC8325 with pMAD- Δ ltaA. The final Δ ltaA genotype of the mutant was confirmed by both PCR and Sanger sequencing.

***S. aureus* phenotypic assay.** Bacteria cells were grown in 3 mL of LB medium at 37 °C, with 200 rpm shaking to OD₆₀₀ = 0.3. For the complementary strains with pLOW vector, a final concentration of 5 μ g/ml of erythromycin was added to the medium. The bacterial culture was then serially diluted. 10 μ L of the original and its serial dilutions were spotted onto C+Y (casitone + yeast extract) agar plates at different pH, without or complemented with 0.1 mM IPTG. In the absence of IPTG, the pLOW vector provides a mild protein expression level⁷⁹, as indicated by growth restoration of the Δ ltaA mutant by ltaA-WT and single point mutants in absence of IPTG, whereas in the presence of IPTG it provides protein overexpression⁷⁹. The plates were incubated at 37 °C with or without 5% CO₂ overnight. The images of the plates were captured by BioRad Gel Doc XR + imaging system.

***S. aureus* complementation assays.** The pLOW vector was used for the construction of ltaA complementary strains. The ltaA fragment was amplified from genomic DNA with oligonucleotides OVL2243 and OVL2244 containing SalI and NotI digestion sites (Supplementary Table 7). The amplified ltaA fragment was cloned into the vector pLOW-dCas9 (ref. ⁷⁹) to produce pLOW-ltaA. This was then transformed into *E. coli* IM08B. Point mutations were introduced by PCR mutagenesis (Supplementary Table 7). Later ltaA variants were cloned into pLOW with the same method described above. The pLOW vector carrying ltaA or variants were then introduced into NCTC8325 Δ ltaA strain by electroporation transformation with erythromycin selection (5 μ g per mL) on LBA plates as described above (Supplementary Notes).

***S. aureus* fluorescent microscopy.** LB medium pre-warmed at 37 °C in the presence of 5% CO₂ overnight (causing acidification to about pH 6.5) or LB medium with low pH (adjusted by dissolving LB medium powder in PBS pH 6.5) were used to grow cells for fluorescence microscopy experiments. Fluorescence microscopy was performed using a Leica DMi8 microscope with a \times 100 phase contrast objective (NA 1.40) with a SOLA Light Engine (Lumencor) light source. A chroma cube nr (Quad = Chroma 89000, mCT_LP = 49017) was used. For Nile red staining, light was filtered through external excitation filter 545/25 nm (Chroma ET545/x25), and the external filter ET605/70 nm was used for emission. An exposure time of 800 ms with 100% of light from SOLA Light Engine was used for capturing images. The images were obtained with LasX software (Leica) and processed with ImageJ (<https://imagej.nih.gov>) (Supplementary Notes).

***S. aureus* transmission electronic microscopy.** The same bacterial cells for fluorescent microscopy were used for transmission electronic microscopy. Ultrathin sections (50 nm) of cells fixed in agarose were cut on a Leica Ultracut (Leica Mikrosysteme) and picked up on a copper slot grid (2 \times 1 mm) coated with a polystyrene film. Sections were poststained with 4% uranyl acetate. Micrographs were collected with a transmission electron microscope Philips CM100 (Thermo Fisher Scientific) at an acceleration voltage of 80 kV with a TVIPS TemCam-F416 digital camera (TVIPS). The final images were processed with ImageJ (<https://imagej.nih.gov>) (see Supplementary Notes).

Immunoblotting detection of LTA in *Staphylococcus aureus* NCTC8325 at different pH. LB media with differing pH were prepared by dissolving LB powder (Difco LB medium, BD) in PBS followed by pH adjustment, and then sterilized by filtering with 0.2- μ m membranes. The sample preparation and western blotting of LTA were performed based on the previous studies of Gründling et al.^{19,22}. Briefly, *S. aureus* cells were cultured in LB at 37°, collected and resuspended in 500 μ L of TBS buffer (20 mM Tris-Cl, pH 7.4, 150 mM NaCl). Bacteria were lysed by bead beater in 4 runs of 30 s per cycle with 6 m s⁻¹. The cell lysate was separated on 12% SDS-PAGE, followed by western blot analysis. LTA was detected with LTA (poly glycerolphosphate)-specific primary antibody (clone 55, HyCult Biotechnology) and antimouse IgG (H + L) HRP antibody (Promega) as the secondary antibody. The blots were developed with SuperSignal west pico plus chemiluminescent substrate (Thermo Fisher Scientific), and the images were obtained with a Fusion FX7 imaging system (Witec). The relative amount of LTA was determined from the band intensities of western blots ($n = 4$) using ImageJ (<https://imagej.nih.gov>).

Preparation of *S. aureus* membranes for LC-MS analysis. *S. aureus* cells were grown in 4 mL of LB medium at 37 °C and 200 r.p.m. shaking to OD₆₀₀ = 0.4. For the complementary strains with pLOW vector, a final concentration of 5 μ g mL⁻¹ of erythromycin and 0.1 mM IPTG were added to the medium. Cells were collected by centrifugation and resuspended in 10 mM Tris-HCl pH 8.0, 1 mM EDTA with lysostaphin, followed by a 0.5 h incubation at 37 °C. Cells were then further subjected to sonication. Membranes were isolated and resuspended in 100 mM Tris-HCl pH 8.5, 5% SDS and 10 mM tris(2-carboxyethyl) phosphine (TECP).

Samples were incubated at 37 °C for 1 h after the addition of chloroacetamide to reduce and alkylate disulfides. Samples were then loaded on an S-Trap Micro Spin column (Protefi). On-column peptide digestion was performed by adding trypsin and incubated at 47 °C for 1 h. Digested peptides were collected by passing 50 mM triethylammonium bicarbonate (TEAB) buffer, 0.2 % formic acid (wt/vol) in distilled water, and 0.2 % formic acid (wt/vol) in 50% acetonitrile (vol/vol) through the column and dried in a SpeedVac (Labconco). Dried peptides were re-suspended in 0.1% formic acid (wt/vol) with iRT normalization peptide mix (Biognosys) and stored at –20 °C.

Targeted PRM LC–MS analysis of LtaA and variants in *S. aureus* membranes.

In the first step, PRM assays⁷⁴ for all possible peptides of LtaA being 6 to 25 amino acids long comprising double- and triple-charged precursor ions were generated. In total, five peptides were found to match the length criteria, leading to a total of ten PRM assays. These were applied to identify LtaA in membrane fractions of wild-type *S. aureus*. The setup of the μ RPLC–MS system was as described previously⁷⁵. Mass spectrometry analysis was performed on a Q-Exactive mass spectrometer equipped with a nano-electrospray ion source (both Thermo Fisher Scientific). Each MS1 scan was followed by high-collision-dissociation (HCD) of the 10 LtaA precursor ions in PRM mode using a global isolation mass list. Using strict identification criteria, three peptide ions of LtaA, LTNYNTRPVK (2⁺ and 3⁺ ion) and MQDSSLNYYANHK (2⁺) could be confidently identified, and were used for label-free PRM quantification. To control for variation in sample amounts, the total ion chromatogram (only comprising peptide ions with two or more charges) of each sample was determined by label-free quantification using Progenesis Q1 (version 2.0, Waters) and used for normalization. The integrated peak areas of the three peptide ions quantified by PRM were summed and employed for LtaA quantification (Supplementary Notes).

Reporting Summary. Further information on research design is available in the Nature Research Reporting Summary linked to this article.

Data availability

Atomic coordinates have been deposited in the Protein Data Bank under accession code PDB 6S7V. Source data for Figs. 1c, 3b,c,e,f, 4a–c and Extended Fig. 1 are available with the paper online.

References

- Zhang, B. & Perez, C. Stabilization and crystallization of a membrane protein involved in lipid transport. *Methods Mol. Biol.* **2127**, 283–292 (2020).
- Kabsch, W. Xds. *Acta Crystallogr. D Biol. Crystallogr.* **66**, 125–132 (2010).
- Karplus, P. A. & Diederichs, K. Linking crystallographic model and data quality. *Science* **336**, 1030–1033 (2012).
- Adams, P. D. et al. PHENIX: a comprehensive Python-based system for macromolecular structure solution. *Acta Crystallogr. D Biol. Crystallogr.* **66**, 213–221 (2010).
- Sheldrick, G. M. A short history of SHELX. *Acta Crystallogr. A Found. Adv.* **64**, 112–122 (2008).
- Collaborative Computational Project, Number 4. The CCP4 suite: programs for protein crystallography. *Acta Crystallogr. D Biol. Crystallogr.* **50**, 760–763 (1994).
- Skubak, P. et al. A new MR-SAD algorithm for the automatic building of protein models from low-resolution X-ray data and a poor starting model. *IUCr* **5**, 166–171 (2018).
- McCoy, A. J. et al. Phaser crystallographic software. *J. Appl. Crystallogr.* **40**, 658–674 (2007).
- Cowtan, K. Recent developments in classical density modification. *Acta Crystallogr. D Biol. Crystallogr.* **66**, 470–478 (2010).
- Waterhouse, A. et al. SWISS-MODEL: homology modelling of protein structures and complexes. *Nucleic Acids Res.* **46**, W296–W303 (2018).
- Jiang, D. et al. Structure of the YajR transporter suggests a transport mechanism based on the conserved motif A. *Proc. Natl Acad. Sci. USA* **110**, 14664–14669 (2013).
- Emley, P., Lohkamp, B., Scott, W. G. & Cowtan, K. Features and development of Coot. *Acta Crystallogr. D Biol. Crystallogr.* **66**, 486–501 (2010).
- Fratamico, P. M. et al. *Escherichia coli* serogroup O2 and O28ac O-antigen gene cluster sequences and detection of pathogenic *E. coli* O2 and O28ac by PCR. *Can. J. Microbiol.* **56**, 308–316 (2010).
- Peterson, A. C., Russell, J. D., Bailey, D. J., Westphall, M. S. & Coon, J. J. Parallel reaction monitoring for high resolution and high mass accuracy quantitative, targeted proteomics. *Mol. Cell Proteomics* **11**, 1475–1488 (2012).
- Ahrne, E. et al. Evaluation and improvement of quantification accuracy in isobaric mass tag-based protein quantification experiments. *J. Proteome Res.* **15**, 2537–2547 (2016).
- Ashkenazy, H. et al. ConSurf 2016: an improved methodology to estimate and visualize evolutionary conservation in macromolecules. *Nucleic Acids Res.* **44**, W344–W350 (2016).
- Trott, O. & Olson, A. J. AutoDock Vina: improving the speed and accuracy of docking with a new scoring function, efficient optimization, and multithreading. *J. Comput. Chem.* **31**, 455–461 (2010).
- Arnaud, M., Chastanet, A. & Debarbouille, M. New vector for efficient allelic replacement in naturally nontransformable, low-GC-content, Gram-positive bacteria. *Appl Environ. Microbiol.* **70**, 6887–6891 (2004).
- Stamsas, G. A. et al. CozEa and CozEb play overlapping and essential roles in controlling cell division in *Staphylococcus aureus*. *Mol. Microbiol.* **109**, 615–632 (2018).
- Monk, I. R., Tree, J. J., Howden, B. P., Stinear, T. P. & Foster, T. J. Complete bypass of restriction systems for major *Staphylococcus aureus* lineages. *MBio* **6**, e00308–e00315 (2015).

Acknowledgements

We thank the staff at the PX beamline of the Swiss Light Source, Switzerland. We thank G. Cebrero and N. Bärländ for providing a control transporter sample. We thank J. Daraspe and M. Rengifo for contributing to TEM images acquisition. We thank U. Lanner, A. Schmidt and T. Müntener for contributing to HPLC–MS and PRM MS studies. This work was supported by the Swiss National Science Foundation (SNSF) (PP00P3_170607 to C.P. and 31003A_172861 to J.W.V.). Further funding came from a JPIAMR grant (40AR40_185533 to J.W.V.) and ERC consolidator grant 771534-PneumoCaTChER (to J.W.V.). E.L. was funded by the Biozentrum International PhD Program.

Author contributions

B.Z. performed purification and crystallization of LtaA. C.P. assisted B.Z. during data collection, structure determination and docking analysis. B.Z., E.L. and C.P. established and performed in vitro flipping assays. C.P., B.Z. and E.L. analyzed the structural and in vitro functional data. E.L. performed reaction products characterization. X.L. and E.L. performed experiments in live cells. X.L., E.L., C.P. and J.W.-V. analyzed in vivo data. G.M. and S.H. performed NMR analysis. C.P. conceived the project and wrote the manuscript with input from all authors.

Competing interests

The authors declare no competing interests.

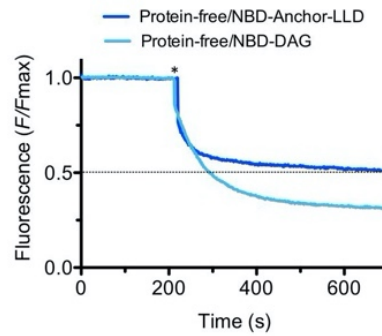
Additional information

Supplementary information is available for this paper at <https://doi.org/10.1038/s41594-020-0425-5>.

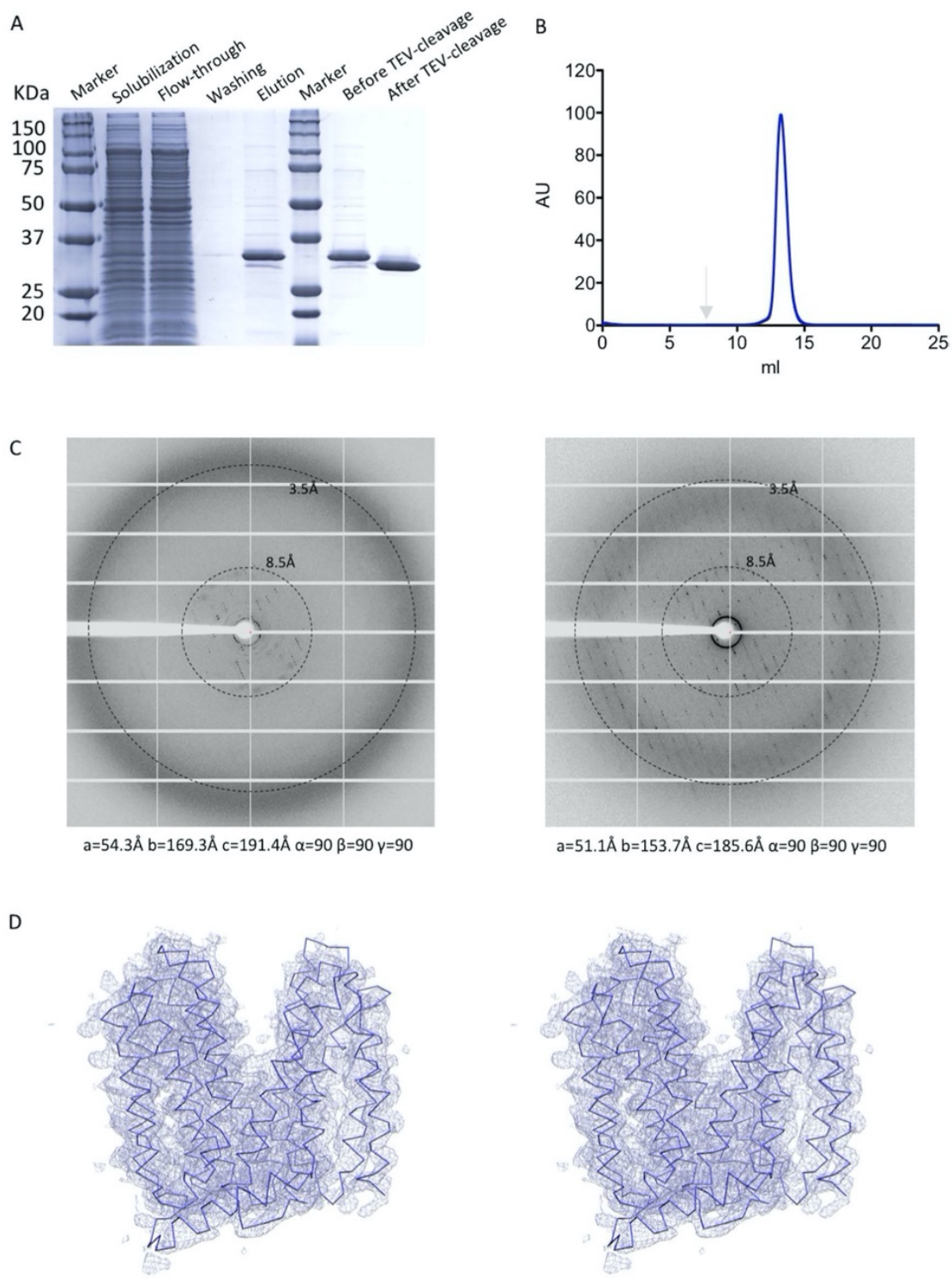
Correspondence and requests for materials should be addressed to C.P.

Peer review information Katarzyna Marcinkiewicz was the primary editor on this article and managed its editorial process and peer review in collaboration with the rest of the editorial team.

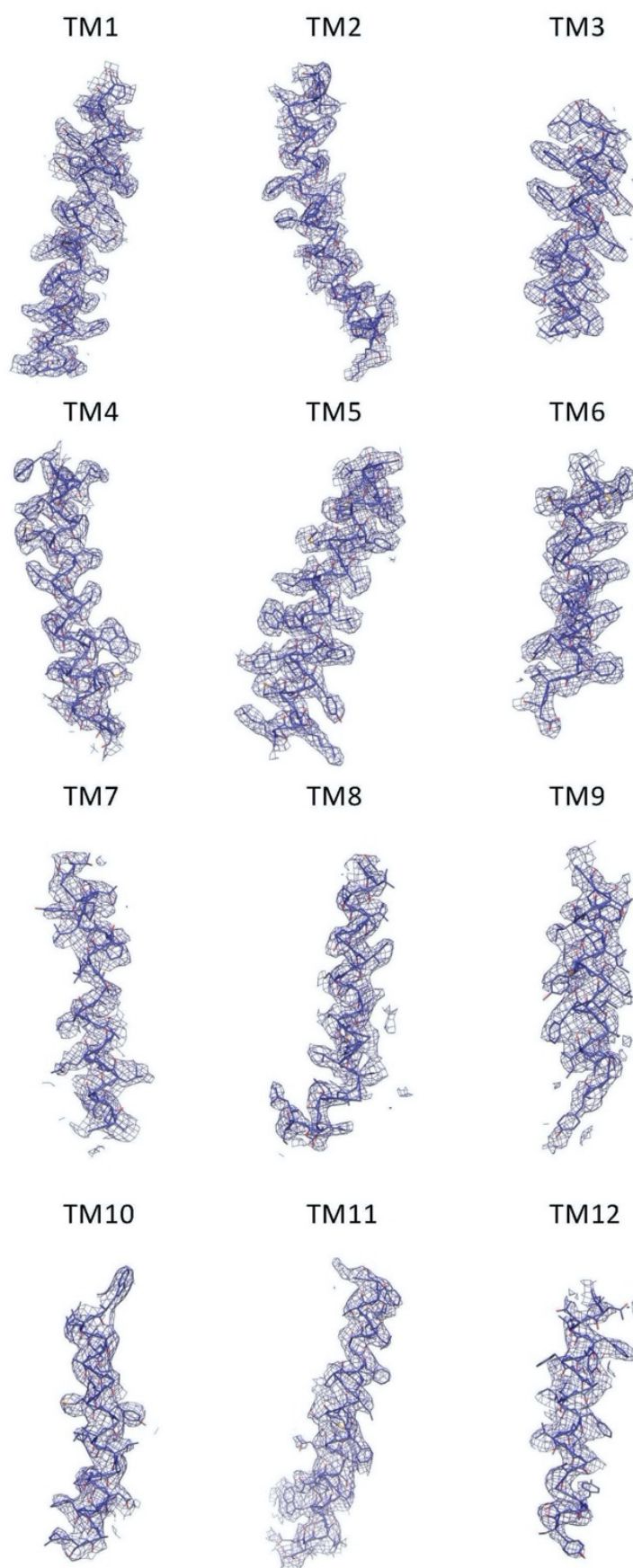
Reprints and permissions information is available at www.nature.com/reprints.



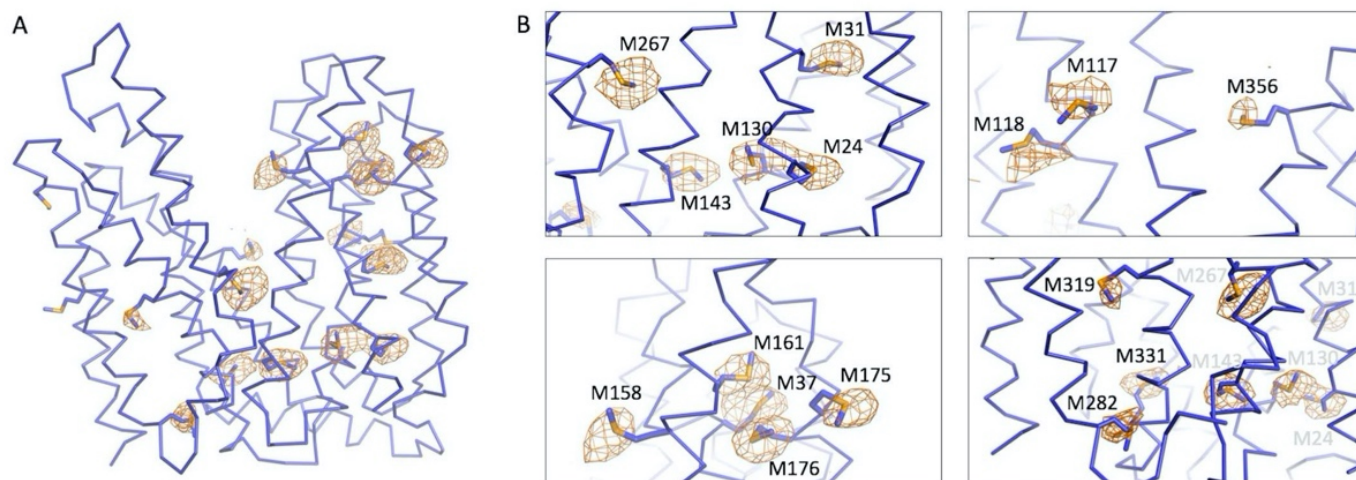
Extended Data Fig. 1 | Fluorescence quenching analysis of protein-free liposomes. Representative traces of quenching of liposomes containing NBD-anchor-LLD or NBD-DAG ($n \geq 3$). Asterisk marks addition of dithionite. Source data are available with the paper online. F correspond to the fluorescence intensity measured for each time point. F_{\max} is the average fluorescence measured during the first 200 seconds.



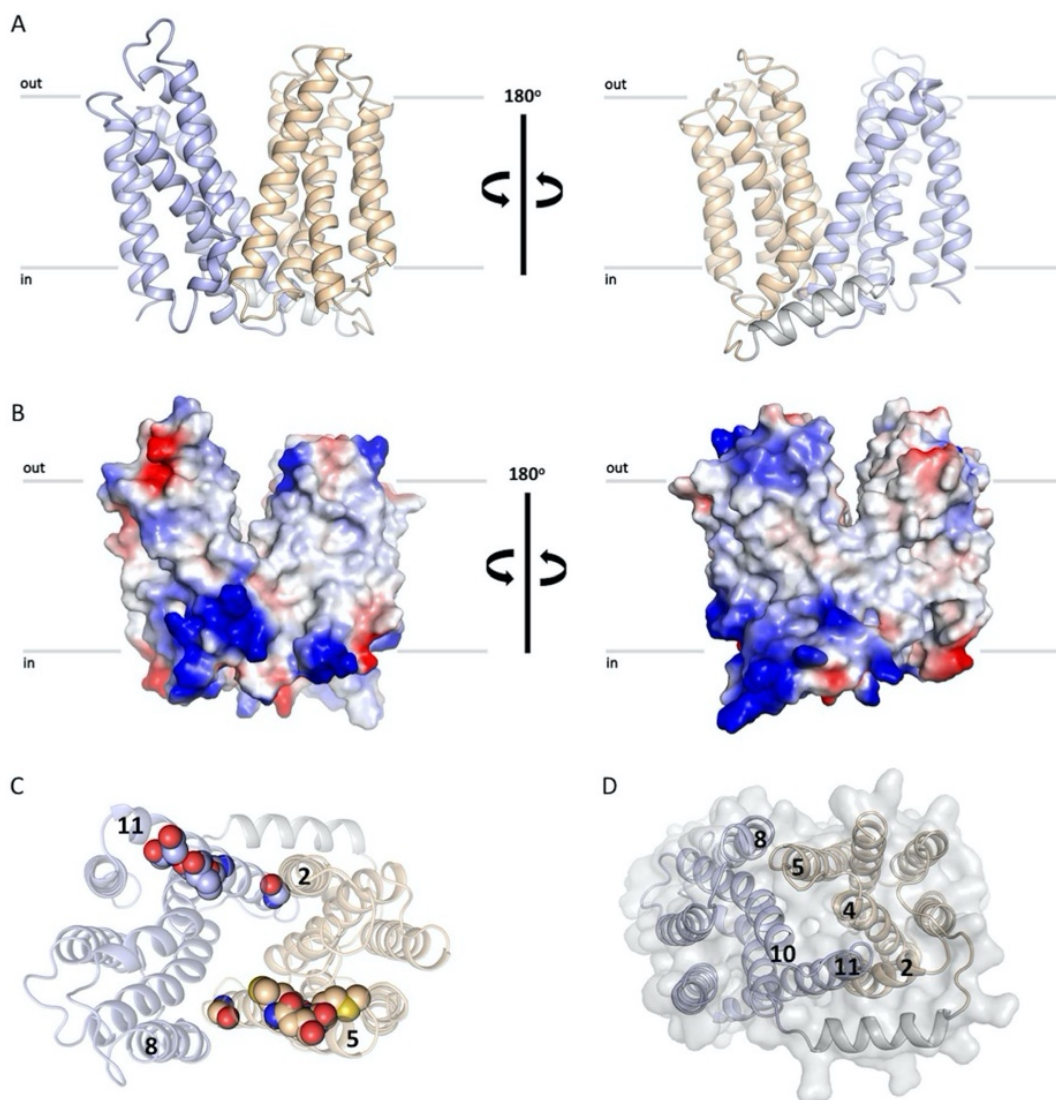
Extended Data Fig. 2 | *S. aureus* LtaA crystallization. **a**, SDS-PAGE of samples from different steps of a LtaA purification experiment. Purified protein after cleavage of the His₁₀-tag was used for crystallization. **b**, Size exclusion chromatography profile of purified LtaA (Superdex 200 10/300 Increase). Gray arrow indicates column void. **c**, Representative X-ray diffraction images of a LtaA crystal before *in situ* annealing (*left*) and after *in situ* annealing (*right*). The difference in unit cell dimensions before and after *in situ* annealing demonstrate shrinking of the unit cell. **d**, Stereo view (wall-eyed) of the $2F_o-F_c$ electron density map of the 3.3 Å structure of LtaA at 1.0σ level.



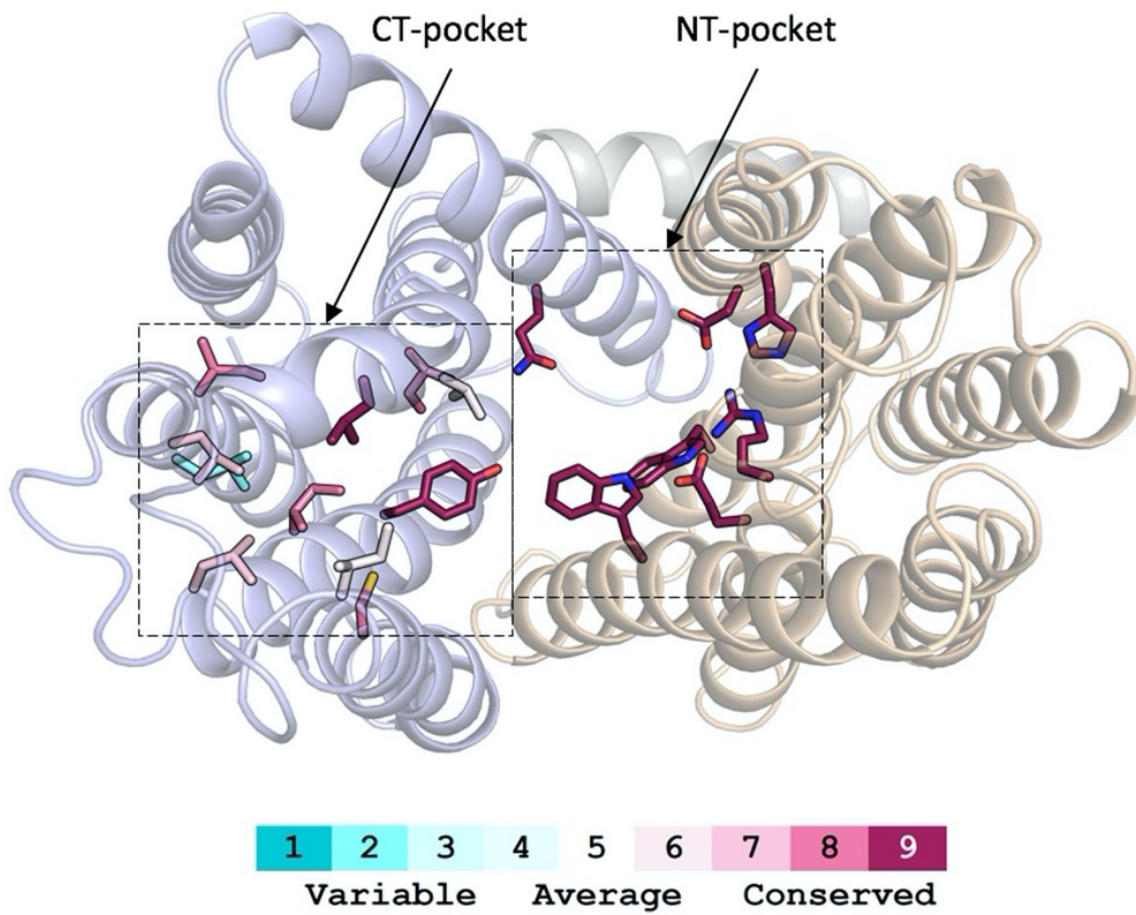
Extended Data Fig. 3 | 2Fo-Fc electron density map. Individual transmembrane segments of the 3.3Å structure of LtaA at 1.0 σ level are shown.



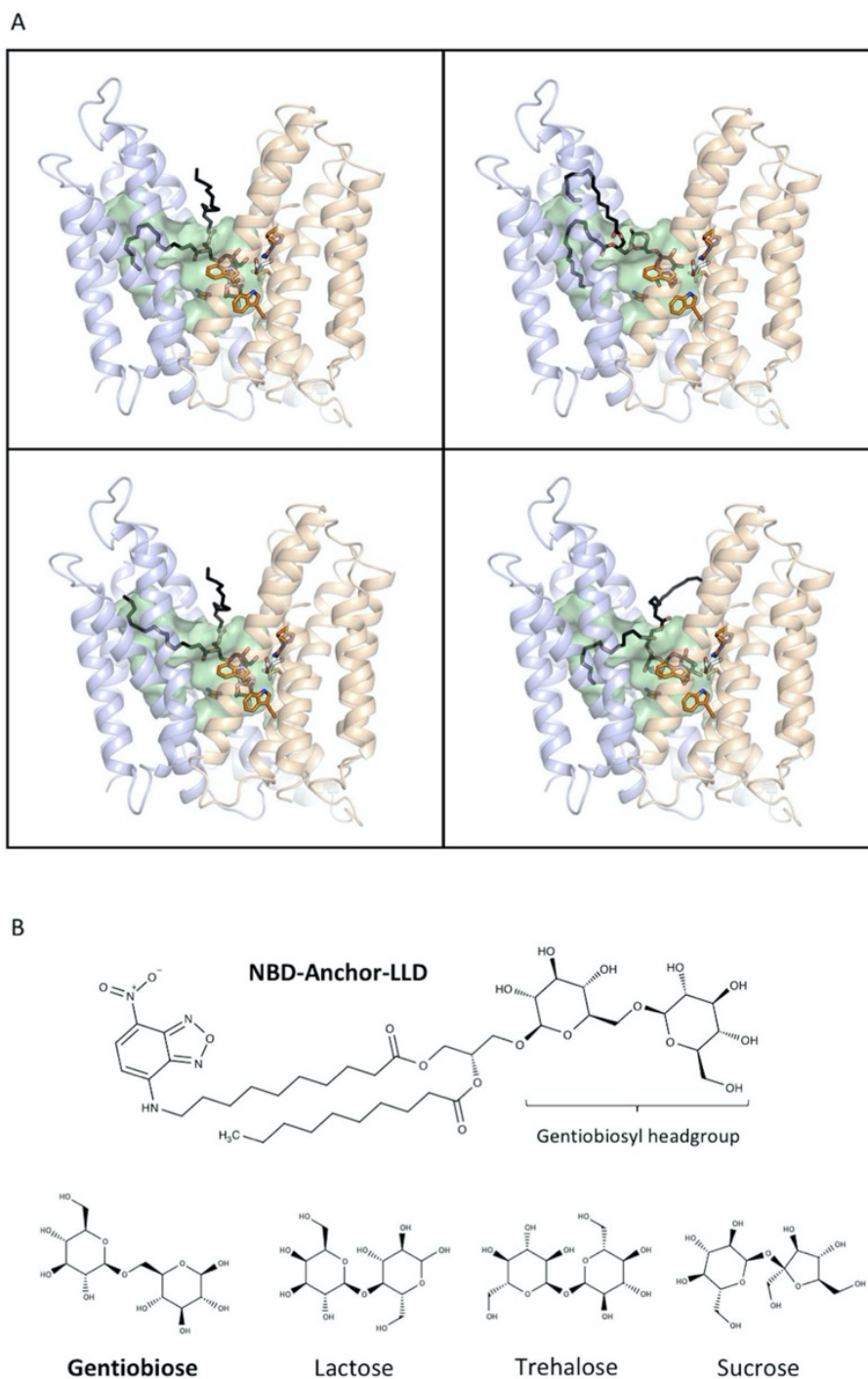
Extended Data Fig. 4 | Validation of side-chain register of LtaA model. a and b, Anomalous electron density map define selenomethionine (SeMet) sites. Contour levels is 4.0σ . Anomalous density was observed for 16 out of 19 SeMet residues in LtaA.



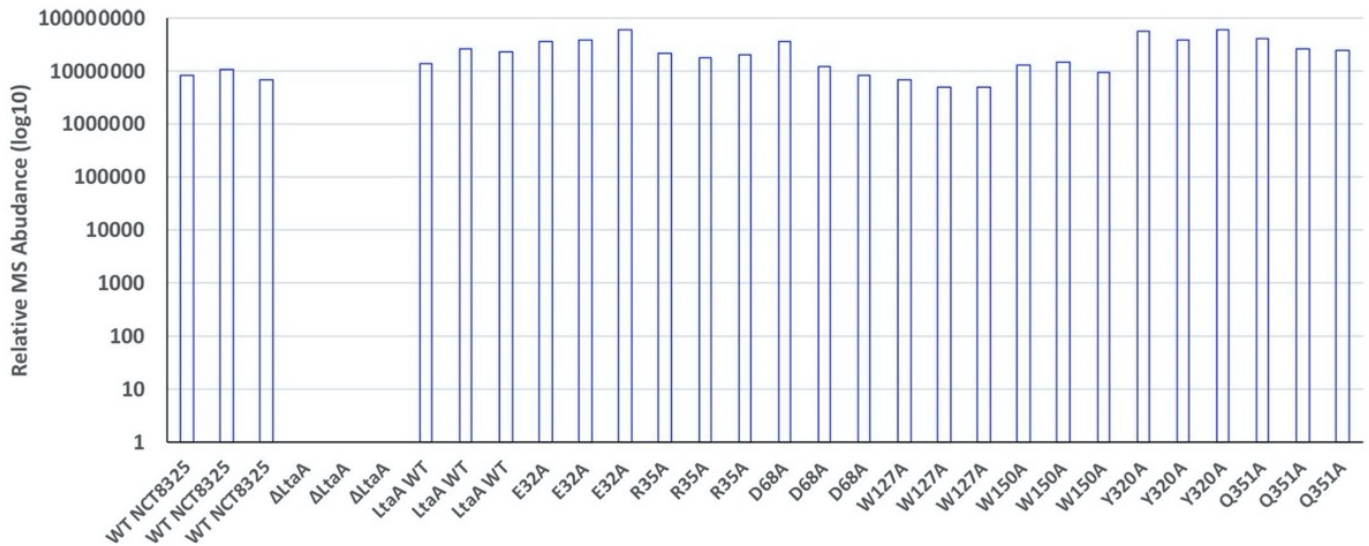
Extended Data Fig. 5 | LtaA structure analysis. **a**, Overall structure of LtaA. The N-terminal domain is shown in light-orange, C-terminal domain is shown in light-blue, the cytoplasmic helical loop connecting the N-terminal and C-terminal domains is shown in gray. **b**, Vacuum electrostatic surface representation of LtaA showing side views of the protein. **c**, Top view of LtaA showing residues participating in the motif-G sequence ($G^{345}(X)_8G(X)_3GP(X)_2GG^{363}$) in TM11 and motif-G-like sequence in TM5. **d**, Cytoplasmic view of LtaA showing TMs and loops blocking the access to the central cavity.



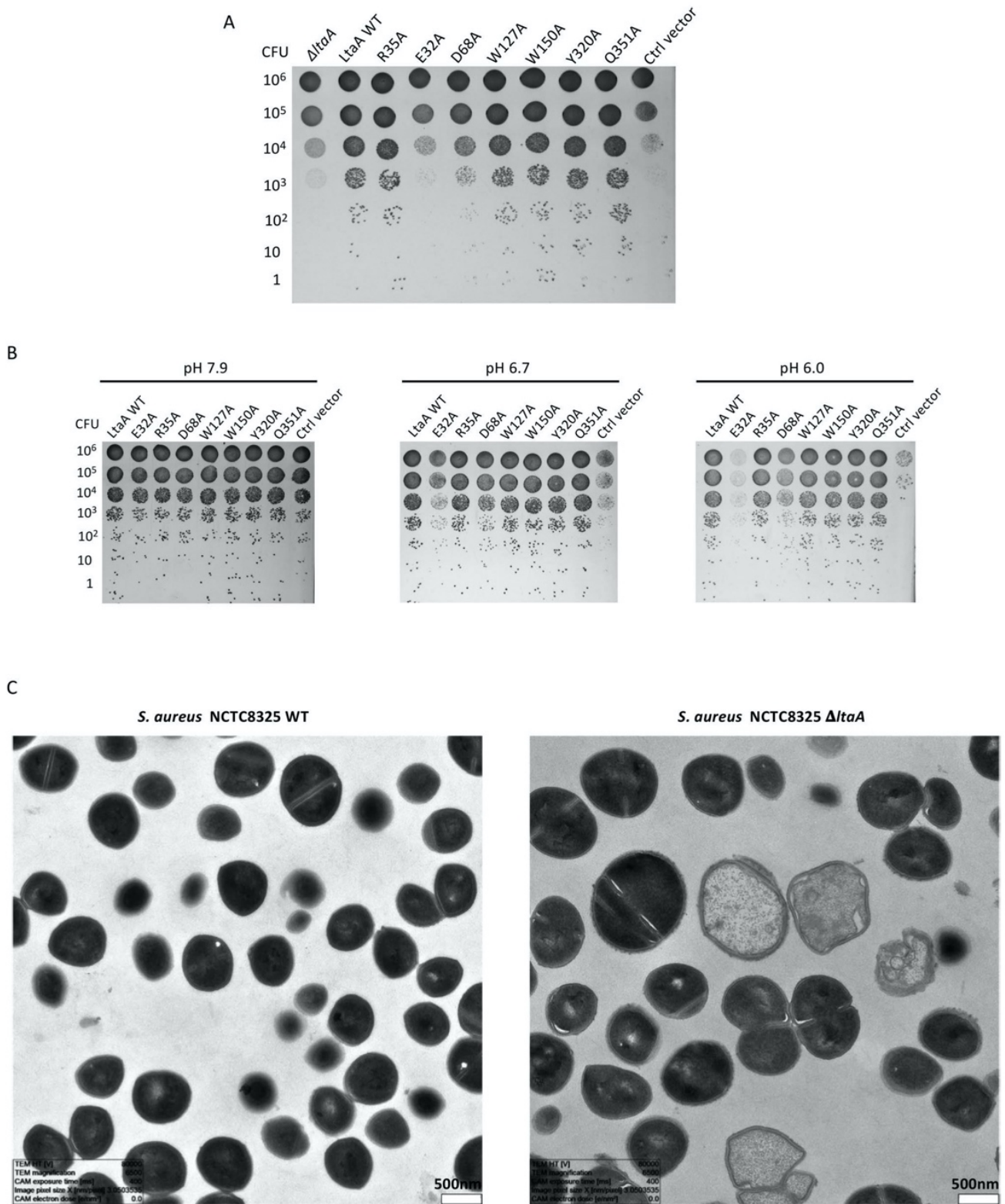
Extended Data Fig. 6 | Sequence conservation analysis. A multiple sequence alignment of 76 LtaA homologues found in related *Staphylococcus* species or other Gram-positive bacteria was generated. Top view of LtaA, residues in N-terminal and C-terminal cavity are colored by sequence conservation (ConSurf server).



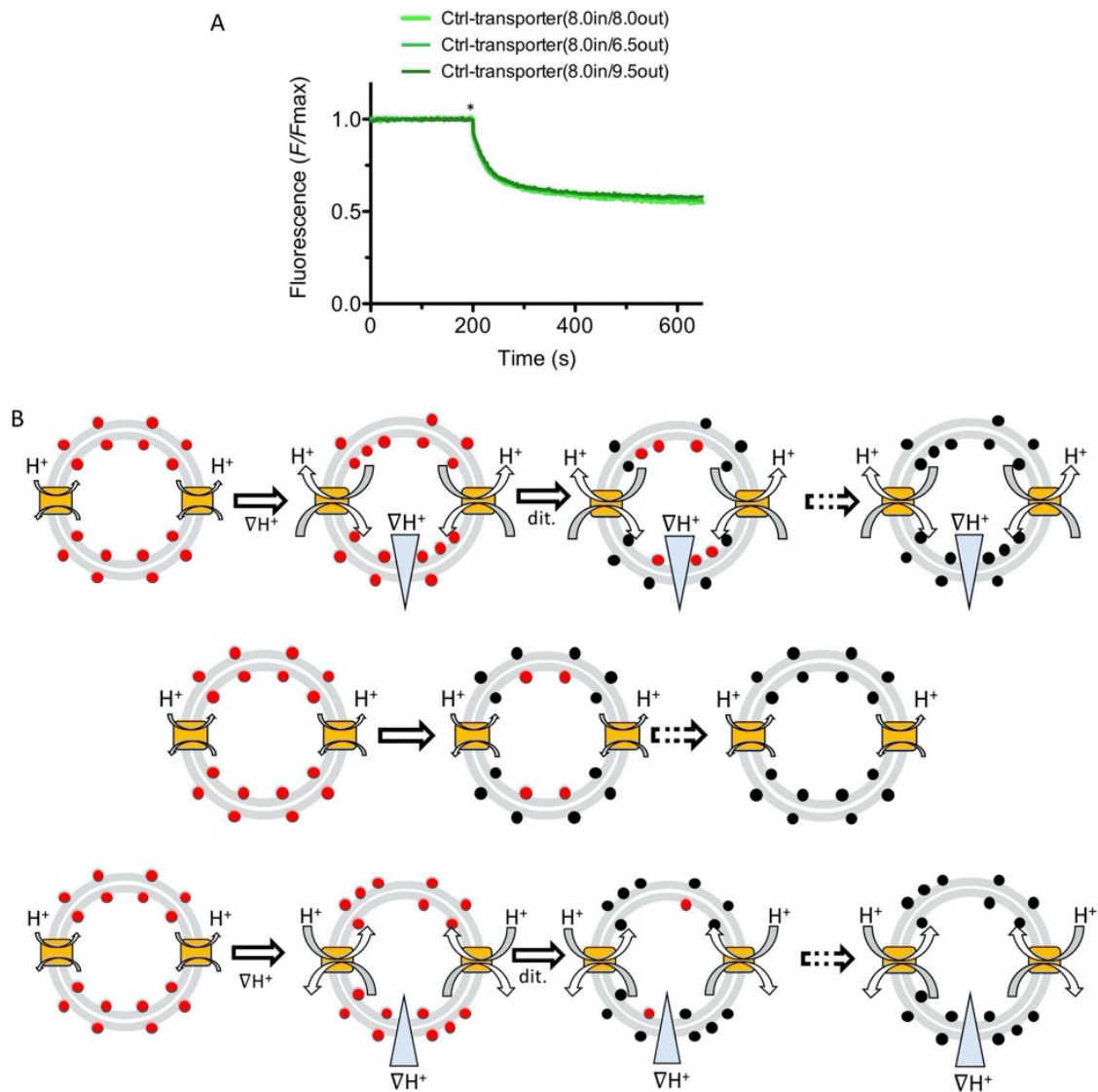
Extended Data Fig. 7 | Docking analysis and structures of compounds used in this study. a, Models of lipid-linked-disaccharide docked into the amphiphilic cavity of LtaA. Lipid-linked-disaccharide is shown in black and red sticks. Green surface shows the amphiphilic central cavity of LtaA. **b**, Structures of disaccharides and Anchor-LLD (β -D-Glc-(1 \rightarrow 6)- β -D-Glc-(1 \rightarrow 3)-diacylglycerol).



Extended Data Fig. 8 | Liquid chromatography mass spectrometry (LC-MS) analysis of relative abundance of LtaA and variants in *S. aureus* membranes. Chromatographic separation of peptides was carried out using an EASY nano-LC 1000 system. Mass spectrometry analysis was performed on a Q-Exactive mass spectrometer equipped with a nanoelectrospray ion source. Three peptide ions of LtaA, LTNYNTRPVK (2+ and 3+ ion) and MQDSSLNYYANHK (2+) could be confidently identified and were used for label-free parallel reaction monitoring (PRM) quantification. The integrated peak areas of the 3 peptide ions quantified by PRM were summed and employed for LtaA quantification. The histogram shows relative abundances of LtaA and variants from independent experiments (n = 3).



Extended Data Fig. 9 | Phenotypes of *S. aureus* WT, Δ *ltaA*, and *LtaA* mutants. a, Over-expression of *LtaA* mutants. *S. aureus* strain NCTC8325 growth on C+Y agar plates in the presence of 0.1 mM IPTG incubated at 37 °C and 5% CO₂. **b**, Over-expression of *LtaA* mutants. *S. aureus* strain NCTC8325 growth on C+Y agar plates in the presence of 0.1 mM IPTG incubated at 37 °C under different pH conditions. *LtaA* WT represents Δ *ltaA* mutant complemented with wild type *ltaA* on pLOW vector; Ctrl vector indicates Δ *ltaA* mutant complemented with pLOW carrying a functionally unrelated gene as vehicle control; the other labels represent Δ *ltaA* mutant complemented with *ltaA* with corresponding point mutations. **c**, Transmission electron microscopy (TEM) images at low magnification showing the morphology of *S. aureus* NCTC8325 WT and Δ *ltaA* mutant.



Extended Data Fig. 10 | LtaA-catalyzed lipid-linked-disaccharide flipping and proton gradients. **a**, Representative traces of flipping assays with a control transporter (bacterial choline transporter) in the presence of different proton gradients, *in* and *out* denote pH of buffer inside and outside of liposomes, respectively ($n \geq 3$). Asterisk marks addition of dithionite. F correspond to the fluorescence intensity measured for each time point. F_{max} is the average fluorescence measured during the first 200 seconds. **b**, Scheme of LtaA-catalyzed lipid-linked-disaccharide flipping under an outward proton gradient (*top*), no gradient (*center*), and an inward proton gradient (*bottom*). Under application of a pH gradient (∇H^+), LtaA (yellow boxes) translocates NBD-anchor-LLD (red spheres) contrary to the proton gradient. Addition of dithionite (dit.) then reduces exposed and exchanged NBD-anchor-LLD (black spheres). The extent of quenching is in accordance to the direction of the pH gradient. Full fluorescence quenching will be achieved after prolonged incubation (dashed arrows).

3. Evidence for a ‘trap-and-flip’ mechanism in a proton-dependent lipid transporter

Elisabeth Lambert^{1†}, Ahmad Reza Mehdipour^{2†}, Alexander Schmidt³, Gerhard Hummer^{4,5}, Camilo Perez^{1*}

¹Biozentrum, University of Basel, Basel, Switzerland

²Center for Molecular Modeling, Ghent University, Zwijnaarde, Belgium

³Proteomics Core Facility, Biozentrum, University of Basel, Basel, Switzerland

⁴Institute of Biophysics, Goethe University Frankfurt, Frankfurt am Main, Germany

⁵Department of Theoretical Biophysics, Max Planck Institute of Biophysics, Frankfurt am Main, Germany

Abbreviated title: Trap-and-flip mechanism in a proton-dependent flippase

*Correspondence should be addressed to C.P. (email: camilo.perez@unibas.ch)

† These authors contributed equally to this work

Reference:

Elisabeth Lambert*, Ahmad Reza Mehdipour*, Alexander Schmidt, Gerhard Hummer, Camilo Perez. “Evidence for a ‘trap-and-flip’ mechanism in a proton-dependent lipid transporter.” Nat. Comm. *in press*. doi: <https://doi.org/10.1101/2021.08.05.453402>

Author Contributions:

- I performed all *in vitro* and *in vivo* biochemical characterization of LtaA and variants
- I performed mass spectrometry analysis together with Alexander Schmidt
- I analyzed computational, structural and functional data
- I contributed to writing and revision of the manuscript

Manuscript

Transport of lipids across membranes is fundamental for diverse biological pathways in cells. Multiple ion-coupled transporters take part in lipid translocation, but their mechanisms remain largely unknown. Major facilitator superfamily (MFS) lipid transporters play central roles in cell wall synthesis, brain development and function, lipids recycling, and cell signaling. Recent structures of MFS lipid transporters revealed overlapping architectural features pointing towards a common mechanism. Here we used cysteine disulfide trapping, molecular dynamics simulations, mutagenesis analysis, and transport assays *in vitro* and *in vivo*, to investigate the mechanism of LtaA, a proton-dependent MFS lipid transporter essential for lipoteichoic acid synthesis in the pathogen *Staphylococcus aureus*. We reveal that LtaA displays asymmetric lateral openings with distinct functional relevance and that cycling through outward- and inward-facing conformations is essential for transport activity. We demonstrate that while the entire amphipathic central cavity of LtaA contributes to lipid binding, its hydrophilic pocket dictates substrate specificity. We propose LtaA catalyzes lipid translocation by a ‘trap-and-flip’ mechanism that might be shared among MFS lipid transporters.

Major facilitator superfamily (MFS) transporters are found in all kingdoms of life and move a large variety of molecules across biological membranes¹⁻⁸. Structural characterization of MFS transporters that participate in the uptake of water-soluble molecules and extrusion of drugs has contributed to a broad understanding of their transport mechanism^{4,8-17}. However, multiple reports have attributed alternative functions to MFS transporters, such as translocation of lipids associated with fundamental biological pathways. Some examples include the bacterial lysophospholipid transporter LpIT, involved in lipids recycling in Gram-negative bacteria^{7,18}; the human transporter MFSD2A, expressed at the blood-brain- and blood-retinal-barrier, contributing to major uptake of docosahexaenoic acid (DHA)^{5,6,19-22}; the human transporters Spns2^{23,24}, and MFSD2B²⁵, which contribute to transport of sphingosine 1-phosphate (S1P) in endothelial cells and erythrocytes; and the gentiobiosyl-diacylglycerol transporter LtaA, involved in cell wall synthesis in *Staphylococcus aureus*^{26,27}. However, despite their well described cellular roles, the mechanisms of MFS lipid transporters remain insufficiently understood.

We have previously shown that LtaA is a proton-dependent MFS lipid antiporter²⁷. It contributes to the adaptation of *S. aureus* to acidic conditions, common in the skin and nasopharynx of the human host²⁷⁻²⁹. LtaA takes part in the assembly of lipoteichoic acid, a phosphate-rich polymer important for control of bacterial cell division, protection from environmental stress, host cell adhesion, antibiotic resistance, biofilm formation, and immune evasion³⁰⁻³³. *S. aureus* lipoteichoic acid displays a polymer of 1,3-glycerol-phosphate repeat units attached to C-6 of the non-reducing glucosyl of the glycolipid gentiobiosyl-diacylglycerol³²⁻³⁴. This glycolipid is synthesized at the cytoplasmic leaflet of the membrane by the glycosyltransferase YpfP and is translocated to the outer leaflet by the activity of LtaA^{26,27}. The essential role of LtaA in adjusting the pool of glycolipids available at the extracellular side of the membrane, makes this protein a central player for lipoteichoic acid assembly and a potential target for drugs aiming to counteract antimicrobial resistant *S. aureus* strains e.g., methicillin-resistance *S. aureus* (MRSA) and vancomycin-resistant *S. aureus* (VRSA)³¹.

Two different general models of transporter-catalyzed lipid translocation have been proposed in the past³⁵⁻⁴³. A ‘trap-and-flip’ model, in which the lipid substrate is retrieved from one leaflet of the membrane, enclosed into a central cavity, and then delivered to the other leaflet^{41,44,45}, and a ‘credit-card’ model that departs from the classical alternating-access model and involves translocation of the lipid head-group across a hydrophilic cleft or cavity in the transport protein, while aliphatic chains remain embedded in the membrane^{37-39,42,43,46,47}. However, it is not known which of these two models describe better the mechanism of MFS lipid transporters. Answering this question is not only important to understand the basis of the processes catalyzed by these proteins but could also provide a foundation for the design of drugs and/or lipid-linked-bioactive molecules targeting cells or organs expressing pharmacologically relevant proteins from this superfamily.

Until now, a high-resolution structure of outward-facing LtaA, and inward- and outward-facing structures of MFSD2A have been elucidated^{21,22,27}. Both transporters display the canonical MFS fold of 12 transmembrane (TM) helices and an amphipathic central cavity that has not been observed in any MFS transporter of water-soluble molecules. The similar architectural features observed in the structures of LtaA and MFSD2A indicate common elements in their transport mechanisms and likely among all MFS lipid transporters. Here, we used cysteine disulfide trapping of outward- and inward-facing LtaA, in combination with molecular dynamics simulations, mutagenesis analysis, and transport assays *in vitro* and *in*

vivo, and showed that cycling through outward- and inward-facing conformations is essential for LtaA activity. We demonstrate that LtaA displays membrane exposed lateral openings with distinct functional relevance and characterized the architecture and biochemical properties of the amphipathic central cavity during alternating-access. Our results indicate that while the hydrophilic pocket of the amphipathic central cavity dictates substrate specificity, the hydrophobic pocket is only relevant for aliphatic chains’ binding. We describe critical mechanistic elements revealing that LtaA adopts a ‘trap-and-flip’ mechanism that might be shared among MFS lipid transporters.

Results

Models of inward-facing LtaA and validation by cysteine cross-linking

To investigate whether LtaA uses a ‘trap-and-flip’ or a ‘credit-card’ mechanism, we first aimed to establish a system that allowed us to perform cysteine disulfide trapping of end-point conformations of LtaA during its transport cycle. The architecture of the previously solved structure of LtaA ²⁷, facilitates cysteine disulfide trapping of outward-facing states, whereas there is no structural information to guide trapping of inward-facing states. Thus, we first generated an inward-facing model of LtaA using ‘repeat-swap’ modeling ⁴⁸. Like other transporters from the MFS superfamily, the topology of LtaA comprises two domains, a N-terminal domain (TM1-TM6; domain-1), and a C-terminal domain (TM7-TM12; domain-2), each of which contains two structural repeats with inverted-topology related by a pseudo-rotational two-fold symmetry axis parallel to the plane of the membrane (Fig. 1A,B). After swapping the conformations of the inverted repeats observed in the outward-facing structure of LtaA (PDB ID 6S7V) ^{27,48}, we constructed a large set of models *in silico* that were refined aiming to improve side chains packing, stereochemistry, and modeling scores. The models with the best scores converged to one conformation (Fig. 1C and Suppl. Table. 1), which displayed multiple interactions between the extracellular parts of TM1-TM7, TM2-TM11, and TM5-TM8, sealing the entrance to the central cavity (Fig. 1C). In contrast, the cytoplasmic regions of helices TM2-TM11, TM5-TM8, and TM4-TM10, lining the entrance to the central cavity from the cytoplasm, are away from each other about 16.0 ± 0.1 Å, 16.0 ± 0.1 Å, and 17.6 ± 0.2 Å, respectively (Fig. 1C). The helical loop between TM6 and TM7 that connects the N- and C-terminal domains was modeled based on the conformation observed in the outward-facing structure.

An additional inward-facing LtaA model was generated by AlphaFold (AF) (Fig. 1D)⁴⁹. In agreement with the models generated by the ‘repeat-swap’ method, in the AF model, the entrance to the central cavity is sealed by multiple interactions between the extracellular parts of TM1-TM7, TM2-TM11, and TM5-TM8 (Fig. 1D), whereas the cytoplasmic regions of helices TM2-TM11, TM5-TM8, and TM4-TM10, lining the cytoplasmic cavity, are away from each other about 25.0 Å, 25.9 Å, and 23.2 Å, respectively (Fig. 1D). Comparison of the AF model and the ‘repeat-swap’ models reveals a wider opening of the cytoplasmic cavity in the model generated by AF (Fig. 1C,D and 3A).

To validate these inward-facing models, we selected pairs of residues among the extracellular regions for which C β -C β distances were less or close to 8.0 Å, but which present C β -C β distances of over 12 Å in the outward-facing structure (Suppl. Fig. 1). We excluded those residues that were predicted to be buried or located in flexible regions. Based on these criteria, we identified the pairs F45-T253, A53-T366, and K166-I250 (Fig. 2A and Suppl. Fig. 1), occupying three different positions that provide good coverage of the conformational change predicted by the models. We then introduced cysteine residues at these positions on a starting construct in which the one native cysteine in LtaA was replaced with serine. The cysteine-less LtaA variant effectively performed glycolipid flipping in proteoliposomes (Suppl. Fig. 2A-C). The three mutants F45C-T253C, A53C-T366C, and K166C-I250C were then irreversibly crosslinked with N,N’-(*o*-phenylene)-dimaleimide (*o*-PDM), which has a spacer arm length of 6 Å. Crosslinked and non-crosslinked LtaA mutants were digested with either trypsin or chymotrypsin, and analyzed by high-resolution liquid chromatography–mass spectrometry (LC–MS) to evaluate the presence of non-crosslinked cysteine containing peptides. The peptides abundance was normalized against an internal reference peptide. We successfully identified non-crosslinked peptides in untreated samples of the three mutants: F45C-T253C, A53C-T366C, and K166C-I250C (Fig. 2A and Suppl. Fig. 3). The abundance of these peptides was clearly diminished in the crosslinked protein samples (Fig. 2A), demonstrating that the selected pairs of residues are in proximity as predicted in the inward-facing models.

As a control, we performed a similar experiment but with pairs of residues that were shown to interact at the cytoplasmic region of the outward-facing structure (Fig. 2B). Thus, we introduced cysteine residues at the positions K80-E339 and K141-N276, present at the cytoplasmic ends of TM2-TM11 and TM5-TM8, respectively. C β -C β distances between these

residues are smaller than 8 Å in the outward-facing structure, but larger than 12 Å in the inward-facing models (Suppl. Fig. 1). LC-MS analysis of the double mutants K80C-E339C and K141C-N276C confirmed the proximity of these residues as non-crosslinked peptides are more abundant in untreated samples, whereas in the presence of the cross-linking agent their abundances decrease substantially (Fig. 2B). In summary, our cross-linking analysis support the predicted conformations and interactions reported by the inward-facing models of LtaA and indicate the position of residues to guide cysteine disulfide trapping of LtaA conformations.

Alternating conformations in proteoliposome membranes

We investigated the conformations displayed by LtaA in membranes by evaluating the cross-linking of double cysteine mutants reconstituted in proteoliposomes (Fig. 2C). The cysteine pairs reported on the conformation of the TM helices that line the lateral openings, TM2-TM11 and TM5-TM8 (Fig. 1C,D). We screened for successful cross-links by using a gel-shift assay in which we first incubated with the o-PDM cross-linker, followed by treating the proteoliposomes with 5-kDa PEG-maleimide (mPEG5k)⁵⁰. This treatment generates a substantial shift in the protein mobility in polyacrylamide gel electrophoresis as mPEG5k irreversibly binds free cysteines. However, if the introduced cysteines are cross-linked by o-PDM, then they will not react with mPEG5k and no shift in gel mobility would be observed. A band indicating LtaA dimer was frequently observed in gels for all variants, including the cysteine-less LtaA (Fig. 2C and Suppl. Fig. 4C). However, since LtaA was shown to be monomeric after purification and reconstitution in nanodiscs (Suppl. Fig. 2D), we consider the dimer band to be an in-gel artifact.

We evaluated the cross-linking of residues A53C-T366C (TM2-TM11) and K166C-I250C (TM5-TM8), positioned at the extracellular region, and K80C-E339C (TM2-TM11) and K141C-N276C (TM5-TM8), located at the cytoplasmic region (Fig. 2C and Suppl. Fig. 4A-C). Before cross-linking, each double-cysteine mutant showed a gel shift after incubation with mPEG5K, thus demonstrating PEGylation of free cysteines (Fig. 2C and Suppl. Fig. 4C). In contrast, after treatment with o-PDM, all the double cysteine mutants were protected from PEGylation, thus showing that all mutants were successfully cross-linked. The cysteine-less control LtaA, did not show a gel shift in any of the conditions (Fig. 2C and Suppl. Fig. 4C), demonstrating that the shifts observed for the mutants were due to PEGylation of cysteines. These results

support that when embedded in the membrane of proteoliposomes, LtaA can adopt conformations where residues at the lateral openings lined by TM2-TM11 and TM5-TM8 display similar distances to those reported by the outward-facing structure and the inward-facing models.

Dynamics of LtaA alternating conformations in membranes

For lipid transporters that adopt a ‘trap-and-flip’ mechanism, substrate binding and release involve movement of lipids through lateral openings of the translocation channel^{18,21,22,41,44,45}. We studied the dynamic behavior of the lateral openings in different conformational states of LtaA when the protein is embedded in a lipid bilayer. To do this, we performed molecular dynamics (MD) simulations of outward- and inward-facing LtaA in a membrane composed of POPG (65%), diacylglycerol (20 %), cardiolipin (10 %), and gentiobiosyl-diacylglycerol (5 %), resembling the membrane of *S. aureus*⁵¹. During the simulations, outward- and inward-facing states were found to be stable as judged by RMSD and RMSF plots (Suppl. Fig. 5A-E). The simulations revealed that all the optimized inward-facing models and the AF model exhibit a cavity which is open to the cytoplasm and closed to the extracellular space, whereas the cavity of the outward-facing state is open to the extracellular space and closed to the cytoplasm (Fig. 3A,B). During the simulations, the AF inward-facing model displayed wide lateral openings, making the central translocation pathway accessible to the surrounding membrane and solvent (Fig. 3A,B). In contrast, the central translocation pathway in the ‘repeat-swap’ inward-facing models was less accessible due to their narrower lateral openings (Fig. 3A,B).

In agreement with the observed wider opening of the extracellular lateral openings, the simulations of outward-facing LtaA showed the intrusion of glycolipid and POPG molecules into the putative translocation pathway (Fig. 3B,C and Movie 1). The glycolipid was seen to intrude from the TM5-TM8 opening, with one of the aliphatic tails reaching to the C-terminal hydrophobic pocket, whereas two POPG molecules intrude from the TM2-TM11 opening (Fig. 3C and Movie 1). In a similar manner, the wide intracellular lateral openings of the AF inward-facing model showed the intrusion of a glycolipid into the putative translocation pathway from the side of the TM5-TM8 opening (Fig. 3D and Movie 2), with the aliphatic tails reaching to the C-terminal hydrophobic pocket. No glycolipid was observed intruding from the TM2-TM11 opening, mainly because of the obstruction by the horizontal

helix (Fig. 3D and Movie 2). Taking together, these results support that binding and release of the glycolipid by LtaA, involves movement of the substrate through lateral openings, which grant direct access to the surrounding bilayer.

Alternating access to the central cavity is essential for function

The cross-linking results described above showed that LtaA could cycle through outward- and inward-facing conformations. In addition, MD simulations suggest that lateral openings allow the passage of lipids to and out of the central cavity. However, the functional relevance of the lateral openings and cycling through alternating conformations is unknown. Understanding this is important because some flippases and scramblases use a 'credit card' mode of transport, where exposing a side cleft or a cavity to one side of the membrane is sufficient for catalysis of lipid transport across the membrane^{37-39,42,52}. Thus, we performed copper chloride catalyzed cross-linking of residues located at the lateral openings lined by TM2-TM11 and TM5-TM8 and then determined proton-coupled glycolipid transport activity of cross-linked LtaA variants in proteoliposomes (Fig. 4A-D and Suppl. Fig. 4D). In this assay, the addition of the K⁺-selective ionophore valinomycin generates a membrane potential of about -60 mV, which drives proton influx. Acidification of the lumen of proteoliposomes quenches the fluorophore 9-amino-6-chloro-2-methoxyacridine (ACMA) causing a decrease in the fluorescence²⁷. The double-cysteine mutants A53C-T366C (TM2-TM11) and K166C-I250C (TM5-TM8) close the extracellular side openings, whereas the mutants K80C-E339C (TM2-TM11) and K141C-N276C (TM5-TM8) close the cytoplasmic openings (Fig. 4A,B and Suppl. Fig. 4A,B). Our results show that individual cross-linking of the lateral openings decreases LtaA activity relative to non-cross-linked samples (Fig. 4A,B). The activity of cross-linked samples of the intracellular side opening lined by TM2-TM11 and that of both extracellular openings was observed to decrease prominently, whereas cross-linking of the lateral opening lined by TM5-TM8 reduces LtaA activity to about two-thirds of its level (Fig. 4A,B).

In addition, we aimed to completely close the cytoplasmic or extracellular cavities and test the effect on LtaA activity (Fig. 4C). To do this, we constructed the mutant A53C-T366C-K166C-I250C that after cross-linking would close the extracellular pathway, while the mutant K80C-E339C-K141C-N276C would close the cytoplasmic pathway (Fig. 4C and Suppl. Fig. 4A,B). Our results show that, in contrast to non-cross-linked proteins, both mutants display

background quenching levels, similar to that observed for protein-free liposomes, thus, indicating strong inhibition of transport activity (Fig. 4C). We confirmed cross-linking of each double- and tetra-cysteine mutant reconstituted in proteoliposomes by gel shift assays after incubation with mPEG5K (Fig. 4D and Suppl. Fig. 4D), which showed that after treatment with copper chloride, all the mutants were protected from PEGylation, whereas before cross-linking a gel shift was observed. This confirmed that all mutants were successfully cross-linked in the proteoliposomes samples used in the assay.

Taking together, these results reveal that alternating opening to both sides of the membrane is a requirement for LtaA function. However, not all lateral openings seem to have the same functional relevance. In particular, our results demonstrate that while both extracellular lateral openings are similarly important for function, the cytoplasmic lateral opening lined by TM2 and TM11 has a more significant role, as revealed by the low activity of the cross-linked variant K80C-E339C. By contrast, cross-linking of the cytoplasmic lateral opening lined by TM5 and TM8, K141C-N276C, affect LtaA function less strongly.

The hydrophobic pocket is relevant for lipid transport

Inspection of the central cavity shows that similar to what was observed in the outward-facing crystal structure of LtaA²⁷, the central cavity of the inward-facing models is amphipathic (Fig. 5A). The cavity displays a hydrophilic pocket, enclosed mainly by residues from the N-terminal domain (E32, R35, D68, W127 and W150), which we have previously shown to be relevant for recognition of the glycolipid headgroup and proton transport²⁷, and a hydrophobic pocket, enclosed mainly by residues from the C-terminal domain (V234, L237, C263, L296, L300, L309, I316, and Y320) (Fig. 5A). The recent structure of the MFSD2A transporter, trapped in an inward-facing conformation, displays a similar amphipathic central cavity (Suppl. Fig. 6)^{21,22}. MD simulations and computational docking of a glycolipid molecule to inward-facing LtaA suggests that the gentiobiosyl headgroup is preferentially accommodated in the hydrophilic pocket, whereas the diacylglycerol aliphatic tails are docked into the hydrophobic pocket (Fig. 3D and 5B).

A striking feature of the central cavity observed in LtaA and MFSD2A^{21,22,27}, and to our knowledge, not observed in other MFS structures available to date, is the presence of the highly hydrophobic pocket at the C-terminal domains of these transporters (Fig. 5A and Suppl. Fig. 6). To test the importance of this pocket in LtaA, we have designed mutants that introduce

polar residues, thus making it more hydrophilic. We then evaluated growth of *S. aureus* NCTC8325 $\Delta ltaA$ cells complemented with ectopic copies of the *ltaA* gene carrying these mutations (Fig. 5C and Suppl. Fig 7). The variants V234T/L237N/I297S, C263S/L309Q/I316N, and Y320R display marked growth defects, whereas the mutant L296D/I316N do not affect growth. Each mutant was also purified and reconstituted into proteoliposomes, followed by determination of their flipping activity (Fig. 5D). In agreement with the results from *S. aureus* growth assays, the mutants V234T/L237N/I297S, C263S/L309Q/I316N, and Y320R display low relative activity compared to LtaA-WT (Fig. 5D), whereas L296D/I316N display the highest activity among all mutants. In contrast, introducing a mutation that scarcely increases the polarity of the cavity but that changes the size of residues V234 and I316, displayed low relative flipping activity compared to LtaA-WT, but does not affect growth of *S. aureus* NCTC8325 $\Delta ltaA$ cells, likely due to the remaining activity of this mutant to suffice for lipoteichoic acid synthesis under *in vivo* conditions (Fig. 5C,D and Suppl. Fig 7). Taken together, these results support a fundamental role of the hydrophobic pocket in glycolipid transport. As suggested by MD simulations and docking analysis, it is likely that this pocket is involved in binding of the aliphatic tails of the glycolipid substrate. The striking hydrophobicity of the C-terminal TM helices 7, 8, and 10 in multiple MFS lipid transporters (Suppl. Fig. 8), and the involvement in coordination of the aliphatic chain of lysophospholipid as revealed by the structure of MFSD2A^{21,22}, suggest a shared mechanistic role of the hydrophobic pocket in lipid-tails binding in MFS lipid transporters.

The hydrophilic pocket dictates substrate specificity

So far, our results suggest that during transport, LtaA encloses the full glycolipid substrate in the amphipathic cavity. However, understanding the relevance of the individual parts of the substrate molecule, headgroup and aliphatic chains, is fundamental for future design of pharmacologically relevant molecules targeting this and other MFS lipid transporters. To gain insight into whether LtaA displays higher selectivity towards the headgroup than for the diacylglycerol moiety, we performed flipping assays with LtaA-WT co-reconstituted in proteoliposomes together with NBD-labeled Glc₂-DAG (gentiobiosyl-diacylglycerol) and increasing concentrations of Gal₂-DAG (digalactosyl-diacylglycerol) (Fig. 5E). Glucose and galactose differ only in the orientation of the -OH group at the C-4 position. Thus, we hypothesized that if the headgroup is more relevant for substrate recognition than

the aliphatic chains, then transport of Glc₂-DAG-NBD will not be affected, since the difference between glucose and galactose would prevent Gal₂-DAG from being a good competitor. On the other hand, if the diacylglycerol moiety is more relevant for substrate recognition, we expect Gal₂-DAG to be a strong competitor, thus resulting in a marked decrease in Glc₂-DAG-NBD transport. Our results show that even under a high excess of Gal₂-DAG, there is no significant effect on Glc₂-DAG-NBD transport (Fig. 5E). We have previously shown that gentiobiose (β -D-Glc-(1,6)-D-Glc), a disaccharide with the same composition and conformation as the glycolipid headgroup (Glc₂-DAG), inhibits lipid transport²⁷. Taken together, these results suggest that an intact headgroup is highly relevant for substrate binding and transport, and that even minor changes to the headgroup abolishes recognition. Independent of the presence of the diacylglycerol moiety and its predicted binding to the hydrophobic pocket, the headgroup seems to dictate whether a glycolipid can be a substrate for LtaA or not.

Discussion

Several transporters of the MFS superfamily have been structurally characterized in one or multiple conformational states^{4,8-17}. However, except for the outward-facing structure of LtaA²⁷, solved by X-ray crystallography, and the inward- and outward-facing structures of MFSD2A^{21,22}, solved by single particle cryo-electron microscopy, there are no additional structures available of MFS lipid transporters. Despite the differences among their lipid substrates, the distinct composition of bacterial and eukaryotic membranes, and their opposite vectorial lipid transport directions, LtaA and MFSD2A share multiple architectural similarities, including a canonical MFS fold of 12 TM helices and an amphipathic central cavity with asymmetric distribution of hydrophobic and hydrophilic residues (Suppl. Fig. 6). A similar arrangement of central cavity residues has been predicted to be present in the bacterial lysophospholipid transporter LpIT¹⁸, and are likely to be part of the architecture of other MFS lipid transporters (Suppl. Fig. 8). These characteristics suggest a common mechanism of substrate recognition and translocation among these proteins. Indeed, LtaA and MFSD2A display strong selectivity towards the headgroup of their lipid substrates^{6,27}. In the case of MFSD2A, the zwitterionic charge of the phosphatidylcholine headgroup is fundamental for ligand transport, whereas LtaA displays strong selectivity towards the gentiobiosyl disaccharide headgroup of the glycolipid. Furthermore, LtaA selects against an isomer of the

disaccharide headgroup, as shown by the poor competition displayed by digalactosyl-diacylglycerol in transport assays (Fig. 5E). In contrast, LpIT has been shown to exhibit a more relaxed specificity towards the lipid headgroup, being able to transport lysophosphatidylethanolamine and lysophosphatidylglycerol lipids¹⁸.

Although MFSD2A and LpIT have been shown to strongly select for lysophospholipids, they display relaxed selectivity towards the length of the aliphatic chains^{6,18}. MFSD2A transports docosahexaenoic acid (DHA), an essential omega-3 fatty acid for brain growth and cognitive function, in the form of lysophosphatidylcholine, but can also transport other lipids with at least 14-carbons acyl chain⁶. It is noteworthy that *S. aureus* membranes are rich in diacylglycerols with chains length ranging from C₁₅ to C₁₈, with the most dominant lipid species having a C₁₈:C₁₅ composition²⁶. This variability among diacylglycerols in *S. aureus*, and the measurable translocation of Glc₂-DAG-NBD²⁷, which has a C₁₀ acyl chain length and an NBD group linked to one of the diacylglycerol chains, suggest that LtaA displays similar relaxed specificity towards the length of the lipid part.

Our results strongly suggest that in contrast to mechanisms proposed for other lipid transporters, LtaA transports gentiobiosyl-diacylglycerol by a ‘trap-and-flip’ mechanism, which follows the classical alternating-access model of transport⁵³, with the entire glycolipid entering and leaving the central translocation pathway (Fig. 5F). The transition between inward- and outward-facing states likely follows the ‘rocker-switch’ alternating access model that describes the mechanism of MFS transporters of water-soluble substrates^{4,54,55}. In this model, the N-terminal and the C-terminal domains rotate about an axis crossing the center of the transporter. This ‘rocking’ motion facilitates switching between the two conformations^{4,54,55}. However, whereas the two extracellular lateral openings display similar widths and dynamics during MD simulations (Fig. 3B) and similar behavior in transport assays (Fig. 4A,B), the cytoplasmic lateral openings seem to display specialized functions during the transport cycle of LtaA (Fig. 4A,B). Entry of the glycolipid into the putative translocation pathway from the side of the TM5-TM8 opening is supported by MD simulations of the AF inward-facing model (Fig. 3D and Movie 2), albeit entry through the opening lined by TM2-TM11 might also be possible since cross-linking of the TM5-TM8 opening (K141C-N276C) decreases LtaA activity moderately (Fig. 4A,B). In contrast, cross-linking of the lateral opening lined by TM2-TM11 decreases LtaA activity significantly (Fig. 4A,B). Since multiple residues located in TM2 likely participate in proton transport as shown before²⁷, we speculate that ‘gating’ of the

TM2-TM11 opening is essential for proton-coupling. A similar role of charged residues in TM2 involved in ion-dependent gating has been postulated for MFSD2A and supported by MD simulations²². Thus, we propose that during its transport cycle (Fig. 5F), inward-facing LtaA binds a glycolipid molecule which enters through the lateral opening lined by TM5 and TM8, triggering the conformational change to outward-facing conformations, in which the glycolipid is released into the membrane presumably through any of the two extracellular lateral openings. Protonation of residues in the hydrophilic pocket allows transition to inward-facing conformations, followed by proton release to the cytoplasm through the lateral opening lined by TM2 and TM11 (Fig. 5F).

In summary, our results provide insights into the molecular mechanism of glycolipid transport by LtaA and support a 'trap-and-flip' model where lateral 'gates' display distinct mechanistic roles. Our data suggests that the highly selective hydrophilic pocket dictates substrate specificity, but that the hydrophobic pocket is fundamental for aliphatic chains' transport. The mechanistic elements described here might be shared by other MFS lipid transporters and can be decisive for the design of drugs targeting these proteins.

Methods

LtaA expression and purification. The gene encoding *S. aureus* LtaA was cloned into a modified pET-19b vector (Novagen), with an N-terminal His₁₀ affinity tag. LtaA WT and mutants were expressed in *E. coli* BL21 Gold (DE3) (Stratagene) cells. Cells were grown in Terrific Broth (TB) medium supplemented with 1% glucose (w/v) at 37°C. Overexpression was induced with 0.2 mM Isopropyl β-D-1-thiogalactopyranoside (IPTG) for 1h. All following steps were performed at 4 °C, unless different specified. Cells were harvested by centrifugation, resuspended in 50mM Tris-HCl, pH 8.0; 500mM NaCl; 5mM β-mercaptoethanol; 0.5mM PMSF and disrupted in a M-110L microfluidizer (Microfluidics) at 10000 psi chamber pressure. Membranes were pelleted by ultracentrifugation and solubilized in 50 mM Tris-HCl, pH 8.0; 200mM NaCl; 20mM Imidazole; 15% glycerol (v/v); 5mM β-mercaptoethanol; 1% Lauryl Maltose Neopentyl Glycol (w/v) (LMNG, Anatrace); 1% N-dodecyl-β-D-maltopyranoside (w/v) (DDM, Anatrace). After removing debris, the supernatant was loaded onto a pre-equilibrated NiNTA superflow affinity column (Qiagen). The column was washed with 50mM Tris-HCl, pH 8.0; 200mM NaCl; 50mM Imidazole; 10% glycerol (v/v); 5mM β-mercaptoethanol; 0.02% LMNG and 0.02% DDM and then further washed with the same buffer only containing 0.02%

LMNG. Elution was performed in the same buffer containing 200mM Imidazole. Buffer exchange to buffer 10 mM Tris-HCl pH 8.0; 150mM NaCl; 0.02% LMNG; with or without 2mM β -mercaptoethanol, was performed using PD-10 columns (GE Healthcare). If necessary, analytical size exclusion chromatography was performed on a Superdex 10/300 GL column (GE Healthcare) in buffer 10 mM Tris-HCl, pH 8.0; 150 mM NaCl; 0.02% LMNG.⁵⁶

Mutagenesis. LtaA mutants were generated using overlap Extension-PCR, followed by DpnI digestion for two hours at 37°C, and transformation into *E. coli* DH5 α cells. The mutations were confirmed by DNA sequencing (Microsynth). All oligos used for mutagenesis are listed in **Suppl. table 2**.

YpfP expression and purification. The gene encoding *S. aureus* YpfP was cloned into a modified pET-19b vector (Novagen) with an N-terminal His₁₀ affinity tag. YpfP was overexpressed in BL-21 Gold (DE3) (Stratagene) cells. Cells were grown in TB medium supplemented with 1% glucose (w/v) at 37 °C until a cell density of OD₆₀₀ = 3. Subsequently, cells were induced with 0.2 mM IPTG for 16h at 24 °C. Cells were harvested by centrifugation and resuspended in buffer A (50mM Tris-HCl pH 8.0; 200mM NaCl; 3% glycerol; 3mM β -mercaptoethanol) plus 0.5mM PMSF. Cells were disrupted using a tip sonication. After differential centrifugation, the supernatant containing YpfP was incubated with NiNTA resin and left stirring for 1h at 4 °C. Washing was performed with buffer A complemented with 50 mM imidazole pH 8.0, followed by elution with buffer A complemented with 200 mM imidazole pH8.0. YpfP was desalted in buffer 50 mM Tris-HCl pH 8.0; 200 mM NaCl; 10% glycerol using PD-10 columns (GE healthcare). If required YpfP was concentrated using a Vivaspin 20 30MWCO until 2.4 mg/ml, flash frozen in liquid nitrogen and stored at -80 °C until further use.

Synthesis of NBD-glycolipid and glycolipid. Synthesis of glycolipid and nitrobenzoxadiazole (NBD)-labelled glycolipid was performed using a modification of the protocol described by Jorasch et al⁵⁷ and Kiriukhin et al⁵⁸. A final concentration of 2mM UDP-Glucose (Sigma), 2mM NBD-decanoyl-2-decanoyl-sn-Glycerol (Cayman), and 1.2mg/ml purified YpfP were incubated together for 16h at 30°C. The reaction product was separated using thin-layer chromatography (TLC) with a silica gel matrix (Sigma) in a solvent mixture consisting of

chloroform:methanol:water (65:25:4, vol/vol/vol). Silica containing the NBD-glycolipid was recovered from plates, and the NBD-glycolipid was extracted from the silica by incubation with a solvent mixture of chloroform:methanol (50:50, vol/vol), followed by drying of the anchor-LLD under argon atmosphere, and subsequently resuspension in 20 mM Tris-HCl pH 8.0; 150 mM NaCl. NBD-glycolipid was flash frozen in liquid nitrogen, and stored at -80°C until further use. Reaction products were previously characterized²⁷. Non-labelled glycolipid was prepared similarly by incubation of 2mM UDP-Glucose, 2 mM 1,2-dimyristoyl-sn-glycerol (Avanti) and 1.2 mg/ml YpfP for 16h at 30°C.

Formation of LtaA proteoliposomes. LtaA was reconstituted in unilamellar liposomes prepared by extrusion through polycarbonate filters (400 nm pore size) from a 3:1 (w/w) mixture of *E. coli* polar lipids and L- α -phosphatidylcholine (Avanti polar lipids) resuspended in 20 mM Tris-HCl pH 8.0; 150mM NaCl and 2mM β -mercaptoethanol. After saturation with DDM (Anatrace), liposomes were mixed with purified LtaA in a 50:1 (w/w) lipids/protein ratio. DDM was removed after incubation with BioBeads (BioRad). Proteoliposomes were centrifugated, washed and resuspended to a final concentration of 20mg/ml lipids; 7.8 μ M LtaA. The proteoliposomes were flash-frozen in liquid nitrogen and stored at -80°C until further use.

***In vitro* flipping assay.** Before performing flipping assays, proteoliposomes were thawed, their resuspension buffer was exchanged to 20 mM MES pH 6.5; 150 mM NaCl, and the product of the NBD-glycolipid synthesis reaction was incorporated by performing freeze/thaw cycles. Proteoliposomes and protein-free liposomes were diluted to a concentration of 2 mg/ml lipids followed by extrusion through polycarbonate filters (400 nm pore size). Proteoliposomes were immediately used for flipping assays. In case of competition assays with digalactosyldiacylglycerol (DGDG). DGDG powder (Avanti) was resuspended in 20 mM Tris-HCl; 150 mM NaCl and incorporated into proteoliposomes during freeze/thaw cycles together with the NBD-glycolipid. Flipping of NBD-glycolipid was assessed by determining the percentage of NBD-fluorescence that is quenched after addition of a 5 mM sodium dithionite (Sigma) after 200 seconds of starting fluorescence recording. 100 seconds before finishing data recording, 0.5% Triton X100 was added to permeabilize the liposomes, making all NBD-glycolipid molecules accessible to dithionite reduction. The fluorescence after Triton X100

addition was used for baseline calculations. Fluorescence was recorded at 20°C using a Jasco Fluorimeter. The excitation and emission wavelengths were 470 and 535 nm, respectively. For analysis the fluorescence intensity was normalized to F/F_{\max} . Relative flipping activities were calculated as follows: relative activity = $100 \times ((F/F_{\max})_i - (F/F_{\max})_{\text{liposomes}}) / ((F/F_{\max})_{\text{wt}} - (F/F_{\max})_{\text{liposomes}})$, where *i* corresponds to each respective treatment/mutants, liposomes corresponds to liposomes without protein, wt corresponds to wild type LtaA and F/F_{\max} values correspond to the normalized fluorescence values at the plateau after addition of sodium dithionite. Curves were plotted using GraphPad Prism 8. Time courses of the dithionite-induced fluorescence decay in liposomes were repeated at least 3 times for each individual experiment.

Proton-transport assay. LtaA proteoliposomes and protein-free liposomes were thawed, and their internal buffer exchanged to 5 mM HEPES pH7.3; 100mM KCl. Glycolipid was incorporated during freeze/thaw cycles followed by extrusion through polycarbonate filters (400 nm pore size). After 90s of sonication, proteoliposomes and protein-free liposomes were diluted 25-fold in buffer containing 5 mM HEPES pH 7.3; 10 mM KCl; 90 mM NaCl; 0.5 μM 9-amino-6-chloro-2-methoxyacridine (ACMA). Fluorescence was recorded using a Jasco Fluorimeter with excitation and emission wavelengths of 410 and 480 nm respectively. When the fluorescence signal was stable, H^+ influx was initiated by establishing a membrane potential by the addition of the potassium ionophore valinomycin (5 nM). Time courses of the proton-transport assay in proteoliposomes were repeated at least 3 times for each individual experiment. Crosslinking was performed before the measurement by addition of 2 mM CuCl_2 to the proteoliposomes during the buffer exchange and incorporation of glycolipid steps. After 1h incubation at RT in the dark, CuCl_2 was removed by centrifugation, and proteoliposomes were resuspended in buffer 5 mM HEPES, pH7.3; 100mM KCl.

LtaA crosslinking and PEGylation. Before performing crosslinking, proteoliposomes were thawed, their resuspension buffer was exchanged to 20 mM Tris-HCl pH 8.0; 150 mM NaCl. LtaA mutants incorporated into proteoliposomes or in detergent micelles were incubated with 2 mM CuCl_2 or *N,N'*-1,2-phenylenedimaleimide (*o*-PDM) for 30 minutes to 1h at RT in the dark. In case of non-crosslinked samples, proteoliposomes were incubated with a proportional volume of DMSO or buffer. Crosslinkers were removed by centrifugation and

washing with buffer or by buffer exchange to 20 mM Tris-HCl, pH 8.0; 150 mM NaCl using Zeba™ Spin Desalting Columns, 7K MWCO, 0.5 mL (ThermoScientific). To PEGylate free cysteines, LtaA mutants were incubated for 3h at RT in the presence of 0.5 mM mPEG5K-Maleimide (Sigma) and 0.5% SDS. Samples were resuspended in PAGE-buffer containing 143 mM β -mercaptoethanol, and the proteins were separated on 15% polyacrylamide gels and visualized with QuickBlue Protein stain (Lubio science).

Sample preparation for LC-MS analysis. LtaA mutants were purified as described above, and concentrated to a concentration of 0.6 mg/ml. Purified LtaA was incubated for 1h at RT in the dark in the absence or presence of 2 mM o-PDM. Afterwards, 10 mM β -mercaptoethanol was added to quench the crosslinker. 1-2 μ g of either crosslinked or non-crosslinked LtaA protein were dissolved in 20 μ l digestion buffer (0.02% of LMNG; 1 M urea; 0.1 M ammoniumbicarbonate; 10 mM tris(2-carboxyethyl) phosphine (TCEP); 15 mM chloroacetamide, pH = 8.5), reduced and alkylated for 1h at 37 °C. Proteins were digested by incubation with either sequencing-grade modified trypsin (1/50, w/w; Promega, Madison, Wisconsin), chymotrypsin sequencing grade (1/50, w/w, Sigma-Aldrich) or lys-C (1/100, w/w, Wako) overnight at 37°C. Then, the peptides were cleaned using iST cartridges (PreOmics, Munich) according to the manufacturer instructions. Samples were dried under vacuum and dissolved in 0.1 % formic acid solution at 0.5 pmol/ μ l. All samples were prepared in triplicates.

Label-free targeted PRM-LC-MS analysis of cysteine-containing peptides. In a first step, parallel reaction-monitoring (PRM) assays⁵⁹ were generated for all the peptides of LtaA WT and the peptides of the 5 different LtaA cysteine mutants, for each protease. These peptides include the reference peptide for normalization, that is shared for all mutants. Therefore, the specific peptide sequences were loaded into Skyline (version 20.2.0.343 (<https://brendanxuw1.gs.washington.edu/labkey/project/home/software/Skyline/begin.view>)) and transitions were predicted using the integrated PROSIT algorithm for double and triple charged precursors. Then, protease and isoform specific isolation mass lists were exported and used to generate specific targeted LC-MS analyses. This analysis was carried as described previously⁶⁰. Chromatographic separation of peptides was carried out using an EASY nano-LC 1000 system (Thermo Fisher Scientific), equipped with a heated RP-HPLC column (75 μ m x 30 cm) packed in-house with 1.9 μ m C18 resin (Reprosil-AQ Pur, Dr. Maisch). Aliquots of 1 pmol total

peptides were analyzed per LC-MS/MS run using a linear gradient ranging from 95% solvent A (0.15% formic acid, 2% acetonitrile) and 5% solvent B (98% acetonitrile, 2% water, 0.15% formic acid) to 30% solvent B over 90 minutes at a flow rate of 200 nl/min. Mass spectrometry analysis was performed on a Q-Exactive plus mass spectrometer equipped with a nano-electrospray ion source (both Thermo Fisher Scientific) using a hybrid DDA (top5)/PRM LC-MS analysis. In detail, each MS1 scan was followed by high-collision-dissociation (HCD) of the precursor masses of the imported isolation list and the 5 most abundant precursor ions with dynamic exclusion for 20 seconds. For each mutant and protease, a specific LC-MS method was generated. Total cycle time was approximately 1 second. For MS1, 3e6 ions were accumulated in the Orbitrap cell over a maximum time of 100 ms and scanned at a resolution of 70,000 FWHM (at 200 m/z). Targeted MS2 scans were acquired at a target setting of 3e6 ions, accumulation time of 100 ms and a resolution of 35,000 FWHM (at 200 m/z) and a mass isolation window to 0.4 Th. MS1 triggered MS2 scans were acquired at a target setting of 1e5 ions, a resolution of 17,500 FWHM (at 200 m/z) and a mass isolation window of 1.4 Th. Singly charged ions and ions with unassigned charge state were excluded from triggering MS2 events. The normalized collision energy was set to 27% and one microscan was acquired for each spectrum. The acquired raw-files were converted to mgf-file format using MSConvert (v 3.0, proteowizard) and searched using MASCOT (Matrix Science, Version: 2.4.1) against a decoy database containing normal and reverse sequences of the predicted SwissProt entries of *Staphylococcus aureus* (strain NCTC 8325 / PS 47, www.ebi.ac.uk, release date 2020/08/21). The 5 LtaA mutants and commonly observed contaminants (in total 6,574 sequences) were generated using the SequenceReverser tool from the MaxQuant software (Version 1.0.13.13). The search criteria were set as following: full tryptic specificity was required (cleavage after lysine or arginine residues); 3 missed cleavages were allowed; carbamidomethylation (C) was set as fixed modification and oxidation (M) as variable modification. The mass tolerance was set to 10 ppm for precursor ions and 0.02 Da for fragment ions. Then, Scaffold (version Scaffold_4.11.1, Proteome Software Inc., Portland, OR) was used to validate MS/MS based peptide and protein identifications. Peptide identifications were accepted if they could be established at a probability greater than 97.0% by the Scaffold Local FDR algorithm. Protein identifications were accepted if they could be established at a probability higher than 99.0% to achieve an FDR less than 1.0% and contained at least 2 identified peptides. Protein probabilities were assigned by the Protein Prophet algorithm⁶¹.

Proteins that contained similar peptides and could not be differentiated based on MS/MS analysis alone were grouped to satisfy the principles of parsimony. Subsequently, all raw-files were imported into Skyline for protein/peptide quantification. To control for variation in sample amounts, all intensities were normalized against the 4 cysteine-free reference peptides. Only peptides that could be confidently identified by database searching were considered for quantification by PRM using the predicted transitions. Statistical analysis and ratio calculations to compare the relative abundance of the peptides between non-crosslinked and crosslinked peptides were performed in Excel. Histograms and P values were generated using Prism 9.

Nanodiscs reconstitution. Purified LtaA was reconstituted in MSP1D1 nanodiscs using a ratio of 2:5:115 (LtaA:MSP1D1:lipids) in a buffer containing 50 mM Tris-HCl, pH 8.0; 50 mM NaCl and 10 % glycerol (v/v). The lipid mixture used consist of 16:0-18:1 POPG:DAG (Avanti) in a 3:1 (w:w) ratio. Detergent was removed by adding Bio-beads SM2 (BioRad). After Bio-beads removal the mixture was centrifuged and loaded on a Superdex 200 Increase 10/300 GL (GE Healthcare) column equilibrated with buffer 50 mM Tris-HCl, pH 8.0; 50 mM NaCl. The peak corresponding to LtaA in nanodiscs was collected and used for mass photometry studies.

Mass photometry assay. Mass photometry experiments were performed using a Refeyn OneMP instrument operated at around 25 °C. Each measurement was made by mixing 2 µl of sample into 18 µl of buffer in a droplet contained by a Grace Bio-Labs CultureWell gasket (Sigma Aldrich) on 24x50 mm area 170±5 µm thickness coverglass (Marienfeld). Calibration of contrast to molecular mass was performed using Nativemark unstained protein standards (ThermoFisher) at a final dilution of 1 in 500 in 0.2 µm filtered PBS. Samples of LtaA in nanodiscs, and of empty nanodiscs, were diluted to 100 nM final concentration in 50 mM Tris-HCl pH 8.0; 150 mM NaCl and contrast events were recorded for 120 s. The resulting movies were analysed to obtain contrast event histograms in the software DiscoverMP 2.3.0 using 5 frame binning with motion correction, a Threshold-1 value of 2, and a Threshold-2 value of 0.25. After applying the molecular mass calibration, contrast event histograms were constructed using a bin-width of 8 kDa. Histograms from two consecutive 120 s measurements on the same sample were merged to include data with a lower protein

deposition rate. To obtain molecular mass averages, histogram peaks were fitted to Gaussians using the manual peak-fitting procedure in the software.

Docking of glycolipid. Both 1,2-dihexadecanoic-3-O-(β -D-glucopyranosyl-1 \rightarrow 6-O- β -D-glucopyranosyl-sn-Glycerol) molecule and the headgroup (β -D-glucopyranosyl-1 \rightarrow 6-O- β -D-glucopyranosyl-sn-Glycerol) were docked to the LtaA 'repeat-swap' inward-facing models with Glide⁶². The initial coordinates of both full-length glycolipid and the headgroup were generated from 2D geometry in LigPrep⁶³. The stereochemistry was corrected. Docking was performed over a search space of 45x45x45 Å³ covering the central cavity.

S. aureus phenotypic complementation assay. Generation of pLOW-ltaA and of *Staphylococcus aureus* NCTC8325 Δ ltaA genotype was previously described²⁷. pLOW vector was used for construction of ltaA complementary strains. Point mutations were generated by extension overlap PCR, and then with restriction-ligation cloning using Sall and NotI cloned into pLOW vector⁶⁴. For cloning purposes *E. coli* IM08B was used⁶⁵. The sequence of the resulting constructs was confirmed by DNA sequencing (Microsynth). After conformation of the correct constructs, pLOW vector carrying ltaA WT or point mutations were introduced into *S. aureus* NCTC8325 Δ ltaA by electrophoresis with erythromycin selection (5 μ g/ml). *S. aureus* cells were grown in 3 ml of Luria-Bertani (LB) medium at 37 °C with 200 rpm until OD₆₀₀ of 0.3. For complementary strains containing a pLOW vector, a final concentration of 5 μ g/ml was added to the medium. For the serial dilutions, 5 μ l of the original and its dilutions were spotted on LB agar plates buffered with sodium phosphate at pH 6.4 complemented with 0.1 mM IPTG. The plates were incubated overnight at 37 °C. Pictures were taken the next morning.

Preparation of S. aureus membranes for LC-MS analysis. *S. aureus* cells were grown in 3 ml LB medium at 37 °C with 200 rpm until OD₆₀₀ of 0.4. For complementary strains containing a pLOW vector, a final concentration of 5 μ g/ml and 0.1 mM IPTG were added to the medium. After harvesting the cells were resuspended in 10 mM Tris pH8.0; 1 mM EDTA; 25 μ g/ml lysostaphin, and incubated for 0.5h at 37 °C. Cells were further subjected to sonication, followed by collection of membranes by ultracentrifugation. The membranes were

resuspended in 100 mM Tris-HCl; 5% SDS; 10 mM tris(2-carboxyethyl) phosphine (TCEP). Samples were sonicated for 10 minutes, followed by shaking for 1h at 37 °C with 500 rpm. To reduce and alkylate the disulfides a final concentration of 15 mM iodoacetamide was added, and the samples were incubated for 0.5h in the dark at room temperature. Samples were loaded on S-trap Micro Spin column (Protifi). After washing, on column peptide digestion was performed by addition of trypsin in 50 mM triethylammonium bicarbonate (TEAB) buffer, and incubation of 1h at 47 °C. Digested peptides were collected by passing 50 mM triethylammonium bicarbonate (TEAB) buffer, 0.2 % formic acid (w/v) in distilled water, and 0.2 % formic acid (w/v) in 50% acetonitrile (v/v) through the column and dried in a SpeedVac (Labconco). Dried peptides were re-suspended in 0.1% formic acid (w/v) and stored at -20 °C.

Targeted PRM LC-MS analysis of LtaA WT and mutants. As a first step, PRM assays⁵⁹ for all possible peptides of LtaA with a length of 6 to 25 amino acids comprising double- and triple-charged precursor ions were created. Five peptides were identified to match the length and charge criteria, leading to ten PRM assays in total. These were used to identify LtaA membrane fractions of wild-type *S. aureus*. The setup of the μ RPLC-MC system was previously described⁶⁰. Mass spectrometry analysis was conducted using a Q-Exactive mass spectrometer with a nano-electrospray ion source (both Thermo Fisher Scientific). Each MS1 scan was followed by high-collision-dissociation (HCD) of the ten LtaA precursor ions in PRM mode using a global isolation mass list. By applying strict identification criteria, three peptide ions of LtaA LTNYNTRPVK (2+ and 3+ ion) and MQDSSLNNYANHK (2+) were identified, and these were used for label-free PRM quantification. To control for protein variation between different samples, the total ion chromatography (only comprising peptide with two or more charges) was determined for each sample by label-free quantification using Progenesis Q1 (version 2.0, Waters) and then used to normalize the samples. The integrated peak areas of the three peptide ions that were quantified by PRM were summed up and used for LtaA quantification.

Modeling of inward-facing conformation. The inward-facing conformation was modelled under the assumption of inverted repeats⁴⁸. Sequence alignments between the two repeats of each domain of LtaA were performed. We structurally aligned R1D1 (residues 16–105) with R2D1 (residues 109-189), and R1D2 (residues 220-302) with R2D2 (residues 309-393) using

the structure alignment program TMalign resulting in two pairs of alignments. These two pairs of alignments were then used together to build up the final pair-wise alignment between the LtaA sequence and a template in which the LtaA sequence repeats were rearranged in the order R1D2-R1D1-R2D2-R2D1. The initial sequence alignment was then refined by removing gaps in the transmembrane regions and in the secondary structure elements. In this step, one gap in the TM6 (between Phe220 and Pro221) and two gaps in TM8 (between Met294 and Ile295 and also between Leu296 and Ile297) in the alignment were removed. Also, residues Asp336 and Glu337 were moved left to remove a gap at the beginning of TM11. Further refinements were made to match the secondary structure as observed in the outward-open crystal structure. In particular, we aimed to maintain the helical regions in the template where possible, subject to the pseudo-symmetry between the two MFS transporter domains. In this step, a gap the loop region between TM11 and TM12 (between Thr368 and Asn369) was introduced to account for correct orientation of TM12 helices.

We used the final refined alignment and the X-ray crystal structure of LtaA (PDB entry 6S7V [<https://doi.org/10.1038/s41594-020-0425-5>])²⁷ to construct the inward-facing model templates using Modeller 9v24. A template for modelling was constructed from the X-ray crystal structure of LtaA (PDB entry 6S7V) in which the coordinates of residues from R1D2, R1D1, R2D2, and R2D1 were placed as the first, second, third, and fourth segments of the template respectively. Then, 100 initial models were generated. Next, we selected 7 models with the highest MODELLER score and the best MolProbity⁶⁶ profile for further analysis. Then, we repacked the side chains using SCWRL4.0⁶⁷ and as a last step the models were energetically minimized after placing them in the lipid bilayer using the Gromacs steepest descent algorithm for 5,000 steps⁶⁸. To further validate the quality of the models, we assessed the stereochemistry. Evaluation of the model using MolProbity showed that the final minimized models have reasonable qualities (MolProbity score: 2.00-2.3, Ramachandran favored: 92.1-93.6%, and Ramachandran outliers: 0.8-1.90%) (Suppl. Table 1).

Molecular dynamics simulations of inward-facing conformation models. To study their dynamics, each of the seven optimized inward-facing models was placed in a heterogenous lipid bilayer (POPG (65%), diacylglycerol (20 %), cardiolipin (10 %), and gentiobiosyl-diacylglycerol (5 %)) and then solvated in TIP3P water with 150 mM NaCl. The all-atom CHARMM36m force field was used for lipids, ions, and protein⁶⁹⁻⁷¹. All simulations were

performed using GROMACS 2019.6⁶⁸. The starting systems were energy-minimized for 5,000 steepest descent steps and equilibrated first for 1 ns of MD simulations in a canonical (NVT) ensemble and then for 7.5 ns in an isothermal-isobaric (NPT) ensemble under periodic boundary conditions. The initial restraints on the positions of nonhydrogen protein atoms were 4,000 kJ·mol⁻¹·nm². During equilibration, these restraints were gradually released. Particle-mesh Ewald summation with cubic interpolation and a 0.12-nm grid spacing was used to treat long-range electrostatic interactions⁷². The time step was initially 1 fs and was then increased to 2 fs during the NPT equilibration. The LINCS algorithm was used to fix all bond lengths⁷³. Constant temperature was set with a Berendsen thermostat⁷⁴, combined with a coupling constant of 1.0 ps. A semi-isotropic Berendsen barostat⁷⁴ was used to maintain a pressure of 1 bar. During production runs, the Berendsen thermostat and barostat were replaced by a Nosé–Hoover thermostat⁷⁵ and a Parrinello–Rahman barostat⁷⁶. The unconstrained production trajectories were analyzed with Visual Molecular Dynamics (VMD)⁷⁷ and MDAnalysis package^{78,79}. MD simulations of 500 ns were performed for each of the seven ‘repeat-swap’ inward-facing models.

Molecular dynamics simulations of outward-facing conformation. The outward-facing structure of LtaA (PDB ID 6S7V [<https://doi.org/10.1038/s41594-020-0425-5>]) was embedded in a lipid bilayer composed of POPG-DAG-CL-gentiobiosyl-diacylglycerol using CHARMM-GUI⁸⁰. The system was then solvated in TIP3P water with 150 mM NaCl. The all-atom CHARMM36m force field was used for lipids, ions, and protein⁶⁹⁻⁷¹. All simulations were performed using GROMACS 2019.6⁶⁸. Simulations were performed with similar protocols as described above for inward-facing models. The simulation of the outward-facing structure was performed for 1.2 μs.

Molecular dynamics simulations of AlphaFold inward-facing model. The inward-facing model of LtaA generated by AlphaFold⁴⁹ was embedded in a lipid bilayer composed of POPG-DAG-CL-gentiobiosyl-diacylglycerol using CHARMM-GUI⁸⁰. The system was then solvated in TIP3P water with 150 mM NaCl. The all-atom CHARMM36m force field was used for lipids, ions, and protein⁶⁹⁻⁷¹. All simulations were performed using GROMACS 2020.2⁶⁸. The simulation was performed with similar protocols as described above for the inward-facing models. The simulation of the AlphaFold model was performed for 1.1 μs.

Data Availability. The data generated in this study are provided in the Supplementary Information/Source Data file. Further, data that support the findings of this study are available from the corresponding author upon reasonable request.

Source data are provided with this paper.

References

1. Wang, S.C. et al. Expansion of the Major Facilitator Superfamily (MFS) to include novel transporters as well as transmembrane-acting enzymes. *Biochimica Et Biophysica Acta-Biomembranes* **1862**(2020).
2. Quistgaard, E.M., Low, C., Guettou, F. & Nordlund, P. Understanding transport by the major facilitator superfamily (MFS): structures pave the way. *Nat Rev Mol Cell Biol* **17**, 123-32 (2016).
3. Reddy, V.S., Shlykov, M.A., Castillo, R., Sun, E.I. & Saier, M.H., Jr. The major facilitator superfamily (MFS) revisited. *FEBS J* **279**, 2022-35 (2012).
4. Drew, D., North, R.A., Nagarathinam, K. & Tanabe, M. Structures and General Transport Mechanisms by the Major Facilitator Superfamily (MFS). *Chem Rev* **121**, 5289-5335 (2021).
5. Ben-Zvi, A. et al. Mfsd2a is critical for the formation and function of the blood-brain barrier. *Nature* **509**, 507-11 (2014).
6. Nguyen, L.N. et al. Mfsd2a is a transporter for the essential omega-3 fatty acid docosahexaenoic acid. *Nature* **509**, 503-6 (2014).
7. Harvat, E.M. et al. Lysophospholipid flipping across the Escherichia coli inner membrane catalyzed by a transporter (LpIT) belonging to the major facilitator superfamily. *J Biol Chem* **280**, 12028-34 (2005).
8. Abramson, J. et al. Structure and mechanism of the lactose permease of Escherichia coli. *Science* **301**, 610-5 (2003).
9. Debrycker, V. et al. An embedded lipid in the multidrug transporter LmrP suggests a mechanism for polyspecificity. *Nature Structural & Molecular Biology* **27**, 829-835 (2020).
10. Heng, J. et al. Substrate-bound structure of the E. coli multidrug resistance transporter MdfA. *Cell Res* **25**, 1060-73 (2015).
11. Deng, D. et al. Molecular basis of ligand recognition and transport by glucose transporters. *Nature* **526**, 391-6 (2015).
12. Deng, D. et al. Crystal structure of the human glucose transporter GLUT1. *Nature* **510**, 121-5 (2014).
13. Nomura, N. et al. Structure and mechanism of the mammalian fructose transporter GLUT5. *Nature* **526**, 397-401 (2015).
14. Sun, L. et al. Crystal structure of a bacterial homologue of glucose transporters GLUT1-4. *Nature* **490**, 361-6 (2012).
15. Billesbølle, C.B. et al. Structure of hepcidin-bound ferroportin reveals iron homeostatic mechanisms. *Nature* **586**, 807-811 (2020).
16. Pan, Y. et al. Structural basis of ion transport and inhibition in ferroportin. *Nature Communications* **11**, 5686 (2020).
17. Qureshi, A.A. et al. The molecular basis for sugar import in malaria parasites. *Nature* **578**, 321-325 (2020).

18. Lin, Y., Deepak, R., Zheng, J.Z., Fan, H. & Zheng, L. A dual substrate-accessing mechanism of a major facilitator superfamily protein facilitates lysophospholipid flipping across the cell membrane. *J Biol Chem* **293**, 19919-19931 (2018).
19. Angers, M., Uldry, M., Kong, D., Gimble, J.M. & Jetten, A.M. Mfsd2a encodes a novel major facilitator superfamily domain-containing protein highly induced in brown adipose tissue during fasting and adaptive thermogenesis. *Biochem J* **416**, 347-55 (2008).
20. Quek, D.Q., Nguyen, L.N., Fan, H. & Silver, D.L. Structural Insights into the Transport Mechanism of the Human Sodium-dependent Lysophosphatidylcholine Transporter MFSD2A. *J Biol Chem* **291**, 9383-94 (2016).
21. Wood, C.A.P. et al. Structure and mechanism of blood-brain-barrier lipid transporter MFSD2A. *Nature* **596**, 444-448 (2021).
22. Cater, R.J. et al. Structural basis of omega-3 fatty acid transport across the blood-brain barrier. *Nature* **595**, 315-319 (2021).
23. Kawahara, A. et al. The sphingolipid transporter spns2 functions in migration of zebrafish myocardial precursors. *Science* **323**, 524-7 (2009).
24. Zhu, X., Ren, K., Zeng, Y.Z., Zheng, Z. & Yi, G.H. Biological function of SPNS2: From zebrafish to human. *Mol Immunol* **103**, 55-62 (2018).
25. Vu, T.M. et al. Mfsd2b is essential for the sphingosine-1-phosphate export in erythrocytes and platelets. *Nature* **550**, 524-528 (2017).
26. Grundling, A. & Schneewind, O. Genes required for glycolipid synthesis and lipoteichoic acid anchoring in *Staphylococcus aureus*. *J Bacteriol* **189**, 2521-30 (2007).
27. Zhang, B. et al. Structure of a proton-dependent lipid transporter involved in lipoteichoic acids biosynthesis. *Nat Struct Mol Biol* **27**, 561-569 (2020).
28. Parlet, C.P., Brown, M.M. & Horswill, A.R. Commensa Staphylococci influence *Staphylococcus aureus* SKin Colorization and Disease. *Trends in Microbiology* **27**, 497-507 (2019).
29. Sakr, A., Bregeon, F., Mege, J.L., Rolain, J.M. & Blin, O. *Staphylococcus aureus* Nasal Colonization: An Update on Mechanisms, Epidemiology, Risk Factors, and Subsequent Infections. *Front Microbiol* **9**, 2419 (2018).
30. Ahn, K.B., Baik, J.E., Yun, C.H. & Han, S.H. Lipoteichoic Acid Inhibits *Staphylococcus aureus* Biofilm Formation. *Front Microbiol* **9**, 327 (2018).
31. Hesser, A.R. et al. The length of lipoteichoic acid polymers controls *Staphylococcus aureus* cell size and envelope integrity. *J Bacteriol* (2020).
32. Xia, G., Kohler, T. & Peschel, A. The wall teichoic acid and lipoteichoic acid polymers of *Staphylococcus aureus*. *Int J Med Microbiol* **300**, 148-54 (2010).
33. Percy, M.G. & Grundling, A. Lipoteichoic acid synthesis and function in gram-positive bacteria. *Annu Rev Microbiol* **68**, 81-100 (2014).
34. Fischer, W., Koch, H.U., Rosel, P., Fiedler, F. & Schmuck, L. Structural Requirements of Lipoteichoic Acid Carrier for Recognition by the Poly(Ribitol Phosphate) Polymerase from *Staphylococcus-Aureus* H - a Study of Various Lipoteichoic Acids, Derivatives, and Related-Compounds. *Journal of Biological Chemistry* **255**, 4550-4556 (1980).
35. Neumann, J., Rose-Sperling, D. & Hellmich, U.A. Diverse relations between ABC transporters and lipids: An overview. *Biochim Biophys Acta Biomembr* **1859**, 605-618 (2017).
36. Pomorski, T.G. & Menon, A.K. Lipid somersaults: Uncovering the mechanisms of protein-mediated lipid flipping. *Prog Lipid Res* **64**, 69-84 (2016).
37. Perez, C. et al. Structure and mechanism of an active lipid-linked oligosaccharide flippase. *Nature* **524**, 433-8 (2015).
38. Brunner, J.D., Lim, N.K., Schenck, S., Duerst, A. & Dutzler, R. X-ray structure of a calcium-activated TMEM16 lipid scramblase. *Nature* **516**, 207-12 (2014).
39. Hiraizumi, M., Yamashita, K., Nishizawa, T. & Nureki, O. Cryo-EM structures capture the transport cycle of the P4-ATPase flippase. *Science* **365**, 1149-1155 (2019).

40. Timcenko, M. et al. Structure and autoregulation of a P4-ATPase lipid flippase. *Nature* **571**, 366-370 (2019).
41. Mi, W. et al. Structural basis of MsbA-mediated lipopolysaccharide transport. *Nature* **549**, 233-237 (2017).
42. Menon, I. et al. Opsin is a phospholipid flippase. *Curr Biol* **21**, 149-53 (2011).
43. Pomorski, T. & Menon, A.K. Lipid flippases and their biological functions. *Cell Mol Life Sci* **63**, 2908-21 (2006).
44. Olsen, J.A., Alam, A., Kowal, J., Stieger, B. & Locher, K.P. Structure of the human lipid exporter ABCB4 in a lipid environment. *Nat Struct Mol Biol* **27**, 62-70 (2020).
45. Kim, Y. & Chen, J. Molecular structure of human P-glycoprotein in the ATP-bound, outward-facing conformation. *Science* **359**, 915-919 (2018).
46. Perez, C., Mehdipour, A.R., Hummer, G. & Locher, K.P. Structure of Outward-Facing PglK and Molecular Dynamics of Lipid-Linked Oligosaccharide Recognition and Translocation. *Structure* **27**, 669-678.e5 (2019).
47. Timcenko, M. et al. Structural Basis of Substrate-Independent Phosphorylation in a P4-ATPase Lipid Flippase. *J Mol Biol*, 167062 (2021).
48. Radestock, S. & Forrest, L.R. The alternating-access mechanism of MFS transporters arises from inverted-topology repeats. *J Mol Biol* **407**, 698-715 (2011).
49. Jumper, J. et al. Highly accurate protein structure prediction with AlphaFold. *Nature* **596**, 583-589 (2021).
50. Basilio, D., Noack, K., Picollo, A. & Accardi, A. Conformational changes required for H(+)/Cl(-) exchange mediated by a CLC transporter. *Nat Struct Mol Biol* **21**, 456-63 (2014).
51. Koch, H.U., Haas, R. & Fischer, W. The role of lipoteichoic acid biosynthesis in membrane lipid metabolism of growing *Staphylococcus aureus*. *Eur J Biochem* **138**, 357-63 (1984).
52. Bi, Y., Mann, E., Whitfield, C. & Zimmer, J. Architecture of a channel-forming O-antigen polysaccharide ABC transporter. *Nature* **553**, 361-365 (2018).
53. Jardetzky, O. Simple allosteric model for membrane pumps. *Nature* **211**, 969-70 (1966).
54. Huang, Y., Lemieux, M.J., Song, J., Auer, M. & Wang, D.N. Structure and mechanism of the glycerol-3-phosphate transporter from *Escherichia coli*. *Science* **301**, 616-20 (2003).
55. Law, C.J., Maloney, P.C. & Wang, D.N. Ins and outs of major facilitator superfamily antiporters. *Annu Rev Microbiol* **62**, 289-305 (2008).
56. Zhang, B. & Perez, C. Stabilization and Crystallization of a Membrane Protein Involved in Lipid Transport. *Methods Mol Biol* **2127**, 283-292 (2020).
57. Jorasch, P., Wolter, F.P., Zahringer, U. & Heinz, E. A UDP glucosyltransferase from *Bacillus subtilis* successively transfers up to four glucose residues to 1,2-diacylglycerol: expression of ypfP in *Escherichia coli* and structural analysis of its reaction products. *Mol Microbiol* **29**, 419-30 (1998).
58. Kiriukhin, M.Y., Debabov, D.V., Shinabarger, D.L. & Neuhaus, F.C. Biosynthesis of the glycolipid anchor in lipoteichoic acid of *Staphylococcus aureus* RN4220: Role of YpfP, the diglucosyldiacylglycerol synthase. *Journal of Bacteriology* **183**, 3506-3514 (2001).
59. Peterson, A.C., Russell, J.D., Bailey, D.J., Westphall, M.S. & Coon, J.J. Parallel reaction monitoring for high resolution and high mass accuracy quantitative, targeted proteomics. *Mol Cell Proteomics* **11**, 1475-88 (2012).
60. Ahrne, E. et al. Evaluation and Improvement of Quantification Accuracy in Isobaric Mass Tag-Based Protein Quantification Experiments. *J Proteome Res* **15**, 2537-47 (2016).
61. Nesvizhskii, A.I., Keller, A., Kolker, E. & Aebersold, R. A statistical model for identifying proteins by tandem mass spectrometry. *Anal Chem* **75**, 4646-58 (2003).
62. Friesner, R.A. et al. Glide: a new approach for rapid, accurate docking and scoring. 1. Method and assessment of docking accuracy. *J Med Chem* **47**, 1739-49 (2004).
63. Schrödinger Release 2021-3: LigPrep, S., LLC, New York, NY, 2021.
64. Heckman, K.L. & Pease, L.R. Gene splicing and mutagenesis by PCR-driven overlap extension. *Nat Protoc* **2**, 924-32 (2007).

65. Monk, I.R., Tree, J.J., Howden, B.P., Stinear, T.P. & Foster, T.J. Complete Bypass of Restriction Systems for Major *Staphylococcus aureus* Lineages. *MBio* **6**, e00308-15 (2015).
66. Chen, V.B. et al. MolProbity: all-atom structure validation for macromolecular crystallography. *Acta Crystallogr D Biol Crystallogr* **66**, 12-21 (2010).
67. Krivov, G.G., Shapovalov, M.V. & Dunbrack, R.L., Jr. Improved prediction of protein side-chain conformations with SCWRL4. *Proteins* **77**, 778-95 (2009).
68. Abraham, M.J. et al. GROMACS: High performance molecular simulations through multi-level parallelism from laptops to supercomputers. *SoftwareX* **1-2**, 19-25 (2015).
69. Best, R.B. et al. Optimization of the Additive CHARMM All-Atom Protein Force Field Targeting Improved Sampling of the Backbone ϕ , ψ and Side-Chain χ_1 and χ_2 Dihedral Angles. *Journal of Chemical Theory and Computation* **8**, 3257-3273 (2012).
70. Jorgensen, W.L., Chandrasekhar, J., Madura, J.D., Impey, R.W. & Klein, M.L. Comparison of simple potential functions for simulating liquid water. *The Journal of Chemical Physics* **79**, 926-935 (1983).
71. Klauda, J.B. et al. Update of the CHARMM All-Atom Additive Force Field for Lipids: Validation on Six Lipid Types. *The Journal of Physical Chemistry B* **114**, 7830-7843 (2010).
72. Darden, T., York, D. & Pedersen, L. Particle mesh Ewald: An N-log(N) method for Ewald sums in large systems. *The Journal of Chemical Physics* **98**, 10089-10092 (1993).
73. Hess, B., Bekker, H., Berendsen, H.J.C. & Fraaije, J.G.E.M. LINCS: A linear constraint solver for molecular simulations. *Journal of Computational Chemistry* **18**, 1463-1472 (1997).
74. Berendsen, H.J.C., Postma, J.P.M., Gunsteren, W.F.v., DiNola, A. & Haak, J.R. Molecular dynamics with coupling to an external bath. *The Journal of Chemical Physics* **81**, 3684-3690 (1984).
75. Hoover, W.G. Canonical dynamics: Equilibrium phase-space distributions. *Phys Rev A Gen Phys* **31**, 1695-1697 (1985).
76. Parrinello, M. & Rahman, A. Polymorphic transitions in single crystals: A new molecular dynamics method. *Journal of Applied Physics* **52**, 7182-7190 (1981).
77. Humphrey, W., Dalke, A. & Schulten, K. VMD: Visual molecular dynamics. *Journal of Molecular Graphics* **14**, 33-38 (1996).
78. Gowers, R. et al. *MDAnalysis: A Python Package for the Rapid Analysis of Molecular Dynamics Simulations*, 98-105 (2016).
79. Michaud-Agrawal, N., Denning, E.J., Woolf, T.B. & Beckstein, O. MDAnalysis: A toolkit for the analysis of molecular dynamics simulations. *Journal of Computational Chemistry* **32**, 2319-2327 (2011).
80. Wu, E.L. et al. CHARMM-GUI Membrane Builder toward realistic biological membrane simulations. *J Comput Chem* **35**, 1997-2004 (2014).

Acknowledgments

We thank Prof. Jan-Willem Veening for providing us the *S. aureus* NCTC8325, *S. aureus* NCTC8325 Δ *ltaA*, *E. coli* IMO8B cells and the pLOW-vector. We thank Xiaochun Li Blatter for assistance in cell expression and membranes preparations. This work was supported by the Swiss National Science Foundation (SNSF) (PP00P3_198903 to C.P), the Helmut Horten Stiftung (HHS) (to C.P), and by the Max Planck Society and the German Research Foundation (SFB 807: Membrane Transport and Communication, to A.R.M and G.H). E.L. was funded by the Biozentrum International PhD Program and the HHS.

Author Contributions

E.L. performed *in vitro* and *in vivo* biochemical characterization of LtaA and variants. A.R.M. performed computational analysis. C.P. supervised the biochemical analysis. G.H. supervised computational analysis. A.S. and E.L. performed mass spectrometry analysis. E.L., A.R.M, and C.P analyzed the computational, structural and functional data. C.P. conceived and directed the project. All authors contributed to manuscript writing and revision.

Author Information

Competing interests: None declared.

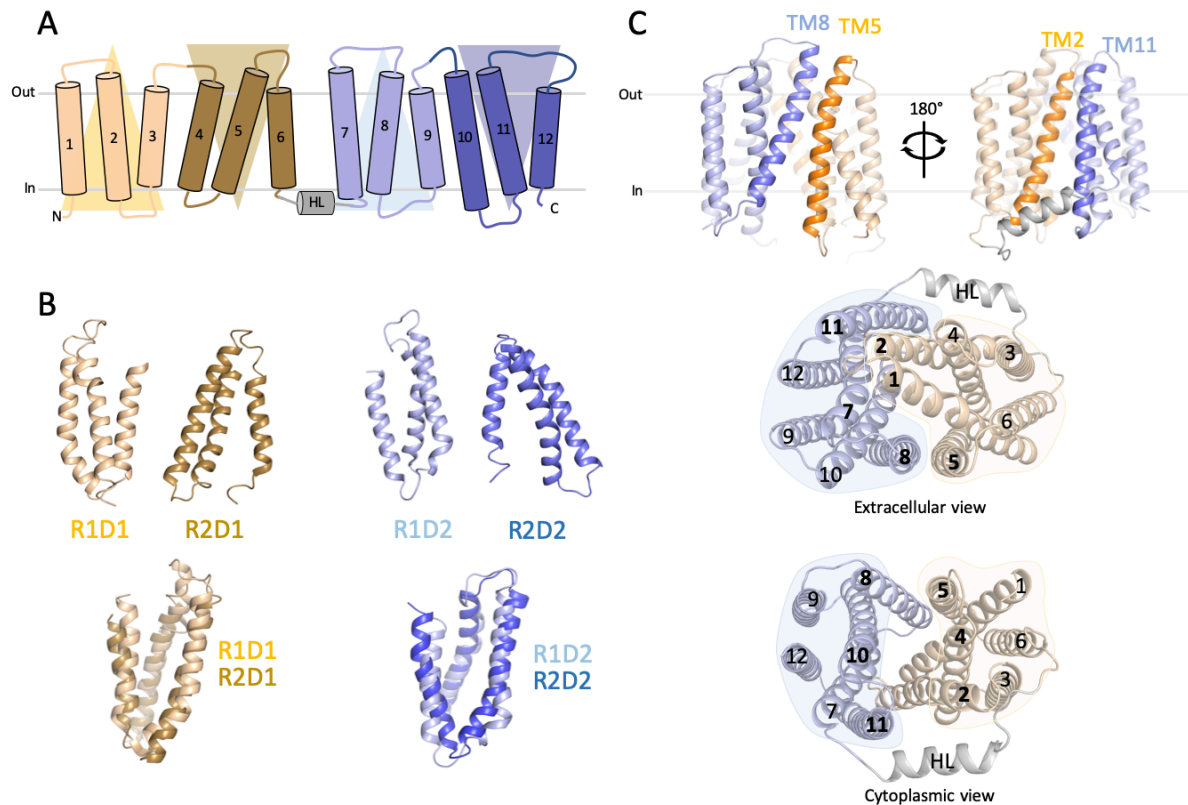
Figures and figure legends

Figure 1. Modeling of inward-facing LtaA. a. Topology representation of LtaA. Domain-1 (N-terminal) and domain-2 (C-terminal) are shown in light orange and light blue, respectively. b. Individual repeat domains as observed in outward-facing LtaA (PDB ID 6S7V), and superposition of inverted repeats (r.m.s.d. = 2.5 Å and 3.0 Å for aligned Ca atoms of R1D1/R2D1 and R1D2/R2D2, respectively). R1D1 and R2D1 indicate the first and second repeats in the N-terminal domain, respectively, whereas R1D2 and R2D2 indicate the first and second repeat in the C-terminal domain, respectively. Colors are according to panel a. c and d. Side-views of inward-facing LtaA models generated by ‘repeat-swap’ and by AlphaFold (AF), respectively. The models show TM helices that line the lateral openings. Extracellular and cytoplasmic views are also shown.

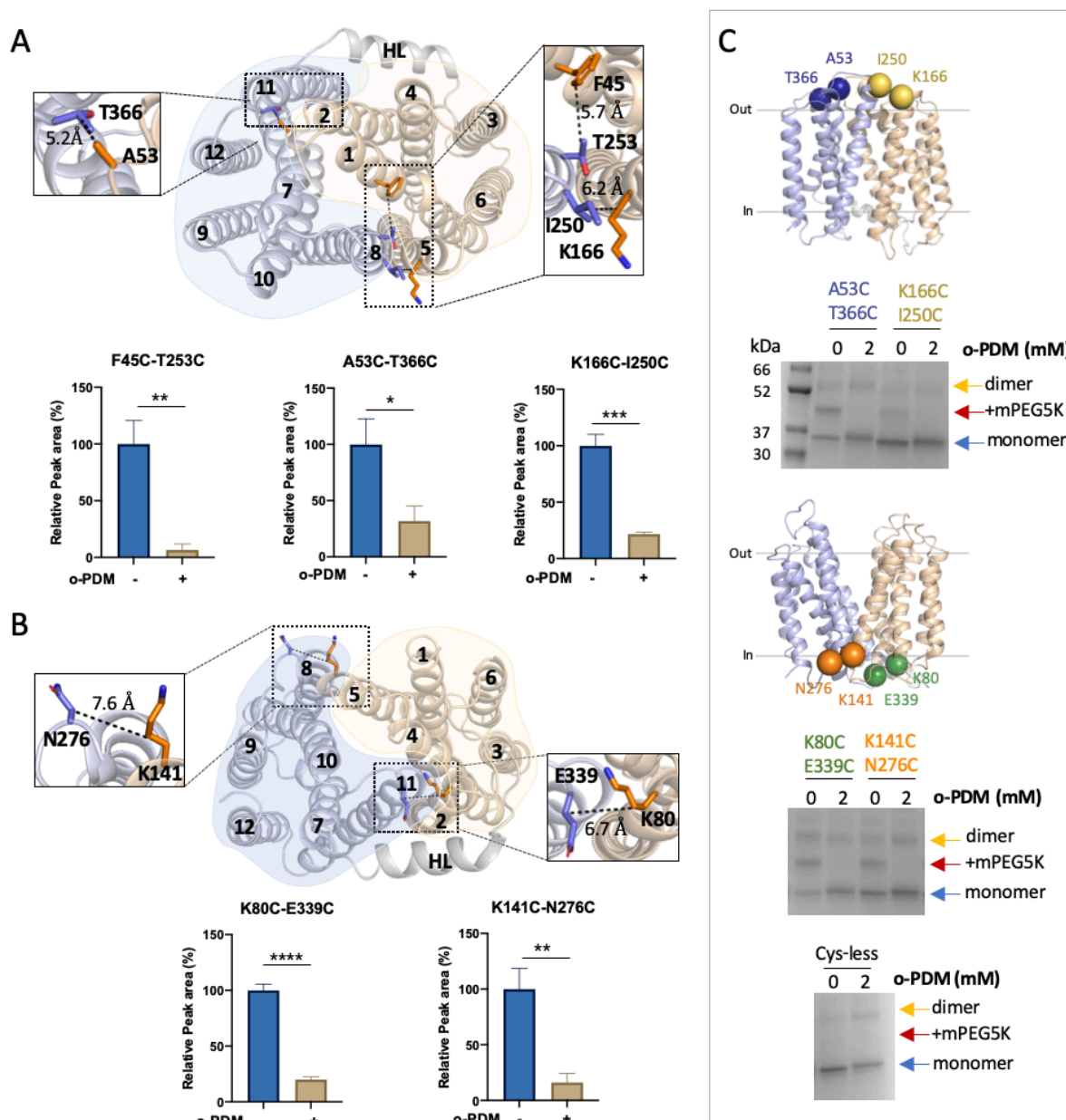


Figure 2. LtaA adopts inward- and outward-facing states. Selected residues for cross-linking of LtaA in inward-facing conformation (a) and outward-facing conformation (b). N-terminal and C-terminal domains are shown in light orange and light blue, respectively. The relative abundance of cysteine containing peptides in absence (-) or presence (+) of N,N'-(o-phenylene)-dimalimide (o-PDM) is shown in histograms. Collision-induced dissociation (CID) spectrum of cysteine containing peptides and elution profiles of peptide fragments are shown in supplementary figure 3. Error bars indicate +/- standard deviation (s.d.) (n=3, biological replicates). *: P≤0.05, **: P≤0.01, ***: P≤0.001, ****: P≤0.0001. Asterisks mark the result from unpaired t-test. c. Cross-linking analysis of LtaA in proteoliposomes. Positions of selected cysteine pairs at the extracellular and cytoplasmic regions of LtaA are shown as spheres. SDS-

PAGE show band shifts of samples treated with mPEG5K after irreversible cross-link with o-PDM. Separated species are indicated with arrows. The complete gel is shown in Suppl. Fig. 4C. SDS-PAGE experiments were independently repeated at least three times with similar results. Source data are provided as a Source Data file.

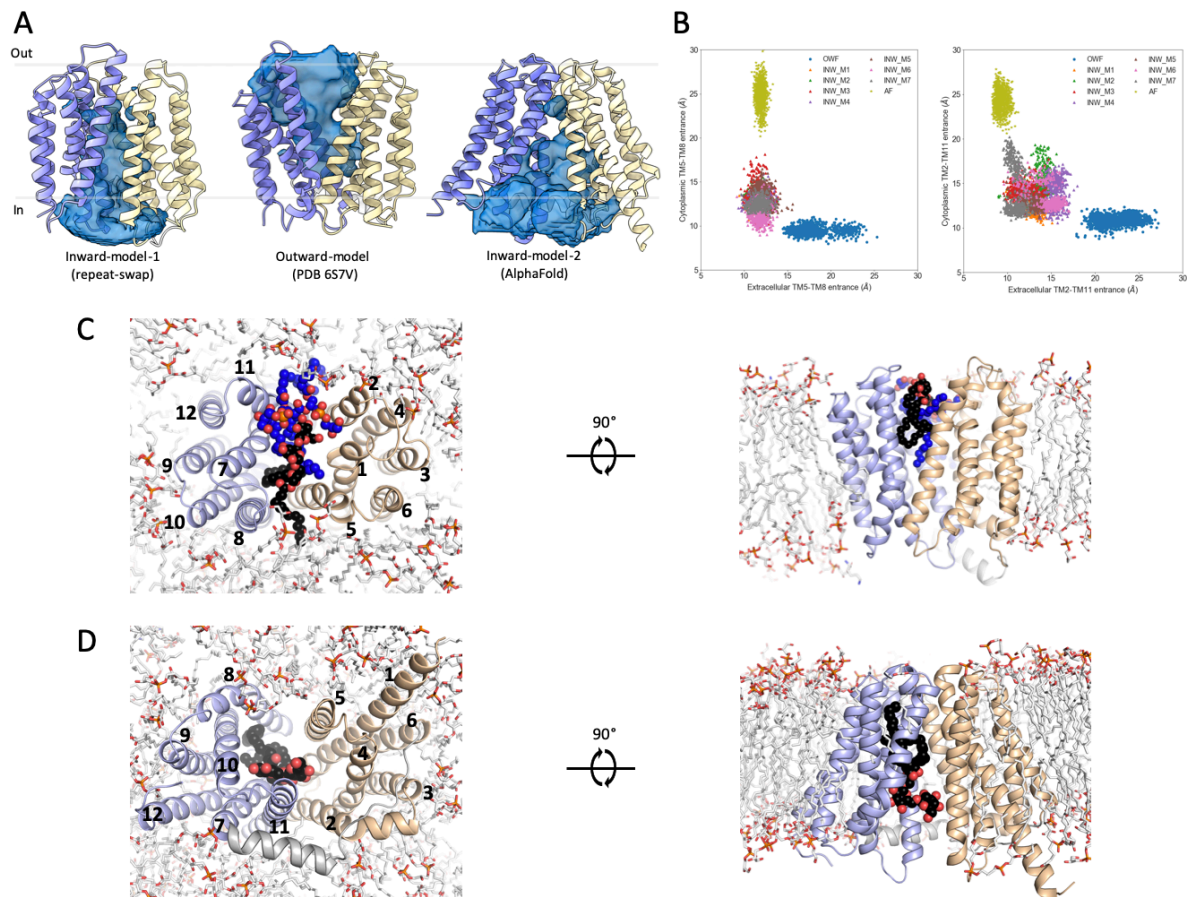


Figure 3. Lateral openings facilitate access of glycolipids to the central translocation pathway. **a.** Representative view of solvent exposed cavity of inward-facing and outward-facing LtaA as observed during MD simulations. **b.** Analysis of distances between TM helices lining the cytoplasmic and extracellular lateral openings of outward-facing and inward-facing models. The center of masses of the C α atoms of extracellular residues 52-57 (TM2), 163-167 (TM5), 250-255 (TM8), 364-367 (TM11), and of cytoplasmic residues 77-81 (TM2), 139-143 (TM5), 273-276 (TM8), 341-344 (TM11), were used for the calculation of inter-TM distances. **c.** Intrusion of gentiobiosyl-diacylglycerol (black spheres) and POPG (blue spheres) molecules in the extracellular cavity of LtaA during simulations. **d.** Intrusion of gentiobiosyl-diacylglycerol (black spheres) in the intracellular cavity of the AF inward-facing model of LtaA during simulations. N-terminal and C-terminal domains are shown in light orange and light blue, respectively.

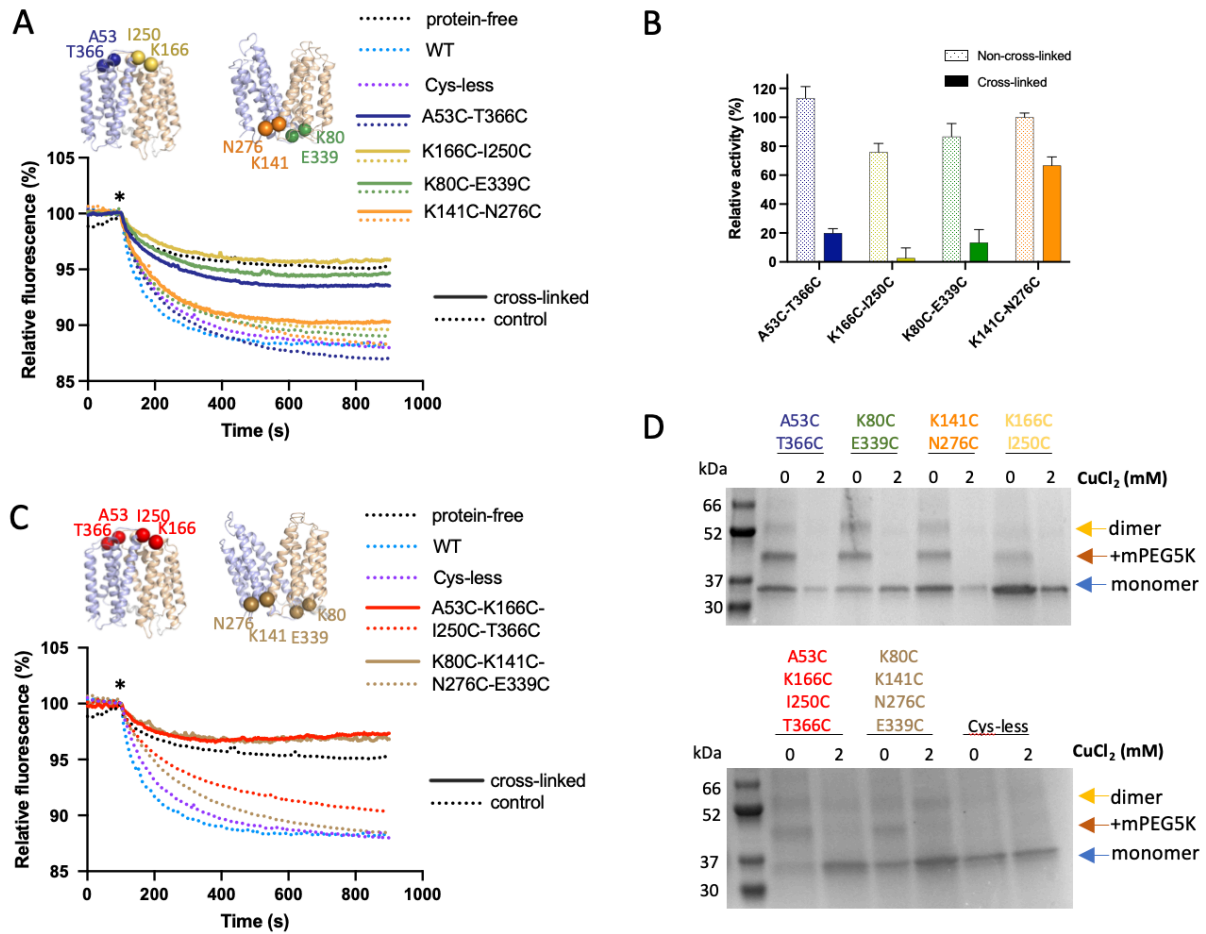


Figure 4. Cycling through outward- and inward-facing conformations is essential for LtaA activity. **a** and **c**. Proton-transport activity of LtaA and variants after chemical crosslinking with CuCl₂ (solid lines) or in absence of cross-linking treatment (dotted lines) (n≥3). Proteoliposomes and protein-free liposomes containing 100 mM KCl were diluted in buffer containing 10 mM KCl, 90 mM NaCl and ACMA. H⁺ influx was initiated by establishing a membrane potential upon addition of the potassium ionophore valinomycin (asterisk). **b**. Relative activity of cross-linked and non-cross-linked LtaA variants measured in A. Relative activity = $100 \times (F'_i - F'_{\text{liposomes}}) / (F'_{\text{wt}} - F'_{\text{liposomes}})$, where i corresponds to each variant, liposomes correspond to protein-free liposomes, and F' correspond to the relative fluorescence at the plateau (800 seconds). Error bars show +/- s.d. of technical replicates, n=3. **d**. SDS-PAGE shows band shifts of proteoliposome samples treated with mPEG5K after cross-link with CuCl₂. Separated species are indicated with arrows. SDS-PAGE experiments were independently repeated at least three times with similar results. Source data are provided as a Source Data file.

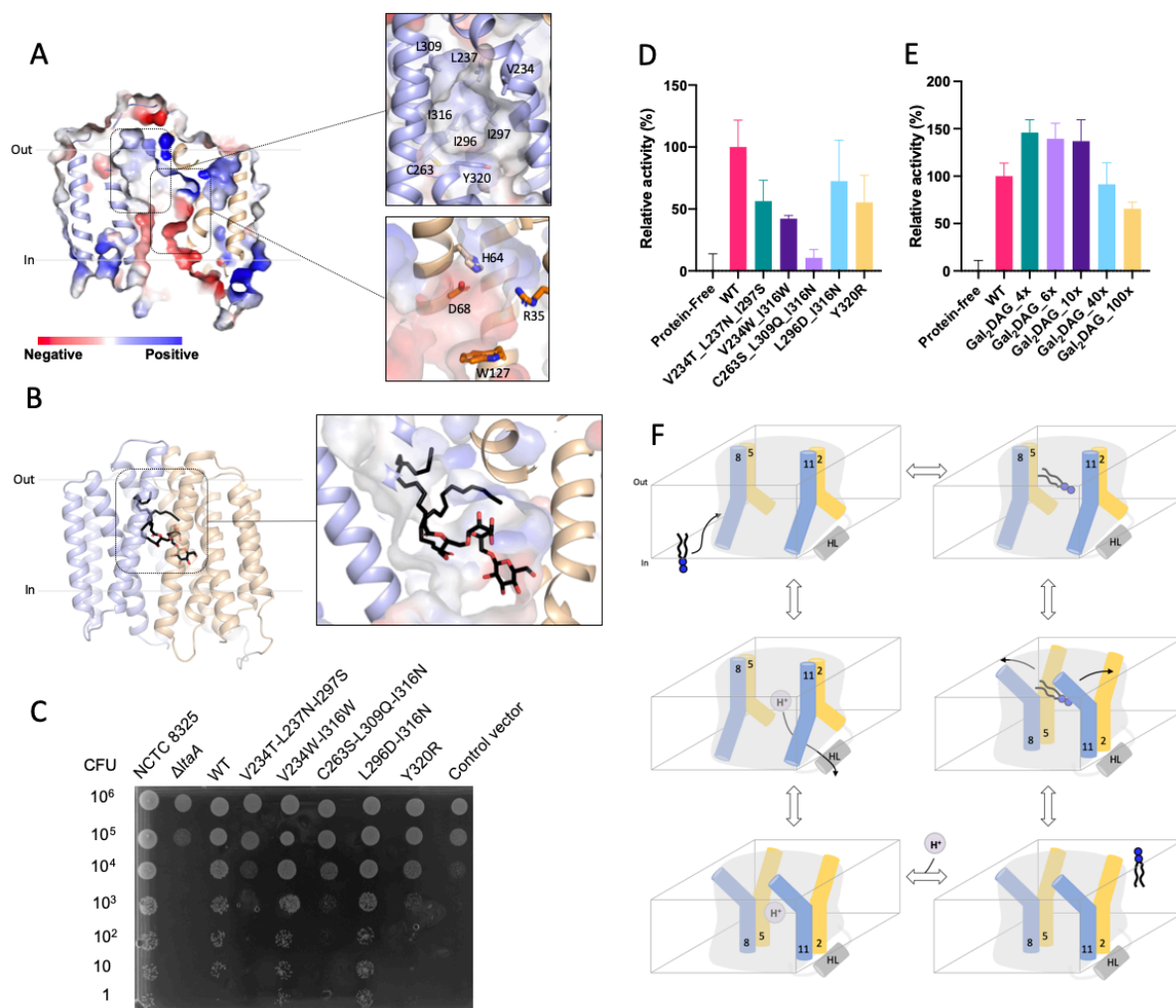


Figure 5. Hydrophilic and hydrophobic cavities participate in ‘trap-and-flip’ of lipids. **A.** Vacuum electrostatic surface representation of inward-facing model of LtaA. Residues forming the hydrophobic and hydrophilic pockets are shown. **b.** A model of a glycolipid molecule docked into the amphipathic cavity of LtaA. The lipid tail length corresponds to C16 chains. N-terminal and C-terminal domains are shown in light orange and light blue, respectively. **c.** *S. aureus* cell growth on LB agar plates containing 0.1 mM IPTG, buffered at pH 6.4. The $\Delta ltaA$ mutant is complemented with pLOW vector carrying a *ltaA*-WT gene or the annotated point mutations; Control vector indicates the pLOW vector carrying an unrelated gene (dCas9). **d.** Mutagenesis analysis of the hydrophobic pocket. Relative flipping activity of LtaA-WT and variants. Error bars show +/- s.d. of technical replicates, n=3. **e.** Headgroup selectivity analysis. Relative flipping activity of LtaA in the presence of different concentrations of digalactosyl-diacylglycerol (Gal₂DAG). Molar excess of Gal₂DAG over Glc₂-DAG-NBD is indicated. Error bars show +/- s.d. of technical replicates, n≥3. Source data are

provided as a Source Data file. **f.** Proposed mechanism of LtaA catalyzed glycolipid transport. Schematic of conformational states throughout LtaA transport cycle.

Supplementary materials

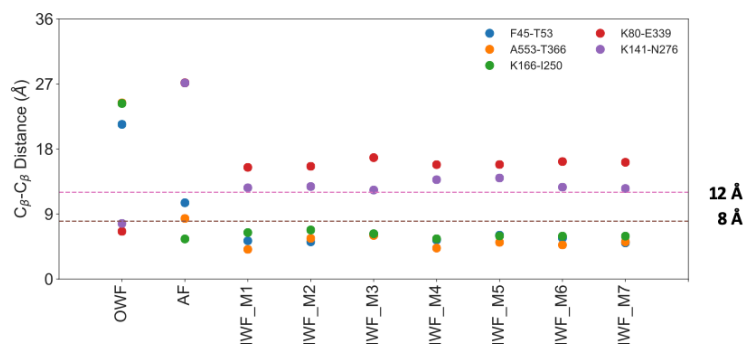
Evidence for a 'trap-and-flip' mechanism in a proton-dependent lipid transporter

Elisabeth Lambert, Ahmad Reza Mehdipour, Alexander Schmidt, Gerhard Hummer, Camilo Perez

*Correspondence should be addressed to C.P. (email: camilo.perez@unibas.ch)

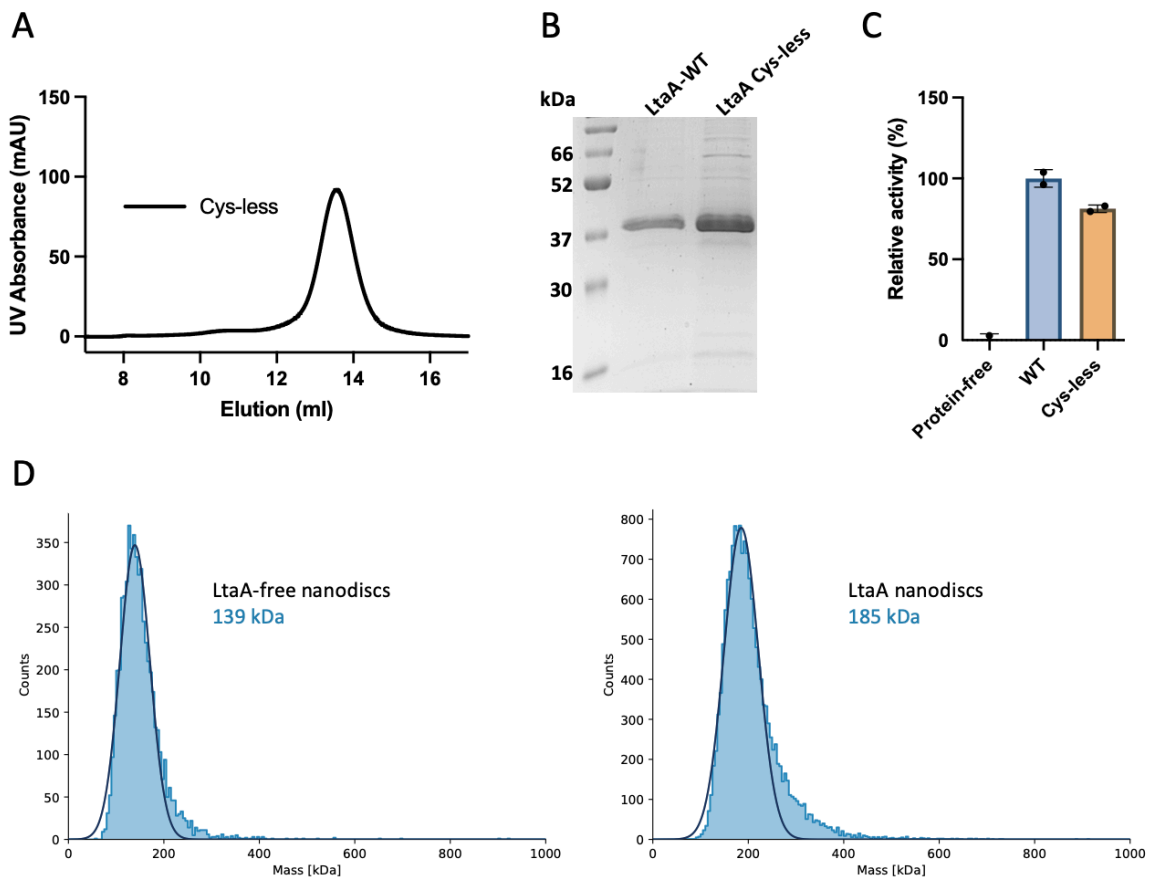
This PDF file includes:

Figs. S1 to S8
Tables S1 to S2

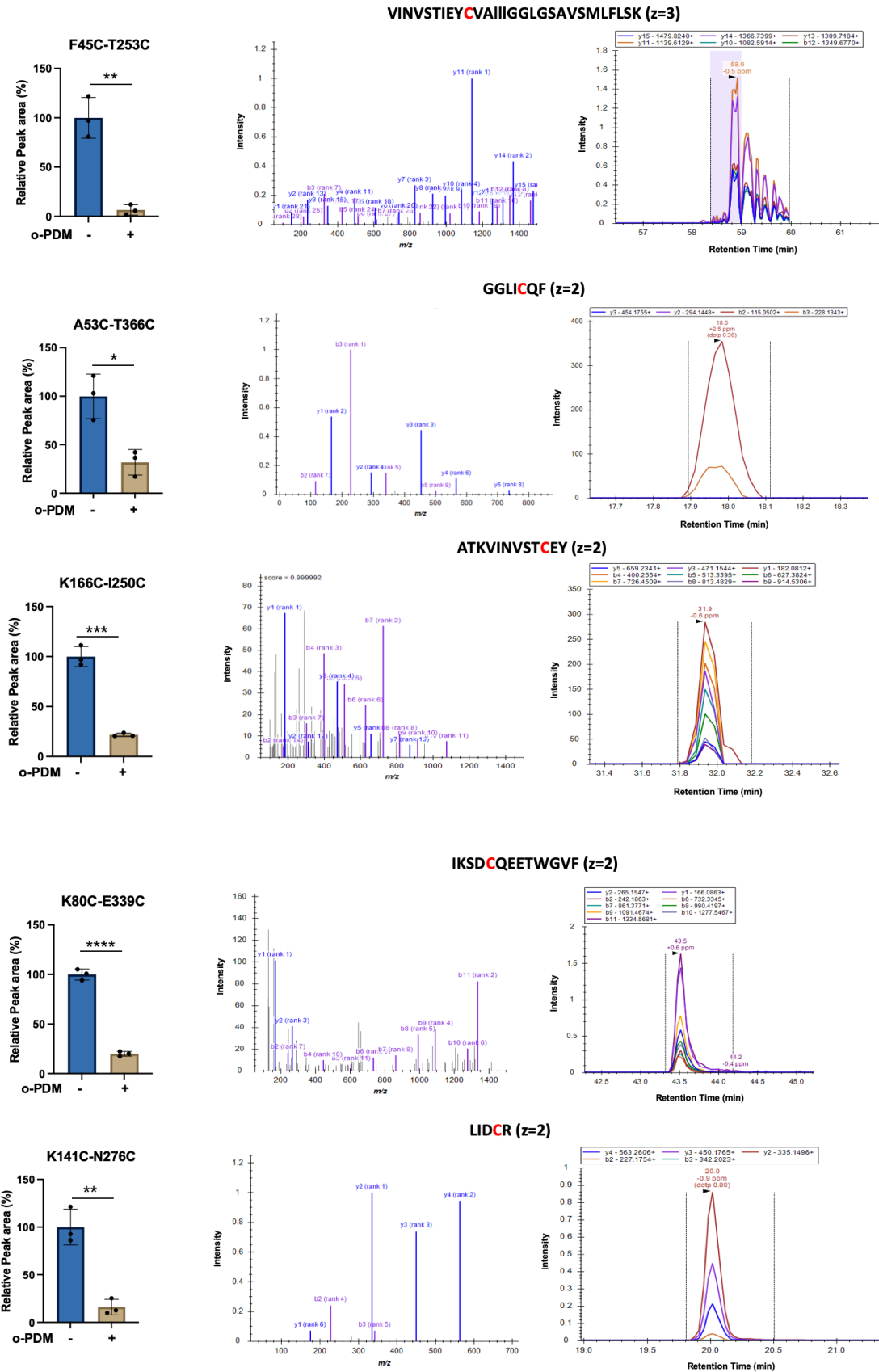


Residues	OWF	AF	IWF_M1	IWF_M2	IWF_M3	IWF_M4	IWF_M5	IWF_M6	IWF_M7
F45-T253	21.4	10.5	5.3	5.2	6.2	5.4	6.1	5.7	5.0
A53-T366	24.4	8.4	4.1	5.7	6.1	4.3	5.1	4.8	5.2
K166-I250	24.3	5.5	6.4	6.8	6.3	5.7	6.0	6.0	6.0
K80-E339	6.7	27.1	15.5	15.6	16.8	15.8	15.8	16.2	16.1
K141-N276	7.6	27.1	12.7	12.8	12.4	13.8	14.0	12.8	12.5

Supplementary figure 1. Distances between residues selected for cross-linking in alternating conformations of LtaA. C β -C β distances between residues selected for cysteine cross-linking in the outward-facing structure (OWF) and in the best inward-facing models (INW_M), and in the AlphaFold (AF) inward-facing model. Distance thresholds considered for selection of residues pairs are shown.

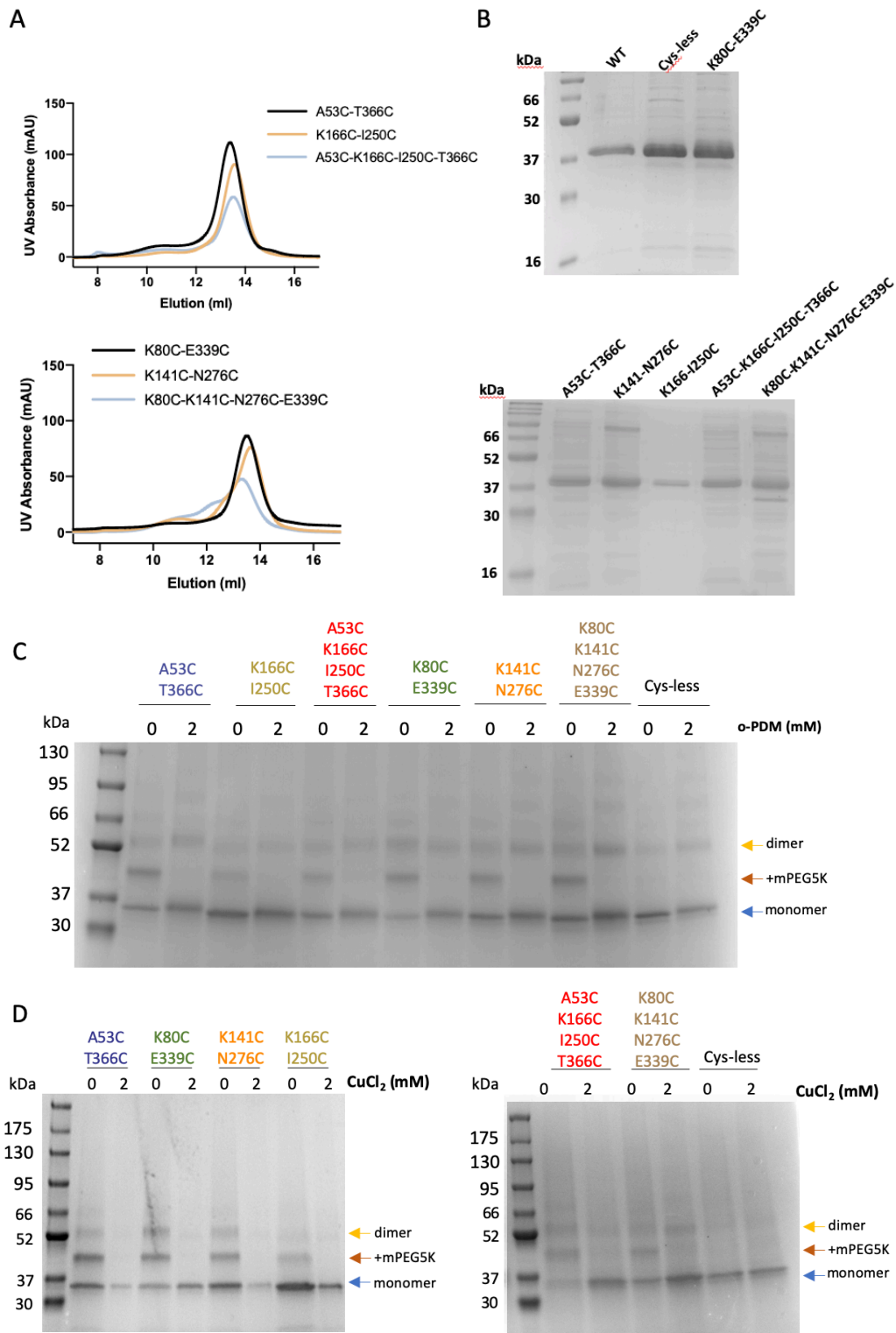


Supplementary figure 2. Analysis of LtaA wild-type and cysteine-less variant. **A.** Size Exclusion Chromatography profile of cysteine-less LtaA in a Superdex 200 Increase 10/300 GL column. **B.** SDS-PAGE of purified LtaA-WT and LtaA Cys-less. **C.** Relative flipping activity of LtaA Cys-less and LtaA-WT. Error bars show s.d. of technical replicates, $n \geq 3$. **D.** Mass photometry analysis of nanodiscs without LtaA (left) and LtaA-reconstituted nanodiscs (right). The approximate molecular mass averages from Gaussian distributions are shown. The resulting apparent molecular mass difference (LtaA mass) is 46 kDa.

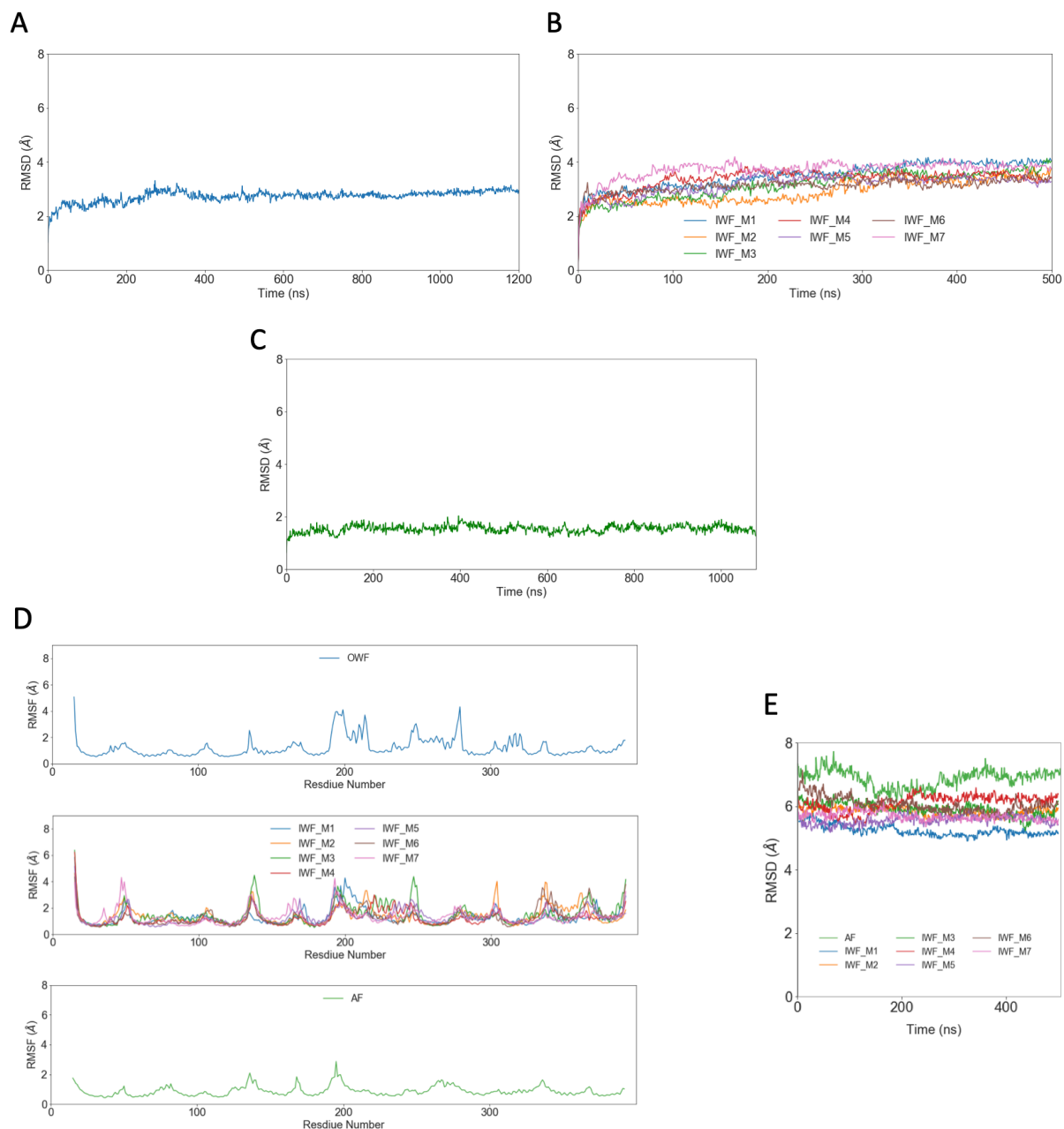


Supplementary figure 3. LC-MS analysis of cysteine cross-linking showing that LtaA adopts inward- and outward-facing states. Selected pairs of residues for cross-linking are shown in Fig. 2. *Left:* Relative abundance of cysteine containing peptides in absence (-) or presence (+)

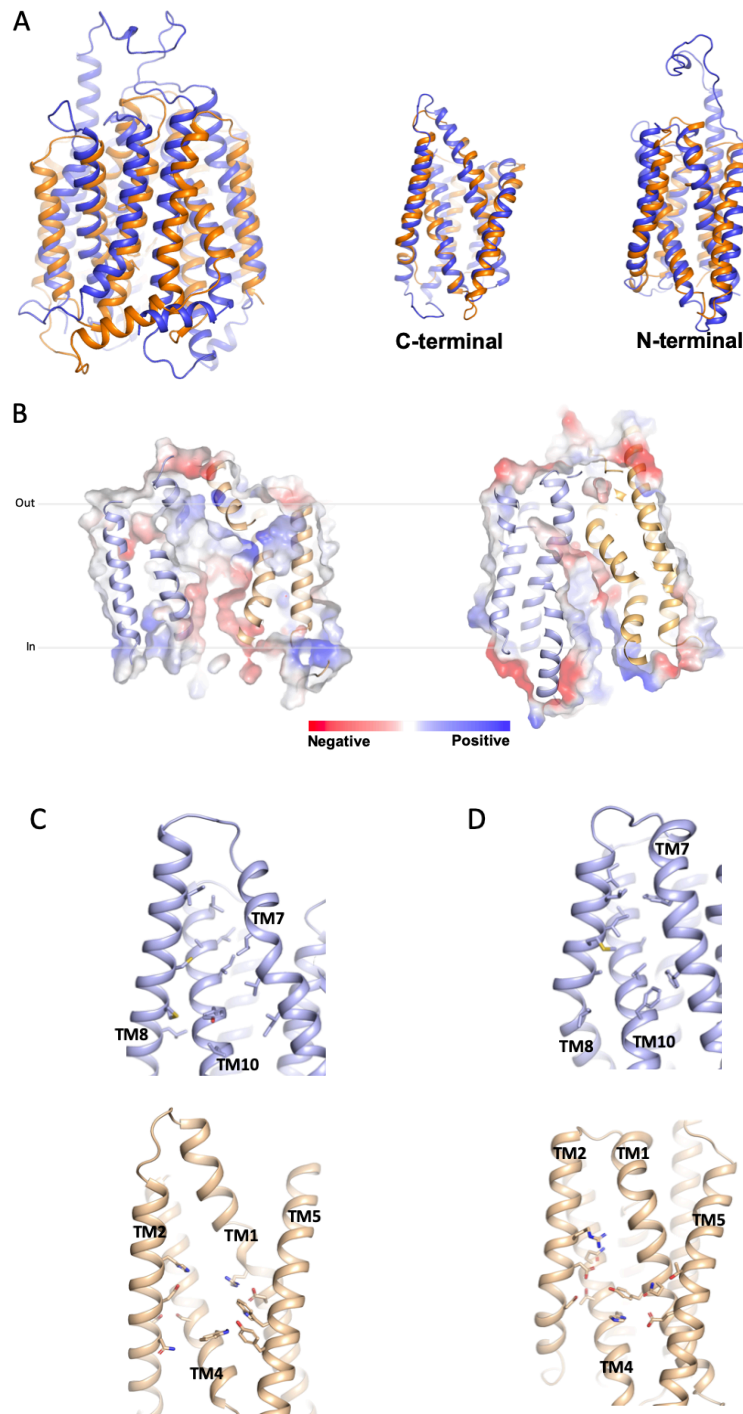
of N,N'-(o-phenylene)-dimaleimide (o-PDM). Error bars indicate s.d., $n \geq 3$. *: $P \leq 0.05$, **: $P \leq 0.01$, ***: $P \leq 0.001$, ****: $P \leq 0.0001$. *Center*: Assigned Collision-Induced Dissociation (CID) spectra obtained from cysteine containing peptides in absence of o-PDM. The position of the alkylated cysteine is indicated in red and the charge state (z) of the identified peptide ion is provided. *Right*: Elution profiles of the peptide fragments (transitions) identified used for peptide quantification by targeted LC-MS analysis. Source data are provided as a Source Data file.



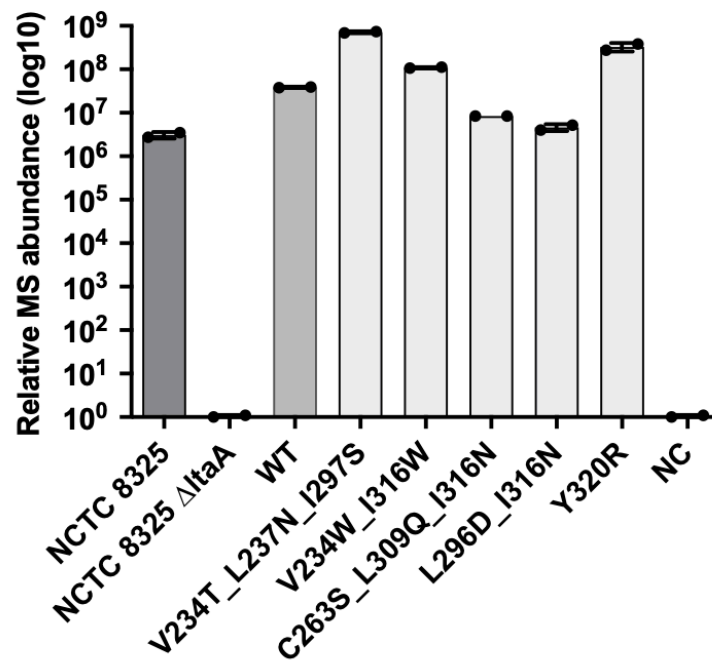
Supplementary figure 4. Purifications and cross-linking in-gel analysis of LtaA variants. A. Size Exclusion Chromatography profile of LtaA variants in a Superdex 200 Increase 10/300 GL column. **B.** SDS-PAGE of purified LtaA WT and variants. **C** and **D.** SDS-PAGE showing band shifts of samples treated with mPEG5K after cross-link with o-PDM or CuCl₂, respectively. SDS-PAGE experiments were independently repeated at least three times with similar results. Source data are provided as a Source Data file.



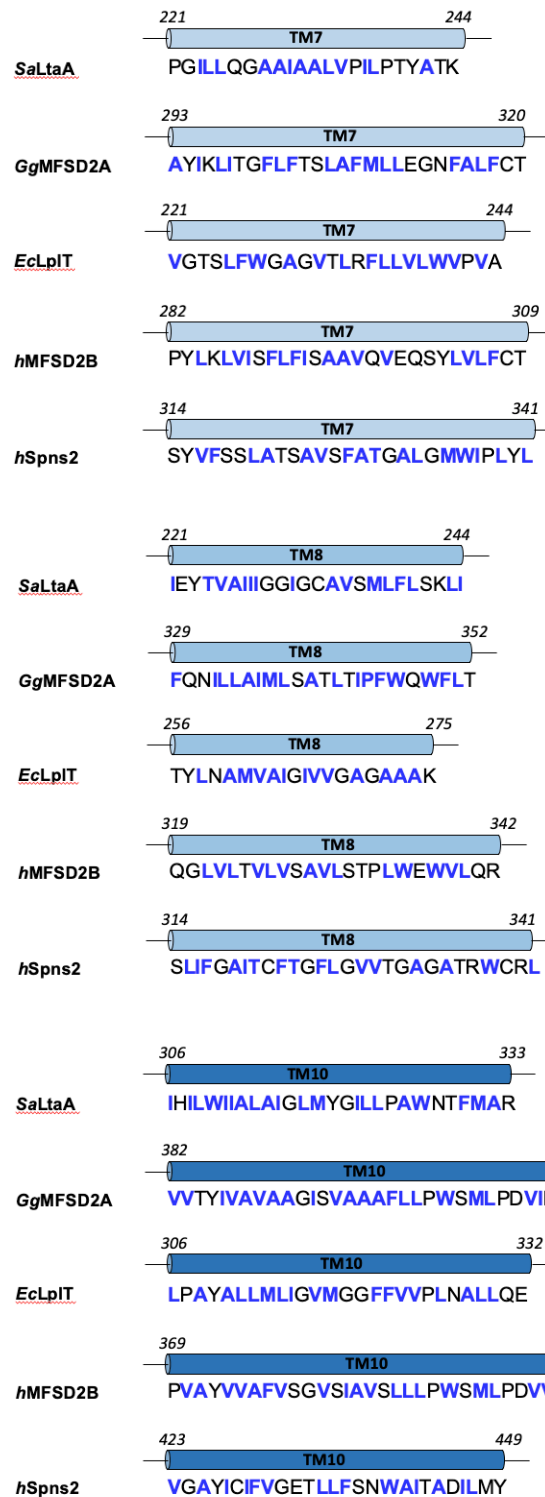
Supplementary figure 5. Stability analysis from molecular dynamics simulations of LtaA in a membrane. **A-C.** Root-mean-square-deviation (RMSD) plots of C α atoms relative to their starting points during MD simulations in a membrane composed of POG (65%), diacylglycerol (20%), cardiolipin (10%), and gentiobiosyl-diacylglycerol (5%). RMSD plots of C α atoms for outward-facing LtaA (**A**), inward-facing LtaA models obtained from the ‘repeatswap’ approach (IWF_M) (**B**), and the inward-facing LtaA model generated by AlphaFold (AF) (**C**) are shown. **D.** Root-mean-square-fluctuation (RMSF) plot of C α atoms for outward-facing (OWF) LtaA, ‘repeat-swap’ inward-facing LtaA models, and the inward-facing LtaA model generated by AlphaFold (AF), calculated for each MD simulation based on the average structure. **E.** RMSD plot of C α atoms of ‘repeat-swap’ inward-facing LtaA models and the AF inward-facing LtaA model during MD simulations relative to the outward-facing structure (PDB ID 6S7V).



Supplementary figure 6. Comparison of LtaA and MFSD2A fold and amphipathic cavity. A. Superposition of LtaA (orange) and MFSD2A (blue) (r.m.s.d = 4.1Å), and individual N- and C-terminal domains (r.m.s.d= 2.6Å and 2.8Å, respectively). **B.** Vacuum electrostatic surface representation of inward-facing model of LtaA (*left*) and inward-facing MFSD2A (PDB ID 7MJS) (*right*). Residues participating in formation of N- and C-terminal hydrophilic and hydrophobic pockets in LtaA (**C**) and MFSD2A (**D**). N-terminal and C-terminal domains are shown in light orange and light blue, respectively.



Supplementary figure 7. LC-MS analysis of relative abundance of LtaA-WT and variants in *S. aureus* membranes. The histogram shows relative abundances of LtaA WT and variants. Error bars show +/- s.d. of technical replicates (n=2).



Supplementary figure 8. C-terminal TM helices participating in formation of hydrophobic pockets in MFS lipid transporters. Residues in TM7, 8, and 10 as seen in the structures of *S. aureus* LtaA (PDB ID 6S7V) and *Gallus gallus* MFSD2A (PDB ID 7MJS), and residues in predicted helical segments corresponding to the same TMs in *E. coli* LpIT, *human* MFSD2B, and *human* Spns2 are shown. Hydrophobic residues are shown in blue.

Supplementary Table 1. Validation parameters of the top seven inward-facing models.
Initial: homology models from Modeler: *SCWRL*; the refined model by *SCWRL4*; *mini*: energy minimization of the model in a bilayer using Gromacs.

Model	Clashscore			MolProbity score			Ramachandran favoured (%)			Ramachandran outliers (%)		
	Initial	SCWRL	mini	Initial	SCWRL	mini	Initial	SCWRL	mini	Initial	SCWRL	mini
1	144.2	125.8	11.5	3.46	2.89	2.03	95.5	95.2	93.4	0.8	1.0	1.0
2	155.0	125.3	11.5	3.49	2.89	2.15	95.2	95.2	92.9	0.8	0.8	1.6
3	145.5	125.1	10.3	3.45	2.91	2.3	94.9	94.9	92.2	1.1	1.1	1.6
4	137.9	117.8	12.0	3.25	2.85	2.05	95.5	95.5	92.9	0.5	0.5	0.8
5	144.9	119.1	10.6	3.34	2.89	1.98	94.9	95.0	93.4	0.8	0.8	1.3
6	134.7	125.7	8.12	3.35	2.89	2.17	95.2	95.2	93.6	1.1	1.1	1.1
7	131.8	125.5	9.81	3.31	2.86	2.18	95.7	95.7	92.3	1.1	1.1	1.1

Supplementary Table 2. Oligo's used in this study. Mutagenesis is underlined

Oligo name	5'-3' sequence
Sa-Sall-FW	GAGAGTCGACGGTCATTCATCACAACC
Sa-V234T-L237N-FW	GGTGCCGCAATTGCTGCCCT <u>AA</u> CCCTATA <u>AA</u> TCCAACATATGCTACTAAGGTTAT
Sa-V234T-L237N-RV	ATAACCTTAGTAGCATATGTTGGATTTATAGGGTTAGGGCAGCAATTGCGGCACC
Sa-V234W-FW	GTGCCGCAATTGCTGCCCT <u>AG</u> CCTATATTACCAACATATGCTAC
Sa-V234W-RV	GTAGCATATGTTGGTAATATAGGCCATAGGGCAGCAATTGCGGCACC
Sa-C263S-FW	CATTATTGGTGGTATCGGCTCTGCAGTTTCGATGCTATTT
Sa-C263S-RV	AAATAGCATCGAACTGCAGAGCCGATACCACCAATAATG
Sa-L296D-FW	TCTAAGCGGATTTATTTTATACATGATAGATTTTTACTCTATCTATGATTGTTAATATTCACA
Sa-L296D-RV	TGTGAATATTAACAATCATAGATAGAGTAAAAAT <u>AT</u> CTATCATGTATAAAATAAATCCGCTTAGA
Sa-I297S-FW	GATTTATTTTATACATGATATTAAGTTTTACTCTATCTATGATTGTTAATATTC
Sa-I297S-RV	GAATATTAACAATCATAGATAGAGTAAAACTTAATATCATGTATAAAATAAATC
Sa-L309Q-I316N-FW	CTATGATTGTTAATATTCACAT <u>CCA</u> ATGGATTATCGCTTTAGCTAATGGTCTAATGTATGGCATCTTATTAC
Sa-L309Q-I316N-RV	GTAATAAGATGCCATACATTAGACCA <u>TT</u> AGCTAAAGCGATAATCCATTGGATGTGAATATTAACAATCATAG
Sa-I316N-FW	CTTGTGGATTATCGCTTTAGCTAATGGTCTAATGTATGGCATCTTATTAC
Sa-I316N-RV	GTAATAAGATGCCATACATTAGACCA <u>TT</u> AGCTAAAGCGATAATCCACAAG
Sa-I316W-FW	CTTGTGGATTATCGCTTTAGCTTGGGGTCTAATGTATGGCATCTTATTAC
Sa-I316W-RV	GTAATAAGATGCCATACATTAGACCCCAAGCTAAAGCGATAATCCACAAG
Sa-Y320R-FW	TTAGCTATCGGTCTAATG <u>CG</u> TGGCATCTTATTACCAGCATG
Sa-Y320R-RV	CATGCTGGTAATAAGATGCC <u>AC</u> GCATTAGACCGATAGCTAA
LtaA-NotI-RV	GAGAGCGGCCGCAATAGTATTGTTAATCGTAGTATGTTTGAATTAATAAGA
F45C-FW	GAGCTACATTA <u>ACTGT</u> CTGCCACCG
F45C-RV	CGGTGGCAGACAGTTAATGTAGCTC
A53C-FW	CCGTGACATCGATT <u>GT</u> GTGCTATTACATC
A53C-RV	GATGTAATAGCGACACA <u>AA</u> TTCGATGTCACGG
K80C-FW	CGTTATCGGCTTCTTATTATGTAAGTTTGGAACTAAGATC
K80C-RV	GATCTTAGTTCCAACTT <u>ACA</u> TAAATAAGAAGCCGATAACG
K141C-FW	GAGGATAAACCGCGGCTGTC <u>AA</u> TGGGCTACGTG
K141C-RV	CACGTAGCCATTTG <u>AC</u> AGCCGCTTTATCCTC
K166C-FW	CTTTATGAATTTGCTGATC <u>GT</u> GTTTCATCCTACTCGCTTCG
K166C-RV	CGAAGCGAGTAGGATGAAC <u>AC</u> AGATCAGCAAATTCATAAAG
I250C-FW	CAAAAGTCATTAATGTATCAACG <u>TG</u> TGAATATACCGTGGCTATTATC
I250C-RV	GATAATAGCCACGGTATATTCA <u>CAC</u> GTTGATACATTAATGACTTTTG
T253C-FW	GTATCAACGATTGAATATTG <u>TG</u> TGGCTATTATCATCGGCGG
T253C-RV	CCGCCGATGATAATAGCCAC <u>ACA</u> AATTTCAATCGTTGATAC
C263S-FW	CGGCGGCATTGGATC <u>G</u> GCCGTTAGTATGTTG
C263S-RV	CAACATACTAACGGCCGATCCAATGCCGCCG
N276C-FW	CTTAGTAAGTTGATCGACTG <u>CC</u> GTTTCGCGTAACTTTATGTAC
N276C-RV	GTACATAAAGTTACGCGAACGGC <u>AG</u> TCGATCAACTTACTAAG
E339C-FW	GCTTCATCAAGAGCGACTGTCAAGAGGAGACCTGG
E339C-RV	CCAGGTCTCCTCTTG <u>AC</u> AGTCGCTCTTGATGAAGC
T366C-FW	GTTTGGCGGATTGATTTG <u>CC</u> AGTTCACCAAC
T366C-RV	GTTGGTGA <u>ACTGG</u> CAAATCAATCCGCCAAAC
LtaA-V234T-L237N-FW	GATTGCGGCTTTGACTCCTATCAACCTACGTATGCCACA
LtaA-V234T-L237N-RV	TGTGGCATACGTAGGGTTGATAGGAGTCAAAGCCGCAATC

Evidence for a 'trap-and-flip' mechanism in a proton-dependent lipid transporter

LtaA-V234W-FW	GATTGCGGCTTTGTGGCCTATCCTGCCTAC
LtaA-V234W-RV	GTAGGCAGGATAGGCCACAAAGCCGCAATC
LtaA-C263S-FW	GCGGCATTGGATCGGCCGTTAGTATG
LtaA-C263S-RV	CATACTAACGGCCGATCCAATGCCGC
LtaA-L296D-FW	GGTTTTATTCTGTATATGATTGATATCTTCACGTTGTCTATG
LtaA-L296D-RV	CATAGACAACGTGAAGATATCAATCATATACAGAATAAAACC
LtaA-I297S-FW	TTATTCTGTATATGATTCTTAGTTTCACGTTGTCTATGATTGTC
LtaA-I297S-RV	GACAATCATAGACAACGTGAAACTAAGAATCATATACAGAATAA
LtaA-L309Q-FW	GTCAACATCCATATCCAATGGATTATTGCCTTGG
LtaA-L309Q-RV	CCAAGGCAATAATCCATTGGATATGGATGTTGAC
LtaA-I316N-FW	TGCCTTGGCGAACGGCCTGATG
LtaA-I316N-RV	CATCAGGCCGTTCCGCAAGGCA
LtaA-I316W-FW	ATTATTGCCTTGGCGTGGGGCCTGATGTAT
LtaA-I316W-RV	ATACATCAGGCCCCACGCCAAGGCAATAAT
LtaA-Y320R-FW	GATCGGCCTGATGCGTGGGATTCTGTTGCCA
LtaA-Y320R-RV	GATCGGCCTGATGCGTGGGATTCTGTTGCCA

4. Further characterization of the amphiphilic cavity

4.1 The hydrophilic N-terminal pocket is specific for a disaccharide anchor headgroup

As described before, synthesis of the Glc₂-DAG starts with the addition of two glucose moieties to the diacylglycerol (DAG) by the glycosyltransferase YpfP. However, YpfP is not only able to perform the addition of 2 glucose residues, but occasionally generates side products as well, by addition of only one or three glucose residues to the DAG^{63,75}. During the preparative thin layer chromatography (TLC) that we used for preparation of the nitrobenzoxadiazole (NBD)-Glc₂-DAG, we detected NBD-DAG, NBD-Glc-DAG, NBD-Glc₂-DAG, NBD-Glc₃-DAG species after visualization under a fluorescence scanner (Fig 4.1a). To further characterize the N-terminal pocket, we wanted to test if LtaA is capable of flipping NBD-Glc-DAG, NBD-Glc₃-DAG as well, or if it's specific for NBD-Glc₂-DAG, as found in the native glycolipid. We extracted all three species, and incorporated them into empty liposomes, and LtaA-proteoliposomes, and performed flipping assays (Fig. 4.1b). If LtaA has a high specificity for the NBD-Glc₂-DAG, we expected that proteoliposomes incorporated with NBD-Glc-DAG, and NBD-Glc₃-DAG will behave the same way as in the absence of LtaA. Indeed, our experimental data shows that only in the presence of LtaA and NBD-Glc₂-DAG there is flipping, whereas the flipping of NBD-Glc-DAG and NBD-Glc₃-DAG is lower. This result indicates that LtaA shows higher specificity for accommodating a two-sugar headgroup within its N-terminal hydrophilic pocket. Less sugar units most likely have not enough interactions with the residues in the pocket, whereas a three-sugar headgroup is probably too bulky, and cannot accommodate within the pocket.

These results are similar to the Gal₂-DAG assay in chapter 3 (Fig. 5E), showing that an intact headgroup is required for substrate binding and transport. Our results show that not only the nature of the sugar is important for substrate recognition, as well as the number of sugars. The headgroup dictates thus if the glycolipid is a substrate for LtaA or not.

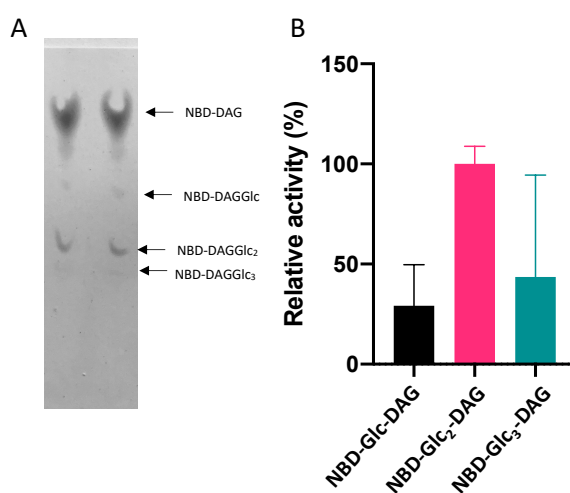


Figure 4.1: Headgroup recognition of LtaA. A. Fluorescence scan of thin layer chromatography (TLC) containing different species. B. Normalized relative flipping activity with NBD-Glc-DAG, NBD-Glc₂-DAG and NBD-Glc₃-DAG. Error bars show s.d. of technical replicates (n ≥ 3).

4.2 LtaA has a preference for Glc₂-DAG with longer lipid lengths

If the C-terminal part of the cavity is necessary for correct translocation of the glycolipid, we hypothesized that there could be a preferred length of the lipid tail, that fits in the C-terminal pocket. It was also shown for MFSD2A and LpIT to display a relaxed selectivity towards the length of the aliphatic chains^{184,223}. We performed flipping assays with LtaA-WT proteoliposomes, in which next to the NBD- Glc₂-DAG, we also incorporated a five-fold excess of DAG or Glc₂-DAG of different lengths as well. This way, we wanted to examine if there is a difference in flipping activity of the NBD-Glc₂-DAG, which would indicate that the lipids or glycolipids compete with the NBD-Glc₂-DAG for LtaA flipping. As expected, the DAGs of different lengths, did not have any a substantial influence on flipping of the NBD-Glc₂-DAG (fig 4.2), as they don't need the energy of a transporter to translocate to the other side of the membrane.

When we compared the activity in the presence of Glc₂-DAG, the relative activity of NBD- Glc₂-DAG remains stable compared to the sample only containing NBD-Glc₂-DAG (indicated as WT), except for Glc₂-DAG with lipid length of C16 that has a relative activity of 250% (fig 4.2). This increase in relative activity is remarkable, as there is an increase in activity and not a decrease as expected. These results suggest that LtaA activity might not only be driven by a pH gradient, but also by a concentration gradient. It could be the case that the activity also increases when a higher amount of Glc₂-DAG is present in the *S. aureus* membrane.

Furthermore, it seems that LtaA has a preference for Glc₂-DAG with longer lipid lengths, as only in the presence of C16 Glc₂-DAG an increase was observed. The *S. aureus* membrane is rich in lipids with chain lengths of C15 to C18⁷⁷. The C-terminal hydrophobic cavity is probably adapted for lipids with longer lengths, although it displays a relaxed specificity towards the length, since there is observable translocation of the NBD-Glc₂-DAG which has an acyl length of C10.

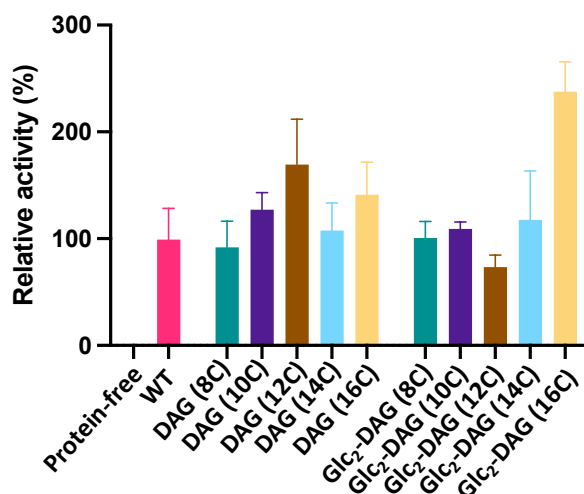


Figure 4.2: Flipping activity in presence of DAG and Glc₂-DAG with different lengths of lipid tails. A five-fold excess of DAG or Glc₂-DAG was added. Error bars show s.d. of technical replicates (n≥3).

5. Discussion

Elucidation of LtaA structure showed the architecture of an MFS flippases for the first time. The functional analysis, which identified LtaA as a proton coupled flippases, constituted also a novelty to the transporters field. Besides MurJ¹³⁴, LtaA is the second characterized secondary flippase. The structure of LtaA showed the canonical MFS fold, similarly as observed for other MFS transporters¹⁰⁹. The cavity was observed to be of an amphiphilic nature, containing a hydrophilic N-terminal domain and a C-terminal hydrophobic domain. This was the first time that such an amphiphilic cavity was observed for MFS flippases, although an amphipathic cavity was observed in the fucose transporter FucP¹⁶⁶, and an electrostatic different cavity was noticed in the peptide transporter YbgH²¹⁹. This is remarkable since MFS transporters are thought to be originated due to internal duplications¹⁵⁵, and suggest that LtaA originates from a heterologous duplication, in which the cavity is adapted for its respective substrate. This amphiphilic state was later observed in the inward-facing model as well.

LtaA was identified to be a proton-coupled antiporter. In particular, E32 was identified as the residue responsible for proton-transport. As for other MFS transporters, this residue lays on TM1, in close contact with the substrate binding site^{168,200,227}. In the substrate binding pocket E32 interacts with other polar residues (R35, D68, W127, W150), which are responsible for accommodating the polar sugar headgroup in the pocket. These residues are most likely also responsible for accommodation of the pKa of E32, shifting it from its theoretical value (pKa 4.25) to a pKa -value of 7.8, accommodating better to physiological pH. In the inward-facing model, these contacts remain close as well. In an outward-facing conformation E32 is in close contact with R35, pointing towards each other, presumably forming a salt-bridge. Protonation of E32 may disrupt the salt-bridge leading to conformational changes to an inward-facing state, followed by substrate loading. The disruption of this salt-bridge could be the driving force for conformational changes from an outward-open to an inward-open conformation.

In the MFS-model transporter LacY, translocation of lactose and a proton is tightly coupled, as one is not translocated without the other²¹⁴. First a proton will bind, which makes it possible for the substrate to bind in the pocket. Substrate binding is then followed by conformational changes to a cytosolic-open conformation, where the substrate is released. This is then followed by deprotonation, leading to conformational changes to an outward-open conformation. A different mechanism is shown for the MFS drug- antiporter MdfA¹⁶⁰. Substrate-bound deprotonation at the cytoplasmic side is followed by thermodynamically favoring conformational changes towards an outward-open state. At the extracellular side, the substrate will then leave the pocket, followed by protonation inducing conformational changes to an inward-open conformation. As LtaA is an antiporter, it is more likely that its mechanism will be more similar to the MdfA mechanism than the LacY mechanism. On the contrary, crystal-structures together with biochemical data of ABC lipid exporters, suggest a

low energy and high substrate affinity inward-open state, and an ATP-mediated high energy and low substrate affinity outward-open state^{129,145,146,228,229}.

In general, MFS transporters are thought to use the induced transition fit model for transport catalysis²³⁰. In this theoretical model, the energy barrier for conversion is lowered by the substrate binding. The fundamental difference with classical enzymes is that in this case the transition state is the activation energy barrier for global conformational changes for transporters instead of catalysis of the substrate. However, the energy landscape of the flippases most likely differs to the ones of soluble substrate transporters. ABC transporters translocating lipids were shown to use between 8.49 and 781.25 ATP molecules to flip one reporter lipid²²⁹. Probably, LtaA uses more than one H⁺. The details on how this would work using the alternating access mechanism for transport has to be investigated, although it was shown for the MDR-MFS antiporters LmrP, NorA and QacA to operate with a electrogenic drug/nH⁺ (with n ≥ 2) transport mode²³¹.

We observed during *in vitro* flipping assays still transport, even in the absence of a proton-gradient. Likewise, the mutant E32A remained to have a basic activity, which is comparable to the activity in the absence of a proton-gradient. So next to proton-transport, there must be at least one additional mechanism contributing to the transport of glycolipid across the cell membrane. One possible explanation is the concentration gradient created by the glycosyl transferase YpfP on the cytoplasmic leaflet. YpfP will synthesize Glc₂-DAG on the cytoplasmic side of the leaflet^{63,75}, after which Glc₂-DAG is translocated to extracellular side by LtaA. At the extracellular side of the membrane the LTA synthase LtaS will continue with the addition GroP residue creating LTAs⁷⁸, leading to the removal of Glc₂-DAG creating a concentration gradient. A predicted MFS flippase, the bacterial lysophospholipid transporter LpIT, has been shown to use the concentration gradient as its energy-source¹⁸³. Besides, the Lipid II flippase MurJ requires a membrane-potential, together with sodium-coupled transport^{144,232}, showing the possibility of more than one energy source necessary for lipid transport in secondary transporters.

We have shown that gentiobiose is an inhibitor for LtaA activity *in vitro*. However, neither in the presence of other disaccharides, nor in the presence of Gal₂-DAG, any effect was observed during *in vitro* flipping assays. This led us to conclude that the sugar headgroup of the Glc₂-DAG dictates the substrate specificity. Remarkably, YpfP can't use galactose as a substrate for synthesis of the glycolipid either⁷⁵, nor is Gal₂-DAG a substrate for LtaS⁹¹. This triple protection mechanism indicates the importance of the gentiobiosyl headgroup of LTAs. It was shown that LTA immediately synthesized on DAG lipids, leads to different cell morphologies⁹³. Our preliminary results show that Glc-DAG is not a substrate for LtaA neither. Moreover, Glc-DAG, is not a substrate for LtaS neither⁹¹. Not only, the nature of the sugars, as well as, the number of sugars seems to be important, highlighting the importance of correct formation of the

gentiobiosyl headgroup of LTAs. The high selectivity for the gentiobiosyl-headgroup provides a foundation for drug design of antimicrobials targeting LtaA.

LtaA was identified as a 'pH sensing' flippase, since it increases the Glc₂-DAG transport under low pH conditions, enlarging the population of LTA at the outer leaflet of the plasma membrane (Chapter 2, fig 5c). This enlarged population of LTA contributes to the survival of *S. aureus* under acidic conditions. Besides the already known functions of LTA in cell growth, cell stability, virulence and cell division³⁸, increased amounts of LTA in the cell wall might provide an efficient way to buffer against acidification due to the negative charge of the LTA backbone polymer. Moreover, it was shown that D-alanylation of LTA, which plays an important role in autolysis, cation homeostasis, host cell adhesion and invasion, biofilm formation and virulence⁵², is more stable at lower pH²³³. Through multiple protective measures against acidic conditions, *S. aureus* enables survival in their slightly acidic natural environment, the skin and nasopharynx of the human host^{2,3}. Remarkably, *S. aureus* is able to adapt to acidic pH of phagolysosomes, and can even replicate within them²³⁴⁻²³⁷, hereby evading critical host defense mechanisms central in the immune responses²³⁸. By enlarging the LTA population, the 'pH sensing' flippase LtaA contributes to immune evasion of the host, additional to survival in slight acidic environments.

During this project, two structures of the mammalian lysophosphatidylcholine docosahexaenoic acid (LPC-DHA) transporter MFSD2A, an inward-facing structure of *Gallus gallus*, and outward-facing structure of the mouse orthologue, were solved by cryo-EM^{152,153}. Regardless of different lipid substrates, a distinct composition of bacterial and eukaryotic membranes, opposite vectorial lipid transport direction (LtaA is an exporter, whereas MFSD2A is an importer) and different ion-energy sources, LtaA and MFSD2A also share multiple architectural similarities. Both proteins demonstrate the canonical MFS fold of 12 TM helices, and a central amphiphilic cavity, with an N-terminal hydrophilic cavity and C-terminal hydrophobic cavity. A computational model of the bacterial lysophospholipid transporter LpIT has predicted to contain a similar arrangement of residues²²³. Most likely, this arrangement of residues is shared between all predicted MFS flippases (Chapter 3, Suppl. Fig.8)^{186,187,239}.

MFSD2A, LpIT and LtaA have been shown to display a strong selectivity for their headgroup. In the case of MFSD2A zwitterionic charge of the phosphatidylcholine headgroup is necessary for selectivity towards the substrate¹⁸⁴, while LpIT was shown to transport lysophosphatidylethanolamine (LPE) and lysophosphatidylglycerol (LPG), but not lysophosphatidylcholine (LPC) and lysophosphatidic acids (LPA), despite that both LPE and LPC are both zwitterionic lipids sharing a quaternary amine head group²²³. LtaA selects its substrate based on the gentiobiosyl-headgroup, and is extremely selective to the nature of the sugars (galactose vs glucose), the bond between the disaccharide (gentiobiose vs trehalose) and the number of sugars.

Although MFSD2A and LpIT have been shown to be strongly selective for lysophospholipids, both of them demonstrate a flexibility towards the length of the lipids. MFSD2A has been demonstrated to transport different LPCs, if they have a acyl chain of C14 or longer¹⁸⁴. Remarkably, *in silico* docking of lysophospholipids with different lengths of acyl chains into LpIT, suggest a role of longer acyl chains in maintaining the selectivity of LPE/LPG versus LPC²²³. The authors suggest that longer acyl chains enhance the structural hindrance of the PC group. *S. aureus* membranes are rich in Glc₂-DAG containing C15 to C18, with the most dominant species C18:C15⁷⁷. The variability among these different Glc₂-DAG in *S. aureus* together with the observation that the relative activity remains stable in the presence of Glc₂-DAG with different lengths shows that LtaA most likely has a similar flexibility towards the lipid length. This is supported by the fact that we can observe active transport activity of the NBD-Glc₂-DAG containing a C10 acyl length. Although LtaA is flexible of translocating lipids with different lengths, it still has a preference for lipids with longer aliphatic chains.

On the extracellular side of MFSD2A, ordered extracellular loops are observed. One of these loops, reaches across the interface of the two domains, and is stabilized by a disulfide bridge with a residue on another loop. Mutating the residues responsible for the disulfide bridge to alanine substantially reduced the transport, suggesting the importance of the stability of this loop¹⁵³. This loop lays in front of extracellular side of the lateral opening between TM5 and TM8 (fig. 5.1a), which was proposed to be the entry side for LPC, based on electron density observed within the structure and mutagenesis analysis of the lateral entry sides¹⁵³. Our molecular dynamics (MD) simulations together with the results from the cysteine trapping assays, suggest that the cytoplasmic lateral opening between TM2 and TM11 is more relevant than the lateral opening between TM5-TM8 for entry of the Glc₂-DAG within the amphiphilic pocket of LtaA. This entry however, is blocked by the helical loop connecting the N-terminal and C-terminal domains (fig. 5.1b). The extracellular loop of MFSD2A and helical loop of LtaA both provide steric hindrance at the entry point of the lipid. It could be that they are important for substrate recognition and selectivity of the lipids that enter into the central cavity, although there are no reports showing an important role in substrate recognition for the helical loop of MFS transporters with soluble substrates. The importance of this hindrance remains to be investigated in the future. Remarkably, the other lateral side is shown to be important for MFSD2A and LtaA suggesting a mirroring effect. As MFS transporters are thought to be originated due to internal duplications¹⁵⁵, it is possible that TM2 and TM8, as well as TM5 and TM11 carry out similar functions.

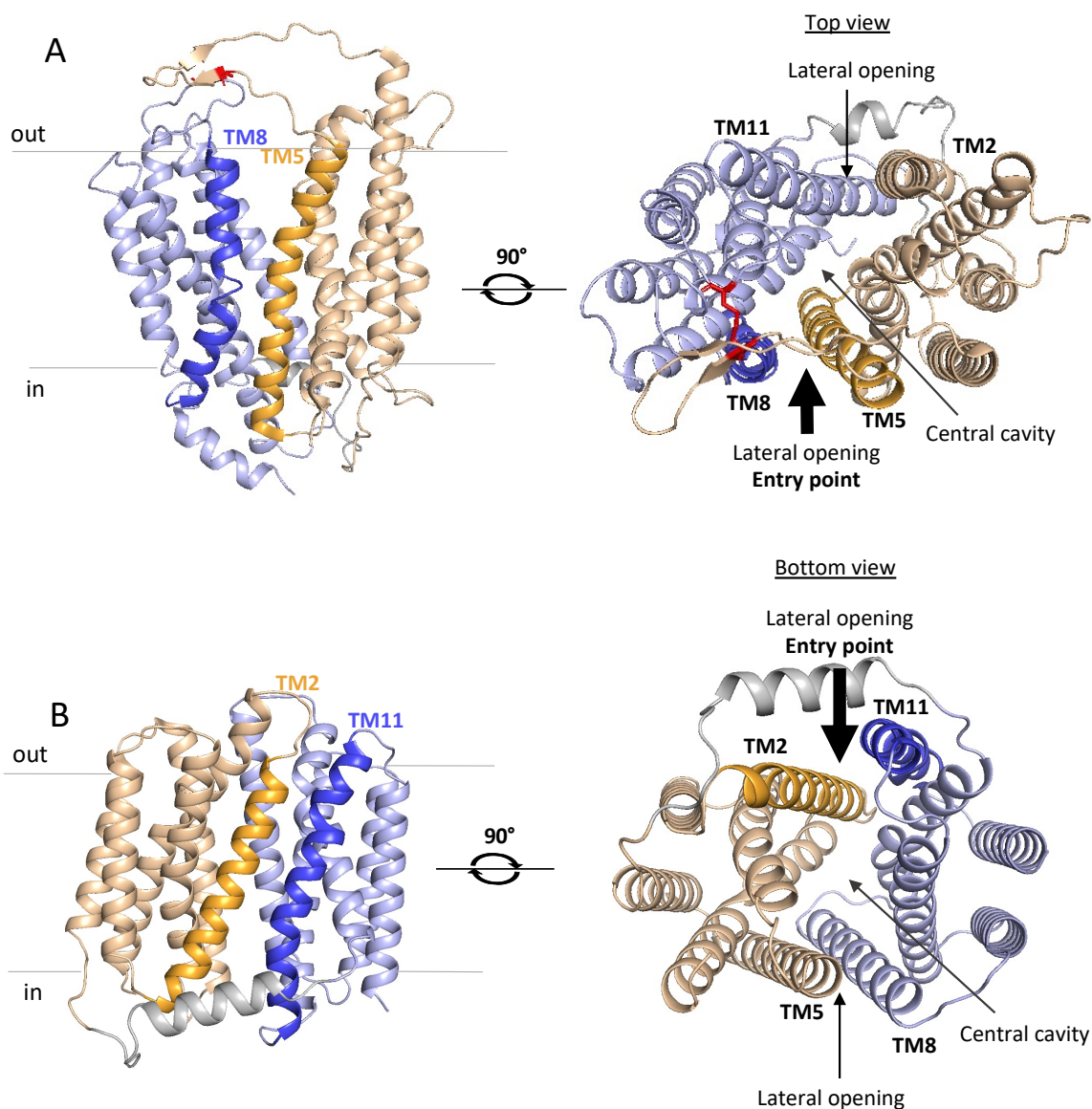


Figure 5.1: Lateral openings of MFSD2A (A) and LtaA (B). A. Outward-open structure of MFSD2A (PDB-ID 7N98)¹⁵³ B. Inward-facing model of LtaA. The N-terminal and C-terminal domain are colored in light orange and light blue respectively, the connecting helical loop is colored in grey, the connecting disulfide bridge is colored in red.

Our MD simulations, showed an asymmetric opening between the lateral openings at the cytosolic side. As mentioned above this lateral opening could be the result of the asymmetric loading of the lipid substrate. Cater *et al.* proposed an asymmetric opening as well, due to the disulfide bridge at extracellular side of MFSD2A, and therefore propose that MFSD2A uses an adapted version of the classical rocker-switch mechanism¹⁵². A similar mechanism was proposed for the MDR-MFS transporter MdfA which has lipophilic substrates²⁴⁰. This asymmetric opening as a result of the disulfide bridge in MFSD2A leads to narrower opening of the extracellular side to the cavity, whereas the cytoplasmic lateral opening is wider¹⁵². Our crystal structure shows wide extracellular openings, while the inward-facing model suggest

narrower cytoplasmic openings. These space-constraints into the cavities on the side where the lipid substrate is recruited, might be participating to substrate selectivity.

The similarities in central amphiphilic cavity, the strong recognition of the headgroup, and asymmetric openings of the lateral entry sides point towards the assumption that LtaA and MFSD2A use a common mechanism of lipid translocation, that could be shared between all MFS flippases. Sequence analysis of other proposed MFS flippases shows that their cavity could possess a similar amphiphilic nature (Chapter 3, Suppl. Fig. 8).

We demonstrate with both *in vitro* flipping assays, as *in vivo* cell growth that both the N-terminal pocket as the C-terminal hydrophobic pocket are relevant for transport of the Glc₂-DAG. On top, we show that alternating-access is essential for transport showed by the disruption of transport in cross-linked variations of LtaA, and provide evidence by MD simulations that the entire Glc₂-DAG enters and leaves the transport pathway. These results strongly suggest that LtaA uses a 'trap-and-flip' mechanism, in which the whole lipid is captured from the membrane, completely enclosed within the substrate cavity and is then released to the other side of the membrane, similar to what has been shown for the lipid A transporter MsbA¹²⁹, human phosphatidylcholine transporter ABCB4¹⁴⁵ and the human multidrug exporter P-glycoprotein¹⁴⁶. Similar to other structures, the inward-facing MFSD2A structure shows the LPC tail bound into the C-terminal hydrophobic cavity (fig 5.2)¹⁵², providing direct evidence for a 'trap-and-flip' mechanism. Per contra, the authors of the outward-facing MFSD2A structure, propose a more 'credit-card' mechanism in which the LPC tail remains into the membrane, similar to lateral entry mechanism of the phospholipid and cholesterol transporter ABC transporter ABCA1¹⁵⁰, P4-ATPases¹³³ and the RND multidrug efflux pump AcrB²⁴¹. As these two papers were simultaneously undergoing the review process, these two views were not compared. A more thorough investigation of MFSD2A could answer this question. Nevertheless, our data supports the 'trap-and-flip' model of the inward-facing model.

Taken all experimental results of this project into account, an LtaA flipping mechanism was proposed (fig. 5.3). (1): Glc₂-DAG will get recognized by LtaA in an inward-open conformation via its gentiobiose headgroup. The substrate will be loaded into the central cavity through the lateral opening between TM2-TM11. (2) The gentiobiose headgroup will accommodate into the hydrophilic N-terminal pocket, while the DAG lipid tails enter in the hydrophobic C-terminal cavity. (3) Binding of the substrate will lead to conformational changes to an outward-open conformation. At the extracellular side of the membrane, Glc₂-DAG is released from the cavity via both lateral exits, TM2-TM11 or TM5-TM8. (4) After substrate release, (5) E32 will get protonated leading to conformational changes to an inward-facing conformation. (6) After deprotonation, a new cycle will start.

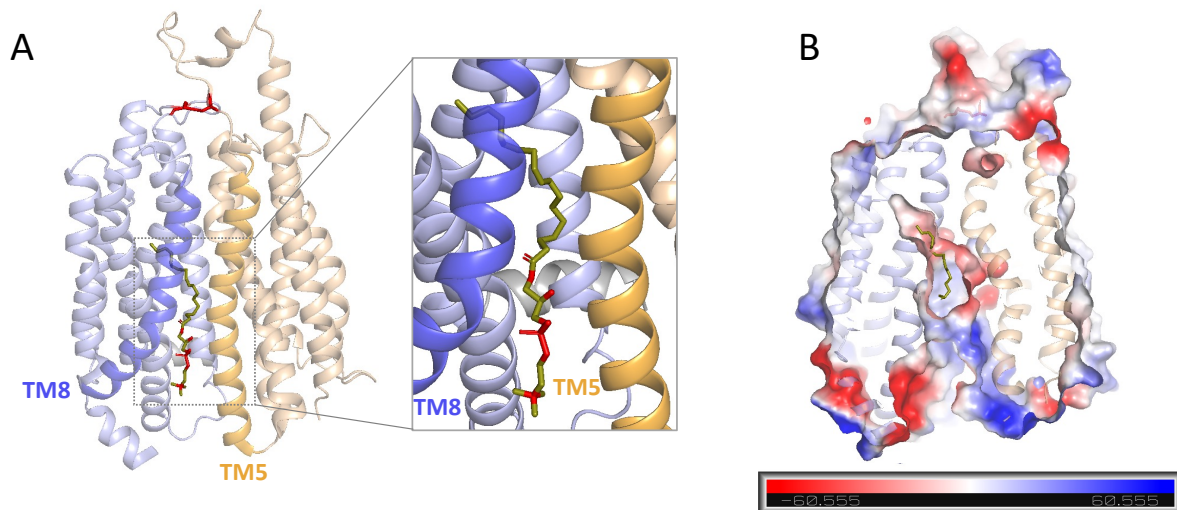


Figure 5.2: Structure of substrate-bound MFSD2A. A. Cartoon representation of the structure-bound MFSD2A with lysophosphatidylcholine (LPC). B. Vacuum electrostatic surface representation of the substrate-bound inward-facing MFSD2A. The N-terminal and C-terminal domain are colored in light orange and light blue, the connecting helical loop is colored in grey, the disulfide bridge is colored in red. LPC is shown in green and red in stick representation. PDB-ID:7mjs

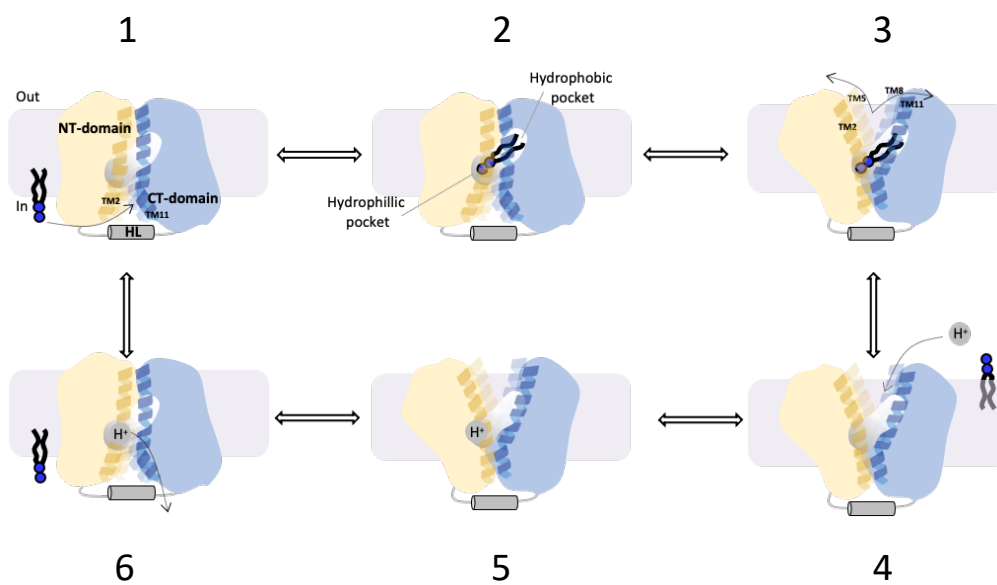


Figure 5.3: Proposed mechanism of catalyzed Glc₂-DAG transport. Schematic representation of conformational states of LtaA through the transport cycle. For explanations: see main text. N- and C-terminal domains are colored in light yellow and light blue respectively.

6. Conclusions and perspectives

Shortly before I joined this project the outward-facing crystal structure of the *S. aureus* gentiobiosyl-diacylglycerol transferase LtaA (PDB-ID: 6S7V) was determined by Bing Zhang in our lab²²⁶. This crystal structure was used as basis for functional studies into the mechanistic details of translocation of Glc₂-DAG by LtaA.

In these studies, it was shown that LtaA contains an amphiphilic cavity that was never observed before for members of the Major Facilitator Superfamily (MFS). The N-terminal cavity was made up by hydrophilic residues, whereas the C-terminal cavity consist of hydrophobic residues. First, we characterized the N-terminal cavity using a docking approach with the natural substrate of LtaA, the Glc₂-DAG and show that the sugar headgroup indeed interacts with the hydrophilic residues in the N-terminal pocket. Sequence analysis showed that these residues are conserved. We have shown using *in vivo* *S. aureus* Δ *ltaA* strains and *in vitro* flipping activity assays that these residues are indeed necessary for flipping activity. On top, we showed that gentiobiose, the diglucose sugar headgroup of the Glc₂-DAG, is able to inhibit LtaA activity *in vitro* concluding that this sugar headgroup could be a starting point for design of LtaA inhibitors.

Subsequently, we have shown that LtaA is a proton-coupled antiporter and that residue E32 plays a key role in proton-sensing activity. *In vivo* experiments using our Δ *ltaA* strain displays aberrant cell morphologies, including enlarged cells, defects in the formation and localization of the division septum and abnormal cell-wall shape. Especially at lower pH the Δ *ltaA* strain shows growth defect. The same effect was observed for mutations in residues making up the N-terminal pocket. LtaA is therefore essential to combat acid stress, which is found in its natural environment, such as the skin or nasopharynx. As we have shown that LtaA is a proton-coupled antiporter necessary to combat acid stress, we named LtaA a 'pH sensing' lipid flippase.

We thoroughly characterized LtaA, its structure and functional role, and therefore, identified the first MFS-flippase, and the first proton-coupled flippase, which raised new questions. Little was known about secondary flippases, and in particular nothing was known about MFS flippases. The next part of this project was thus to elucidate the mechanistic details of LtaA. We generated an inward-facing model using 'repeat-swap' methodology based on the outward-facing structure of LtaA, which was confirmed using crosslinking methods and mass spectrometry. Further analyses were based on both the outward-facing structure, as well as the inward-facing model. Mutants containing cysteine residues at the lateral entrances both on the cytoplasmic, as extracellular side were created. Using these cysteine mutations LtaA could be locked in both an inward-facing and an outward-facing conformation, proving that LtaA adapts alternating conformations, and both conformations were shown to be necessary for proton transport. However, the cytoplasmic lateral opening, between TM5 and TM8 is not

essential for the LtaA activity, and was also shown to be less active during MD simulations. Presumably, LtaA uses an asymmetric opening for loading of the glycolipid into the amphiphilic cavity. The exit of the glycolipid however, seems able to happen via both lateral gates. The asymmetric opening of the lateral gates, appears to be something related of all MFS flippases, as the two structures of MFSD2A suggest^{152,153}. The following question was how exactly LtaA translocates the lipid tails of the diacylglycerol across the membrane. The amphiphilic nature of the LtaA cavity suggest a 'trap-and-flip' mechanism, where the lipid tails would be enclosed in the cavity as well. Mutations of residues making up the hydrophobic cavity display severe growth defects *in vivo*, and lower flipping activity *in vitro*, highlighting the fundamental role of the hydrophobic cavity in glycolipid transport. However, it seems that the N-terminal hydrophilic cavity dictates the substrate specificity. Together, our data present strong evidence that LtaA uses a 'trap-and-flip' mechanism following the alternating-access model of transport, leading to the proposition of an almost complete model for LtaA mediated flipping.

Although we have generated an inward-facing model, and biochemical data to prove the mechanistic details of transport of the Glc₂-DAG by LtaA, direct evidence is missing. A first way to answer this question, would be the elucidation of LtaA structures in different conformations (e.g. inward-facing, occluded). These structures would provide us the information necessary to thoroughly investigate the whole transport cycle of LtaA. One way, this could be achieved would be by using cysteine mutants locked in one conformation by crosslinking. Secondly, a co-structure of LtaA with the Glc₂-DAG would provide direct information about the residues involved in recognition of the gentiobiosyl-headgroup, as well about the position of the lipid tails, and provide direct information about a 'trap-and-flip' versus 'credit-card' model. As the lipid tails are rather flexible, obtaining good density for them might be challenging. A co-structure, however, with the gentiobiose headgroup could already provide some of the answers, particularly since gentiobiose is able to inhibit the LtaA activity *in vitro*. Detailed interaction of the headgroup with LtaA in its pocket, could provide valuable information that can be used for structure-based drug design. Beside a co-structure together with the Glc₂-DAG, more information about the specificity of the length of the acyl tail would be valuable information. In particular, since it was shown for other MFS flippases that the length could be important for substrate specificity. Thirdly, structures of LtaA in a membrane embedded environment, such as nanodiscs, could give us information about the interaction of LtaA in the membrane.

The energy-profile of secondary flippases is unknown. Translocating a charged lipid across the plasma membrane might give a completely different energy landscape compared with transport of small molecules. Here, we provide evidence that LtaA is a proton-coupled antiporter, but how does LtaA flipping work in the absence of a proton-gradient? A plausible explanation is that the gradient of glycolipid is the driving source for this reaction, but this remains to be investigated. Another unanswered question is the amount of protons necessary

to translocate one glycolipid across the membrane. Probably this won't be comparable with other MFS transporters, such as sugar transporters.

LTAs are essential for the survival of *S. aureus* under stress conditions, including antibiotic stress, such as the presence of β -lactam antibiotics. Therefore, structural investigation of all enzymes in the LTA biosynthesis pathway would be interesting. The substrate of LtaA, Glc₂-DAG, is synthesized by the membrane-associated YpfP, which sequence overlaps with the sequence of LtaA⁷⁷. Most likely, there are interactions between those proteins, and perhaps also with LtaS, the third enzyme in the pathway (fig 1.6a). As a result, it would be interesting to obtain structures of protein complexes to visualize these interactions, and investigate the importance of complex formation.

As *S. aureus* is such a complex severe pathogen, and antibiotic strains are increasing, the demand for development of new antibiotics is high. In this thesis, a thorough investigation of LtaA is performed, resulting in unveiling important structural and mechanistic details that could be used in structure-based drug design for agents inhibiting the LtaA activity.

7. Bibliography

1. Thammavongsa, V., Kim, H. K., Missiakas, D. & Schneewind, O. Staphylococcal manipulation of host immune responses. *Nat. Rev. Microbiol.* **13**, 529–543 (2015).
2. Sakr, A., Brégeon, F., Mège, J. L., Rolain, J. M. & Blin, O. Staphylococcus aureus nasal colonization: An update on mechanisms, epidemiology, risk factors, and subsequent infections. *Front. Microbiol.* **9**, 1–15 (2018).
3. Parlet, C. P., Brown, M. M. & Horswill, A. R. Commensal Staphylococci Influence Staphylococcus aureus Skin Colonization and Disease. *Trends Microbiol.* **27**, 497–507 (2019).
4. Gagnaire, J. *et al.* Epidemiology and clinical relevance of Staphylococcus aureus intestinal carriage: a systematic review and meta-analysis. *Expert Rev. Anti. Infect. Ther.* **15**, 767–785 (2017).
5. Tong, S. Y. C., Davis, J. S., Eichenberger, E., Holland, T. L. & Fowler, V. G. Staphylococcus aureus infections: Epidemiology, pathophysiology, clinical manifestations, and management. *Clin. Microbiol. Rev.* **28**, 603–661 (2015).
6. Wertheim, H. F. L. *et al.* The role of nasal carriage in Staphylococcus aureus infections. *Lancet Infect. Dis.* **5**, 751–762 (2005).
7. David, M. Z. & Daum, R. S. Community-Associated Methicillin-Resistant Staphylococcus aureus: Epidemiology and Clinical Consequences of an Emerging Epidemic. *Clin. Microbiol. Rev.* **23**, 616–687 (2010).
8. Lee, A. S. *et al.* Methicillin-resistant Staphylococcus aureus. *Nat. Rev. Dis. Prim.* **4**, 1–23 (2018).
9. Turner, N. A. *et al.* Methicillin-resistant Staphylococcus aureus: an overview of basic and clinical research. *Nat. Rev. Microbiol.* **17**, 203–218 (2019).
10. Lee, A. S. *et al.* Methicillin-resistant Staphylococcus aureus. *Nat. Publ. Gr.* **4**, (2018).
11. Lade, H. & Kim, J. S. Bacterial targets of antibiotics in methicillin-resistant staphylococcus aureus. *Antibiotics* **10**, (2021).
12. World Health Organization. Global priority list of antibiotic-resistant bacteria to guide research, discovery and development of new antibiotics. (2017).
13. Richter, S. G. *et al.* Small molecule inhibitor of lipoteichoic acid synthesis is an antibiotic for Gram-positive bacteria. *Proc. Natl. Acad. Sci. U. S. A.* **110**, 3531–3536 (2013).
14. Spaan, A. N., Surewaard, B. G. J., Nijland, R. & Van Strijp, J. A. G. Neutrophils versus staphylococcus aureus: A biological tug of war. *Annu. Rev. Microbiol.* **67**, 629–650 (2013).
15. Laarman, A., Milder, F., Van Strijp, J. & Rooijackers, S. Complement inhibition by gram-positive pathogens: Molecular mechanisms and therapeutic implications. *J. Mol. Med.* **88**, 115–120 (2010).
16. Bera, A., Herbert, S., Jakob, A., Vollmer, W. & Götz, F. Why are pathogenic staphylococci so lysozyme resistant? The peptidoglycan O-acetyltransferase OatA is the major determinant for lysozyme resistance of Staphylococcus aureus. *Mol. Microbiol.* **55**, 778–787 (2005).
17. Peschel, A. *et al.* Inactivation of the *dlt* operon in Staphylococcus aureus confers sensitivity to defensins, protegrins, and other antimicrobial peptides. *J. Biol. Chem.* **274**, 8405–8410 (1999).
18. Ernst, C. M. & Peschel, A. Broad-spectrum antimicrobial peptide resistance by MprF-

- mediated aminoacylation and flipping of phospholipids. *Mol. Microbiol.* **80**, 290–299 (2011).
19. Friedrich, R. *et al.* Staphylocoagulase is a prototype for the mechanism of cofactor-induced zymogen activation. *Nature* **425**, 535–539 (2003).
 20. Becker, S., Frankel, M. B., Schneewind, O. & Missiakas, D. Release of protein A from the cell wall of *Staphylococcus aureus*. *Proc. Natl. Acad. Sci. U. S. A.* **111**, 1574–1579 (2014).
 21. Forsgren, A. & Nordstrom, K. Protein A from *Staphylococcus aureus*: Biological significance of its reaction with IgG. *Ann. NY Acad. Sci.* **236**, 252–266 (1974).
 22. Forsgren, A. & Quie, P. G. Effects of Staphylococcal Protein a on Heat Labile Opsonins. *J. Immunol.* **112**, 1177–1180 (1974).
 23. Reygaert, W. C. An overview of the antimicrobial resistance mechanisms of bacteria. *AIMS Microbiol.* **4**, 482–501 (2018).
 24. Lee, J. H. Perspectives towards antibiotic resistance: from molecules to population. *J. Microbiol.* **57**, 181–184 (2019).
 25. Cox, G. & Wright, G. D. Intrinsic antibiotic resistance: Mechanisms, origins, challenges and solutions. *Int. J. Med. Microbiol.* **303**, 287–292 (2013).
 26. Christaki, E., Marcou, M. & Tofarides, A. Antimicrobial Resistance in Bacteria: Mechanisms, Evolution, and Persistence. *J. Mol. Evol.* **88**, 26–40 (2020).
 27. Holmes, A. H. *et al.* Understanding the mechanisms and drivers of antimicrobial resistance. *Lancet* **387**, 176–187 (2016).
 28. Munita, J. M. & Arias, C. A. Mechanisms of antibiotic resistance. *Microbiol. Spectr.* **4**, 1–24 (2016).
 29. Chancey, S. T., Zähler, D. & Stephens, D. S. Acquired inducible antimicrobial resistance in Gram-positive bacteria. *Future Microbiology* **7**, 959–978 (2012).
 30. Schwarz, S., Kehrenberg, C., Doublet, B. & Cloeckaert, A. Molecular basis of bacterial resistance to chloramphenicol and florfenicol. *FEMS Microbiology Reviews* **28**, 519–542 (2004).
 31. Bush, K. & Bradford, P. A. β -lactams and β -lactamase inhibitors: An overview. *Cold Spring Harb. Perspect. Med.* **6**, a025247 (2016).
 32. Beceiro, A., Tomás, M. & Bou, G. Antimicrobial resistance and virulence: A successful or deleterious association in the bacterial world? *Clinical Microbiology Reviews* **26**, 185–230 (2013).
 33. Sauvage, E., Kerff, F., Terrak, M., Ayala, J. A. & Charlier, P. The penicillin-binding proteins: Structure and role in peptidoglycan biosynthesis. *FEMS Microbiology Reviews* **32**, 234–258 (2008).
 34. Soto, S. M. Role of efflux pumps in the antibiotic resistance of bacteria embedded in a biofilm. *Virulence* **4**, 223–229 (2013).
 35. Van Acker, H., Van Dijck, P. & Coenye, T. Molecular mechanisms of antimicrobial tolerance and resistance in bacterial and fungal biofilms. *Trends in Microbiology* **22**, 326–333 (2014).
 36. Villagra, N. A. *et al.* The carbon source influences the efflux pump-mediated antimicrobial resistance in clinically important Gram-negative bacteria. *J. Antimicrob. Chemother.* **67**, 921–927 (2012).
 37. Blair, J. M. A., Webber, M. A., Baylay, A. J., Ogbolu, D. O. & Piddock, L. J. V. Molecular mechanisms of antibiotic resistance. *Nature Reviews Microbiology* **13**, 42–51 (2015).
 38. Fisher, J. F. & Mobashery, S. β -Lactams against the Fortress of the Gram-Positive

- Staphylococcus aureus Bacterium. *Chem. Rev.* **121**, 3412–3463 (2021).
39. Katayama, Y., Ito, T. & Hiramatsu, K. A New Class of Genetic Element, Staphylococcus Cassette Chromosome mec, Encodes Methicillin Resistance in Staphylococcus aureus. **44**, (2000).
 40. Hartman, B. J. & Tomasz, A. Low-affinity penicillin-binding protein associated with β -lactam resistance in Staphylococcus aureus. *J. Bacteriol.* **158**, 513–516 (1984).
 41. Fuda, C. C. S., Fisher, J. F. & Mobashery, S. Review β -Lactam resistance in Staphylococcus aureus: the adaptive resistance of a plastic genome. *Cell. Mol. Life Sci* **62**, 2617–2633 (2005).
 42. Shalaby, M. A. W., Dokla, E. M. E., Serya, R. A. T. & Abouzid, K. A. M. Penicillin binding protein 2a: An overview and a medicinal chemistry perspective. *Eur. J. Med. Chem.* **199**, 112312 (2020).
 43. De Lencastre, H. & Tomasz, A. Reassessment of the number of auxiliary genes essential for expression of high-level methicillin resistance in Staphylococcus aureus. *Antimicrob. Agents Chemother.* **38**, 2590–2598 (1994).
 44. Berger-Bächi, B., Barberis-Maino, L., Strässle, A. & Kayser, F. H. FemA, a host-mediated factor essential for methicillin resistance in Staphylococcus aureus: Molecular cloning and characterization. *MGG Mol. Gen. Genet.* **219**, 263–269 (1989).
 45. Reynolds, P. E. *Structure, Biochemistry and Mechanism of Action of Glycopeptide Antibiotics.* *Eur. J. Clin. Microbiol. Infect. Dis* **8**, (1989).
 46. Weigel, L. M. *et al.* Genetic Analysis of a High-Level Vancomycin-Resistant Isolate of Staphylococcus aureus. *Science (80-)*. **302**, 1569–1571 (2003).
 47. Chang, S. *et al.* Infection with Vancomycin-Resistant Staphylococcus aureus Containing the vanA Resistance Gene. *N. Engl. J. Med.* **348**, 1342–1347 (2003).
 48. Mwangi, M. M. *et al.* Tracking the in vivo evolution of multidrug resistance in Staphylococcus aureus by whole-genome sequencing. *Proc. Natl. Acad. Sci. U. S. A.* **104**, 9451–9456 (2007).
 49. King, D. T., King, A. M., Lal, S. M., Wright, G. D. & Strynadka, N. C. J. Molecular Mechanism of Avibactam-Mediated β -Lactamase Inhibition. **50**, 14 (2015).
 50. Madigan, M. T., Martinko, J. M., Stahl, D. A. & Clark, D. P. *Brock Biology of Microorganisms, 13th Edition. International Microbiology* (2012). doi:10.1038/hr.2014.17
 51. Xia, G., Kohler, T. & Peschel, A. The wall teichoic acid and lipoteichoic acid polymers of Staphylococcus aureus. *Int. J. Med. Microbiol.* **300**, 148–154 (2010).
 52. Percy, M. G. & Gründling, A. Lipoteichoic acid synthesis and function in gram-positive bacteria. *Annual Review of Microbiology* **68**, 81–100 (2014).
 53. Vollmer, W., Blanot, D. & De Pedro, M. A. Peptidoglycan structure and architecture. *FEMS Microbiol. Rev.* **32**, 149–167 (2008).
 54. Kleanthous, C. & Armitage, J. P. The bacterial cell envelope. *Philosophical Transactions of the Royal Society B: Biological Sciences* **370**, 1–17 (2015).
 55. Egan, A. J. F., Errington, J. & Vollmer, W. Regulation of peptidoglycan synthesis and remodelling. *Nat. Rev. Microbiol.* doi:10.1038/s41579-020-0366-3
 56. Brown, S., Santa Maria, J. P. & Walker, S. Wall Teichoic Acids of Gram-Positive Bacteria. *Annu. Rev. Microbiol.* **67**, 313–336 (2013).
 57. Ahn, K. B., Baik, J. E., Yun, C. H. & Han, S. H. Lipoteichoic acid inhibits Staphylococcus aureus biofilm formation. *Front. Microbiol.* **9**, 1–13 (2018).
 58. Hesser, A. R. *et al.* The length of lipoteichoic acid polymers controls staphylococcus

- aureus cell size and envelope integrity. *J. Bacteriol.* **202**, 1–15 (2020).
59. Sheen, T. R. *et al.* Penetration of the blood-brain barrier by staphylococcus aureus: Contribution of membrane-anchored lipoteichoic acid. *J. Mol. Med.* **88**, 633–639 (2010).
60. Collins, L. V. *et al.* *Staphylococcus aureus* Strains Lacking D-Alanine Modifications of Teichoic Acids Are Highly Susceptible to Human Neutrophil Killing and Are Virulence Attenuated in Mice. *The Journal of Infectious Diseases* **186**, (2002).
61. Simanski, M. *et al.* Staphylococcus aureus subverts cutaneous defense by d-alanylation of teichoic acids. *Exp. Dermatol.* **22**, 294–296 (2013).
62. Weidenmaier, C. *et al.* DltABCD- and MprF-mediated cell envelope modifications of Staphylococcus aureus confer resistance to platelet microbicidal proteins and contribute to virulence in a rabbit endocarditis model. *Infect. Immun.* **73**, 8033–8038 (2005).
63. Kiriukhin, M. Y., Debabov, D. V., Shinabarger, D. L. & Neuhaus, F. C. Biosynthesis of the glycolipid anchor in lipoteichoic acid of Staphylococcus aureus RN4220: Role of YpfP, the diglucoxydiacylglycerol synthase. *J. Bacteriol.* **183**, 3506–3514 (2001).
64. Oku, Y. *et al.* Pleiotropic roles of polyglycerolphosphate synthase of lipoteichoic acid in growth of Staphylococcus aureus cells. *J. Bacteriol.* **91**, 141–151 (2009).
65. Neuhaus, F. C. & Baddiley, J. A Continuum of Anionic Charge: Structures and Functions of d -Alanyl-Teichoic Acids in Gram-Positive Bacteria. *Microbiol. Mol. Biol. Rev.* **67**, 686–723 (2003).
66. Corrigan, R. M., Abbott, J. C., Burhenne, H., Kaefer, V. & Gründling, A. C-di-amp is a new second messenger in staphylococcus aureus with a role in controlling cell size and envelope stress. *PLoS Pathog.* **7**, (2011).
67. Schneewind, O. & Missiakas, D. Lipoteichoic acids, phosphate-containing polymers in the envelope of gram-positive bacteria. *J. Bacteriol.* **196**, 1133–1142 (2014).
68. Neuhaus, F. C. & Baddiley, J. A Continuum of Anionic Charge: Structures and Functions of D- Alanyl- Teichoic Acids in Gram- Positive Bacteria. *Microbiol. Mol. Biol. Rev.* **67**, 686 (2003).
69. Weidenmaier, C. & Peschel, A. Teichoic acids and related cell-wall glycopolymers in Gram-positive physiology and host interactions. *Nature Reviews Microbiology* **6**, 276–287 (2008).
70. Kohler, T., Weidenmaier, C. & Peschel, A. Wall teichoic acid protects Staphylococcus aureus against antimicrobial fatty acids from human skin. *J. Bacteriol.* **191**, 4482–4484 (2009).
71. Ho, S. S., Michalek, S. M. & Nahm, M. H. Lipoteichoic acid is important in innate immune responses to gram-positive bacteria. *Infect. Immun.* **76**, 206–213 (2008).
72. Kang, S. S., Sim, J. R., Yun, C. H. & Han, S. H. Lipoteichoic acids as a major virulence factor causing inflammatory responses via Toll-like receptor 2. *Arch. Pharm. Res.* **39**, 1519–1529 (2016).
73. Hong, S. W. *et al.* Lipoteichoic acid of Streptococcus mutans interacts with Toll-like receptor 2 through the lipid moiety for induction of inflammatory mediators in murine macrophages. *Mol. Immunol.* **57**, 284–291 (2014).
74. Rismondo, J., Gillis, A. & Gründling, A. Modifications of cell wall polymers in Gram-positive bacteria by multi-component transmembrane glycosylation systems. *Curr. Opin. Microbiol.* **60**, 24–33 (2021).
75. Jorasch, P., Wolter, F. P., Zähringer, U. & Heinz, E. A UDP glucosyltransferase from

- Bacillus subtilis successively transfers up to four glucose residues to 1,2-diacylglycerol: Expression of ypfP in Escherichia coli and structural analysis of its reaction products. *Mol. Microbiol.* **29**, 419–430 (1998).
76. Jorasch, P., Warnecke, D. C., Lindner, B., Zähringer, U. & Heinz, E. Novel processive and nonprocessive glycosyltransferases from Staphylococcus aureus and Arabidopsis thaliana synthesize glycolipids, glycolipids, glycosphingolipids and glycosylsterols. *Eur. J. Biochem.* **267**, 3770–3783 (2000).
 77. Gründling, A. & Schneewind, O. Genes required for glycolipid synthesis and lipoteichoic acid anchoring in Staphylococcus aureus. *J. Bacteriol.* **189**, 2521–2530 (2007).
 78. Gründling, A. & Schneewind, O. Synthesis of glycerol phosphate lipoteichoic acid in Staphylococcus aureus. *Proc. Natl. Acad. Sci. U. S. A.* **104**, 8478–8483 (2007).
 79. Lu, D. *et al.* Structure-based mechanism of lipoteichoic acid synthesis by Staphylococcus aureus LtaS. *Proc. Natl. Acad. Sci. U. S. A.* **106**, 1584–1589 (2009).
 80. Vickery, C. R., Wood, B. M. K., Morris, H. G., Losick, R. & Walker, S. Reconstitution of Staphylococcus aureus Lipoteichoic Acid Synthase Activity Identifies Congo Red as a Selective Inhibitor. *J. Am. Chem. Soc.* **140**, 876–879 (2018).
 81. KOCH, H. U., HAAS, R. & FISCHER, W. The role of lipoteichoic acid biosynthesis in membrane lipid metabolism of growing Staphylococcus aureus. *Eur. J. Biochem.* **138**, 357–363 (1984).
 82. Reichmann, N. T. *et al.* Differential localization of LTA synthesis proteins and their interaction with the cell division machinery in Staphylococcus aureus. *Mol. Microbiol.* **92**, 273–286 (2014).
 83. Reichmann, N. T. & Gründling, A. Location, synthesis and function of glycolipids and polyglycerolphosphate lipoteichoic acid in Gram-positive bacteria of the phylum Firmicutes. *FEMS Microbiol. Lett.* **319**, 97–105 (2011).
 84. Osman, K. T., Du, L., He, Y. & Luo, Y. Crystal Structure of Bacillus cereus d-Alanyl Carrier Protein Ligase (DltA) in Complex with ATP. *J. Mol. Biol.* **388**, 345–355 (2009).
 85. Du, L., He, Y. & Luo, Y. Crystal structure and enantiomer selection by D-alanyl carrier protein ligase DltA from Bacillus cereus. *Biochemistry* **47**, 11473–11480 (2008).
 86. Yonus, H. *et al.* Crystal structure of DltA: Implications for the reaction mechanism of non-ribosomal peptide synthetase adenylation domains. *J. Biol. Chem.* **283**, 32484–32491 (2008).
 87. McKay Wood, B., Santa Maria, J. P., Matano, L. M., Vickery, C. R. & Walker, S. A partial reconstitution implicates DltD in catalyzing lipoteichoic acid D-alanylation. *J. Biol. Chem.* **293**, 17985–17996 (2018).
 88. Ma, D. *et al.* Crystal structure of a membrane-bound O-acyltransferase. *Nature* (2018). doi:10.1038/s41586-018-0568-2
 89. Kho, K. & Meredith, T. C. Salt-Induced Stress Stimulates a Lipoteichoic Acid-Specific Three-Component Glycosylation System in Staphylococcus aureus. *J. Bacteriol.* **200**, e00017-18 (2018).
 90. Ronald Archibald, A., Baddiley, J. & Heptinstall, S. The alanine ester content and magnesium binding capacity of walls of Staphylococcus aureus H grown at different pH values. *BBA - Biomembr.* **291**, 629–634 (1973).
 91. Hesser, A. R., Schaefer, K., Lee, W. & Walker, S. Lipoteichoic acid polymer length is determined by competition between free starter units. *Proc. Natl. Acad. Sci. U. S. A.* **117**, 29669–29676 (2020).

92. Coe, K. A. *et al.* Multi-strain Tn-Seq reveals common daptomycin resistance determinants in *Staphylococcus aureus*. *PLoS Pathog.* **15**, 1–26 (2019).
93. Fedtke, I. *et al.* A *Staphylococcus aureus* ypfP mutant with strongly reduced lipoteichoic acid (LTA) content: LTA governs bacterial surface properties and autolysin activity. *Mol. Microbiol.* **65**, 1078–1091 (2007).
94. Pasquina, L. W., Santa Maria, J. P. & Walker, S. Teichoic acid biosynthesis as an antibiotic target. *Curr. Opin. Microbiol.* **16**, 531–537 (2013).
95. Yi, X. Y. *et al.* Immunization with a peptide mimicking Lipoteichoic acid protects mice against *Staphylococcus aureus* infection. *Vaccine* **37**, 4325–4335 (2019).
96. Ohsawa, H., Baba, T., Enami, J. & Hiramatsu, K. Protective activity of anti-lipoteichoic acid monoclonal antibody in single or combination therapies in methicillin-resistant *Staphylococcus aureus*-induced murine sepsis models. *J. Infect. Chemother.* **26**, 520–522 (2020).
97. Wallin, E. & Von Heijne, G. *Genome-wide analysis of integral membrane proteins from eubacterial, archaean, and eukaryotic organisms*. *Protein Science* (Cambridge University Press, 1998).
98. Ren, Q. & Paulsen, I. T. Large-Scale Comparative Genomic Analyses of Cytoplasmic Membrane Transport Systems in Prokaryotes. *J Mol Microbiol Biotechnol* **12**, 165–179 (2007).
99. Bosshart, P. D. & Fotiadis, D. *Secondary Active Transporters*. *Subcellular Biochemistry* **92**, (Springer International Publishing, 2019).
100. Yan, N. A Glimpse of Membrane Transport through Structures—Advances in the Structural Biology of the GLUT Glucose Transporters. *J. Mol. Biol.* **429**, 2710–2725 (2017).
101. Marger, M. D. & Saier, M. H. A major superfamily of transmembrane facilitators that catalyse uniport, symport and antiport. *Trends Biochem. Sci.* **18**, 13–20 (1993).
102. Fitzgerald, G. A. *et al.* Quantifying secondary transport at single-molecule resolution. *Nature* (2019). doi:10.1038/s41586-019-1747-5
103. Saier, M. H. A Functional-Phylogenetic Classification System for Transmembrane Solute Transporters. *Microbiol. Mol. Biol. Rev.* **64**, 354–411 (2000).
104. Busch, W. & Saier, M. H. The Transporter Classification (TC) system, 2002. *Crit. Rev. Biochem. Mol. Biol.* **37**, 287–337 (2002).
105. Shi, Y. Common folds and transport mechanisms of secondary active transporters. *Annu. Rev. Biophys.* **42**, 51–72 (2013).
106. Pao, S. S., Paulsen, I. T. & Saier, M. H. Major Facilitator Superfamily (MFS). *Microbiol. Mol. Biol. Rev.* **62**, 1–34 (1998).
107. Oleg, J. Simple allosteric model for membrane pumps. *Nature* **211**, 969–970 (1966).
108. Drew, D. & Boudker, O. Shared Molecular Mechanisms of Membrane Transporters. *Annu. Rev. Biochem.* **85**, 543–572 (2016).
109. Abramson, J. *et al.* Structure and mechanism of the lactose permease of *Escherichia coli*. *Science* **301**, 610–615 (2003).
110. Huang, Y., Lemieux, M. J., Song, J., Auer, M. & Wang, D.-N. *Structure and Mechanism of the Glycerol-3-Phosphate Transporter from Escherichia coli*.
111. Yan, N. Structural investigation of the proton-coupled secondary transporters. *Curr. Opin. Struct. Biol.* **23**, 483–491 (2013).
112. Karpowich, N. & Wang, D.-N. Symmetric transporters for asymmetric transport. *Science (80-.)*. **321**, 781–782 (2008).

113. Forrest, L. R. & Rudnick, G. The rocking bundle: A mechanism for ion-coupled solute flux by symmetrical transporters. *Physiology* **24**, 377–386 (2009).
114. Yamashita, A., Singh, S. K., Kawate, T., Jin, Y. & Gouaux, E. Crystal structure of a bacterial homologue of Na⁺/Cl⁻-dependent neurotransmitter transporters. *Nature* **437**, 215–223 (2005).
115. Penmatsa, A. & Gouaux, E. The Journal of Physiology Neuroscience How LeuT shapes our understanding of the mechanisms of sodium-coupled neurotransmitter transporters. *J Physiol* **592**, 863–869 (2014).
116. Reyes, N., Ginter, C. & Boudker, O. Transport mechanism of a bacterial homologue of glutamate transporters. *Nature* (2009). doi:10.1038/nature08616
117. Lee, C. *et al.* A two-domain elevator mechanism for sodium/ proton antiport. *Nature* (2013). doi:10.1038/nature12484
118. Cao, Y. *et al.* Crystal structure of a phosphorylation-coupled saccharide transporter. *Nature* **473**, 50–54 (2011).
119. Luo, P. *et al.* Crystal structure of a phosphorylation-coupled vitamin C transporter. *Nat. Struct. Mol. Biol.* **22**, 238–241 (2015).
120. Mancusso, R., Gregorio, G. G., Liu, Q. & Wang, D. N. Structure and mechanism of a bacterial sodium-dependent dicarboxylate transporter. *Nature* **491**, 622–626 (2012).
121. Wöhlert, D., Grötzinger, M. J., Kühlbrandt, W. & Yildiz, Ö. Mechanism of Na⁺-dependent citrate transport from the structure of an asymmetrical CitS dimer. *Elife* **4**, (2015).
122. Johnson, Z. L., Cheong, C. G. & Lee, S. Y. Crystal structure of a concentrative nucleoside transporter from *Vibrio cholerae* at 2.4 Å. *Nature* **483**, 489–493 (2012).
123. Bolla, J. R. *et al.* Crystal structure of the *Alcanivorax borkumensis* YdaH transporter reveals an unusual topology. *Nat. Commun.* **6**, (2015).
124. Quistgaard, E. M., Löw, C., Guettou, F. & Nordlund, P. Understanding transport by the major facilitator superfamily (MFS): Structures pave the way. *Nat. Rev. Mol. Cell Biol.* **17**, 123–132 (2016).
125. Pak, J. E. *et al.* Structures of intermediate transport states of ZneA, a Zn(II)/proton antiporter. *Proc. Natl. Acad. Sci.* **110**, 18484–18489 (2013).
126. Bai, J. & E. Pagano, R. Measurement of Spontaneous Transfer and Transbilayer Movement of BODIPY-Labeled Lipids in Lipid Vesicles. *Biochemistry* **36**, 8840–8848 (1997).
127. Nakano, M. *et al.* Flip-Flop of Phospholipids in Vesicles: Kinetic Analysis with Time-Resolved Small-Angle Neutron Scattering. *J. Phys. Chem. B* **113**, 6745–6748 (2009).
128. Perez, C. *et al.* Structure and mechanism of an active lipid-linked oligosaccharide flippase. *Nature* **524**, 433–438 (2015).
129. Mi, W. *et al.* Structural basis of MsbA-mediated lipopolysaccharide transport. *Nature* **549**, 233–237 (2017).
130. Bi, Y., Mann, E., Whitfield, C. & Zimmer, J. Architecture of a channel-forming O-antigen polysaccharide ABC transporter. *Nature* **553**, 361–365 (2018).
131. Chen, L. *et al.* Cryo-electron microscopy structure and transport mechanism of a wall teichoic acid ABC transporter. *MBio* **11**, 1–13 (2020).
132. Timcenko, M. *et al.* Structure and autoregulation of a P4-ATPase lipid flippase. *Nature* **571**, 366–370 (2019).
133. Lyons, J. A., Timcenko, M., Dieudonné, T., Lenoir, G. & Nissen, P. P4-ATPases: how an old dog learnt new tricks — structure and mechanism of lipid flippases. *Curr. Opin.*

- Struct. Biol.* **63**, 65–73 (2020).
134. Kuk, A. C. Y., Mashalidis, E. H. & Lee, S. Y. Crystal structure of the MOP flippase MurJ in an inward-facing conformation. *Nat. Struct. Mol. Biol.* **24**, 171–176 (2017).
 135. Zhang, B. *et al.* Crystal Structures of Membrane Transporter MmpL3, an Anti-TB Drug Target. *Cell* **176**, 636–648.e13 (2019).
 136. Brunner, J. D., Lim, N. K., Schenck, S., Duerst, A. & Dutzler, R. X-ray structure of a calcium-activated TMEM16 lipid scramblase. *Nature* **516**, 207–212 (2014).
 137. Ernst, O. P. & Menon, A. K. Phospholipid scrambling by rhodopsin. *Photochem. Photobiol. Sci.* **14**, 1922–1931 (2015).
 138. Menon, A. K. Flippases. *Trends Cell Biol.* **5**, 355–360 (1995).
 139. Ruiz, N. Lipid flippases for bacterial peptidoglycan biosynthesis. *Lipid Insights* **2015**, 21–31 (2015).
 140. Breitling, J. & Aebi, M. N-linked protein glycosylation in the endoplasmic reticulum : focus on the RFT1 flippase. *Cold Spring Harb. Perspect. Biol.* **5**, 1–16 (2013).
 141. Sharom, F. J. Flipping and flopping-lipids on the move. *IUBMB Life* **63**, 736–746 (2011).
 142. Liston, S. D., Mann, E. & Whitfield, C. Glycolipid substrates for ABC transporters required for the assembly of bacterial cell-envelope and cell-surface glycoconjugates. *Biochim. Biophys. Acta - Mol. Cell Biol. Lipids* **1862**, 1394–1403 (2017).
 143. Caffalette, C. A., Corey, R. A., Sansom, M. S. P., Stansfeld, P. J. & Zimmer, J. A lipid gating mechanism for the channel-forming O antigen ABC transporter. *Nat. Commun.* **10**, 1–11 (2019).
 144. Kuk, A. C. Y., Hao, A., Guan, Z. & Lee, S. Y. Visualizing conformation transitions of the Lipid II flippase MurJ. *Nat. Commun.* **10**, (2019).
 145. Olsen, J. A., Alam, A., Kowal, J., Stieger, B. & Locher, K. P. Structure of the human lipid exporter ABCB4 in a lipid environment. *Nat. Struct. Mol. Biol.* **27**, 62–70 (2020).
 146. Kim, Y. & Chen, J. Molecular structure of human P-glycoprotein in the ATP-bound, outward-facing conformation. *Science (80-.)*. **359**, 915–919 (2018).
 147. Pomorski, T. & Menon, A. K. Lipid flippases and their biological functions. *Cell. Mol. Life Sci.* **63**, 2908–2921 (2006).
 148. Hiraizumi, M., Yamashita, K., Nishizawa, T. & Nureki, O. Cryo-EM structures capture the transport cycle of the P4-ATPase flippase. *Science (80-.)*. **365**, 1149–1155 (2019).
 149. Perez, C., Mehdipour, A. R., Hummer, G. & Locher, K. P. Structure of Outward-Facing PglK and Molecular Dynamics of Lipid-Linked Oligosaccharide Recognition and Translocation. *Structure* **27**, 669–678.e5 (2019).
 150. Qian, H. *et al.* Structure of the Human Lipid Exporter ABCA1. *Cell* **169**, 1228–1239.e10 (2017).
 151. Kumar, S., Rubino, F. A., Mendoza, A. G. & Ruiz, N. The bacterial lipid II flippase MurJ functions by an alternating-access mechanism. *J. Biol. Chem.* **294**, 981–990 (2019).
 152. Cater, R. J. *et al.* Structural basis of omega-3 fatty acid transport across the blood–brain barrier. *Nature* **595**, 315–319 (2021).
 153. Wood, C. A. P. *et al.* Structure and mechanism of blood–brain-barrier lipid transporter MFSD2A. *Nature* **596**, 444–448 (2021).
 154. Yan, N. Structural Biology of the Major Facilitator Superfamily Transporters. *Annu. Rev. Biophys.* **44**, 257–283 (2015).
 155. Reddy, V. S., Shlykov, M. a, Castillo, R., Sun, E. I. & Saier, M. H. The Major Facilitator Superfamily (MFS) Revisited. *FEBS J.* **279**, 2022–2035 (2012).

156. Saier, M. H. *et al.* The Transporter Classification Database (TCDB): Recent advances. *Nucleic Acids Res.* **44**, D372–D379 (2016).
157. Wang, S. C. *et al.* Expansion of the Major Facilitator Superfamily (MFS) to include novel transporters as well as transmembrane-acting enzymes. *Biochim. Biophys. Acta - Biomembr.* **1862**, 183277 (2020).
158. Cura, A. J. & Carruthers, A. The role of Monosaccharide Transport Proteins in carbohydrate assimilation, distribution, metabolism and homeostasis. *Compr Physiol.* **2**, 863–914 (2012).
159. Smith, D. E., Cl  men  on, B. & Hediger, M. A. Proton-coupled oligopeptide transporter family SLC15: Physiological, pharmacological and pathological implications. *Mol. Aspects Med.* **34**, 323–336 (2013).
160. Zhao, Y. *et al.* Substrate-bound structure of the E. coli multidrug resistance transporter MdfA. *Cell Res.* **25**, 1060–1073 (2015).
161. Deng, D. *et al.* Crystal structure of the human glucose transporter GLUT1. *Nature* **510**, 121–125 (2014).
162. Wright, N. J. & Lee, S.-Y. Structures of human ENT1 in complex with adenosine reuptake inhibitors. *Nat. Struct. Mol. Biol.* doi:10.1038/s41594-019-0245-7
163. Jin, J., Guffanti, A. A., Beck, C. & Krulwich, T. A. Twelve-Transmembrane-Segment (TMS) Version (  TMS VII-VIII) of the 14-TMS Tet(L) Antibiotic Resistance Protein Retains Monovalent Cation Transport Modes but Lacks Tetracycline Efflux Capacity. *J. Bacteriol.* **183**, 2667–2671 (2001).
164. Hirai, T. *et al.* Three-dimensional structure of a bacterial oxalate transporter. *Nat. Struct. Biol.* **9**, 597–600 (2002).
165. Yan, N. Structural advances for the major facilitator superfamily (MFS) transporters. *Trends Biochem. Sci.* **38**, 151–159 (2013).
166. Dang, S. *et al.* Structure of a fucose transporter in an outward-open conformation. *Nature* **467**, 734–738 (2010).
167. Newstead, S. *et al.* Crystal structure of a prokaryotic homologue of the mammalian oligopeptide-proton symporters, PepT1 and PepT2. *EMBO J.* **30**, 417–426 (2011).
168. Sun, L. *et al.* Crystal structure of a bacterial homologue of glucose transporters GLUT1-4. *Nature* **490**, 361–366 (2012).
169. Nagarathinam, K. *et al.* Outward open conformation of a Major Facilitator Superfamily multidrug/H⁺ antiporter provides insights into switching mechanism. *Nat. Commun.* **9**, (2018).
170. Bibi, E. & Kaback, H. R. In vivo expression of the lacY gene in two segments leads to functional lac permease. *Proc. Natl. Acad. Sci. U. S. A.* **87**, 4325–4329 (1990).
171. Kaback, H. R., Sahin-T  th, M. & Weinglass, A. B. The kamikaze approach to membrane transport. *Nat. Rev. Mol. Cell Biol.* **2**, 610–620 (2001).
172. Sahin-T  th, M., Dunten, R., Gonzalez, A. & Kaback, H. Functional interactions between putative intramembrane charged residues in the lactose permease of Escherichia coli. *PNAS* **89**, 10547–10551 (2014).
173. Kumar, S. *et al.* Functional and structural roles of the major facilitator superfamily bacterial multidrug efflux pumps. *Microorganisms* **8**, (2020).
174. Kakarla, P. *et al.* Functional Roles of Highly conserved amino acid sequence Motifs A and C in Solute Transporters of the Major Facilitator Superfamily. in *Drug Resistance in Bacteria, Fungi, Malaria, and Cancer* (eds. Arora, G., Sajid, A. & Kalia, V. C.) 111–140 (2017). doi:10.1007/978-3-319-48683-3

175. Henderson, P. J. & Maiden, M. C. Homologous sugar transport proteins in *Escherichia coli* and their relatives in both prokaryotes and eukaryotes. *Philos. Trans. R. Soc. Lond. B. Biol. Sci.* **326**, 391–410 (1990).
176. Stochaj, U. *et al.* Truncated forms of *Escherichia coli* lactose permease: models for study of biosynthesis and membrane insertion. *J. Bacteriol.* **170**, 2639–2645 (1988).
177. Yamaguchi, A. *et al.* Metal-tetracycline/H⁺ antiporter of *Escherichia coli* encoded by transposon Tn10. *J. Biol. Chem.* **267**, 7490–7498 (1992).
178. Jiang, D. *et al.* Structure of the YajR transporter suggests a transport mechanism based on the conserved motif A. *Proc. Natl. Acad. Sci. U. S. A.* **110**, 14664–14669 (2013).
179. Rouch, D. A., Cram, D. S., Di Berardino, D., Littlejohn, T. G. & Skurray, R. A. Efflux-mediated antiseptic resistance gene *qacA* from *Staphylococcus aureus*: common ancestry with tetracycline- and sugar-transport proteins. *Mol. Microbiol.* **4**, 2051–2062 (1990).
180. Varela, M. F., Sansom, C. E. & Griffith, J. K. Mutational analysis and molecular modelling of an amino acid sequence motif conserved in antiporters but not symporters in a transporter superfamily. *Mol. Membr. Biol.* **12**, 313–319 (1995).
181. Paulsen, I. T., Brown, M. H. & Skurray, R. A. Proton-dependent multidrug efflux systems. *Microbiol. Rev.* **60**, 575–608 (1996).
182. Yaffe, D., Radestock, S., Shuster, Y., Forrest, L. R. & Schuldiner, S. Identification of molecular hinge points mediating alternating access in the vesicular monoamine transporter VMAT2. *Proc. Natl. Acad. Sci. U. S. A.* **110**, (2013).
183. Harvat, E. M. *et al.* Lysophospholipid flipping across the *Escherichia coli* inner membrane catalyzed by a transporter (LplT) belonging to the major facilitator superfamily. *J. Biol. Chem.* **280**, 12028–12034 (2005).
184. Nguyen, L. N. *et al.* *Mfsd2a* is a transporter for the essential omega-3 fatty acid docosahexaenoic acid. *Nature* **509**, 503–506 (2014).
185. Ben-Zvi, A. *et al.* *Mfsd2a* is critical for the formation and function of the blood-brain barrier. *Nature* **509**, 507–511 (2014).
186. Vu, T. M. *et al.* *Mfsd2b* is essential for the sphingosine-1-phosphate export in erythrocytes and platelets. *Nature* **550**, 524–528 (2017).
187. Kawahara, A. *et al.* The sphingolipid transporter *Spns2* functions in migration of zebrafish myocardial precursors. *Science (80-.).* **323**, 524–527 (2009).
188. Zhu, X., Ren, K., Zeng, Y. Z., Zheng, Z. & Yi, G. H. Biological function of SPNS2: From zebrafish to human. *Mol. Immunol.* **103**, 55–62 (2018).
189. Thevelein, J. M. & Voordeckers, K. REVIEW Functioning and Evolutionary Significance of Nutrient Transceptors. doi:10.1093/molbev/msp168
190. Diallinas, G. Transceptors as a functional link of transporters and receptors. *Microb. Cell* **4**, 69–73 (2017).
191. Gojon, A., Krouk, G., Perrine-Walker, F. & Laugier, E. Nitrate transceptor(s) in plants. *J. Exp. Bot.* **62**, 2299–2308 (2011).
192. Ho, C. H., Lin, S. H., Hu, H. C. & Tsay, Y. F. CHL1 Functions as a Nitrate Sensor in Plants. *Cell* **138**, 1184–1194 (2009).
193. Schwöppe, C., Winkler, H. H. & Neuhaus, H. E. Properties of the glucose-6-phosphate transporter from *Chlamydia pneumoniae* (HPTcp) and the glucose-6-phosphate sensor from *Escherichia coli* (UhpC). *J. Bacteriol.* **184**, 2108–2115 (2002).
194. Schwöppe, C., Winkler, H. H. & Neuhaus, H. E. Connection of transport and sensing by

- UhpC, the sensor for external glucose-6-phosphate in *Escherichia coli*. *Eur. J. Biochem.* **270**, 1450–1457 (2003).
195. Özcan, S., Dover, J. & Johnston, M. Glucose sensing and signaling by two glucose receptors in the yeast *Saccharomyces cerevisiae*. *EMBO J.* **17**, 2566–2573 (1998).
196. Moriya, H. & Johnston, M. Glucose sensing and signaling in *Saccharomyces cerevisiae* through the Rgt2 glucose sensor and casein kinase I. *Proc. Natl. Acad. Sci. U. S. A.* **101**, 1572–1577 (2004).
197. Scharff-Poulsen, P., Moriya, H. & Johnston, M. Genetic analysis of signal generation by the Rgt2 glucose sensor of *Saccharomyces cerevisiae*. *G3 Genes, Genomes, Genet.* **8**, 2685–2696 (2018).
198. Ishida, H. *et al.* Cryo-EM structures of Toll-like receptors in complex with UNC93B1. *Nat. Struct. Mol. Biol.* **28**, (2021).
199. Huang, Y., Lemieux, M. J., Song, J., Auer, M. & Wang, D. N. Structure and mechanism of the glycerol-3-phosphate transporter from *Escherichia coli*. *Science (80-.)*. **301**, 616–620 (2003).
200. Drew, D., North, R. A., Nagarathinam, K. & Tanabe, M. Structures and General Transport Mechanisms by the Major Facilitator Superfamily (MFS). *Chemical Reviews* **121**, 5289–5335 (2021).
201. Parker, J. L. *et al.* Structural basis of antifolate recognition and transport by PCFT. *Nature* (2021). doi:10.1038/s41586-021-03579-z
202. Ronald Kaback, H. & Guan, L. It takes two to tango: The dance of the permease. (2019). doi:10.1085/jgp.201912377
203. Fluman, N. & Bibi, E. Bacterial multidrug transport through the lens of the major facilitator superfamily. *Biochim. Biophys. Acta - Proteins Proteomics* **1794**, 738–747 (2009).
204. Heng, J. *et al.* Substrate-bound structure of the *E. coli* multidrug resistance transporter MdfA. *Cell Res.* **25**, 1060–1073 (2015).
205. Wu, H. H., Symersky, J. & Lu, M. Structure and mechanism of a redesigned multidrug transporter from the Major Facilitator Superfamily. *Sci. Rep.* **10**, 1–15 (2020).
206. Liu, M., Heng, J., Gao, Y. & Wang, X. Crystal structures of MdfA complexed with acetylcholine and inhibitor reserpine. *Biophys. Reports* **2**, 78–85 (2016).
207. Yin, Y., He, X., Szewczyk, P., Nguyen, T. & Chang, G. Structure of the Multidrug Transporter EmrD from *Escherichia coli*. *Science* **312**, 741–744 (2006).
208. Fukuda, M. *et al.* Structural basis for dynamic mechanism of nitrate/nitrite antiport by NarK. *Nat. Commun.* **6**, (2015).
209. Qureshi, A. A. *et al.* The molecular basis for sugar import in malaria parasites. *Nature* **578**, 321–325 (2020).
210. Drew, D. & Boudker, O. Shared Molecular Mechanisms of Membrane Transporters. *Annu. Rev. Biochem.* **85**, 543–572 (2016).
211. Nomura, N. *et al.* Structure and mechanism of the mammalian fructose transporter GLUT5. *Nature* **526**, 397–401 (2015).
212. Fowler, P. W. *et al.* Gating topology of the proton-coupled oligopeptide symporters. *Structure* **23**, 290–301 (2015).
213. Deng, D. *et al.* Molecular basis of ligand recognition and transport by glucose transporters. *Nature* **526**, 391–396 (2015).
214. Smirnova, I. N., Kasho, V. & Kaback, H. R. Protonation and sugar binding to LacY. *Proc. Natl. Acad. Sci. U. S. A.* **105**, 8896–8901 (2008).

215. Parker, J. L. *et al.* Proton movement and coupling in the POT family of peptide transporters. doi:10.1073/pnas.1710727114
216. Ullmann, G. M. *et al.* Investigating the mechanisms of photosynthetic proteins using continuum electrostatics. *Photosynth. Res.* **97**, 33–53 (2008).
217. Antosiewicz, J. M. & Shugar, D. Poisson-Boltzmann continuum-solvation models: Applications to pH-dependent properties of biomolecules. *Mol. Biosyst.* **7**, 2923–2949 (2011).
218. Madej, M. G., Sun, L., Yan, N. & Kaback, H. R. Functional architecture of MFS D-glucose transporters. *Proc. Natl. Acad. Sci. U. S. A.* **111**, (2014).
219. Zhao, Y. *et al.* Crystal structure of the E. coli peptide transporter YbgH. *Structure* **22**, 1152–1160 (2014).
220. Carrasco, N. *et al.* Characterization of Site-Directed Mutants in the lac Permease of Escherichia coli. 2. Glutamate-325 Replacements. *Biochemistry* **28**, 2533–2539 (1989).
221. Ethayathulla, A. S. *et al.* Structure-based mechanism for Na(+)/melibiose symport by MelB. *Nat. Commun.* **5**, 3009 (2014).
222. Neyfakh, A. A. Mystery of multidrug transporters: the answer can be simple. *Mol. Microbiol.* **44**, 1123–1130 (2002).
223. Lin, Y., Deepak, R. N. V. K., Zheng, J. Z., Fan, H. & Zheng, L. A dual substrate-accessing mechanism of a major facilitator superfamily protein facilitates lysophospholipid flipping across the cell membrane. *J. Biol. Chem.* **293**, 19919–19931 (2018).
224. Angers, M., Uldry, M., Kong, D., Gimble, J. M. & Jetten, A. M. Mfsd2a encodes a novel major facilitator superfamily domain-containing protein highly induced in brown adipose tissue during fasting and adaptive thermogenesis. *Biochem. J.* **416**, 347–355 (2008).
225. Quek, D. Q. Y., Nguyen, L. N., Fan, H. & Silver, D. L. Structural insights into the transport mechanism of the human sodium-dependent lysophosphatidylcholine transporter MFSD2A. *J. Biol. Chem.* **291**, 9383–9394 (2016).
226. Zhang, B. *et al.* Structure of a proton-dependent lipid transporter involved in lipoteichoic acids biosynthesis. *Nat. Struct. Mol. Biol.* **27**, 561–569 (2020).
227. Iancu, C. V., Zamoon, J., Sang, B. W., Aleshin, A. & Choe, J. Y. Crystal structure of a glucose/H⁺ symporter and its mechanism of action. *Proc. Natl. Acad. Sci. U. S. A.* **110**, 17862–17867 (2013).
228. Verhalen, B. *et al.* Energy transduction and alternating access of the mammalian ABC transporter P-glycoprotein. *Nat. Publ. Gr.* **543**, (2017).
229. Shukla, S. & Baumgart, T. Enzymatic trans-bilayer lipid transport: Mechanisms, efficiencies, slippage, and membrane curvature. *Biochim. Biophys. Acta - Biomembr.* **1863**, 183534 (2021).
230. Klingenberg, M. Ligand-protein interaction in biomembrane carriers. The induced transition fit of transport catalysis. *Biochemistry* **44**, 8563–8570 (2005).
231. Putman, M., van Veen, H. W. & Konings, W. N. Molecular Properties of Bacterial Multidrug Transporters. *Microbiol. Mol. Biol. Rev.* **64**, 672–693 (2000).
232. Rubino, F. A., Kumar, S., Ruiz, N., Walker, S. & Kahne, D. E. Membrane Potential Is Required for MurJ Function. *J. Am. Chem. Soc.* **140**, 4481–4484 (2018).
233. Childs, W. C. & Neuhaus, F. C. *Biosynthesis of D-Alanyl-Lipoteichoic Acid: Characterization of Ester-Linked D-Alanine in the In Vitro-Synthesized Product.* *JOURNAL OF BACTERIOLOGY* **143**, (1980).
234. Lehar, S. M. *et al.* Novel antibody-antibiotic conjugate eliminates intracellular S.

- aureus. *Nature* **527**, 323–328 (2015).
235. Flannagan, R. S., Heit, B. & Heinrichs, D. E. Intracellular replication of *Staphylococcus aureus* in mature phagolysosomes in macrophages precedes host cell death, and bacterial escape and dissemination. *Cell. Microbiol.* **18**, 514–535 (2016).
236. Surewaard, B. G. J. *et al.* Identification and treatment of the *Staphylococcus aureus* reservoir in vivo. *J. Exp. Med.* **213**, 1141–1151 (2016).
237. Gresham, H. D. *et al.* Survival of *Staphylococcus aureus* Inside Neutrophils Contributes to Infection. *J. Immunol.* **164**, 3713–3722 (2000).
238. Flannagan, R. S., Cosío, G. & Grinstein, S. Antimicrobial mechanisms of phagocytes and bacterial evasion strategies. *Nat. Rev. Microbiol.* **7**, 355–366 (2009).
239. Perland, E., Bagchi, S., Klaesson, A. & Fredriksson, R. Characteristics of 29 novel atypical solute carriers of major facilitator superfamily type: Evolutionary conservation, predicted structure and neuronal co-expression. *Open Biol.* **7**, (2017).
240. Yardeni, E. H., Mishra, S., Stein, R. A., Bibi, E. & Mchaourab, H. S. The Multidrug Transporter MdfA Deviates from the Canonical Model of Alternating Access of MFS Transporters. *J. Mol. Biol.* **432**, 5665–5680 (2020).
241. Nikaido, H. Structure and mechanism of RND-type multidrug efflux pumps. *Adv. Enzymol. Relat. Areas Mol. Biol.* **77**, 1–60 (2010).

8. Curriculum Vitae

Elisabeth Lambert

Personal details

Date of birth 19/03/1994
Place of birth Gent, Belgium
Nationality Belgian
Email elisabeth.lambert@live.com

Education

PhD in Structural Biology 10/2017-12/2021
Research group of Prof. Camilo Perez, *Biozentrum, University of Basel, Switzerland*
“Investigation of the mechanistic basis of substrate recognition and translocation by the MFS flippase LtaA”

M. Sc. in Biochemistry and Biotechnology 09/2015-07/2017
Ghent University, Belgium
Cum Laude
Master thesis in the laboratory of Prof. Savvas Savvides “Towards structural insights into the murine Interleukin-12 signaling assembly: crystal structure of murine IL-12”

Erasmus exchange student, Leiden University, The Netherlands 09/2015-07/2016
Research project in group of Sander van Kasteren “Production and Crystallization of Major Histocompatibility Complex I”

B.Sc. in Biochemistry and Biotechnology 09/2012-09/2015
Ghent University, Belgium
Cum Laude

Secondary school Diploma, Science and Mathematics 2012
Sint-Lievenscollege, Gent, Belgium

Publications

Bing Zhang*, Xue Liu*, **Elisabeth Lambert***, Guillaume Mas, Sebastian Hiller, Jan-Willem Veening, Camilo Perez “Structure of a proton-dependent lipid transporter involved in lipoteichoic acids biosynthesis.” *Nat Struct Mol Biol* 27, 561–569 (2020). <https://doi.org/10.1038/s41594-020-0425-5>

Elisabeth Lambert, Ahmad Reza Mehdipour, Alexander Schmidt, Gerhard Hummer, Camilo Perez “Evidence for a ‘trap-and-flip’ mechanism in a proton-dependent lipid transporter” *bioRxiv* 2021.08.05.453402; doi: <https://doi.org/10.1101/2021.08.05.453402>

Scholarships

Fellowship for Excellence at the Biozentrum, University of Basel, Switzerland 10/2017-12/2020

Erasmus fellowship, Leiden University, the Netherlands 09/2015-07/2016

Teaching

Teaching assistant for the structural biology blockcourse, University of Basel, Switzerland 09/2020-10/2021